Colors and shapes of light from the Fast Radio Burst 20180916B

Dissertation
zur
Erlangung des Doktorgrades (Dr. rer. nat.)
der
Mathematisch-Naturwissenschaftlichen Fakultät
der
Rheinischen Friedrich-Wilhelms-Universität Bonn

vorgelegt von
suryarao bethapudi
aus
Nanda, Indien

Bonn, 02.12.2025

Angefertigt mit Genehmigung der Mathematisch-Naturwissenschaftlichen Fakultät der Rheinischen Friedrich-Wilhelms-Universität Bonn

Gutachter/Betreuer:	Prof. Dr. Michael Kramer
Gutachter:	Prof. Dr. Norbert Langer
Tag der Promotion:	09.03.2026
Erscheinungsjahr:	2026

for my dead father
für meinen verstorbenen Vater
chanipaina na nana kosam

Abstract

This thesis presents three works that study spectral and polarization properties of emissions from an extragalactic transient source, Fast Radio Burst 20180916B. This source emits bursts of emission, with milliseconds of duration and hundreds of MHz of bandwidth, which have been detected across frequencies ranging from 100 MHz to 6 GHz. The transient source was localized to the outer edge of a quiescent spiral galaxy at a redshift of 0.0337. Observations with the Hubble Space Telescope or with the European VLBI Network did not reveal any persistent source at the FRB location. Although bursts from this source follow Poissonian statistics up to timescales of hours, they reveal a periodic behavior on timescales of days, wherein the bursts detected at 600 MHz only appear in a five-day active window that is periodic with a period of 16.34 days. Several low frequency ($\lesssim$ 1 GHz) studies showed variations in the active window against observing frequency, such that active windows shift and scale with frequency. Polarimetric studies determined bursts to have high linear polarization fractions, almost no circular polarization fractions, and unchanging orientations (or Position Angle, PA) of the bursts. Continuous polarimetric monitoring also revealed the Rotation Measure (RM) of the bursts to vary in steps, where RM only varies stochastically during certain times and secularly during a specific epoch.

The first work of this thesis studies the variations in the active windows as a function of frequency. The frequency dependency in periodicity is termed “chromaticity”. This work included modeling of the active windows of low-frequency detections of bursts using power law models and testing the model at high frequencies by conducting observations with the 100-meter Effelsberg Radio Telescope at 4-8 GHz in the predicted active windows. The observations led to the first high-frequency detection of bursts from this source. Detection of the bursts confirmed the chromaticity and the burst activity at higher frequencies.

The second work of this thesis involves tracking the RM variations of the bursts detected using upgraded Giant Metrewave Radio Telescope (uGMRT) in 550-750 MHz. First, a versatile polarization calibration pipeline was developed, that can work with different calibration sources. The pipeline was used to polarization calibration all the bursts. Thereafter, an RM measurement strategy was devised, which was used to make all the measurements. The RM measurements corroborated with measurements made using different instruments. Additionally, the sensitivity of uGMRT allowed for a thorough study of burst statistics against their fluences.

The third and final work of this thesis measures and interprets PAs of the bursts detected using uGMRT. It begins with fitting one RM and one PA to the bursts of an observation and showing that PAs vary less than 7 degrees within four hours. In addition, it reports the PA variations to follow the periodicity of the source, suggesting that PA variations and periodicity have the same cause. It also tentatively reports PA to vary within an active window by few deg hr^{-1}, and from one active window to another at the same phase by 0.1 deg day^{-1}. Notwithstanding, the non-variability of PA is used to set constraints on the source models that explain the long-term periodicity.

If the frequency of light can be perceived as its color, polarization of light can be perceived as its shape. Therefore, the title of the thesis reads

Colors and shapes of light from the
Fast Radio Burst 20180916B.

The Chapter 1 of this thesis shows how polarization of light traces an ellipse that has an orientation, an axial ratio, and a sense of rotation. Thereafter, it derives independent and additive parameterization of polarization, proposed by G. G. Stokes and named in his honor, the Stokes parameters. Lastly, the effect of Faraday rotation on the orientation of polarization of light is understood.

The Chapter 2 of the thesis describes the phenomena of Fast Radio Bursts. It also describes the process of searching for a Fast Radio Burst, measuring different types of observables from the bursts, and the range of sciences that can be done with the measurements. The Chapter 3 of this thesis focuses solely on Fast Radio Burst 20180916B, which is regarded as the protagonist of this thesis. It contains all the known information about the source in one place. The Chapters 4, 5, and 6 are the science chapters of this thesis, which describe my contributions to the aforementioned three works of this thesis. Lastly, the final Chapter 7 concludes this thesis by describing my aspirations and motivations for my future.

Contents

CHAPTER 1

Theory

Physics is best expressed with Mathematics as the language. Therefore, this chapter lays the mathematical foundation of everything that is deemed necessary to fully appreciate this thesis. The first half of this chapter starts with defining light, polarization of light and defining Stokes parameters using the procedure first laid out by G. G. Stokes in 1851. It is seen that a natural consequence of following Stokes formalism leads to the Poincare sphere. Lastly, the simplest linear transformation of polarization of light is discussed which leads to Jones/Müller matrix formalism. In the second half, the propagation of light through unmagnetized and magnetized plasma is dealt with the help of Ohm's law. The effect of magnetic field on polarization which leads to Faraday rotation is highlighted.

1.1 Light

Light is the vacuum solution of the Maxwells equations, that is, when there is no source or medium present. Maxwells equations in the form put by Heaviside in SI units are (Hampshire, 2018):

$$\begin{aligned} \nabla \cdot \mathbf{E} &= \frac{\rho}{\epsilon_0} \\ \nabla \times \mathbf{E} &= -\frac{\partial \mathbf{B}}{\partial t} \\ \nabla \cdot \mathbf{B} &= 0 \\ \nabla \times \mathbf{B} &= \mu_0 \left(\mathbf{J} + \epsilon_0 \frac{\partial \mathbf{E}}{\partial t} \right) \end{aligned} , \tag{1.1}$$

where ϵ_0 is electric permittivity and μ_0 is the magnetic permeability. Vacuum solutions can be recovered by setting $\rho = 0$ and $\mathbf{J} = 0$. Then, using the identity that for some vector field $\mathbf{X}$,

$$\nabla \times (\nabla \times \mathbf{X}) = \nabla(\nabla \cdot \mathbf{X}) - \nabla^2 \mathbf{X}$$

yields,

$$\begin{aligned} \mu_0 \epsilon_0 \frac{\partial^2 \mathbf{E}}{\partial t^2} - \nabla^2 \mathbf{E} &= 0 \\ \mu_0 \epsilon_0 \frac{\partial^2 \mathbf{B}}{\partial t^2} - \nabla^2 \mathbf{B} &= 0 \end{aligned} . \tag{1.2}$$

Eq. 1.2 can be recognized as a wave equations of **E** and **B**. The known values of μ_0 and ϵ_0 suggest $(\mu_0\epsilon_0)^{-\frac{1}{2}} = c$, where c is the speed of light. It was actually on this basis, light is understood as an electromagnetic disturbance propagating through space and time.

The most basic solutions of the above equation are the plane wave solutions of light:

$$\begin{aligned} \mathbf{E}(\mathbf{r},t) &= \Re\left\{\mathbf{E_0}\ \exp\left[j\left(\mathbf{k}\cdot\mathbf{r} - \omega t\right)\right]\right\} \\ \mathbf{B}(\mathbf{r},t) &= \Re\left\{\mathbf{B_0}\ \exp\left[j\left(\mathbf{k}\cdot\mathbf{r} - \omega t\right)\right]\right\} \end{aligned}. \tag{1.3}$$

The **k** is known as the wave-vector whose magnitude is the inverse wavelength and direction is the propagation direction. ω is the angular frequency of light. $\mathbf{E_0}$ and $\mathbf{B_0}$ are three dimensional complex vectors which completely parameterize the EM wave. The electric and magnetic fields are to be real at all space and time, so only the real part of RHS is taken using $\Re$.

Putting Eq. 1.3 into Eq. 1.2 yields relations between wave-vector **k** and ω, which are known as dispersion relations:

$$k^2 = \omega^2 c^2. \tag{1.4}$$

In addition, taking $\nabla\cdot$ of Eq. 1.3 and from source free Maxwells equations yield,

$$\mathbf{k}\cdot\mathbf{E} = \mathbf{k}\cdot\mathbf{B} = 0.$$

Vanishing dot products suggest the propagation vector is perpendicular to both electric and magnetic fields. Such waves where the disturbances are perpendicular to the propagation direction are called transverse waves. There are three degrees of freedom for **E**. However, the electric field has to be perpendicular to propagation direction, which implies that there are only two degrees of freedom. These two degrees of freedom correspond to polarization of light.

1.2 Polarization

The two degrees of freedom of **E** are to be characterized. Assume the direction of propagation is $\hat{z}$, then a right-handed Cartesian coordinate system such that $\hat{z}$-axis is along the direction of propagation can be easily constructed. Then, $\mathbf{k} = k\hat{z}$ and to ensure $\mathbf{k}\cdot\mathbf{E}$ vanishes, the z component of $\mathbf{E_0}$, $E_{0,z}0$, has to be zero. That implies, $\mathbf{E_0}$ is a complex vector only consisting of $E_{0,x}$ and $E_{0,y}$. Then, if **E** is decomposed into $\hat{x}$ and $\hat{y}$ axes, because of Vector law of addition, the following holds:

$$|E_{x,0}|^2 + |E_{y,0}|^2 = |E_0|^2. \tag{1.5}$$

The modulus is also required since each of $E_{x,0}$ and $E_{y,0}$ is complex. Both $|E_{x,0}|$ and $|E_{y,0}|$ can be parameterized as a function of arbitrary angle ψ such that $|E_{x,0}| = |E_0|\ \cos(\psi)$ and $|E_{y,0}| = |E_0|\ \sin(\psi)$. Moreover, since Eq. 1.5 only involves magnitudes, there can be any arbitrary phases to each of $E_{x,0}$ and $E_{y,0}$, which will be denoted by ϕ_x and ϕ_y respectively. Therefore, the most basic form of solutions of Eq. 1.5 is

$$\mathbf{E_0} = |E_0| \begin{bmatrix} \cos(\psi)\ \exp(j\phi_x) \\ \sin(\psi)\ \exp(j\phi_y) \end{bmatrix}.$$

Which ultimately means,

$$\mathbf{E}(\mathbf{r},t) = \begin{bmatrix} E_x \\ E_y \end{bmatrix} = |E_0| \, \Re \begin{bmatrix} \cos(\psi) \; \exp\left[j \; (\phi_x - \omega \, t)\right] \\ \sin(\psi) \; \exp\left[j \; (\phi_y - \omega \, t)\right] \end{bmatrix}. \tag{1.6}$$

Eq. 1.6 is expressed in the $z = 0$ plane. It can be studied in any other arbitrary plane by simply shifting z. $\Re$ refers to taking the real part.

Two complex quantities, $E_{0,x}$ and $E_{0,y}$, together contain four degrees of freedom. The complete characterization of polarization thus requires four parameters. At this point, these four parameters are

$$\left\{|E_0|, \psi, \phi_x, \phi_y\right\}.$$

Note that there is only one intensity-like quantity and the rest are phase-like quantities.

1.2.1 Ellipse

All the possible values for E_x and E_y at all times can be realized by eliminating the time dependency in Eq. 1.6, which yields,

$$\frac{E_x^2}{\cos^2(\psi)} + \frac{E_y^2}{\sin^2(\psi)} - 4E_x \, E_y \frac{\cos(\delta)}{\sin(2\psi)} = |E_0|^2 \; \sin^2(\delta). \tag{1.7}$$

δ is defined to be the phase difference such that $\delta = \phi_x - \phi_y$. Eq. 1.7 is an equation of ellipse. It is the path the electric field vector traces in one cycle in the fixed plane (in this case, $z = 0$ plane). This shape that light draws is polarization. It is not static but dynamic as light draws this shape every cycle.

Fig. 1.1 shows the polarization ellipse for $\psi = 75°$ and $\delta = 65°$. Although there is no time or phase dependency in Eq. 1.7, phase dependency can be brought in using Eq. 1.6. This phase dependency is expressed using color which is mapped using the colorbar. The black dashed line is along the major axis of the ellipse and the red dotted line is along the minor axis of the ellipse. The sense of rotation, that is the direction in which the phase increases, can be visualized by the progression of colors from red to violet. It is also denoted by the rotating arrow symbol.

A straightforward observation is that the polarization ellipse does not depend on absolute phases but only on phase difference δ. More features of polarization ellipse can be realized by observing the ellipses for certain special values of (ψ, δ), as shown in Fig. 1.2. Figure shows $(60°, 45°)$ in (a), $(60°, -45°)$ in (b), $(240°, 45°)$ in (c) and $(240°, -45°)$ in (d). The intensities of (a) and (c) are chosen to be less than that of (b) and (d). The black filled diamond is the start of the trace. The major axis of the polarization ellipse is plotted with dotted lines. Following observations can be made:

1. The magnitudes of major and minor axes are the same when the intensities are same. More importantly, the ratio of the magnitudes of Minor axis to Major axis does not change.

2. The sign of δ wholly determines the handedness of the light. That is, the sense of rotation of the light.

3. The major axis line is the same irrespective of sign of δ and of 180° offset to ψ. Which implies, the major axis does not depend on handedness and is 180° degenerate with respect to ψ. Implying, the major axis is not a direction but orientation.

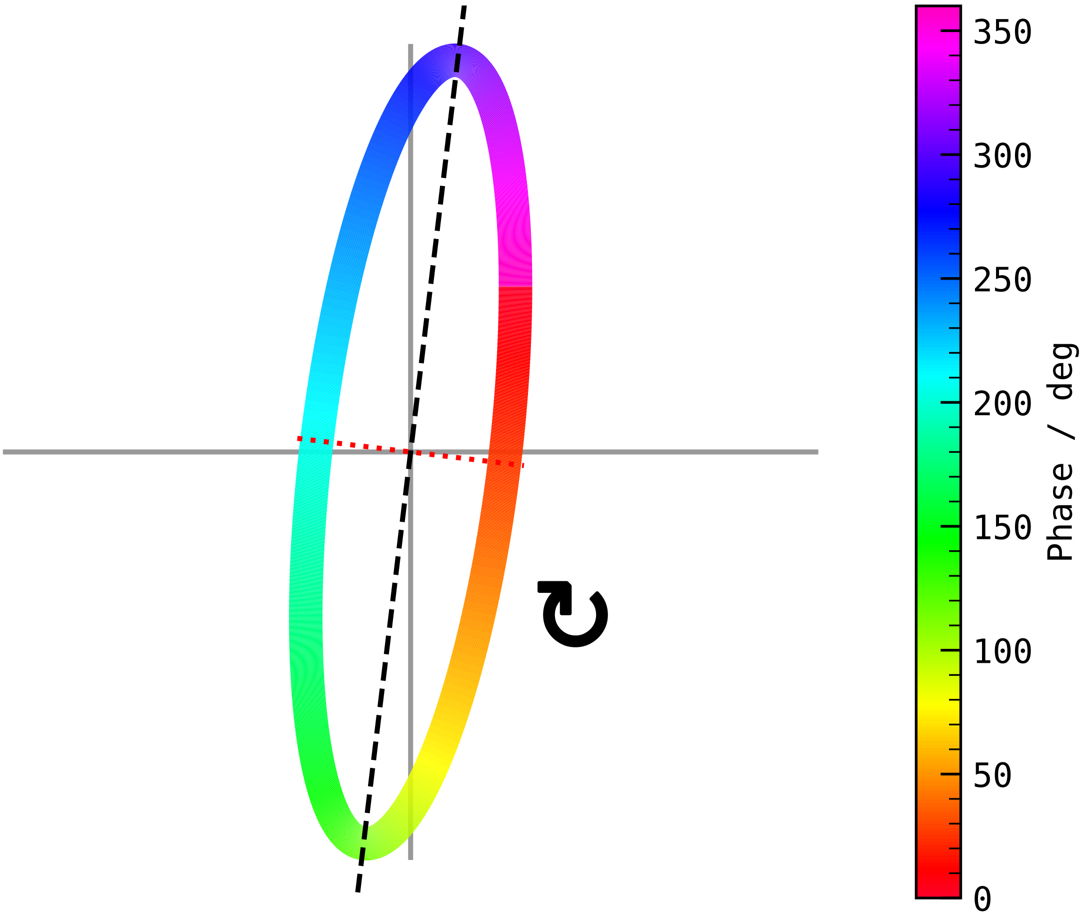

Figure 1.1: Polarization ellipse of light. The color of ellipse maps to the phase in degrees. The gray lines form the coordinate axis. The sense of rotation is also denoted by the rotating arrow symbol. The black dashed line is along the major axis of the ellipse. The dotted red line is along the minor axis of the ellipse. This Polarization Ellipse corresponds to $\psi = 75^\circ$ and $\delta = 65^\circ$ using Eq. 1.7.

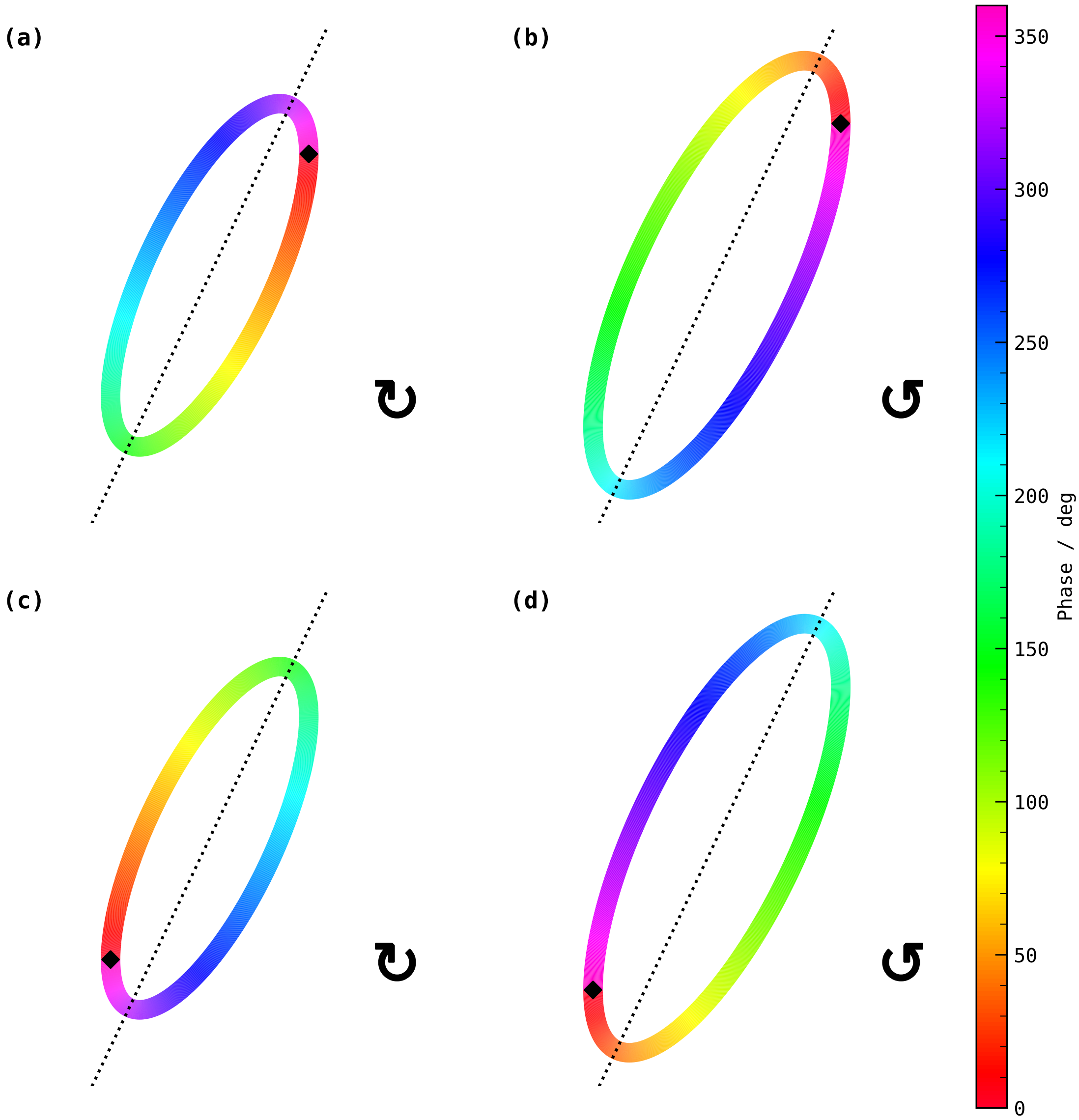

Figure 1.2: Polarization ellipses for different ψ and δ. The start point is denoted by the diamond. The dotted line is the major axis of the Polarization ellipse. (ψ, δ) shown are (a) $(60^\circ, 45^\circ)$, (b) $(60^\circ, -45^\circ)$, (c) $(240^\circ, 45^\circ)$ and (d) $(240^\circ, -45^\circ)$.

Each of these observations assist in parameterizing the polarization ellipse such that the parameterization does not depend on intensities or phases. Let the orientation of the major axis of the polarization ellipse be denoted by α and let $\tan(\beta)$ denote the signed ratio of the magnitudes of the axes, where the sign of β is decides the sign of δ. All the phase terms of the wave can be collected into $\phi + \epsilon$, where

$$\phi = \mathbf{k} \cdot \mathbf{r} - \omega t \tag{1.8}$$

and ϵ is arbitrary phase offset. Then, trace of the electric field vector (or shape of the light) can be shown to be

$$\begin{bmatrix} E_x \\ E_y \end{bmatrix} = |E| \begin{bmatrix} \cos(\alpha) & -\sin(\alpha) \\ \sin(\alpha) & \cos(\alpha) \end{bmatrix} \begin{bmatrix} \cos(\beta) & 0 \\ 0 & \sin(\beta) \end{bmatrix} \begin{bmatrix} \cos(\phi + \epsilon) \\ \sin(\phi + \epsilon) \end{bmatrix}. \tag{1.9}$$

However, it was noted that there are four degrees of freedom in polarization. Two of them are α and β. The remaining two are the total intensity of light and intensity of polarized component of light, which need not be the same. That is, the light need not be completely polarized. Insofar, a hidden assumption has been that light is completely polarized, that is, intensity of polarized light is the total intensity. This assumption need not hold. Therefore, the four parameters that fully characterize polarization of light are

$$\left\{ |E_0|, |E_0|_p, \alpha, \beta \right\},$$

where $|E_0|_p$ denotes the intensity of the polarized light.

However, in a general setting, only magnitude-like quantities can be directly measured. Meaning, angle-like quantities, like α or β, cannot be directly measured. Therefore, it would be much more beneficial to characterize the polarization of light through magnitude-like quantities. The search for a polarization representation which is intensity-like and fully specify the two spatial complex degrees of freedom leads to Stokes parameters.

1.2.2 Stokes parameters

This whole section is a mere rephrasing of the original work done by Stokes in his seminal paper - G. G. Stokes (1851), *On the Composition and Resolution of Streams of Polarized Light from different Sources*, Transactions of the Cambridge Philosophical Society **9** 399, https://doi.org/. The core idea of Stokes was to formulate such an intensity representation of polarization of light which adds linearly when combining differently polarized light sources. G. G. Stokes worked on this formulation around the time when the theory of interference of light was newly established. Whereas the interference of light fluctuated the intensity of light that depended on constructive or destructive interference, polarization of light did not show such phase dependency. This fact led Stokes to formulate his own polarization representation such that the resultant representation of polarization of light is the sum of individual representations of polarizations of component light. That is, sum of intensities does not depend on any phase differences.

The procedure of Stokes is as follows: A given elliptically polarized light with the parameters α, β, intensity c_0^2 and absolute phase offset ϵ, is decomposed into two different rays of elliptical component light, each of which is parameterized by α_i, β_i, intensities c_i^2 and absolute phases ϵ_i for indices $i = 1, 2$, such that the superposition of the component rays is the same as the given ray of light. The superposition is visualized using each individual's polarization ellipses, as shown in Fig. 1.3. A decomposition of a ray of generic elliptical polarized light into two different rays of elliptical polarized light is always possible. Moreover, this decomposition is non-unique, that is, many pairs of component light exist which result

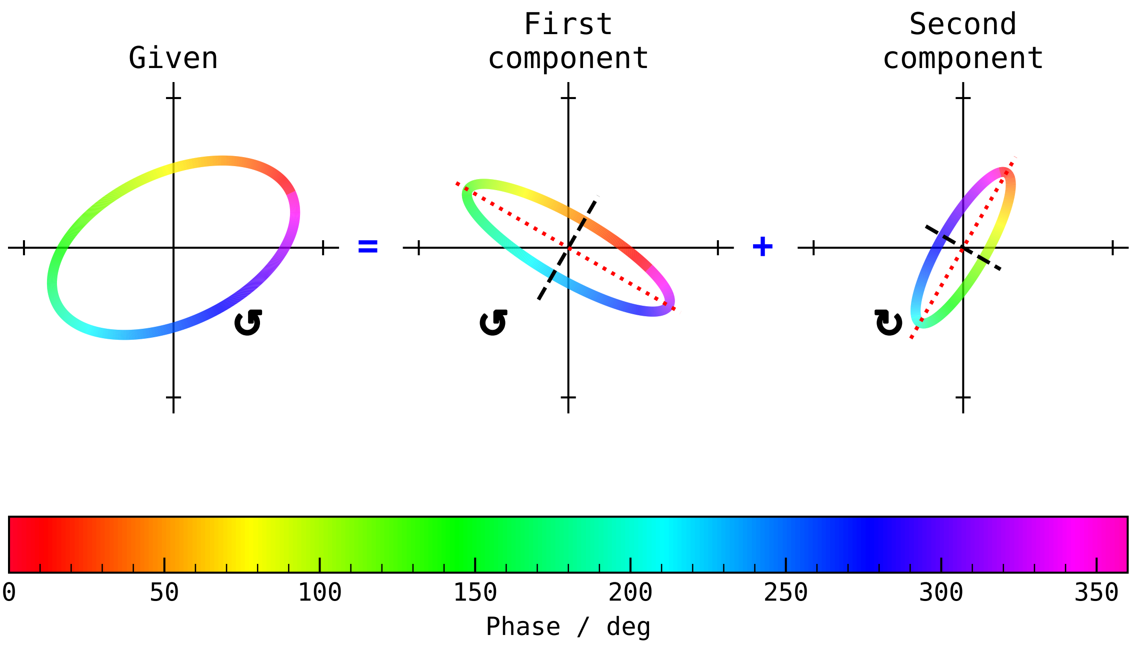

Figure 1.3: Schematic of the decomposition of given ray of polarized light (*left*) as summation of two components (*middle* and *right*). Each light is represented by its polarization ellipse where phase is shown with color. The dashed black lines are the orientations of the component polarization ellipses. The dotted red lines are the perpendiculars to the orientations of those components . The superposition of the two components' polarization ellipses results in the given polarization ellipse.

to the given ray of light. Refer to Stokes (1851) for the proof. The idea, henceforth, is to identify such a decomposition where the component light parameters, namely their α and β, are independent from given ray of light. In addition, the choice of α and β are to be such that the intensities of the rays of the component light sum to the intensity of the given ray of light.

Mathematically, light is parameterized with $(c_0^2, \alpha, \beta, \epsilon)$. Given light is to be decomposed into two components of light such that the decomposition is always valid independent of intensity and any arbitrary phase of light. In other words, the decomposition should only depend of α_i and β_i, both of which are independent of α and β. α_i and β_i can always be chosen to decompose any given light into components such that the components make it easier to characterize the given light. Moreover, out of all the possible choices, only those values of α_i and β_i are chosen that ensure

$$c_0^2 = c_1^2 + c_2^2, \tag{1.10}$$

that is, the intensity of given light is the sum of intensities of component lights. Such polarized components are termed as opposite. Usually, sum of intensities have a cross-phase term, however, if the choice of α_i and β_i is such that resulting light representation does not depend on the phase ϵ_i then the intensities are governed by simple addition.

The following holds due to superposition,

$$\begin{bmatrix} E_x^1 \\ E_y^1 \end{bmatrix} + \begin{bmatrix} E_x^2 \\ E_y^2 \end{bmatrix} = \begin{bmatrix} E_x \\ E_y \end{bmatrix}.$$

And from Eq. 1.9, when α orientation is brought from the RHS to the LHS, it yields,

$$c_1 \begin{bmatrix} \cos(\alpha_1 - \alpha) & -\sin(\alpha_1 - \alpha) \\ \sin(\alpha_1 - \alpha) & \cos(\alpha_1 - \alpha) \end{bmatrix} \begin{bmatrix} \cos(\beta_1) \cos(\phi + \epsilon_1) \\ \sin(\beta_1) \sin(\phi + \epsilon_1) \end{bmatrix} +$$
$$c_2 \begin{bmatrix} \cos(\alpha_2 - \alpha) & -\sin(\alpha_2 - \alpha) \\ \sin(\alpha_2 - \alpha) & \cos(\alpha_2 - \alpha) \end{bmatrix} \begin{bmatrix} \cos(\beta_2) \cos(\phi + \epsilon_2) \\ \sin(\beta_2) \sin(\phi + \epsilon_2) \end{bmatrix} =$$
$$c_0 \begin{bmatrix} \cos(\beta) \cos(\phi + \epsilon) \\ \sin(\beta) \sin(\phi + \epsilon) \end{bmatrix}.$$

Firstly, the above expression has to hold independent of ϕ. This is achieved by setting the coefficients of $\sin(\phi)$ and $\cos(\phi)$ to zero in the resultant equation. There are four such coefficients, two in each of the two rows, which yields four equations in the end. In addition, let $z_i = c_i \exp(j\epsilon_i)$ so that all "nuiscance" unknowns of the light can be collected into z. After a lot of simplification, the four equations can be condensed into a matrix equation:

$$Xz = Z, \tag{1.11}$$

where

$$z = \begin{bmatrix} z_1 \\ z_2 \end{bmatrix},$$
$$Z = c_0 \begin{bmatrix} \cos(\beta) \\ \sin(\beta) \end{bmatrix}.$$

And X is defined to be

$$X = \begin{bmatrix} \cos(\beta_1)\cos(\gamma_1) - j\sin(\beta_1)\sin(\gamma_1) & \cos(\beta_2)\cos(\gamma_2) - j\sin(\beta_2)\sin(\gamma_2) \\ \sin(\beta_1)\cos(\gamma_1) - j\sin(\gamma_1)\cos(\beta_1) & \sin(\beta_2)\cos(\gamma_2) - j\sin(\gamma_2)\cos(\beta_2) \end{bmatrix},$$

where for shorthand, $\gamma_i = \alpha - \alpha_i$. Since only the rays of component light are going to be used in characterizing the given ray of light, z can be found by the following:

$$z = X^{-1}Z.$$

Considering Eq. 1.11, the additive property of intensities (Eq. 1.10) can only be realized by setting $||X|| = X^\dagger X$ to be identity matrix.

$$||X|| = \begin{bmatrix} 1 & \begin{matrix} \cos(\beta_1 - \beta_2)\cos(\gamma_1 - \gamma_2) \\ + j\sin(\beta_1 + \beta_2)\sin(\gamma_1 - \gamma_2) \end{matrix} \\ \begin{matrix} \cos(\beta_1 - \beta_2)\cos(\gamma_1 - \gamma_2) \\ - j\sin(\beta_1 + \beta_2)\sin(\gamma_1 - \gamma_2) \end{matrix} & 1 \end{bmatrix}.$$

We achieve so by setting the off-diagonal element to zero. This happens under three conditions:

Same orientation In this case, $\gamma_2 = \gamma_1$ and $\beta_2 = \beta_1 + \frac{\pi}{2}$. The same γ implies the orientations of the two components of light is the same. The $\Delta\beta = \frac{\pi}{2}$ suggests the phase delay between the two components is of $\frac{\pi}{2}$, that is of a quarter-wavelength. This decomposition is generic as the components have the same orientation.

Circular polarized In this case, $\beta_1 = \frac{\pi}{4}$ and $\beta_2 = -\frac{\pi}{4}$ This is circularly polarized case. As in circularly polarized light does not have any orientation, there is no constraint on γ_i. Moreover, this is a special case of the first case as $\Delta\beta = \frac{\pi}{2}$.

Oppositely polarized In this case, $\gamma_2 = \gamma_1 + \frac{\pi}{2}$ and $\beta_2 = -\beta_1$. The orientations of the component rays of light differ by $\frac{\pi}{2}$, quarter of a wavelength. In addition, β of component light is the negative of the other. Note that sign of β records the handedness of the light. Hence, by having two oppositely signed, this decomposition captures both the handedness. By far, this is the most powerful decomposition as the choice of orientation of the component lights is unique. Moreover, circular polarization can also be treated as a special case of this decomposition.

Using the oppositely polarized decomposition (third case), z becomes:

$$z = c_0 \begin{bmatrix} \cos(\gamma_1)\cos(\beta - \beta_1) + j\sin(\gamma_1)\sin(\beta + \beta_1) \\ -\sin(\gamma_1)\cos(\beta + \beta_1) + j\cos(\gamma_1)\sin(\beta - \beta_1) \end{bmatrix}. \tag{1.12}$$

Taking the magnitudes,

$$|z|^2 = c_0^2 \begin{bmatrix} \sin^2(\alpha - \alpha_1)\sin^2(\beta + \beta_1) + \cos^2(\alpha - \alpha_1)\cos^2(\beta - \beta_1) \\ \sin^2(\alpha - \alpha_1)\cos^2(\beta + \beta_1) + \cos^2(\alpha - \alpha_1)\sin^2(\beta - \beta_1) \end{bmatrix}, \tag{1.13}$$

and after a lot of simplification,

$$\begin{aligned} |z_1|^2 = {} & c_0^2 \frac{1}{2} \\ & + c_0^2 \frac{\sin(2\beta)\ \sin(2\beta_1)}{2} \\ & + c_0^2 \frac{\cos(2\beta)\cos(2\alpha)\ \cos(2\beta_1)\cos(2\alpha_1)}{2} \\ & + c_0^2 \frac{\cos(2\beta)\sin(2\alpha)\ \cos(2\beta_1)\sin(2\alpha_1)}{2}. \end{aligned}$$

A similar expression can be written for $|z_2|^2$ but is not shown here. Revisiting the visual example of decomposition shown in Fig. 1.3, the two components are in fact oppositely polarized. The sense of rotation of first component is the reverse of the other. The orientations of the components which are shown with black dashed lines are perpendicular to each other. The perpendiculars of the orientations are shown with red dotted lines. The perpendicular of one of the components is parallel to the orientation of the other. The intensities of each of the component sum up to the intensity of the given ray of light. The c_i and ϵ_i for each of the component are actually computed using Eq. 1.12.

Until now, given ray of light was decomposed into two oppositely polarized rays of light components such that the superposition of the component rays results in the given ray of light and the sum of intensities of the components is the total intensity of the given light. There is complete freedom to choose the parameters of decomposition. Let the parameter of decomposition be $\alpha_\star, \beta_\star$. This fixing is akin to selecting the polarization filter and then studying the light after it passes through the filter. The polarization filter is known as "analyzer". Instead of just one ray of light, suppose a collection of rays of light, each with their own parameters, is given. The given collection of rays of light (which shall be indexed with σ) can be decomposed into component rays of light using the fixed polarization filter ($\alpha_\star$ and $\beta_\star$). Given the linearity of light and since the decomposition is valid for all ϕ and irrespective of ϵ_i, the resultant $|z_1|^2$ are,

$$\begin{aligned} |z_1|^2 = &\sum_\sigma \frac{1}{2} c_\sigma^2 \\ &+ \sin(2\beta_\star) \sum_\sigma \frac{1}{2} c_\sigma^2 \sin(2\beta_\sigma) \\ &+ \cos(2\beta_\star)\cos(2\alpha_\star) \sum_\sigma \frac{1}{2} c_\sigma^2 \cos(2\beta_\sigma)\cos(2\alpha_\sigma) \\ &+ \cos(2\beta_\star)\sin(2\alpha_\star) \sum_\sigma \frac{1}{2} c_\sigma^2 \cos(2\beta_\sigma)\sin(2\alpha_\sigma) \end{aligned}. \tag{1.14}$$

The terms containing $\star$ only correspond to polarization filter of choice and can be brought out of the summation appropriately. In other words, polarization filter strictly pertains to the choice of the $\alpha_\star, \beta_\star$ parameters and do not depend on the arbitrary collection of given light. If that is the case, the following four parameters seem more fundamental as they do not depend on the choice of $\alpha_\star$ or $\beta_\star$:

$$\begin{aligned} I &= \sum_\sigma \frac{1}{2} c_\sigma^2 \\ V &= \sum_\sigma \frac{1}{2} c_\sigma^2 \sin(2\beta_\sigma) \\ Q &= \sum_\sigma \frac{1}{2} c_\sigma^2 \cos(2\beta_\sigma)\cos(2\alpha_\sigma) \\ U &= \sum_\sigma \frac{1}{2} c_\sigma^2 \cos(2\beta_\sigma)\sin(2\alpha_\sigma), \end{aligned} \tag{1.15}$$

and which only depend on the given collection of light. These four parameters, I, Q, U, V, can be seen as intensity-like quantities which fully characterize the polarization of the light. Moreover, these parameters are additive. That is, any arbitrary mixtures of light measured in I, Q, U, V, if combined, would have as the resultant parameters the simple algebraic summations of the parameters. These four parameters are known as Stokes parameters.

1.2.3 Poincare sphere

From Eq. 1.15, considering only one source of light yields,

$$\begin{aligned} I &= c_0^2 \\ V &= c_0^2 \sin(2\beta) \\ Q &= c_0^2 \cos(2\beta)\cos(2\alpha) \\ U &= c_0^2 \cos(2\beta)\sin(2\alpha), \end{aligned} \tag{1.16}$$

where summation, a factor of $\frac{1}{2}$ and the subscript σ are omitted. Notice how similar this parametrization is with spherical coordinates. The Cartesian representation of spherical coordinate system where signed

Table 1.1: Select values of parameters of polarization ellipse in degrees which correspond to pure Stokes parameter. α and β refer to the orientation and arctan of ratio of axes of polarization ellipse (see Eq. 1.9). ψ and δ denote arbitrary angle and phase delay as described in Eq. 1.6. Refer to Fig. 1.4. α in case of pure V is not defined.

Sign of Stokes	α	β	ψ	δ
$Q > 0$	0	0	0	0
$Q < 0$	90	0	90	0
$U > 0$	45	0	45	0
$U < 0$	-45	0	-45	0
$V > 0$	-	45	45	, 90
$V < 0$	-	-45	45	-90

latitude is used instead of co-latitude is

$$
\begin{aligned}
x &= r\cos(\theta)\cos(\phi) \\
y &= r\cos(\theta)\sin(\phi) \\
z &= r\sin(\theta),
\end{aligned}
$$

with radius r, signed latitude θ and azimuth ϕ. By direct comparison, $\theta = 2\beta$ and $\phi = 2\alpha$ and x, y, z is V, Q, U respectively. This representation of the Stokes parameters as points of the sphere naturally falls out of the Stokes parameter definition. This sphere is called Poincare sphere (Kahr, 2021).

1.2.4 IQUV

The Stokes parameters parameterize the polarization ellipse. Therefore, pure values of Q, U and V, that is when only one of Q, U or V is non-zero, should correspond to special configurations of the polarization ellipse. Select values of α and β which correspond to pure Q, U and V are shown in Table 1.1. As already noted in previous section, select values of α, β correspond to select values of ψ and δ of polarization ellipse which are also tabulated in the same table. Using Eq. 1.9, the trace of the polarization ellipse is plotted in Fig. 1.4. Furthermore, Q, U and V are signed quantities. So each case of Q, U and V being > 0 and < 0 are separately visualized. In reality, this is how Stokes parameters are actually introduced[1].

The sign of δ determines the handedness. This directly corresponds to the sign of V. And since, handedness of light is exclusively a property of circular polarization, this implies V corresponds to circular polarization of light. The pure values of Q and U have collapsed into a line, as shown in Fig. 1.4. Thus, Q and U are said to correspond to linear polarization. Lastly, α can be computed from Q and U using the Eq. 1.15 as

$$\alpha = \frac{1}{2}\arctan\left(\frac{U}{Q}\right). \tag{1.17}$$

With this formalism, α, which is the orientation of the ellipse, can be computed using U and Q. In nomenclature, α is the Position Angle of the light.

---

[1] This is how even i explained to a certain individual who did not like my explanation and rebuked it. This whole exercise is just to convince myself and them about how Stokes parameters actually came to be. Unsurprisingly, that certain individual has no recollection of their comments.

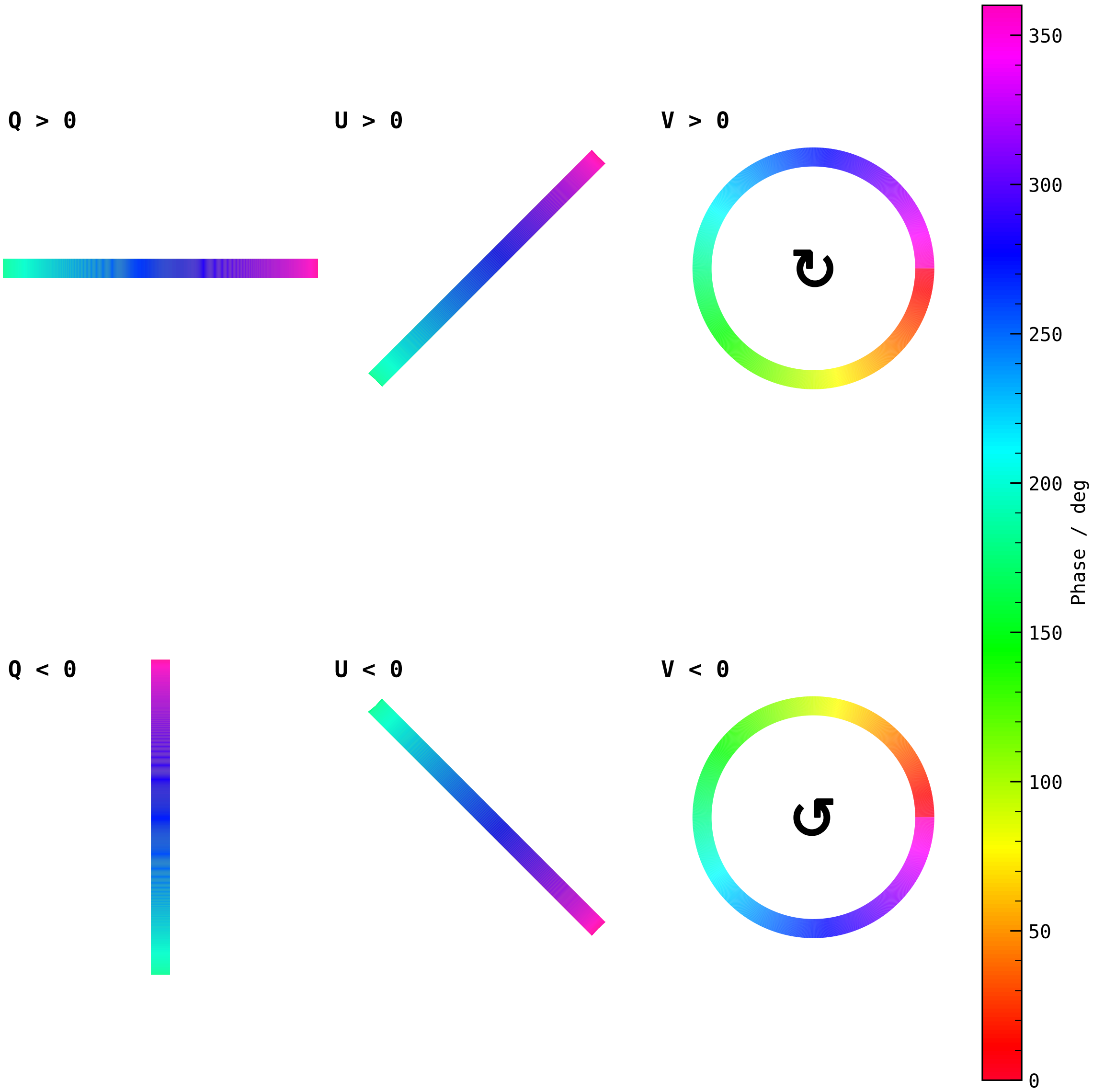

Figure 1.4: Select values for ψ and δ to show pure Q, U, V parameters. Note that Phase goes from 0 to 360 deg in all the cases but in case of Q and U, it overlaps over the first half-cycle which is not seen. See Table 1.1.

Table 1.2: Intensity measured in $|z_1|^2$ using select values of $\beta_\star$ and $\alpha_\star$ and how Stokes parameters can be derived using the intensity measurements.

Filter	$\beta_\star$	$\alpha_\star$	Intensity	Label
Linear	0°	0°	$\frac{1}{2}(I+Q)$	I_1
		45°	$\frac{1}{2}(I+U)$	I_2
		90°	$\frac{1}{2}(I-Q)$	I_3
Circular	45°		$\frac{1}{2}(I+V)$	I_4

Measuring Stokes parameters

Stokes parameters are measured by setting $\alpha_\star, \beta_\star$ to specific values and measuring the intensity of light, and then applying algebraic relations to finally obtain Stokes parameters. Fixing $\alpha_\star$ and $\beta_\star$ is equivalent to using a particular polarization filter. Every choice of $\alpha_\star, \beta_\star$ leads to some combination of $IQUV$, which can then be algebraically solved to compute each of $IQUV$. In practice, realizing an arbitrary polarization filter is difficult, therefore, there are only two known polarization filters - linear and circular, which have $\beta_\star = 0°$ and $\beta_\star = 45°$ respectively. $\alpha_\star$ can be arbitrarily set simply by rotating the filter with respect to the beam of light. Using the circular and linear polarization filters with $\alpha_\star$ and $\beta_\star$ as mentioned in the respective columns of Table 1.2, and measuring intensities labeled in the Label column of the same table, Stokes parameters can be found with the following algebra:

$$
\begin{aligned}
I &= I_1 + I_3 & Q &= I_1 - I_3 \\
U &= 2I_2 - I & V &= 2I_4 - I.
\end{aligned}
$$

The above algebra is derived using $|z_1|^2$, given in Eq. 1.14 . This way, Stokes parameters of any given ray of light's polarization can be measured by simply using a linear and circular polarization filter.

Coherence parameters

While Stokes parameters can be measured by using linear and circular polarization filters, in practice and whenever possible, the coherence matrix is recorded, from which coherence parameters are extracted. The coherence matrix is defined as $\rho = zz^\dagger$, which for the z from Eq. 1.12 becomes:

$$
\begin{aligned}
\rho_{11} &= c_0^2 \sin^2(\alpha - \alpha_\star)\sin^2(\beta + \beta_\star) + \cos^2(\alpha - \alpha_\star)\cos^2(\beta - \beta_\star) \\
\rho_{22} &= c_0^2 \sin^2(\alpha - \alpha_\star)\cos^2(\beta + \beta_\star) + \cos^2(\alpha - \alpha_\star)\sin^2(\beta - \beta_\star) \\
\rho_{12} &= -c_0^2 \left(\sin(\alpha - \alpha_\star)\cos(\beta + \beta_\star) + j\sin(\beta - \beta_\star)\cos(\alpha - \alpha_\star)\right) \\
&\quad \left(\cos(\alpha - \alpha_\star)\cos(\beta - \beta_\star) + j\sin(\alpha - \alpha_\star)\sin(\beta + \beta_\star)\right),
\end{aligned}
\tag{1.18}
$$

where individual elements of coherence matrix are written to save space. ρ_{11} and ρ_{22} are the auto-correlations of z_1 and z_2 and directly correspond to $|z_1|^2$ and $|z_2|^2$, and lastly, ρ_{12} is the cross-correlation. Note that since ρ is a correlation matrix, $\rho_{12} = \rho_{21}^\star$ where * denotes complex conjugation. In practice, the elements of ρ are written in `AABBCRCI` where `AA` and `BB` are the auto-correlations, and `CR` and `CI` are the real and imaginary parts of ρ_{12}. The coherence parameters and Stokes parameters are algebraically equivalent. Lastly, while Stokes parameters are additive and provide geometrical interpretation (Fig. 1.4), coherence parameters are not additive but a provide signal processing interpretation. Therefore, from a strictly signal processing perspective, modern data taking instruments record coherence parameters.

1.2.5 Common polarization basis

Measuring Stokes parameters is fundamental to characterizing the polarization of light. While Stokes parameters are independent of any polarization filter used, measuring Stokes parameters requires the use of such filters. Therefore, the action of each filter on the measured coherence parameters is studied and the algebra needed to extract Stokes parameters from the coherence parameters is expressed. The choice of filters are limited to linear and circular as they are the widely used filters.

Linear basis

Linear polarization filter is akin to setting $\alpha_\star = 0$ and $\beta_\star = 0$, (also see Table 1.2). It only allows that linear polarization of light to propagate which is aligned with the filter axis. The polarization filter which is opposite to this filter would be one which is perpendicular to the linear filter (see third case of Sect. 1.2.2). When the above mentioned values of $\alpha_\star$ and $\beta_\star$ are put in Eq. 1.12 (in place of α_1, β_1), z then, corresponds to:

$$z = \begin{bmatrix} \cos(\alpha)\cos(\beta) + j\sin(\alpha)\sin(\beta) \\ -\sin(\alpha)\cos(\beta) + j\cos(\alpha)\sin(\beta) \end{bmatrix},$$

where c_0 has been conveniently set to one. The above z can be seen as rotation by $-\alpha$ applied on $\begin{bmatrix}\cos(\beta) & j\sin(\beta)\end{bmatrix}^T$. Which, supposing given ray of light has $\beta = 0$, then, the above z is simply $\begin{bmatrix}1 & 0\end{bmatrix}^T$, the $\hat{x}$ axis. z observed with the opposite polarization filter, after similar simplification, becomes $\begin{bmatrix}0 & 1\end{bmatrix}^T$, the $\hat{y}$ axis. Therefore, this filter directly leads to a Cartesian basis with $\hat{x}$ and $\hat{y}$ axes to describe the polarization of light. This basis is known as linear basis.

From Eq. 1.18 and using Stokes parameters definition from Eq. 1.15 yields the following coherence matrix

$$\rho_{\text{lin}} = \begin{bmatrix} I + Q & U - jV \\ U + jV & I - Q \end{bmatrix}.$$

The coherence parameters are denoted with `XXYYCRCI` where `X`, `Y` is in place of `A`, `B` to denote linear filter. Stokes parameters can be estimated from coherence matrix using

$$I = \frac{1}{2}(\mathtt{XX} + \mathtt{YY}) \qquad Q = \frac{1}{2}(\mathtt{XX} - \mathtt{YY})$$

$$U = \Re\{\rho_{12}\} \qquad V = \Im\{\rho_{12}\},$$

where $\Re$ and $\Im$ denote the real and imaginary parts.

Circular basis

With a circular polarization filter, $\beta_\star = \frac{\pi}{4}$ and $\alpha_\star$ is inconsequential for circular filter. The oppositely polarized filter is simply $\beta = -\frac{\pi}{4}$. The two polarized filters are of opposite sense of rotation. Again computing z from Eq. 1.12 by putting $\beta_1 = \pm\frac{\pi}{4}$ for both the components yields,

$$\left\{ \frac{1}{\sqrt{2}} \begin{bmatrix} \exp(j\gamma_1) \\ -j\exp(-j\gamma_1) \end{bmatrix}, \frac{1}{\sqrt{2}} \begin{bmatrix} \exp(-j\gamma_1) \\ j\exp(j\gamma_1) \end{bmatrix} \right\},$$

where γ_1 is not expressed because α_1 is not unique in case of circular polarization filter. Forcing $\gamma_1 = 0$ yields $\begin{bmatrix}1 & -j\end{bmatrix}^T$ and $\begin{bmatrix}1 & j\end{bmatrix}^T$ respectively. These are the basis elements for circular basis of light, where each corresponds to Right Circular and Left Circular.

Computing coherence matrix, ρ, yields

$$\rho_{\text{circ}} = \begin{bmatrix} I+V & -Q-jU \\ -Q+jU & I-V \end{bmatrix}. \tag{1.19}$$

The coherence parameters are denoted with `RRLLLCRCI` where `R, L` is in place of `A, B`. Stokes parameters can be estimated from coherence matrix using

$$I = \frac{1}{2}(\mathtt{RR} + \mathtt{LL}) \qquad V = \frac{1}{2}(\mathtt{RR} - \mathtt{LL})$$
$$Q = \Re\{\rho_{12}\} \qquad U = \Im\{\rho_{12}\}.$$

1.2.6 Transformation

The entire polarization information is contained within a 2 × 1 complex vector expressed in a suitable basis, for example linear or circular basis as seen in Sect. 1.2.5. Any linear transformation on the 2 × 1 complex vector can be modeled with a 2 × 2 complex matrix. When the input is the polarization vector, the linear transforming matrix is called the Jones matrix. Suppose given input is

$$I = \begin{bmatrix} z_1 \\ z_2 \end{bmatrix} \text{ and}$$
$$\rho = II^\dagger = \begin{bmatrix} z_1^\dagger\, z_1 & z_1^\dagger\, z_2 \\ z_1\, z_2^\dagger & z_2\, z_2^\dagger \end{bmatrix},$$

where I is the input 2 × 1 complex vector and ρ is the coherence matrix.

Under the following generic transformation with no coupling between z_1 and z_2, such that $z_i \to g_i e^{j\phi_i} z_i$ where g_i and ϕ_i are gain and phase terms.

$$\begin{bmatrix} z_1 \\ z_2 \end{bmatrix} \to \begin{bmatrix} g_1\, e^{j\phi_1} & 0 \\ 0 & g_2\, e^{j\phi_2} \end{bmatrix} \begin{bmatrix} z_1 \\ z_2 \end{bmatrix},$$
$$\rho \to \begin{bmatrix} g_1^2\, z_1^\dagger\, z_1 & g_1\, g_2\, e^{j(\phi_2-\phi_1)}\, z_1^\dagger\, z_2 \\ g_1\, g_2\, e^{j(\phi_1-\phi_2)}\, z_2^\dagger\, z_1 & g_2^2\, z_2^\dagger\, z_2 \end{bmatrix}.$$

The resulting coherence matrix only depends on the relative phase difference $|\phi_2 - \phi_1|$. Moreover, every term in the coherence matrix has g_i^2-like term. Noting this, the generic transformation can be re-written as

$$G \begin{bmatrix} e^{\gamma + j\phi} & 0 \\ 0 & e^{-\gamma - j\phi} \end{bmatrix}, \tag{1.20}$$

where $G = \sqrt{g_1 g_2}$, $e^\gamma = \sqrt{\frac{g_1}{g_2}}$ and $\phi = \phi_1 - \phi_2$. This is the most simplest linear model which transforms polarization. G is a scalar gain term which affects all the coherence parameters. γ and ϕ account for differential gain and differential phase between the two dimensions.

On applying the transformation, ρ becomes

$$G^2 \begin{bmatrix} e^{2\gamma}\, z_1^\dagger\, z_1 & e^{2j\phi}\, z_1^\dagger\, z_2 \\ e^{-2j\phi}\, z_1\, z_2^\dagger & e^{-2\gamma}\, z_2\, z_2^\dagger \end{bmatrix}.$$

Given the transformed coherence matrix, the transformed Stokes parameters can be also be found. As the Jones matrix linearly transforms the polarization vector, there should also be a linear transformation which transforms the Stokes vector. This matrix transformation is called the Müller matrix. Which under linear or circular basis of polarization computes to be:

$$G^2 \begin{bmatrix} \cosh(2\gamma) & \sinh(2\gamma) & 0 & 0 \\ \sinh(2\gamma) & \cosh(2\gamma) & 0 & 0 \\ 0 & 0 & \cos(2\phi) & -\sin(2\phi) \\ 0 & 0 & \sin(2\phi) & \cos(2\phi) \end{bmatrix}. \tag{1.21}$$

With the above matrix, it is again noted that G is the scalar gain affecting all the Stokes parameters, γ is differential gain which is affecting only those Stokes parameters derived from autocorrelation terms. ϕ is differential phase which affects those Stokes parameters derived from cross-correlation term.

1.3 Ohm's law

Ohm's law states that in a medium some current density **j** is linearly related to electric field **E** as

$$\mathbf{j} = \ \mathbf{E}. \tag{1.22}$$

is treated as a tensor and is the measure of conductivity of the medium. Maxwell's equations cannot be used to derive Ohm's law. Ohm's law is empirical in nature. As all things in Physics, the imposed linearity paves way to understand and model physics, but this linearity does not always hold. Such media are called non-ohmic and not discussed here.

Putting the plane wave solutions to Maxwell equations, as shown in Eq. 1.3, into the curl identities of Maxwell equations of Eq. 1.1 yields:

$$\begin{aligned} \mathbf{k} \times \mathbf{E} &= -j\omega\, \mathbf{B} \\ \mathbf{k} \times \mathbf{B} &= \mu_0\, \left(\mathbf{J} + -j\omega\epsilon_0 \mathbf{E}\right). \end{aligned} \tag{1.23}$$

Eliminating **B** yields,

$$\left(\mathbf{kk} - |\mathbf{k}|^2 + \frac{\omega^2}{c^2}\right) \mathbf{E} + j\omega\mu_0 \mathbf{J} = 0.$$

Now, using Ohm's law from Eq. 1.22 gives:

$$= 1 + \frac{j\mu_0}{\omega}$$

$$\left(\mathbf{kk} - |\mathbf{k}|^2 + \frac{\omega^2}{c^2} \ \right) \mathbf{E} = 0.$$

In the literature, is known as the dielectric tensor, which is a function of ω in plasma. However, in vacuum, = 0.

M is a tensor such that

$$\begin{aligned}\mathbf{M} &= \mathbf{k}\mathbf{k} - |\mathbf{k}|^2 + \frac{\omega^2}{c^2}\ . \\ \mathbf{M}.\mathbf{E} &= 0\end{aligned} \tag{1.24}$$

In case of plasma, the conductivity and hence the dielectric constant is written as

$$\begin{aligned}\sigma &= j\frac{n\,q^2}{\omega\,m} \\ \epsilon &= 1 - \left(\frac{\frac{n\,q^2}{m\,\epsilon_0}}{\omega^2}\right).\end{aligned}$$

Defining $\omega_p^2 = \frac{n\,q^2}{m\,\epsilon_0}$ as the plasma frequency, **M** takes the form

$$\mathbf{M} = \begin{bmatrix} -|\mathbf{k}|^2 + \frac{\omega^2-\omega_p^2}{c^2} & 0 & 0 \\ 0 & -|\mathbf{k}|^2 + \frac{\omega^2-\omega_p^2}{c^2} & 0 \\ 0 & 0 & \frac{\omega^2-\omega_p^2}{c^2} \end{bmatrix}.$$

The different modes of transmission are given by the zeroes of the eigen values of **M**. Such modes are called eigenmodes. However, in this case where **M** is purely a diagonal matrix, finding eigen modes is extremely straightforward. There are two modes: (i) Longitudinal where $\omega = \omega_p$, and (ii) Transverse where

$$\omega^2 = c^2k^2 + \omega_p^2 \tag{1.25}$$

Eq. 1.25 is a dispersion relation (compare with Eq. 1.4).

1.3.1 Non-magnetized

Insofar, the plasma considered does not have any magnetic field threading in it. The effect of plasma on propagation can be probed using group velocity. Information travels at group velocity, v_g, which is $\frac{\partial\omega}{\partial k}$. Simplifying using Eq. 1.25 computes

$$v_g(\omega) = c\left(\sqrt{1 - \frac{\omega_p^2}{\omega^2}}\right).$$

Note how different frequencies have different group velocities, which implies light consisting of multiple wavelengths after propagating through such a medium get dispersed. The total delay a frequency, ν, undergoes can be found by computing

$$\tau(\nu) = \int_0^L \frac{dl}{v_g(\nu)}.$$

Noting for the case that $\frac{\omega_p}{\omega} \ll 1$,

$$\begin{aligned} \tau(\nu) &= \frac{L}{c} + \frac{e^2}{8\pi^2 m c \epsilon_0} \int_0^L n\, dl \left(\frac{1}{\nu^2}\right) \\ &= \frac{L}{c} + \mathscr{D}\ \mathrm{DM}\left(\frac{1}{\nu^2}\right) \end{aligned} . \tag{1.26}$$

Where $\mathrm{DM} = \int_0^L n\, dl$ is known as the dispersion measure and $\mathscr{D} = \frac{e^2}{8\pi^2 c \epsilon_0\, m}$. n corresponds to the number density of the plasma and L is the total length the electromagnetic radiation travels through the plasma. The DM has the unit of pc cm^{-3}.

The first part of the RHS of Eq. 1.26 is the geometric delay and the second part is the frequency dependent dispersion delay. A more interesting quantity is the delay between two frequencies, ν_1 and ν_2,

$$t(\nu_1) - t(\nu_2) = 4.148\ \mathrm{DM}_{\mathrm{pc\ cm^{-3}}} \left(\frac{1}{\nu^2_{1,\mathrm{GHz}}} - \frac{1}{\nu^2_{2,\mathrm{GHz}}}\right)\ \mathrm{ms} \tag{1.27}$$

Obviously, higher frequencies arrive earlier than lower frequencies.

1.3.2 Magnetized

If the plasma medium has magnetic field along the light propagating direction, it gives rise to the phenomena of dispersion and Faraday rotation. Starting from Lorentz force equation,

$$m\frac{\partial \mathbf{v}}{\partial t} = q\left(\mathbf{E} + \mathbf{v} \times \mathbf{B}\right),$$

solving for current, $\mathbf{j} = nq\mathbf{v}$ and using Ohm's law yields,

$$= \begin{bmatrix} \omega_p^2 \frac{j\omega}{\omega^2 - \Omega_B^2} & -\omega_p^2 \frac{\Omega_B}{\omega^2 - \Omega_B^2} & 0 \\ \omega_p^2 \frac{\Omega_B}{\omega^2 - \Omega_B^2} & \omega_p^2 \frac{j\omega}{\omega^2 - \Omega_B^2} & 0 \\ 0 & 0 & j\frac{\omega_p^2}{\omega^2} \end{bmatrix}.$$

can be computed, which when put into Eq. 1.6, gives us a tensorial expression for $\mathbf{M}$:

$$\mathbf{M} = \frac{1}{c^2} \begin{bmatrix} \omega^2\left(1 - S\right) - c^2k^2 & -jD\omega^2 & 0 \\ jD\omega^2 & \omega^2\left(1 - S\right) - c^2k^2 & 0 \\ 0 & 0 & \omega^2\left(1 - Z\right) \end{bmatrix}. \tag{1.28}$$

Where S, D, Z are defined the following way:

$$\begin{aligned} S &= \frac{\omega_p^2}{\omega^2 - \Omega_B^2} \\ D &= \frac{\omega_p^2}{\omega} \frac{\Omega_B}{\omega^2 - \Omega_B^2} . \\ Z &= \frac{\omega_p^2}{\omega^2} \end{aligned}$$

The basis so far has been Cartesian. When transforming to a circular basis by applying,

$$\begin{bmatrix} E_l \\ E_r \\ E_z \end{bmatrix} = \frac{1}{\sqrt{2}} \begin{bmatrix} 1 & j & 0 \\ 1 & -j & 0 \\ 0 & 0 & \sqrt{2} \end{bmatrix} \begin{bmatrix} E_x \\ E_y \\ E_z \end{bmatrix}.$$

If **R** denotes the transformation matrix, then

$$\begin{aligned} \mathbf{E} &\rightarrow \mathbf{RE} \\ \mathbf{M} &\rightarrow \mathbf{RMR}^{-1}. \end{aligned}$$

In doing so,

$$\mathbf{M} = \frac{1}{c^2} \begin{bmatrix} \left(-c^2k^2 + \omega^2 \left(1 - (S + D)\right)\right) & 0 & 0 \\ 0 & \left(-c^2k^2 + \omega^2 \left(1 - (S - D)\right)\right) & 0 \\ 0 & 0 & \omega^2 \left(1 - Z\right) \end{bmatrix}. \tag{1.29}$$

Like before, eigen modes are isolated and dispersion relations are written. We note that it is different for different hands. On simplifying we get,

$$\omega^2 = c^2k^2 + \frac{\omega_p^2}{1 \pm \left(\frac{\Omega_B}{\omega}\right)}, \tag{1.30}$$

the top sign is for right circular element of circular basis (R) and bottom sign is for left circular element (L). This phenomena when different components of light suffer from different k is known as birefringence.

Faraday rotation

Solving the dispersion relation of magnetized plasma (Eq. 1.30) yields

$$k = \frac{\omega}{c} \sqrt{1 - \frac{\omega_p^2}{\omega^2} \pm \frac{\omega_p^2 \, \Omega_B}{\omega^3}}.$$

k can be suitably approximated for the purposes discussed here by assuming $\frac{\omega_p}{\omega} \ll 1$ and only keeping terms until ω^{-2} with

$$k \approx \frac{\omega}{c} \left\{ 1 - \frac{\omega_p^2}{\omega^2} \pm \frac{1}{2} \frac{\omega_p^2 \, \Omega_B}{\omega^3} \right\}.$$

The different k leads to different phases (ϕ_R, ϕ_L) of the light according to Eq. 1.8 such that

$$\begin{aligned} \phi_R &= k_R z - \omega t \\ \phi_L &= k_L z - \omega t. \end{aligned}$$

As only the difference in phase matters, it can be re-written as

$$\phi_R = +\frac{1}{2c}\frac{\omega_p^2 \Omega_B}{\omega^2} z$$
$$\phi_L = -\frac{1}{2c}\frac{\omega_p^2 \Omega_B}{\omega^2} z.$$

The whole transform can then be written in Jones matrix formalism (Sect. 1.2.6) as

$$\begin{bmatrix} e^{j\mathscr{R}z} & 0 \\ 0 & e^{-j\mathscr{R}z} \end{bmatrix}, \tag{1.31}$$

where

$$\mathscr{R} = \frac{1}{2c}\frac{\omega_p^2 \Omega_B}{\omega^2}.$$

Linear polarized light in circular basis takes the following form (see Sect. 1.2.5):

$$\frac{1}{\sqrt{2}}\begin{bmatrix} e^{j\psi} \\ -je^{-j\psi} \end{bmatrix},$$

where ψ is the orientation of the polarization ellipse. The resultant light after it travels through magnetized plasma by an infinitesimal amount, dz can be found by the action of Jones matrix of Eq. 1.31,

$$\frac{1}{\sqrt{2}}\begin{bmatrix} e^{j(\psi+\mathscr{R}dz)} \\ -je^{-j(\psi+\mathscr{R}dz)} \end{bmatrix}.$$

The magnetized plasma changes the orientation of the light (or PA) changes. The infinitesimal change in PA is

$$d\psi = \frac{e^3}{8\pi^2 m^2 c\epsilon_0}\frac{1}{\nu^2} n B_\parallel dz.$$

Note that $\mathscr{R}$ can be completely expressed here.

If the light travels in total a distance of L, the total rotation exerted on PA can be found simply by integrating. Which computes to be,

$$\Delta\psi = \frac{e^3}{8\pi^2 m^2 c^3 \epsilon_0}\lambda^2 \int_0^L n B_\parallel dz.$$

Note that RM can be defined as

$$\mathrm{RM} = 0.81 \int_0^L n B_\parallel \, dz.$$

Although based on this definition, the units of RM involves magnetic field, number density and length units. In practice, RM is measured using

$$\Delta\psi = \mathrm{RM}\lambda^2,$$

hence carries the units of rad m^{-2}. This definition of RM suggests RM is the slope of the change of PA against λ^2.

The action on Stokes parameters can be found by computing the coherence matrix using resultant light. The coherence matrix computes to be

$$\begin{bmatrix} 1 & e^{2j(\psi+\mathcal{R}dz)} \\ e^{-2j(\psi+\mathcal{R}dz)} & 1 \end{bmatrix}.$$

Comparing with coherence matrix in circular basis (Eq. 1.19) yields,

$$Q + jU = \exp\left\{2j(\psi + \mathcal{R}dz)\right\}.$$

Integrating over a length of L and reusing the definitions from above yields Faraday rotation in the form best understood:

$$Q + jU = \exp\left\{2j(\psi + \mathrm{RM}\lambda^2)\right\}.$$

Differential dispersion

Group velocity of light passing through magnetized plasma computes to be,

$$v_g(\omega) = \frac{\partial \omega}{\partial k} = c\frac{\sqrt{1 - \frac{\omega_p^2}{\omega^2}}}{1 \pm \frac{\Omega_B}{2}\left(\frac{\omega_p^2}{\omega^3}\right)}, \tag{1.32}$$

where, as before, the top sign is for the right circular basis element and the bottom sign for the left circular basis element. Noting that $\frac{\omega_p}{\omega} \ll 1$, following approximation holds

$$\frac{1}{v_g(\nu)} \approx \frac{1}{c}\left\{1 + \frac{1}{2}\frac{\omega_p^2}{\omega^2} \pm \frac{\Omega_B}{2}\frac{\omega_p^2}{\omega^3}\right\}$$

where only terms until ω^{-3} are kept.

As done in previous section, delay incurred by light of frequency ν is calculated as,

$$\begin{aligned} \tau(\nu) &= \int_0^L \frac{dl}{v_g(\omega)} \\ &= \frac{L}{c} + \frac{e^2}{8\pi^2 mc\epsilon_0}\frac{1}{\nu^2}\int_0^L n\,dl + \frac{e^3}{16\pi^3 m^2 c\epsilon_0}\frac{1}{\nu^3}\int_0^L nB_{\parallel}\,dl\cdot \\ &= \frac{L}{c} + \mathcal{D}\,\mathrm{DM}\left(\frac{1}{\nu^2}\right) \pm \frac{\mathrm{RM}}{2\pi c}\lambda^3 \end{aligned}$$

The definitions of $\mathcal{D}$, DM and RM have been used in simplifying. The first part is purely geometric and the second part is purely dispersion, as already seen in previous section. The last part is due to the magnetic field.

The delay between the R and the L is

$$\tau_R(\lambda) - \tau_L(\lambda) = \frac{\mathrm{RM}}{c\pi}\lambda^3.$$

CHAPTER 2

Fast Radio Burst phenomena

Fast Radio Bursts (FRBs) are short timescale (order of milliseconds) and finite bandwidth (100s of MHz) transient signals at radio wavelengths (Petroff, Hessels, and Lorimer, 2019; Petroff, Hessels, and Lorimer, 2022). Radio waves traveling through astrophysical plasma suffer from dispersion, where the amount of dispersion is proportional to the density of the plasma and the distance traveled through the plasma. The signature of dispersion is the different times-of-arrival (measured as Δt) for different frequencies, which follow an inverse square formulation parameterized by a single parameter - Dispersion Measure (DM):

$$\Delta t = 4.148 \times 10^3 \, \mathrm{DM} \left(\frac{1}{\nu^2_{\mathrm{low,MHz}}} - \frac{1}{\nu^2_{\mathrm{high,MHz}}} \right) \mathrm{s},$$

where $\nu_{\mathrm{high,MHz}}$ and $\nu_{\mathrm{low,MHz}}$ are the highest and lowest frequencies measured in MHz. DM is defined as,

$$\mathrm{DM} = \int_0^l n_e \, dl,$$

where l is the distance traveled through the plasma. It is typically expressed in the units of pc cm^{-3}. The dispersion of an FRB signal is much more than what Milky Way can cause, which suggests that FRBs originate from outside the galaxy. This means FRBs are detectable at extragalactic distances, which ultimately implies that they are an extremely energetic phenomena.

The first FRB was serendipitously discovered in 2007 in archival data taken in 2001 using the 64-m Parkes Murriyang radio telescope (Lorimer et al., 2007). The FRB event was extremely bright, showed large dispersion (see above equation and Eq. 1.27) suggesting an extremely large inferred distance of > 1 Gpc, which lent itself to be identified as a new type of transient signal. This was the only burst seen in over 90 hours of observations, suggesting the burst to be a singular event. A single transient event, which possibly traveled extremely large distances, naturally puzzled and intrigued astronomers. It paved the way to FRB phenomena.

The transient and extremely bright nature of the FRBs raised the following question: if it is ever possible to observe more than one transient event (or burst) from the same source? The above question can also be interpreted in a different way: are there emission mechanisms that make available such vast amounts of energy more than once? Naturally, it might seem unlikely, which brought forth many cataclysmic progenitor models to explain FRBs, which are collected in a catalogue of FRB theories (Platts et al., 2019). However, the discovery of multiple bursts from FRB 20121102A by the 305-meter Arecibo radio

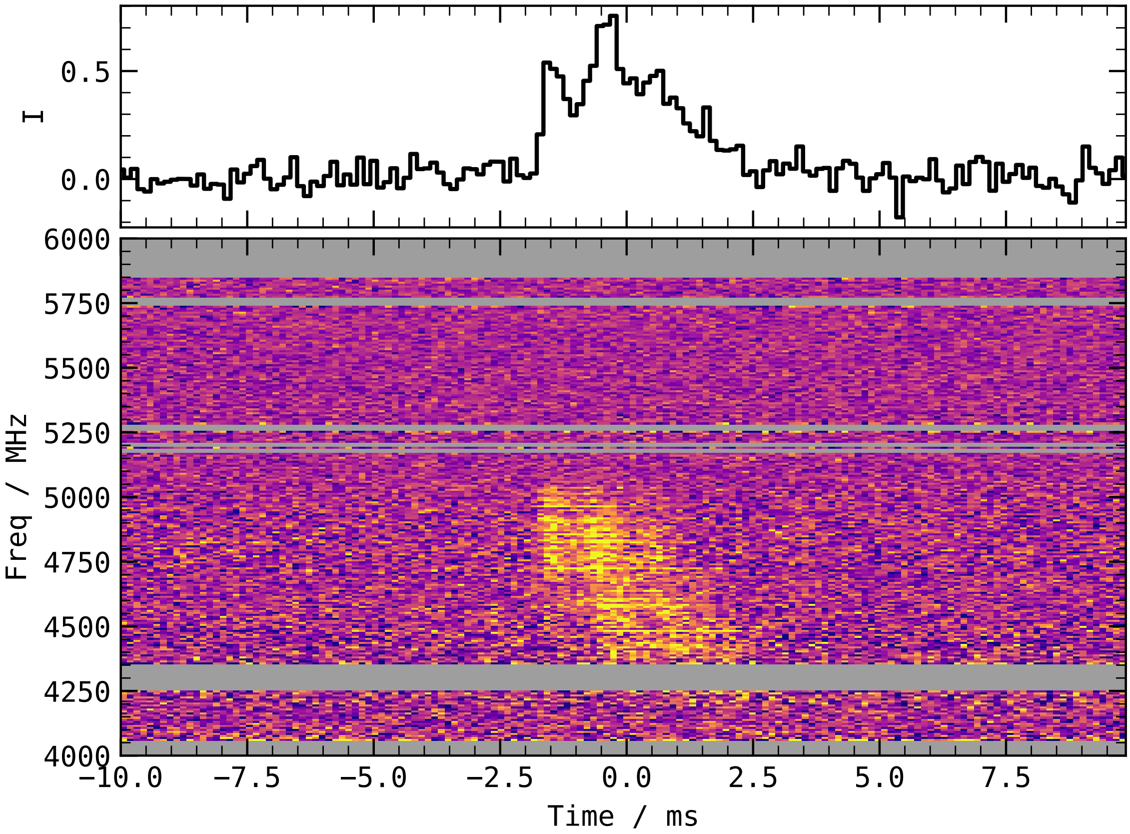

Figure 2.1: A de-dispersed dynamic spectrum and frequency averaged time series of a burst from FRB 20180916B detected using 100-meter Effelsberg Radio Telescope in 4-6 GHz (Bethapudi et al., 2023).

telescope (Spitler et al., 2016) changed the landscape of FRBs. It showed that there are some FRB sources which emit more than one burst, but it also raised another question if all the FRB sources eventually will emit more than one burst. That is, if all sources are repeaters and only observational biases have not yet allowed detection of multiple bursts.

A typical FRB is visualized with a dynamic spectrum, which is defined as intensity as a function of time and frequency, thereby offering both time and frequency resolution. Dispersion of FRB is purely a propagation effect and therefore, should be removed and the process of removing dispersion is called de-dispersion. A de-dispersed dynamic spectrum is plotted in Fig. 2.1 (*bottom*). Post de-dispersion, the frequency axis can be averaged over to produce an intensity time series of the event. This is shown also shown in Fig. 2.1 (*top*). The OFF-ON-OFF structure in time is indicative of its transient nature. The temporal extent is known as the width (W) and extent along the frequency dimension is called the bandwidth ($\Delta\nu$). The center frequency of the burst is denoted with ν. If the dynamic spectrum is suitably flux calibrated, that is if intensity data scales to physical units of spectral flux, one can measure several quantities of interest from it. In radio astronomy, spectral flux is measured in unit of Jansky (Jy) where $1\ \mathrm{Jy} = 10^{-26}\mathrm{W\ m^{-2}Hz^{-1}}$. One quantity of interest is peak flux density (S_{peak}), that is, the maximum flux in the entire burst duration, measured in Jy. Another quantity is fluence (F), which is the integration of the flux density over the burst duration and has the units of Jy ms. The ratio of fluence to flux is known as

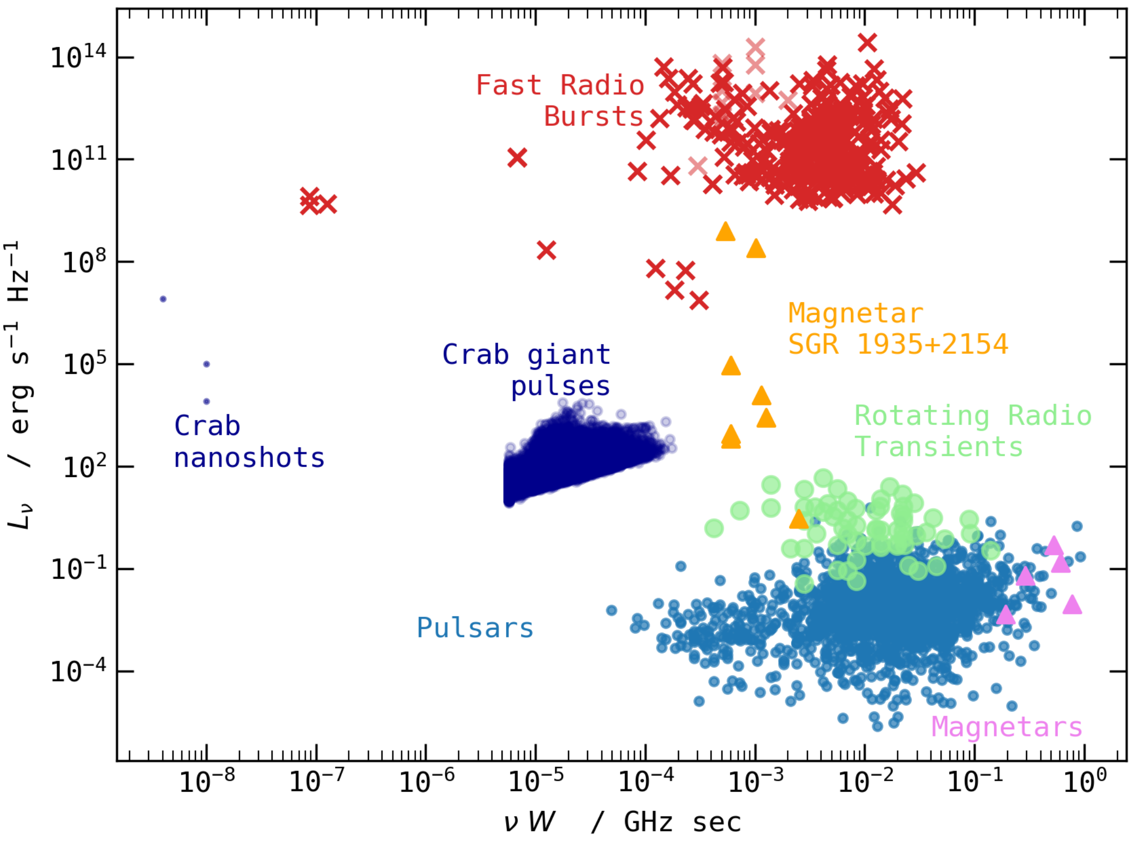

Figure 2.2: Spectral luminosity versus transient timescale phase space of transients. See text for the references.

equivalent width (W_{eq}) as it has the units of ms. The spectral luminosity of a burst, L_ν, can be computed in the following way:

$$L_\nu = 4\pi\, D_L^2\, S_{\mathrm{peak}},$$

where D_L is the luminosity distance to the source. L_ν is expressed in the units of erg s^{-1} Hz^{-1}.

The phase space for transients allows for phenomenological classification of different kinds of transients. A natural choice for phase space of transients is a measure of luminosity against the timescale of the transient. Here, the transient phase space is constructed using L_ν and νW following Keane (2018) and Nimmo et al. (2023) in Fig. 2.2. It includes the following: Repeating and non-repeating FRBs are shown in red crosses (see Nimmo et al., 2023, and references therein). Rapidly rotating neutron stars, known as pulsars (Lorimer and Kramer, 2004), which emit electromagnetic radiation along its dipolar magnetic field, are plotted in light blue dots. Rotating radio transients (RRAT; McLaughlin et al., 2006) are sources like pulsars but which emit pulses only intermittently, and are shown in light green circles. One of the pulsars, PSR J0534+2200, which is located in the Crab nebula (also colloquially known as Crab pulsar), is known to emit highly energetic pulses in addition to regular pulsar emission. The highly energetic pulses are known as Giant pulses (e.g. Karuppusamy, Stappers, and van Straten, 2010). Moreover, this pulsar is also observed to emit extremely short time resolved giant pulses known as nanoshots (e.g. Jessner et al., 2010; Hankins, Eilek, and Jones, 2016). Both of which are shown in dark blue dots. There is another specie of neutron stars, which have much larger magnetic fields than pulsars, known as magnetars (Kaspi and Beloborodov, 2017). They are shown in violet triangles.

Of all the species shown in the phase space in Fig. 2.2, only the FRBs are extragalactic and obviously the most energetic phenomena. Only the bursts detected by magnetar SGR 1935+2154 (Bochenek et al., 2020; CHIME/FRB Collaboration et al., 2020) is bridging the gap between galactic transients and FRBs, thus, providing a link between the two different regimes of transient activity. This connection brought forth many FRB progenitor models and emission mechanism based on magnetar like compact object. It provided an explanation to FRB phenomena which is a natural extension of known ms timescale radio transient phenomenon of pulsars: extragalactic magnetars can power FRB-like phenomena. Even still, much about FRB phenomena is still not known. This thesis is one step towards the goal of demystifying the FRB phenomena by studying one particular repeating FRB source in great detail.

2.1 Searching for a burst

Search for bursts starts with radio telescopes which convert incoming electric field radiation into voltage signals that are digitally sampled. Since the incoming radiation is extremely weak, telescopes not only need to collect larger and larger amounts of radiation, but also need sophisticated equipment that amplifies the incoming radiation. Thereafter, every time contiguous chunk of the voltage signal is channelized (that is, Fourier Transformed) to provide sufficient frequency resolution for that duration of the chunk. These spectra are averaged in time and stored to provide frequency as well as time resolution. The whole operation is known as filterbanking. Ultimately, each of the time/frequency bin is detected to form what is known as a dynamic spectrum. The detection process converts voltages into intensities. Thereby, as already defined before, dynamic spectrum is constructed as intensity as function of time and frequency. Search for bursts is then done on the dynamic spectrum.

The dispersion phenomenon is purely a propagation effect and needs to be removed (or de-dispersed) if bursts have to be searched using the dynamic spectrum. However, the challenging part is that the DM of the bursts is not always known apriori. In which case, multiple DM trials have to be performed to search for that one particular DM that maximizes the concentration of signal along time axis, that is, which completely removes the inter-channel time separation of the signal. In case of the true DM, the entire frequency axis can be collapsed by averaging over it. The averaging operation helps in reducing the noise, thus boosting the signal concentration. De-dispersion at multiple DMs yields frequency-averaged time series for every DM. Searching for bursts is then to simply look for maximum signal concentration in each of the time-series. To illustrate the inter channel delay, suppose the center frequency of observing is 650 MHz with 200 MHz bandwidth, the time resolution is 327.68 μs and the frequency resolution 97.65625 kHz (2048 channels). Then, Fig. 2.3 shows the simulated dispersed transients for DMs of $100, 150, 200, 250$ pc cm^{-3}, where for each of the DM, the start of the simulated dispersed transient is the same.

When the number of DM-trials is extremely large, which is easily the case when DM is not known, computing de-dispersed time series requires extremely large amounts of computing power. Fast Dispersion Measure Transform (FDMT Zackay and Ofek, 2017) is an algorithm which takes advantage of the redundant computations which occur when de-dispersing at two close enough DMs and optimizes the whole operation. It is by far the fastest algorithm to do so[1].

Frequency averaged time series for different DM trials exhibit an interesting structure. When intensity is plotted as a function of time and dispersed DM around the true DM of a signal, it shows a “bowtie”-like

---

[1] It is also one of my favorite algorithms.

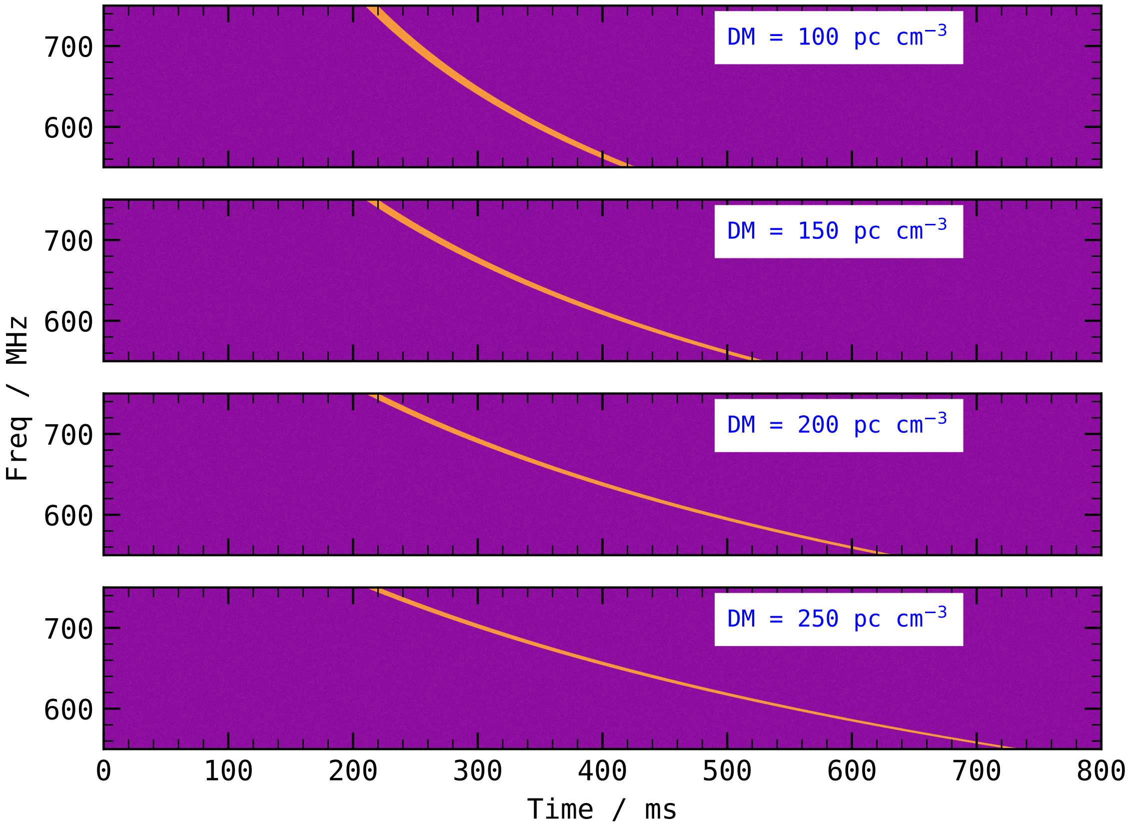

Figure 2.3: Dynamic spectra showing simulated inter channel dispersion delays for different DMs in each panel.

morphology as shown in Fig. 2.4 (*right*). These 2D data are thus also known as the bowtie-plane. Naïvely, the algorithm to generate bowtie plane is performing de-dispersion at each DM-trial and averaging over frequency. FDMT algorithm can be used here which optimizes the whole computation.

Radio receivers inherently generate noise with certain power. This noise is naturally present in the de-dispersed time series and is modeled as additive white Gaussian noise. Meaning, the noise is Gaussian random deviates, which are superimposed with any signal received by the telescope. The mean of the noise need not always be zero, meaning the noise could have a constant component. The standard deviation of the noise is proportional to the power. The veracity of any detected signal is characterized by how large in magnitude it is compared to the instrumental noise. The metric which achieves this is known as the Signal-to-Noise (S/N). S/N values directly measure the significance of the detections, hence, signals are flagged based on their S/N values. Therefore, the frequency averaged time series needs to be brought into S/N units. That is, the mean and standard deviation of the noise has to be zero and one respectively. This process is called normalizing the time series. Searching for signals of interest is now as simple as applying a threshold of some S/N. Any instance in some de-dispersed normalized time-series, where the S/N is above a threshold is called a candidate with the DM used to de-disperse at that time when the S/N is above the threshold. Naturally, for the same signal, if the noise power of the radio telescope is lower, the S/N will be higher. However, noise power is a property of the instrument and cannot be arbitrarily lowered.

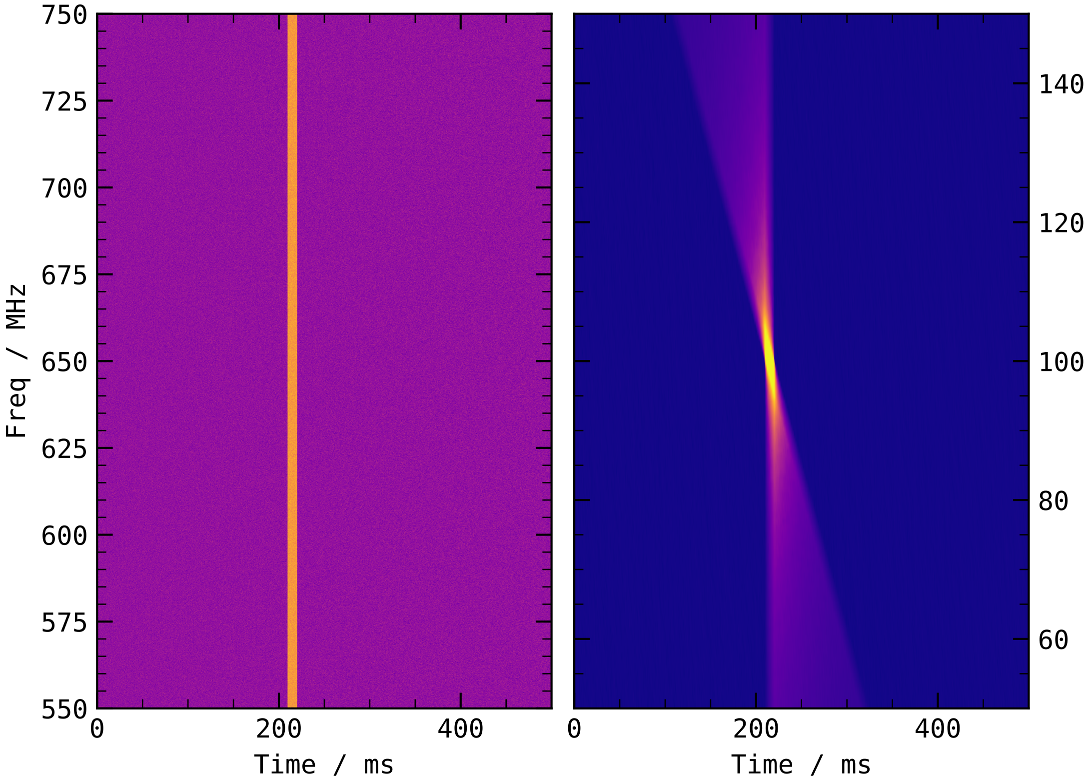

Figure 2.4: Using the simulated dynamic spectrum with DM= 100 pc cm^{-3} (as shown in *top* panel of Fig. 2.3), *left* shows the de-dispersed dynamic spectrum at the true DM. *Right* shows frequency averaged Intensity as a function of time and dispersed DM, which is known as the bowtie plane.

The operation of S/N-thresholding is not optimal if the width of the burst is not comparable with the time resolution of the data. Mismatch between the width of the burst and the time resolution penalizes the S/N of the signal. However, just like the DM, the width of the burst is also not known apriori. Therefore, in addition to DM trials, each time series has to be searched for multiple widths by means of boxcar filtering. The width trials are judiciously chosen to be computationally efficient without causing adverse degradation of the S/N. Fig. 2.5 shows the simulated drop in S/N when the trial width is deviates from the actual width of the candidate. The true width of the simulated burst is shown with dashed blue line.

The same transient event can be above a S/N threshold for multiple DM- and width-trials. Therefore, there must be a step to cluster all flagged candidates, and identify one such candidate which is representative of the true transient. This step is known as clustering. It not only reduces the number of candidates but also helps in cleaning spurious candidates. This effect is best illustrated comparing the bowtie planes of a dispersed event and a spurious event which is modeled with a linear chirp in frequency. Fig. 2.6 shows the dynamic spectra of dispersed event (*top-left*) and linear chirp event (*top-right*). The S/N of both the events is the same and is arbitrarily set to 10. The *bottom* panels of Fig. 2.6 show the bowtie plane above the threshold of 8. That is, everything seen in the bowtie plane will be flagged as a candidate by the search. The DM axis is chosen around the true DM and the slope of the linear chirp is also judiciously chosen which mimics the full band DM delay. As is evident, the flagged bowtie plane of dispersed event

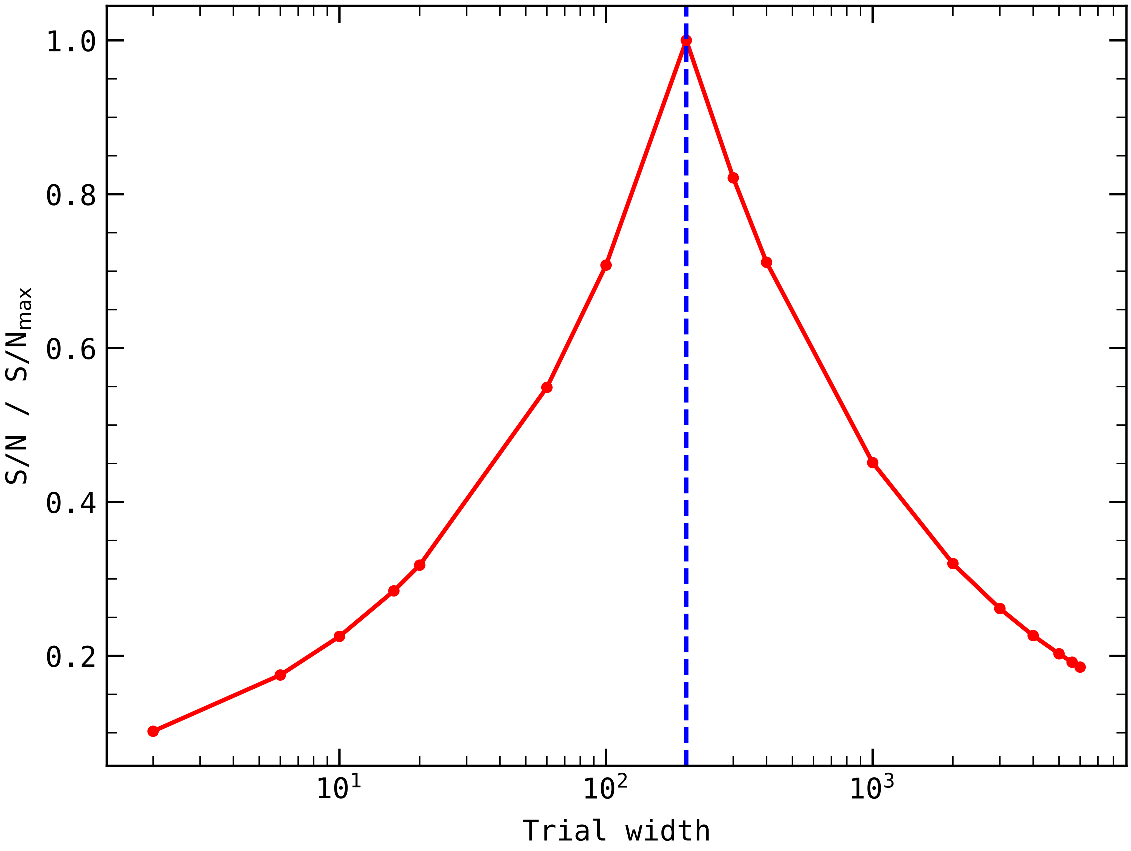

Figure 2.5: Penalty in S/N when width of the burst does not match with time resolution. The true width of the burst is shown with vertical dashed blue line.

is concentrated around the true candidate whereas there is a large range of candidates in case of linear chirp signal.

The slope of linear chirp does not matter. Furthermore, in reality, spurious signals need not always be like a linear chirp. However, when doing a blind search across a large range of DMs, the chances of flagging spurious candidates increase manyfold. This excerpt is a mere illustration of the effect. A significant number of such spurious candidates are due to human-made radio signals and are known as Radio Frequency Interference (RFI) in astronomy parlance. Strong presence of RFI hinders the search for short timescale transients such as FRBs. In addition to the human-made candidates, the instrumental noise itself causes spurious candidates. Such candidates are not astrophysical or terrestrial, but are still yielded by the search strategy due to the instrument noise. Given purely Gaussian statistics, a significance or S/N of 8 implies the probability of having a event ≥ 8 under the hypothesis that observed S/N is purely by chance is around 10^{-15}. While it may seem unlikely for a noise candidate to exceed a S/N threshold, there are extremely large number of time samples as the time resolution is extremely fine and the duration of observation is large. Due to which, even a chance probability of 10^{-15} causes noise candidates to appear. In short, pure noise cannot be overcome.

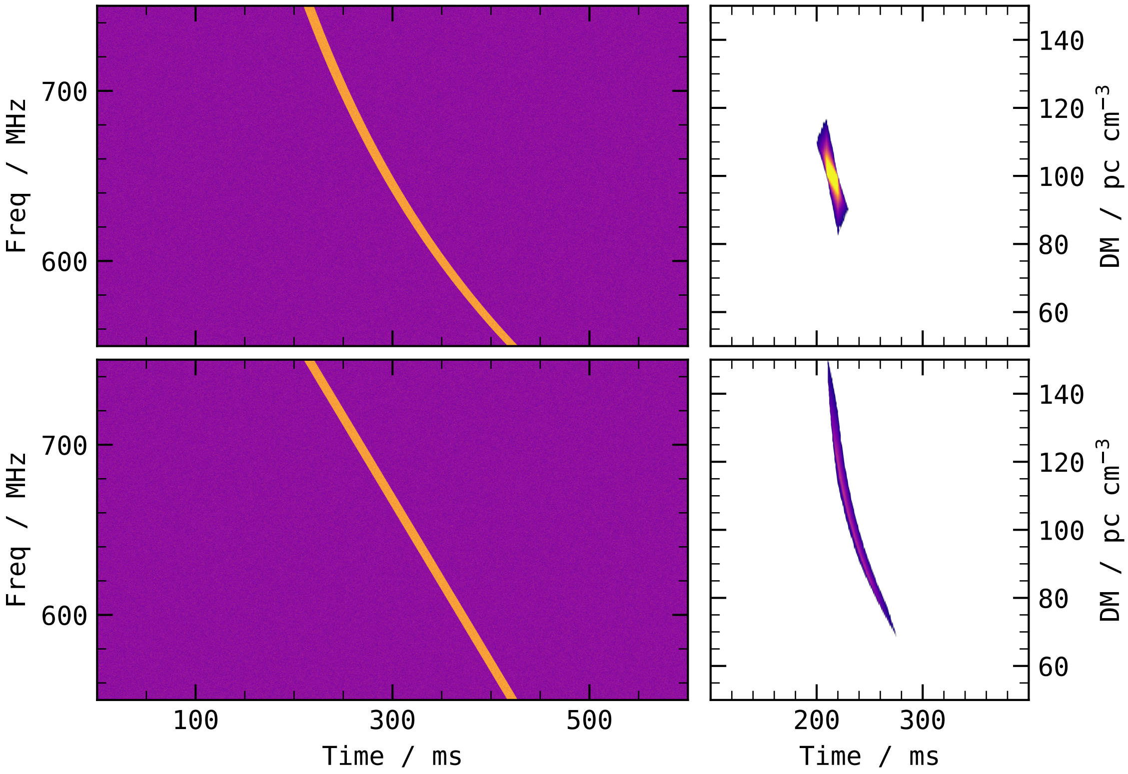

Figure 2.6: Dispersed signal (*top*) and linear chirp signal (*bottom*) shows how clustering can be crucial. The *left* panels show the simulated dynamic spectra and the *right* panels show the bowtie-plane after applying a suitable threshold to mimic search operation.

2.2 Localizing a burst

The resolving power of radio telescopes is limited by diffraction. That is, the smallest angular resolution possible with a single dish radio telescope of diameter D operating at a wavelength λ is θ such that

$$\theta = 1.22\,\frac{\lambda}{D}.$$

This has the following implication: a radio telescope when pointing to a particular direction would receive radiation from all the sources that are within θ around the pointing direction. For FRBs, which are originating from some location in their host galaxies, the possible number of galaxies which fall within θ around the pointing direction is so extremely large that the exact location, let alone the exact host galaxies, of the FRBs cannot be accurately pin pointed.

Pin pointing the location of an FRB to its location within its host galaxy is crucial to understand the origin of FRBs. The procedure is called localizing the FRB. Since a single dish telescope cannot localize an FRB, intereferometers are used. A radio interferometer is a collection of spatially separated radio telescopes operating in sync as if they all work as one telescope. The resolving power, θ, of an interferometer is

$$1.22\frac{\lambda}{B_{\text{max}}},$$

where B_{max} is the maximum separation between two radio telescopes. Telescope arrays can be constructed that provide sufficient angular resolution by which FRBs can be localized. Localizing a FRB adds more challenges and requires using interferometers to detect the burst. Given the random nature of FRB activity in time and over sky, it is challenging, and therefore, not all FRBs have been localized.

2.3 Era of large FOV surveys

Discovery of FRBs is a challenging endeavor. The random and short timescale nature of the transient requires high time resolution and large fields of view to discover adequate events within human timeline. Moreover, since the amount of dispersion and width is not known, searching for FRBs requires performing many dispersion and width trials across the whole field of view to find the bursts, all of which require tremendous amounts of computing power. These hurdles have to be overcome to drive FRB discovery. Despite these challenges, earlier discoveries of FRBs were made using either commensal or survey data. The first confirmation of FRBs arrived six years after the discovery by Thornton et al. (2013), which presented four discoveries from pulsar survey data taken with the Parkes Radio Telescope. Immediately following which, all available data (archived or new) was sieved through for FRBs. These efforts led to discoveries of several other FRBs from various instruments. For example, Burke-Spolaor and Bannister (2014), Ravi, Shannon, and Jameson (2015), and Champion et al. (2016) reported discoveries with Parkes, Spitler et al. (2016) with Arecibo Observatory (AO) and Masui et al. (2015) with Green Bank Telescope (GBT) Discoveries were also made by interferometers, such as those reported by Caleb et al. (2017) and Bannister et al. (2017). To make the searches tractable, Graphical Processing Unit (GPU) based specialized search engine was developed (Barsdell et al., 2012). Even so, the amount of science produced has been largely limited by the small number of FRB discoveries. Over a span of 10 years, there were only around 60 discoveries. The low yield is not only due to technological challenges but also due to lack of a dedicated instrument to rapidly survey large fields of view.

The inception of large field of view survey instruments caused the discovery rate of FRBs to skyrocket, which revolutionized the field. One such instrument worth mentioning is Canadian Hydrogen Intensity Mapping Experiment/Fast Radio Burst (CHIME/FRB) experiment (CHIME/FRB Collaboration et al., 2018). It offered more than 200 deg^2 field of view and housed sufficient computing resources to search for highly dispersed signals all throughout its field of view. CHIME/FRB alone has detected over 500 FRBs within an year of operation, essentially causing an exponential growth in the field (CHIME/FRB Collaboration et al., 2021). It also led to the discovery of over fifty repeating FRBs within four year of operation (CHIME/FRB Collaboration et al., 2019b; Chime/Frb Collaboration et al., 2023). The success of CHIME/FRB has to be really underlined because if not for one of their discoveries, this thesis would not exist.

FRBs are named with the Gregorian date of discovery in the following format: `FRB YYYYMMDDX`. The `YYYY`, `MM` and `DD` correspond to the four digit year, two digit month and two digit date in the calendar month of discovery. If there were multiple FRBs discovered in the same day, `X` is an alphabet starting from `A` through `Z` to assign unique names to such FRBs. The naming convention comes from Transient Name Server (https://www.wis-tns.org/) which is currently the living catalogue of bursts discovered by any instrument.

2.4 Observables from FRB bursts

The following sections describe how dynamic spectra of bursts are processed so that information present in them is representative of the true information. Additionally, they also describe various observables that can be extracted from the bursts and lay out the procedure in which observables can be measured.

2.4.1 Calibrating bursts

Measuring observables from bursts requires measured dynamic spectra of bursts to be brought to meaningful and true physical quantities. This is done via flux calibration and polarization calibration.

Flux density calibration

Voltages sampled by a radio telescope are digitized samples, that is, they are just numbers and do not carry any physical units. Measurements of energy, flux density, fluence and luminosity require the sampled data to possess a physical unit. This is achieved by a flux density scaling step where digitized samples are appropriately scaled to measure physical quantities using a reference astrophysical source of known flux density.

A radio telescope can be thought as a device that outputs voltage (denoted with V) when looking at a source with flux density (denoted with F). However, the device has operating noise. That is, it outputs voltage even if not looking any source. The noise power can be interpreted as a fiducial astrophysical source within the device with flux density F_{sys} where the subscript denotes system. A crucial assumption is that radio telescope as a device linearly scales flux density of the astrophysical source to voltages measured by the telescope. That is, it has a multiplicative factor called gain, G, which satisfies

$$V = GF.$$

Flux scaling can be mathematically understood with the following. Voltage measured when looking at nothing can be denoted with V_{OFF}. Voltage measured when looking at a source with known flux density F can be denoted with V_{F}. Mathematically,

$$\begin{aligned} V_{\mathrm{F}} &= G\left(F + F_{\mathrm{sys}}\right) \\ V_{\mathrm{OFF}} &= G\left(F_{\mathrm{sys}}\right), \end{aligned}$$

and with a bit of algebra,

$$F_{\mathrm{sys}} = \left(\frac{V_{\mathrm{OFF}}}{V_{\mathrm{F}} - V_{\mathrm{OFF}}}\right) F.$$

F_{sys} is the flux density of the system, and is often called System Equivalent Flux Density (SEFD).

Now, when looking at a source with unknown flux density F_{u}, if the telescope measures V_{u}. Having determined F_{sys}, with a bit more of algebra, F_{u} can be measured:

$$F_{\mathrm{u}} = \left(\frac{V_{\mathrm{u}} - V_{\mathrm{OFF}}}{V_{\mathrm{OFF}}}\right) F_{\mathrm{sys}}.$$

The above equation further simplifies to be

$$F_{\mathrm{u}} = \left(\frac{V_{\mathrm{u}} - V_{\mathrm{OFF}}}{V_{\mathrm{F}} - V_{\mathrm{OFF}}}\right) F.$$

The term in the parenthesis is known as deflection.

Polarization calibration

To completely capture polarization information, a radio telescope has to output two series of voltage signals - one for each dimension of polarization (see Sect. 1.2.1). Depending on how the two dimensions of polarization are realized, that is, the basis of polarization chosen, the voltages can be converted into Stokes parameters - I, Q, U and V (see Sect. 1.2.2).

The Stokes parameters outputted by the radio telescope need not represent the true polarization of the source. Radio telescope as a device will have its own polarization response, which corrupts the true Stokes parameters of the source while measuring. The transformation of true Stokes parameters into observed Stokes parameters is modeled linearly. The matrix which transforms is known as Müller matrix in literature (see Sect. 1.2.6). If the Müller matrix of a radio telescope is known, observed Stokes parameters can be transformed into true Stokes parameters. Therefore, polarization calibration is simply measuring the Müller matrix and applying the inverse of it to observed Stokes parameters.

The simplest Müller matrix model for a radio telescope is known as Single Axis model, which has three parameters. It has been derived in Sect. 1.2.6, which is repeated here for easier reference. To remind, the three parameters are Gain (G), differential gain (γ) and differential phase (ϕ). G is a scalar multiplicative gain, which is equivalent to the flux scaling as described above. γ and ϕ model the gain and phase mismatch between the two voltage streams. There are these three parameters for every frequency channel of the dynamic spectra and have to be estimated.

$$G^2 \begin{bmatrix} \cosh(2\gamma) & \sinh(2\gamma) & 0 & 0 \\ \sinh(2\gamma) & \cosh(2\gamma) & 0 & 0 \\ 0 & 0 & \cos(2\phi) & -\sin(2\phi) \\ 0 & 0 & \sin(2\phi) & \cos(2\phi) \end{bmatrix}$$

The three parameters are estimated using a reference noise source, which is usually situated within the radio telescope. The noise source emits pure Stokes-U by injecting equal amounts of power into both the dimensions of the polarization with same phase and duty cycle across the whole observing band. The actual parameter estimation of the Müller matrix uses the coherence parameters (the auto- and cross-correlations of the voltages streams, Sect. 1.2.2). The solution for the parameters is provided in Britton (2000).

2.4.2 Measuring observables

Measuring all possible observables from the FRB burst makes it possible to study the FRB phenomena in much greater detail. Every burst carries with itself a measurement of its properties such as DM, Rotation Measure (RM), scintillation bandwidth, and Polarization Position Angle (PPA or simply PA). Following sub-sections go through the entire process of measuring each of the different observables.

Dispersion Measure

Dispersion causes inter-channel delay in the arrival times of the burst. Therefore, a precise measurement of the inter-channel delay would lead to a precise measurement of the DM, which requires sufficiently high time resolution of the data. The precision of DM that can be measured is that which causes a delay across the whole observing band that is around the time resolution. As the amount of inter-channel delay scales as ν^{-2}, the precision with which DM can be measured decreases if the frequency of operation is high for the same time resolution. In other words, the accuracy of measuring DM and S/N depends not only on time resolution but also on frequency of operation. The standard procedure to measure DM is by performing multiple DM-trials and choosing that one DM which gives the maximum S/N - that is, maximizes the signal content in a particular time bin. This procedure works well if the burst structure is simple (OFF-ON-OFF) and has no frequency dependent structure, and the time resolution is sufficient to unambiguously resolve any structure of that burst. That is, sufficient to robustly identify the temporal extent of the burst. Obviously, high S/N bursts lead to robust DM measurement.

The precise DM measurement is illustrated with a burst of FRB 20200120E (Bhardwaj et al., 2021) detected using the 100-metre Effelsberg Radio Telescope at L-band (Pearlman et al., 2025). Fig. 2.7 (*left*) shows the frequency averaged total intensity time series and the dynamic spectrum of the burst. This burst has a simple morphology, and the time resolution of the data is sufficiently high (64 μs) to confidently identify the OFF-ON-OFF burst structure. Using this burst, multiple DM trials are performed and S/N is measured for each DM. Fig. 2.7 (*right*) shows measured S/N for multiple DM trials. The points follow a parabola that can be fitted to measure the center line of the parabola that yields the DM estimate for which the S/N is the maximum, is the precise DM of the burst.

Scintillation bandwidth

Inhomogeneities in the propagation medium cause the emission from the FRB to interfere when observed from the Earth. A consequence of which is that intensity of emission scintillates (or modulates) against frequency. Although the modulation is random in nature, the bandwidth of the modulation, which is known as scintillation bandwidth, carries information about the dimensions of the scale of inhomogeneities and is informative. It is a measure of bandwidth which shows correlated modulation. Therefore, the full width at half maximum of Autocorrelation Function (ACF) of the modulated intensity against frequency yields a measure of scintillation bandwidth. However, in practice, a Lorentzian is fitted to the ACF and the width of the Lorentzian is treated as the scintillation bandwidth. Scintillation bandwidth scales with frequency usually as ν^{α} where α is determined by the properties of the inhomogeneities. This short description of the phenomena does not do any justice to the richness of the science underneath it. Readers are urged to refer to Tim Sprenger (2024) for a thorough presentation of the subject.

Measuring scintillation bandwidth can be illustrated using a burst of FRB 20180916B (CHIME/FRB Collaboration et al., 2019b) detected using 100-meter Effelsberg Radio Telescope at 5 GHz (Bethapudi et al., 2023)[2]. Fig. 2.8 (*leftmost*) shows the dynamic spectrum of the burst zoomed in to show the scintillation pattern. To account for the scintillation bandwidth frequency variation, two distinct sub-bands are identified which are situated at 4972 and 4684 MHz. *Second-to-left* of the same figure shows the time averaged, intensity normalized frequency profiles of both the sub-bands with blue and red colors. The random relative variability in the intensity is the scintillation pattern. In *right-most* of Fig. 2.8, the ACFs and the best fit Lorentzians are shown for each of the identified sub-bands. The scintillation bandwidths of blue and red measure to be $4.4(6)$ and $3.3(3)$ MHz.

---

[2] This paper is the basis for Chapter 4.

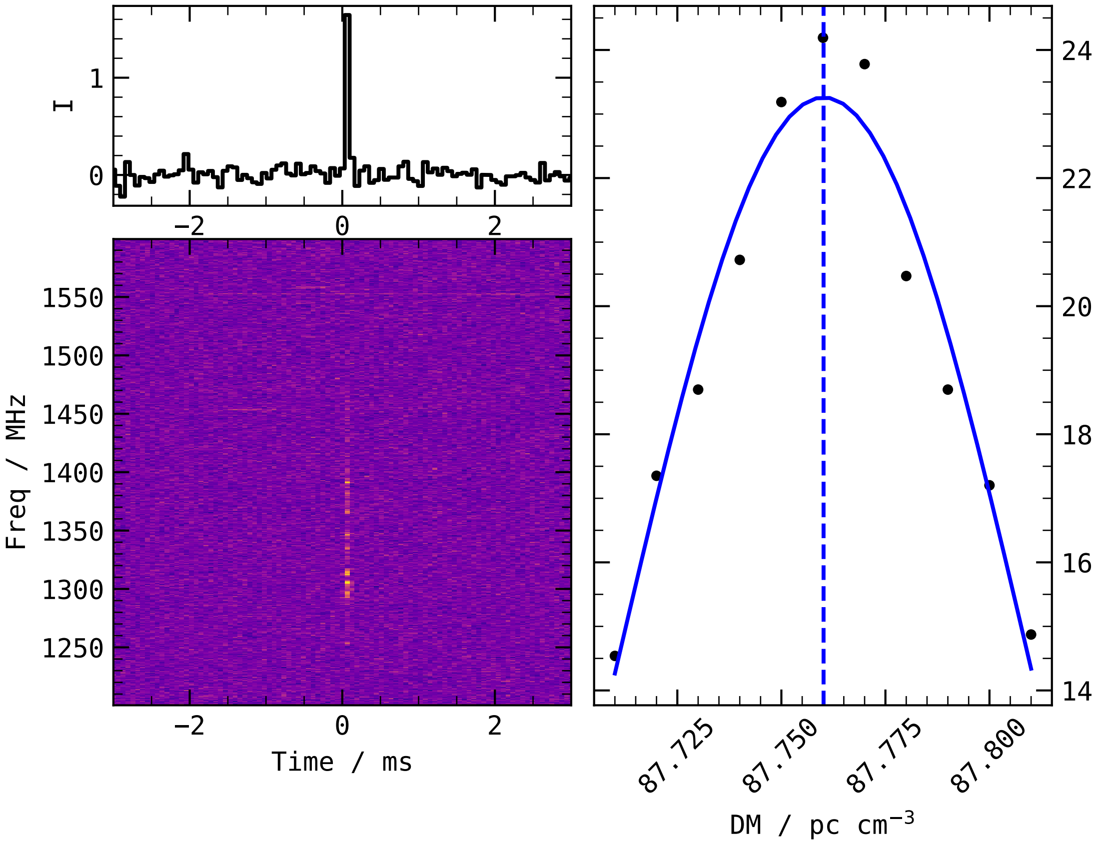

Figure 2.7: Burst from FRB 20200120E detected using 100-meter Effelsberg Radio Telescope at L-band (Pearlman et al., 2025). *Left* shows the total intensity time series and dynamic spectrum, both de-dispersed with the DM which gives the maximum S/N. *Right* shows S/N for different DM trials. The blue line is the best fit parabola and the center line is the DM which gives the maximum S/N.

Rotation Measure and Position Angle

Linear polarized light of FRBs, when passing through magnetized plasma where the magnetic field orientation is parallel to the emission propagation, causes the PA to rotate. This phenomena is known as Faraday rotation. The mathematics of which is described in detail in Sect. 1.3.2 and repeated here:

$$Q + jU = L \exp\left\{2j\left(\mathrm{RM}\lambda^2 + \mathrm{PA}_0\right)\right\}.$$

PA_0 is the initial PA before rotation.

The same effect can also be visualized using the following definition

$$\mathrm{PA} = \frac{1}{2}\arctan\left(\frac{U}{Q}\right),$$

then

$$\mathrm{PA} = \mathrm{RM}\lambda^2 + \mathrm{PA}_0.$$

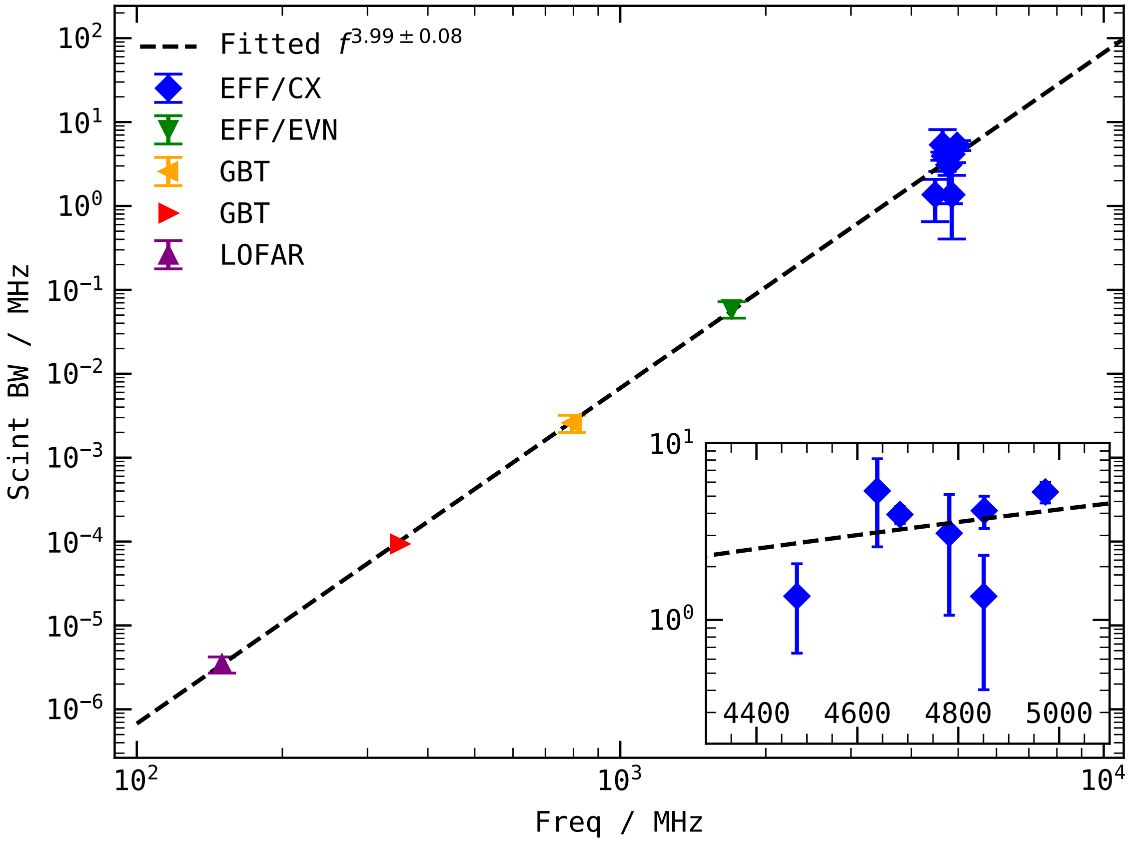

Figure 2.8: Dynamic spectrum, time averaged intensity normalized frequency profiles and the Auto-correlation Function of the frequency profiles. The burst is detected using 100-meter Effelsberg Radio Telescope from FRB 20180916B (Bethapudi et al., 2023).

In terms of Q and U, Faraday rotation causes sinusoidal rotation in Q, U against λ^2. And in terms of PA, Faraday rotation linearly changes PA against λ^2. The PA is the orientation of the light and is limited to be in $[-90°, 90°)$.

This effect can be illustrated using a polarization calibrated burst of FRB 20180916B (Bethapudi et al., 2025b)[3]. In Fig. 2.9, the dynamic spectra of calibrated Stokes- I, Q and U are plotted. The red and blue modulation seen in Q and U is Faraday rotation. To illustrate the effect against λ^2, a single time slice from the dynamic spectrum is chosen that has the highest S/N. Fig. 2.10 shows the time slice of Q, U and PA against λ^2. The top-axes in each of the panels show the observing frequency. Measuring RM is now simply fitting the models to the data. In the same figure, the best fit curves are also plotted. The RMs from QU-fitting and RMλ^2 model is $-116.1(2)$ and $-116.0(9)$ rad m^{-2} respectively. The PAs measured are $-90(2)$ and $-88(11)$ deg.

---

[3] This paper is the basis for Chapter 5.

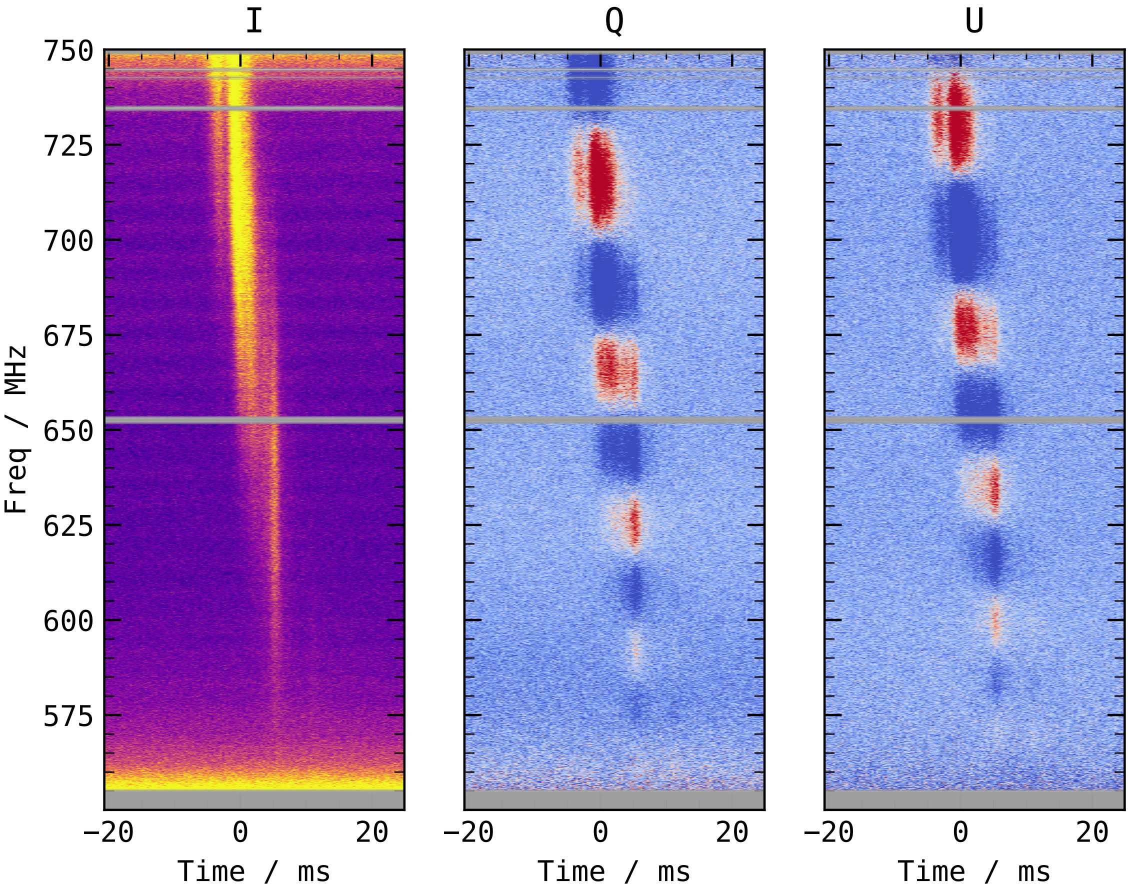

Figure 2.9: Polarization calibrated I, Q and U dynamic spectra of a burst from FRB 20180916B using the uGMRT between 550 and 750 MHz (Bethapudi et al., 2025b). The gray horizontal bands are removed channels due to RFI.

2.5 Sciences from repeating FRBs

The power of studying repeating FRBs is not only that large number of bursts can be detected, but also that variability in the observables from the bursts can be tracked. For example, it is seen that FRB 20121102A has not just RM varying with time (Hilmarsson et al., 2021) but also the DM (Wang et al., 2022). Sometimes, the variability is extremely drastic as in case of FRB 20190520B, which saw two sign flips in RM suggesting an actual flip in the orientation of the magnetic field (Anna-Thomas et al., 2023). The variability need not be drastic as seen in case of FRB 20201124A where RM variability died down towards the end of its activity (Xu et al., 2022). Not all variability is related to the source. The relative motion between the Earth and the thin scattering screen causes a doppler shift, which can be tracked by measuring scintillation bandwidths as done in FRB 20201124A (Main et al., 2022; Main et al., 2023). The variability in RM is seen as a common feature across repeaters, as noted by Mckinven et al. (2023b). This thesis focuses on a single repeating FRB source and tries to track the variability in the observables from its bursts.

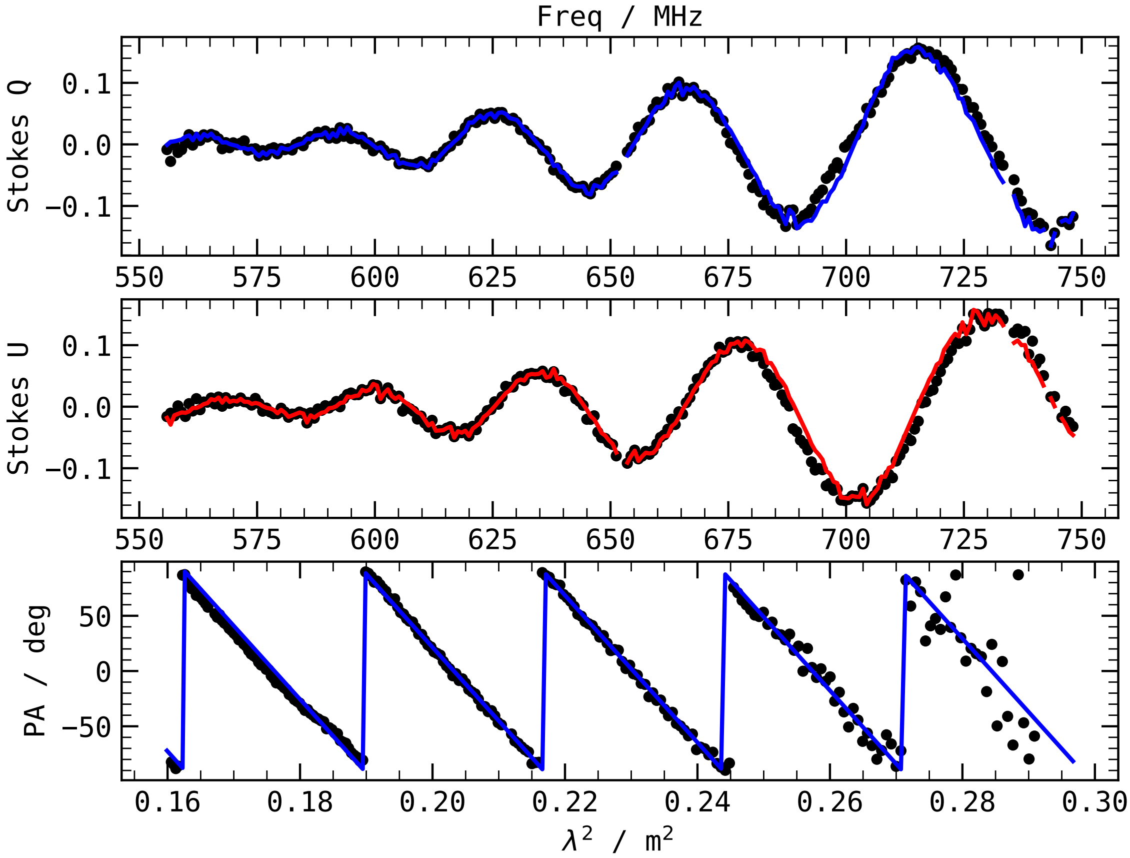

Figure 2.10: Measuring RM using QU-fitting and RMλ^2 model fitting. The *top* two panels show Q and U against frequency with data denoted by black dots and the model by solid line. The *bottom* panel shows PA against λ^2. It is the same burst shown in Fig. 2.9.

CHAPTER 3

FRB 20180916B

FRB 20180916B is a repeating FRB source discovered by the CHIME/FRB experiment (CHIME/FRB Collaboration et al., 2019b). It is the third repeating FRB to be discovered. The first is FRB 20121102A (discussed in Chapter 2) and the second is FRB 20180814, which was also discovered by CHIME/FRB (CHIME/FRB Collaboration et al., 2019a). Therefore, this source is also colloquially known as R3, the third repeater. FRB 20180916B is the protagonist of this thesis. The following three science chapters will be focusing on this singular source. Therefore, in the following sections of this chapter, everything known about this source will be covered. It will also include contributions from the science chapters so that this one chapter tries provide all the known knowledge about the source in one place.

3.1 Observational

All the published detections of FRB 20180916B are listed here from the lowest frequency to highest: LOFAR 150 MHz (Pastor-Marazuela et al., 2021; Pleunis et al., 2021; Gopinath et al., 2024), SRT 300 MHz (Pilia et al., 2020), GBT 300 MHz (Chawla et al., 2020), uGMRT 300 MHz (Pleunis et al., 2021; Sand et al., 2022), Northern Cross 400 MHz (Trudu et al., 2022), CHIME 600 MHz (CHIME/FRB Collaboration et al., 2019b; Chime/Frb Collaboration et al., 2020; Pleunis et al., 2021; Mckinven et al., 2023a), uGMRT 650 MHz (Marthi et al., 2020; Bethapudi et al., 2025b), GBT 800 MHz (Sand et al., 2022), APERTIF 1370 MHz (Pastor-Marazuela et al., 2021), Effelsberg 1700 MHz (Nimmo et al., 2021), Effelsberg 5000 GHz (Bethapudi et al., 2023).

Scattering timescale or scintillation bandwidth has been measured from 150 MHz to 5 GHz by various telescopes (Chawla et al., 2020; Marcote et al., 2020; Pastor-Marazuela et al., 2021; Sand et al., 2022; Bethapudi et al., 2023). Fig. 3.1 shows scintillation bandwidth versus observing frequency. Scintillation bandwidth clearly follows the ν^{-4} trend consistent with a thin screen scattering model where the screen in situated somewhere within the Milky Way. This implies that between the Earth and the source, there is only one dominant scattering screen which is responsible for the scattering we see.

Detection of large number of bursts allows for performing statistics with the observables. One such statistics is to model cumulative rate above a fluence threshold as a power law function of the threshold. Mathematically,

$$\text{Rate}(\geq F) \propto F^{\Gamma}. \tag{3.1}$$

Using the datasets of CHIME/FRB (Pleunis et al., 2021; Sand et al., 2023) and uGMRT (Bethapudi et

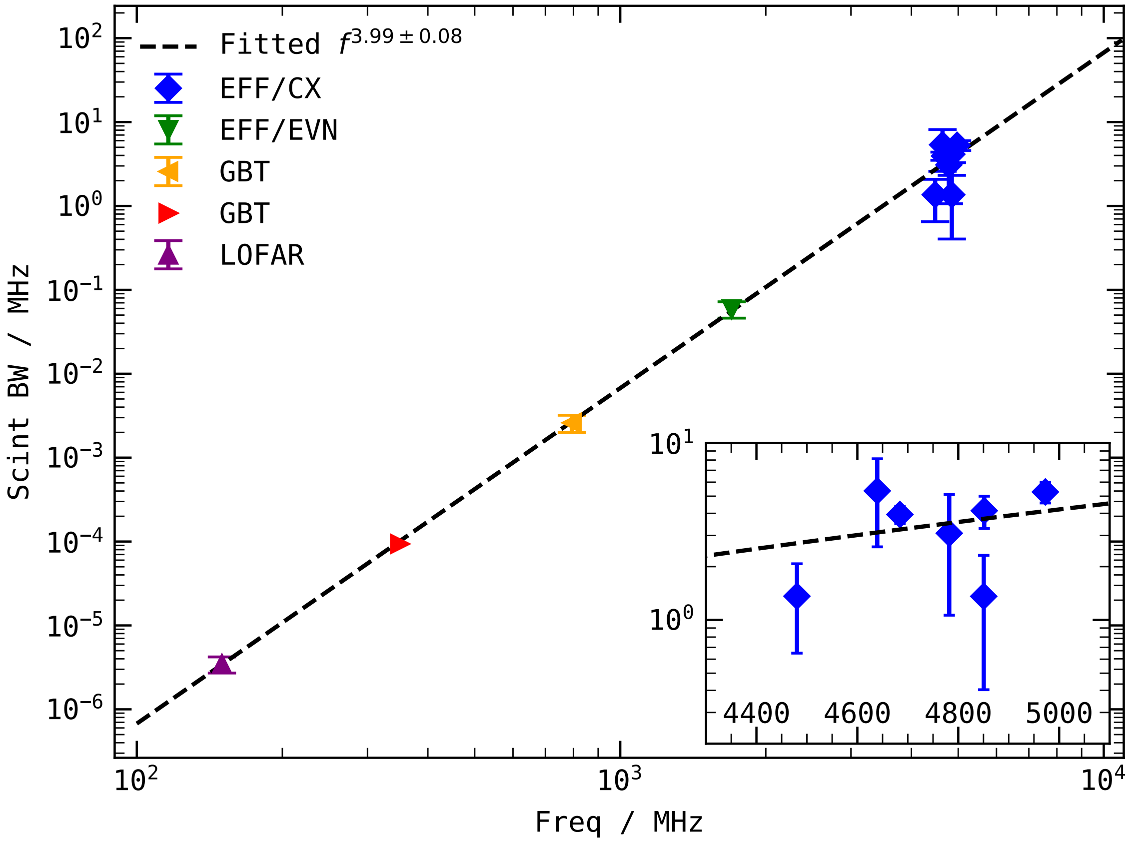

Figure 3.1: Measured scintillation bandwidth versus observing frequency. Following are the references: LOFAR (Pastor-Marazuela et al., 2021), GBT (red triangle to right; Chawla et al., 2020) and (orange triangle to left; Sand et al., 2022), EFF/EVN (Marcote et al., 2020), and EFF/CX (Bethapudi et al., 2023). The fitted power law is shown in dashed line.

al., 2025b), cumulative rate versus F is plotted in Fig. 3.2. The rate versus fluence is fitted with power laws as per Eq. 3.1 with breakpoints added at places determined by the fitting algorithm. The first breakpoints is treated as the fluence completeness limit. It shows that uGMRT is much more sensitive than CHIME/FRB. Possibly because of which, Γ is shallower compared to high energies. Published rates of FRB 20180916B reported by Pastor-Marazuela et al. (2021), Pleunis et al. (2021), Sand et al. (2023), Bethapudi et al. (2023), and Bethapudi et al. (2025b) after being brought to the same fluence threshold using Eq. 3.1 are plotted against frequency in Fig. 3.3. The best fit power law model is shown with dashed violet line in the same figure.

An interesting property appears when plotting widths and bandwidths of the bursts, shown in Fig. 3.4. Each marker is color-coded with the center frequency of the burst. At lower frequencies, the bursts are wider and possess less bandwidth while at higher frequencies, the bursts are narrower and possess large bandwidth. Although it could be that bursts are lower frequencies are simply broadened due to scattering, it however, does not explain why bursts at higher frequencies have larger bandwidths. Additionally, in the same figure, the scattering timescales at multiple frequencies are color-coded and shown with vertical dashed lines. Even if the scatter broadening has been accounted for, the bursts still show this structure.

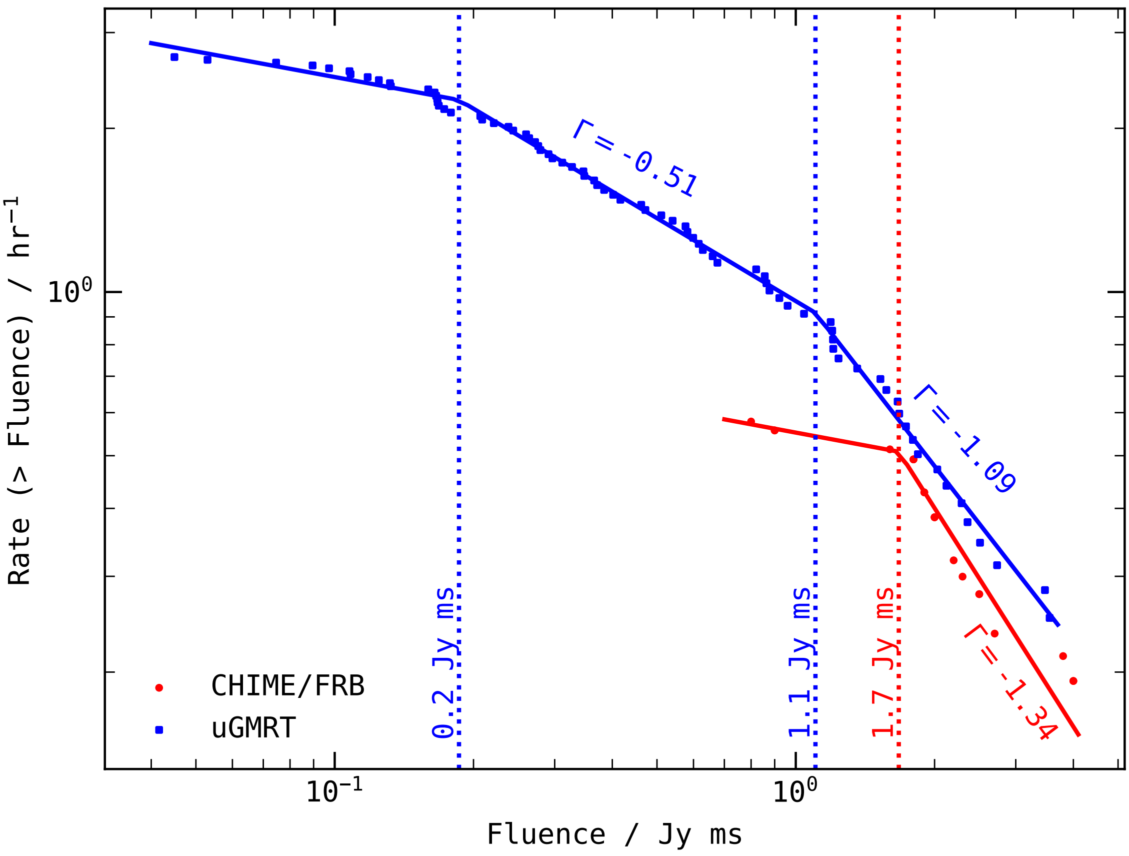

Figure 3.2: Cumulative rate above a fluence threshold versus fluence for CHIME/FRB (Pleunis et al., 2021; Sand et al., 2023) and uGMRT (Bethapudi et al., 2025b) datasets. The vertical dotted lines are the fluence breakpoints and the Γ corresponds to the fluence exponent (Eq. 3.1).

Ultimately, implying this could be a quirk of the underlying emission mechanism.

3.2 Host galaxy

FRB 20180916B was localized to the edge of a spiral galaxy SDSS J015800.28+654253.0 using the European VLBI network (EVN) at mas-level accuracy (Marcote et al., 2020). Spectroscopic analysis of the galaxy determined the redshift to be 0.0337 and comoving redshift distance of 149 Mpc. Deep imaging with EVN did not detect any persistent radio source at the FRB location. The flux constraint on the luminosity of PRS is $< 1.3 \times 10^{36}$ erg s^{-1} (Marcote et al., 2020). Optical imaging of the host galaxy with Gemini-North revealed a coincidence of FRB location and a 'V' shaped star-forming clump (Marcote et al., 2020). Moreover, Marcote et al. (2020) suggested this region could have undergone an interaction which triggered star formation. Kaur, Kanekar, and Prochaska (2022) performed HI spectroscopy of the host galaxy of FRB 20180916B using uGMRT and identified the host galaxy to be gas-rich but having low star formation rate, suggesting the host galaxy to have undergone a minor merger event in recent past. This corroborates with what has been reported in Marcote et al. (2020). Moreover, using Doppler shifts of

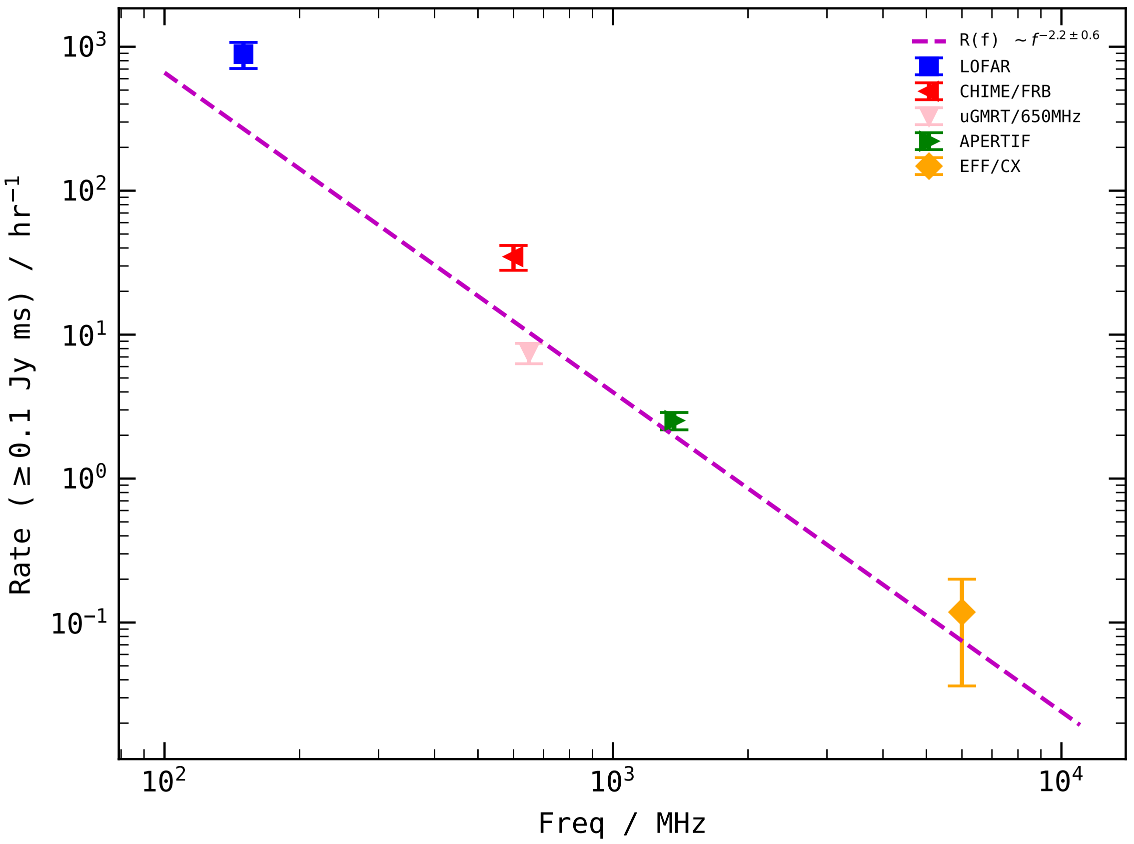

Figure 3.3: Observed rate versus observing frequency of FRB 20180916B. Measurements are collected from (Pastor-Marazuela et al., 2021; Pleunis et al., 2021; Sand et al., 2023; Bethapudi et al., 2023; Bethapudi et al., 2025b). The violet dashed line is the best fit power law model.

the HI line, Kaur, Kanekar, and Prochaska (2022) noted that the FRB location is in between two opposing velocity fields, as shown in Fig. 3.5. With this, they hypothesize that FRB location is where the minor merger event might have taken place.

The local environment of the FRB region has been closely studied with Hubble Space Telescope (HST) in visible and infrared bands by Tendulkar et al. (2021). The HST image is shown in Fig. 3.6 with the FRB location with red circle (Marcote et al., 2020). They also did not find any point source at the FRB location. Furthermore, they constrained the Hα luminosity and the local star-formation rate to be $\lesssim 10^{37}$ erg s^{-1} and $\lesssim 10^{-4}$M$_\odot$ yr^{-1}, respectively. Using the same limit for Hα luminosity, they successfully ruled out the presence of supergiant O-type stars. Interestingly, Tendulkar et al. (2021) note that the FRB location is around 190 pc away from the apex of the ‘V’ shaped structure found in the Gemini optical image (c.f. (Marcote et al., 2020)). In addition, they note that this ‘V’ shaped structure is actually part of the host galaxy and is co-rotating with the rest of the galaxy. Tendulkar et al. (2021) also report that the FRB location is around 250 pc away from the nearest young stellar population. Using this distance and typical velocities of compact objects, like pulsars and magnetars, they provide a constraint on the age of the FRB source to be of the order of Myr. The supposed old age of the FRB source is at odds with the relatively short lifespans of magnetars ($\sim$ 100 kyr). Lastly, Tendulkar et al. (2021) also presents a

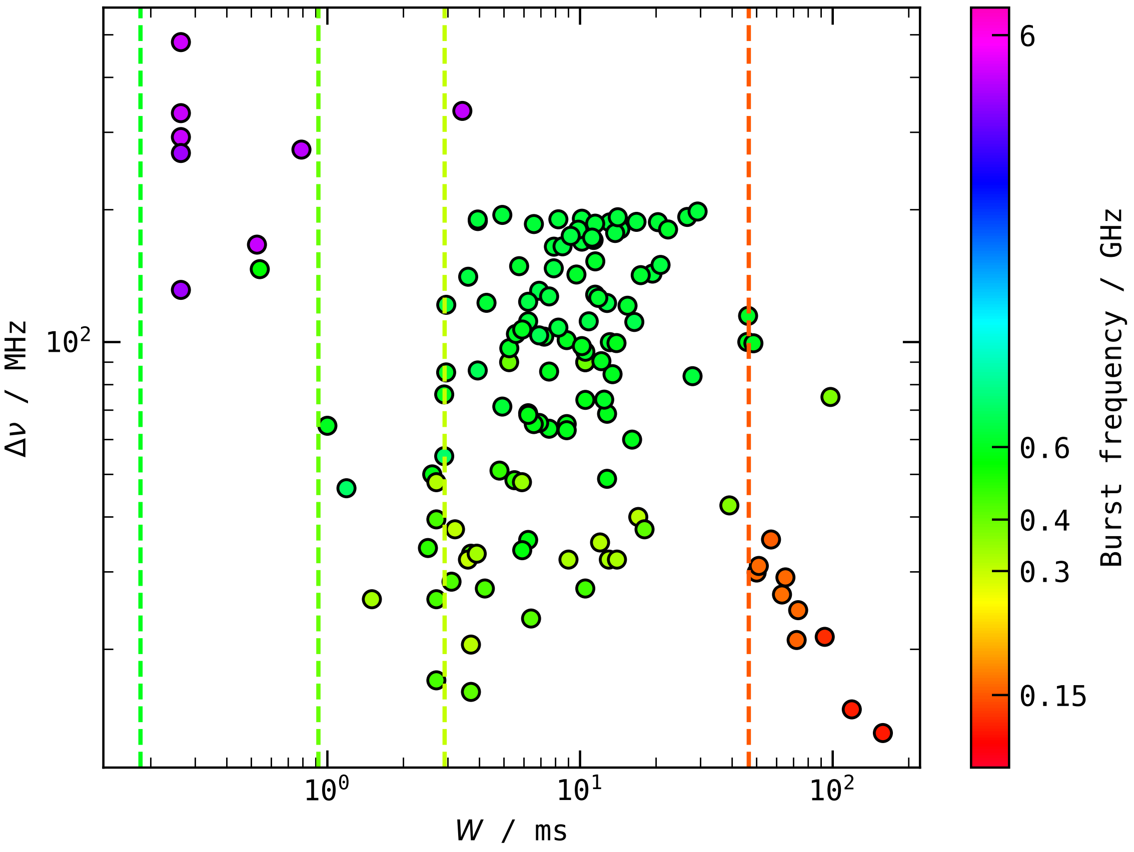

Figure 3.4: Observed bandwidth versus width of bursts of FRB 20180916B. The vertical dashed lines are scattering timescales at frequencies corresponding to their colors. See Sect. 3.1 for the list of detections.

comparison between high-mass X-ray binaries and γ-ray binaries and the FRB. In these systems, there is a compact object executing binary motion with a high-mass star companion. The periodicity of the FRB is explained by the orbital period. They highlight that spatial offsets between HXMBs and nearest star forming region is of the same order as that of FRB. In addition, they also highlight the ages of HXMBs and FRB are comparable suggesting the FRB could be a similar type of system.

3.3 Periodicity and chromaticity

Repeated daily observations of FRB 20180916B by CHIME/FRB led to multiple detections of bursts. These detections unraveled a periodicity in the activity of the source: all the bursts appear in a window of time that repeats every 16 days. That is, the active window of this FRB is periodic. With the detected bursts, the active window was measured to be 5.1 days and the periodicity of the active window to be 16.34 days (Chime/Frb Collaboration et al., 2020).

The periodicity model is referenced to MJD 58369.4 with a period of 16.34 days (Sand et al., 2023). The Activity Phase of the FRB periodicity is a number in $[0,1)$ when linearly mapped to the Period of the FRB, and the Activity Cycle denotes the integer number of elapsed turns since the reference MJD.

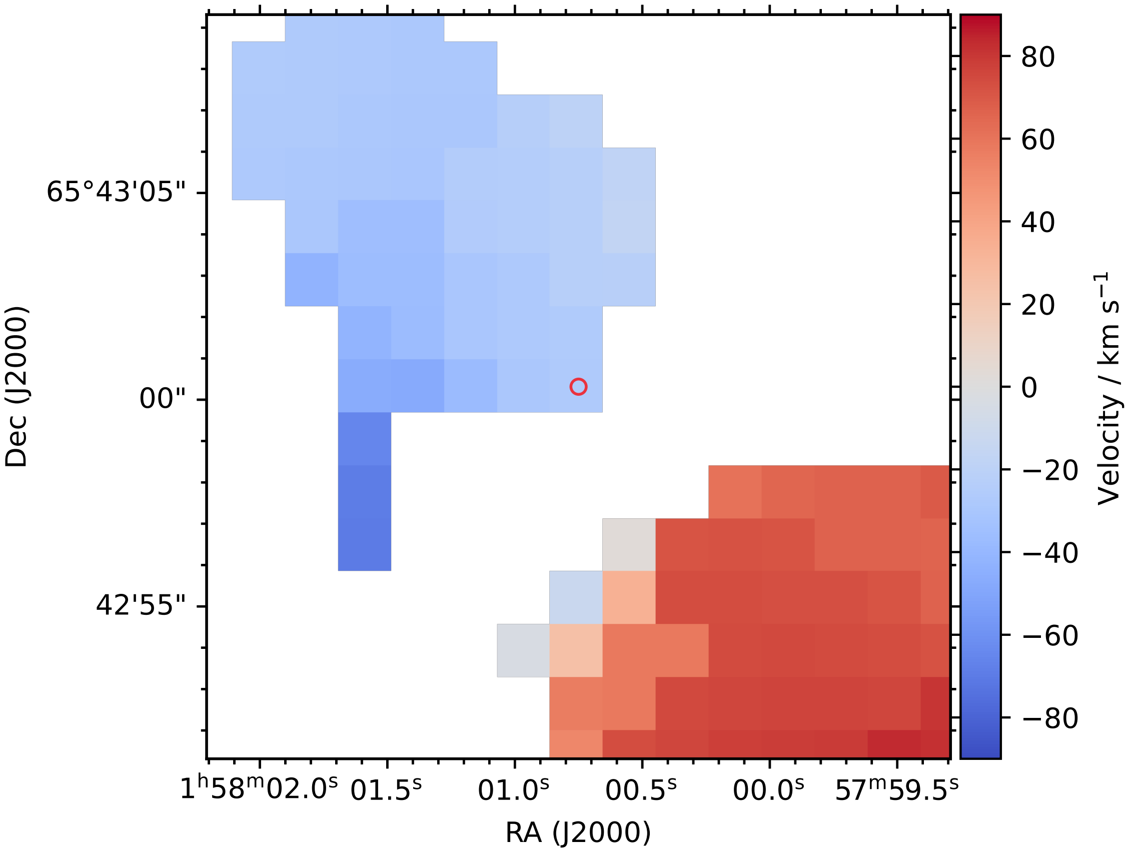

Figure 3.5: HI velocity field (Kaur, Kanekar, and Prochaska, 2022) of the host galaxy of FRB 20180916B measured by uGMRT. The FRB location is shown with red circle (Marcote et al., 2020).

Even after studying periodicity over a timespan of over 120 Activity Cycles (approximately 1945 days), the period did not appear to change (Sand et al., 2023; Lan et al., 2024). In other words, the derivative of the period is effectively zero.

While the activity window possesses periodicity, the bursts themselves do not possess any. This is evident when looking at the residuals after folding at some trial period, as shown in the *bottom panel* of Fig. 3.8 The plot used all the bursts detected in a single longest observation of FRB 20180916B, taken on MJD 59243 using uGMRT (Bethapudi et al., 2025b). The *top panel* shows the standard deviation of the residuals for every trial period. An unique minimum standard deviation is indicative of periodicity, which is not seen here. The periodicity on long timescale but not on short timescale is discussed in Cordes et al. (2022), who enlist and investigate different effects which destroy any short time scale periodicity. Primary reason, according to Cordes et al. (2022), is the phase jitter in the emission beam due to different emission heights for different bursts which causes phase noise, essentially culling any periodicity.

Observational campaigns at 150 MHz, 600 MHz and 1.3 GHz revealed that active windows depend on the observing frequency (Pastor-Marazuela et al., 2021; Pleunis et al., 2021). That is, the active window shifts and changes in length with the observing frequency. The frequency dependency, termed as chromaticity, was studied and modeled with a power law in Bethapudi et al. (2023). The modeling involved

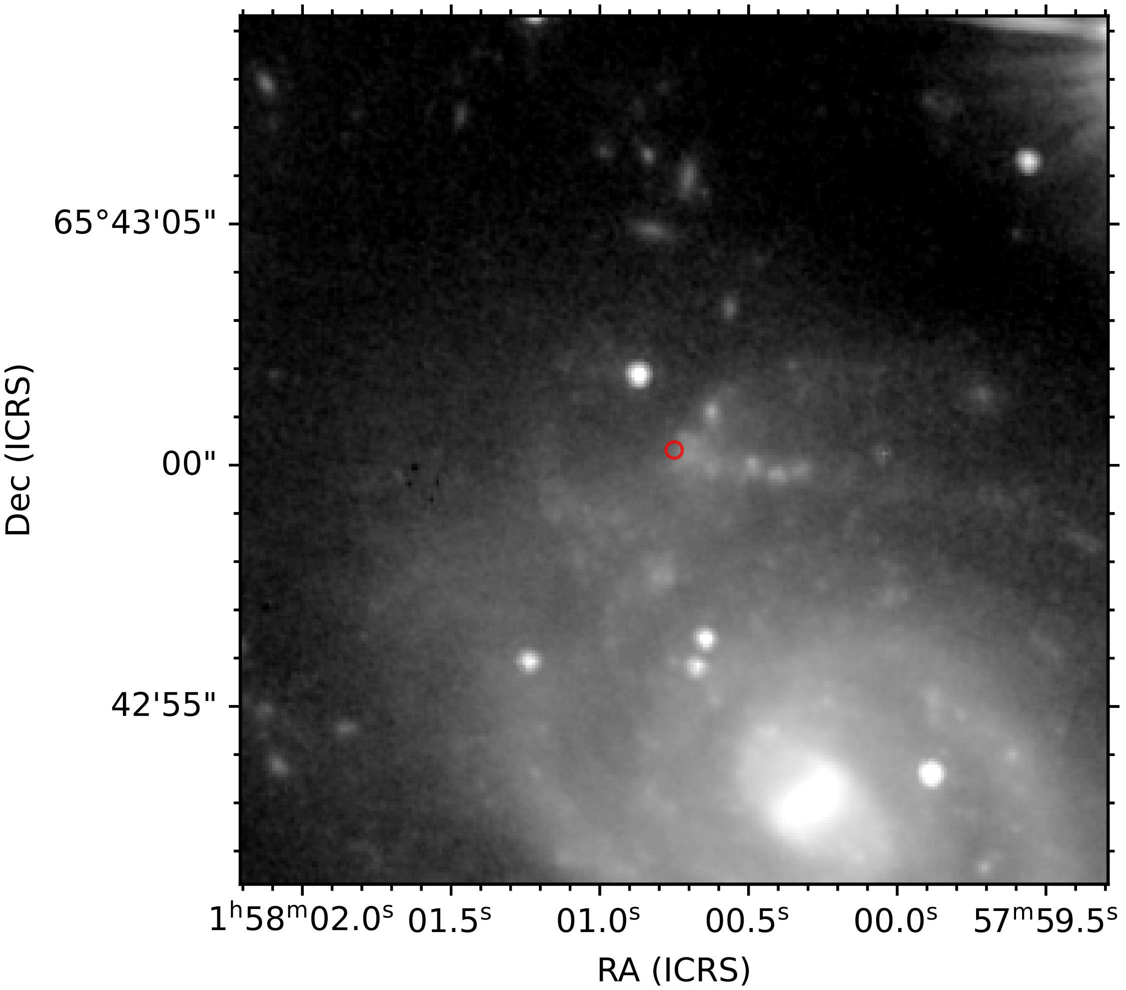

Figure 3.6: HST 110W image (Tendulkar et al., 2021) of the host galaxy of FRB 20180916B. The FRB location is shown with red circle (Marcote et al., 2020).

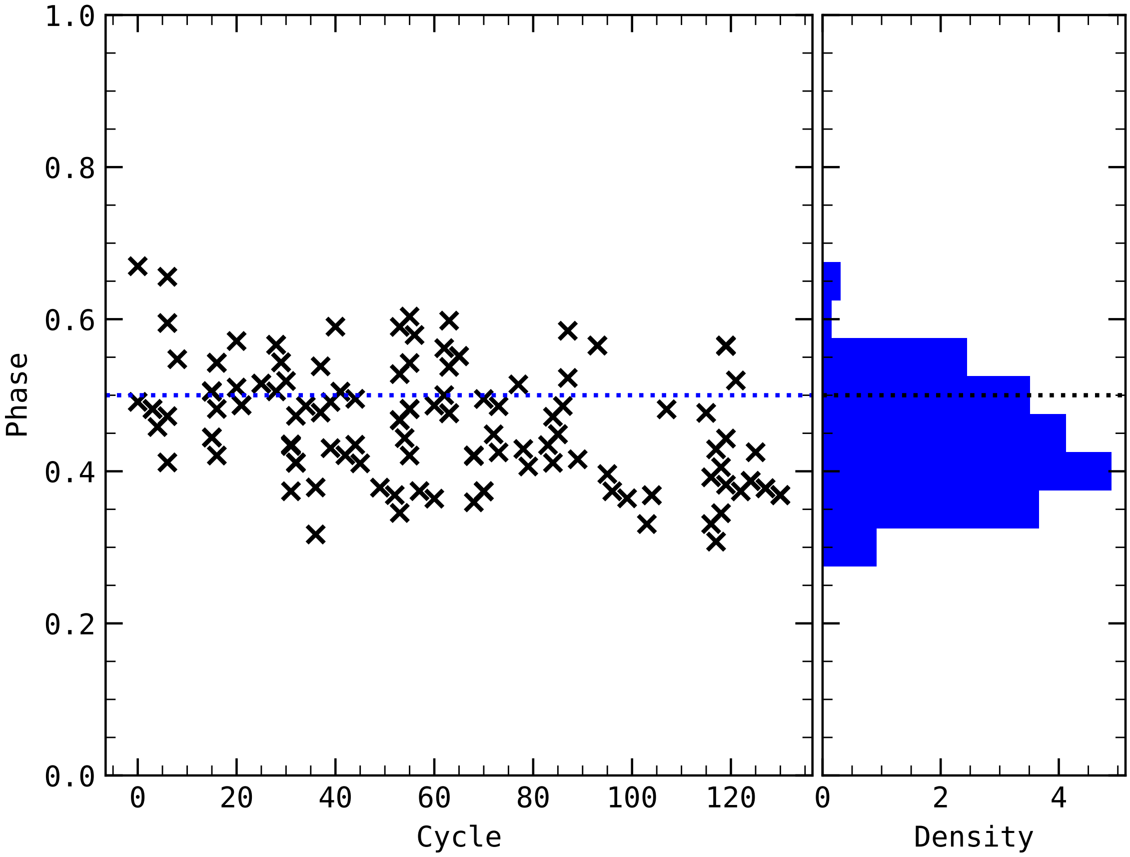

Figure 3.7: Activity Cycle versus Activity Phase of bursts detected by CHIME/FRB (Chime/Frb Collaboration et al., 2020). The *right* panel shows the normalized histogram. The horizontal dotted line is drawn at Phase of 0.5.

fitting the center and width of the Active Windows at 1370 MHz (Pastor-Marazuela et al., 2021), 600 MHz (Chime/Frb Collaboration et al., 2020; Pleunis et al., 2021) and 150 MHz (Pastor-Marazuela et al., 2021; Pleunis et al., 2021) with a power law. Thereafter, the power law was used to extrapolate the position and duration of the Active Window at 5 GHz. By scheduling and detecting bursts in that predicted active window, the power law model was verified (Bethapudi et al., 2023).

3.4 Polarimetric properties

Polarimetry of bursts of FRB 20180916B have been performed using multiple instruments at various frequency bands. Pastor-Marazuela et al. (2021) and Pleunis et al. (2021) performed polarimetry using LOFAR at 150 MHz, Chawla et al. (2020) using GBT at 300 MHz, Pleunis et al. (2021), Mckinven et al. (2023a), and Ng et al. (2025) using CHIME/FRB at 600 MHz, Bethapudi et al. (2025b) using uGMRT at 650 MHz, Sand et al. (2022) using GBT at 800 MHz, Pastor-Marazuela et al. (2021) using APERTIF at 1370 MHz, Nimmo et al. (2021) using Effelsberg at 1700 MHz, and lastly Bethapudi et al. (2023) using Effelsberg at 5000 MHz. Bursts from FRB 20180916B are known to have linear polarization and no circular polarization, across the frequency sprectrum.

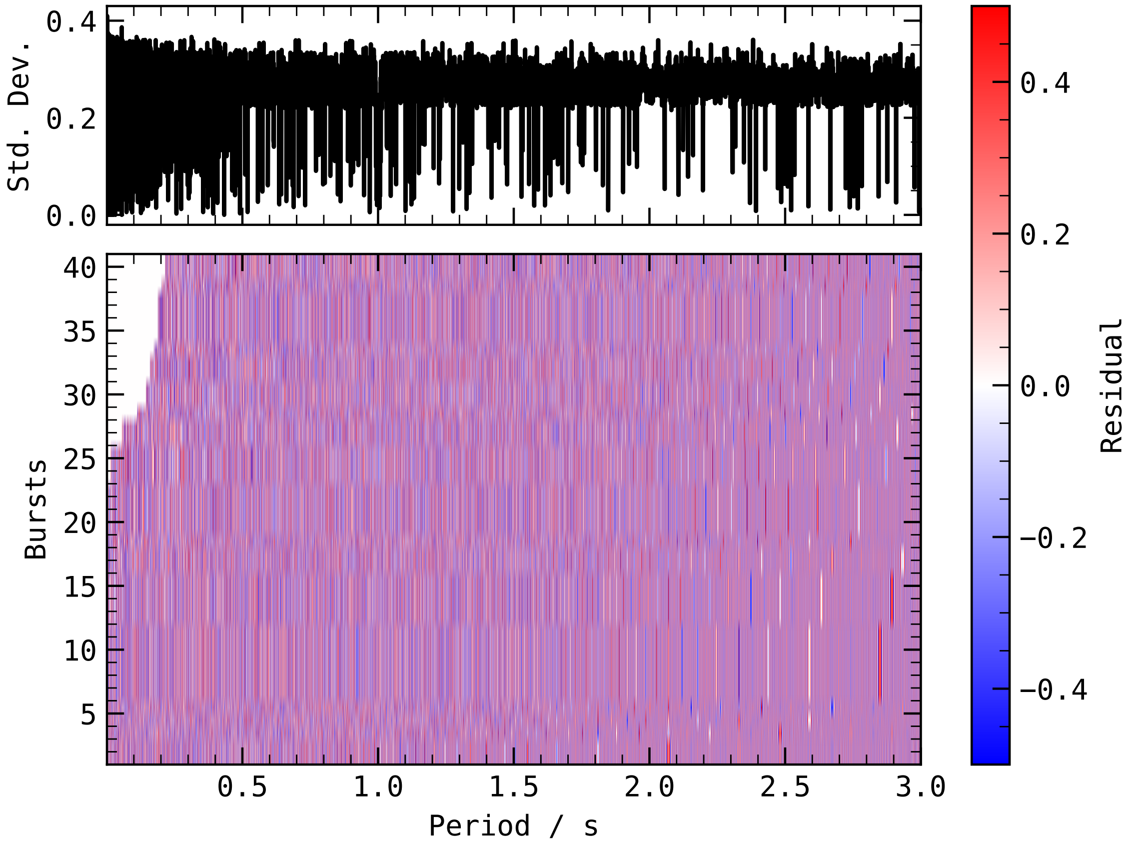

Figure 3.8: Residuals of bursts of FRB 20180916B detected within one observation on MJD 59243 (Bethapudi et al., 2025b) after folding with multiple trial periods. Residuals are within $[-0.5, 0.5)$ and are shown with colormap in the *bottom panel*. The *top panel* shows the standard deviation of all the residuals for a given trial period.

The linear polarization fractions of the bursts varies with observing frequency due to frequency dependent depolarization (Feng et al., 2022). Fig. 3.10 plots the linear polarization fractions against frequency. The depolarization-λ dependency is parameterized by σ_{RM} as follows:

$$\exp\left\{-2\sigma_{\mathrm{RM}}^2\lambda^4\right\}.$$

The cause of this depolarization is due to the multi path propagation of radio emission along magnetized paths, which depolarizes due to superposition of waves with random offsets. As the multi path propagation scales with λ, so does the depolarization. For FRB 20180916B, Feng et al. (2022) report a $\sigma_{\mathrm{RM}} = 0.12$ rad m^{-2}. It is plotted with a black line in Fig. 3.10.

The RM of bursts of FRB 20180916B varies in a step-like fashion. Since its discovery (MJD 58377) until MJD 59250, the RM was noted to only vary stochastically (Mckinven et al., 2023a). But from MJD 59250 until MJD 59650, the RM clearly showed a linear increasing trend (Mckinven et al., 2023a; Bethapudi et al., 2025b). Thereafter, from MJD 59650, the RM was again noted to be only varying in a stochastic fashion (Bethapudi et al., 2025b; Ng et al., 2025). The staggered step-like variability of RM has not been seen before. The RM versus MJD is plotted in Fig. 3.11.

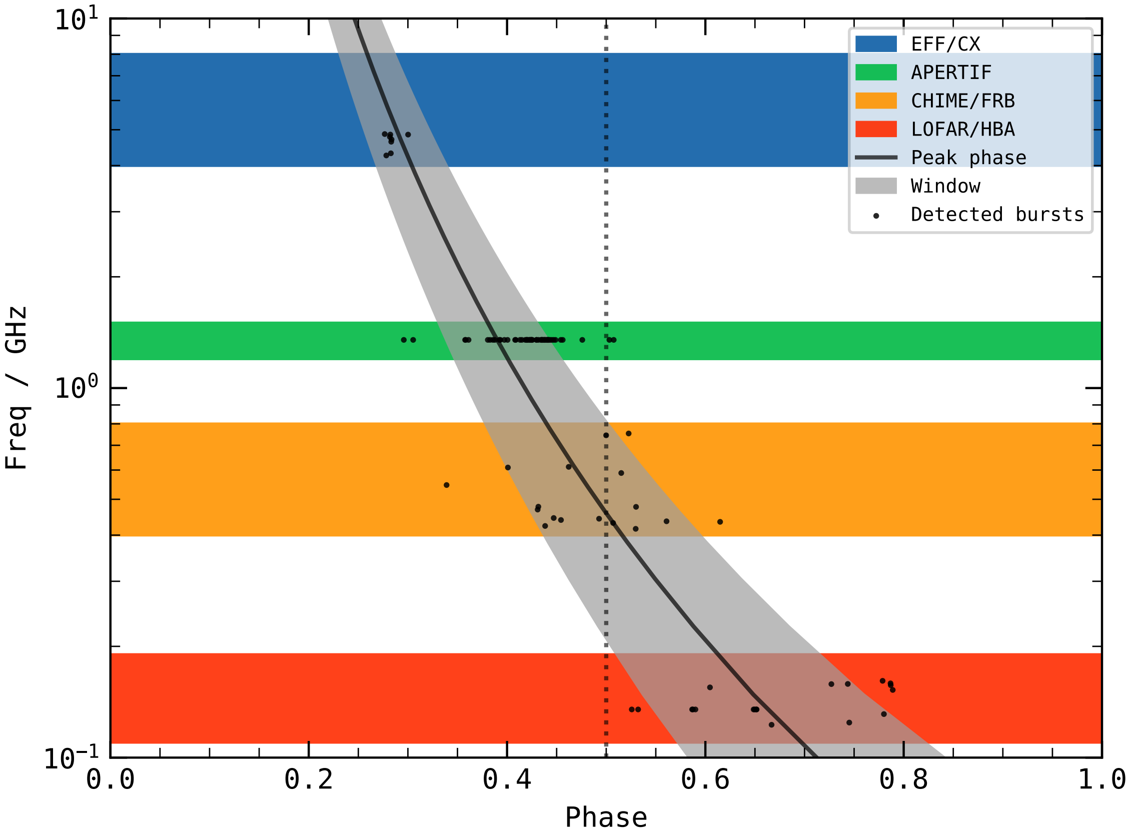

Figure 3.9: Center frequency of bursts versus Activity Phase. The colored bands are the respective instrument bandwidths. The vertical dotted line is at Phase of 0.5. Detections are taken from LOFAR/HBA (Pastor-Marazuela et al., 2021; Pleunis et al., 2021), CHIME/FRB (Chime/Frb Collaboration et al., 2020; Pleunis et al., 2021), APERTIF (Pastor-Marazuela et al., 2021) and EFF/CX (Bethapudi et al., 2023). The peak phase and window refer to the chromaticity model as described in Bethapudi et al. (2023).

In addition to having high linear polarization fraction, the Position Angle was noted to be flat within the bursts detected at wide range of frequencies, from 110 MHz to 5 GHz (Pleunis et al., 2021; Nimmo et al., 2021; Mckinven et al., 2023a; Bethapudi et al., 2023). This is seen to be true even if the bursts possess complex morphology. The long term study of PA of bursts done using uGMRT at 650 MHz reports that variability in PA is constrained to be $\lesssim 7$ deg over four hours. Moreover, they also report inter-cycle variability that PAs of bursts around the same Activity Phase but from different Activity Cycles is different.

3.5 Multi-wavelength campaigns

There are two motivations for performing multi-wavelength campaigns - (i) detection of persistent emission in any other wavelength regime, or (ii) detection of simultaneous emission in radio and in any other wavelength regime (usually X-ray or optical). Each of the motivations are summarized below.

Persistent emission at the FRB location would provide information about the kind of source that is

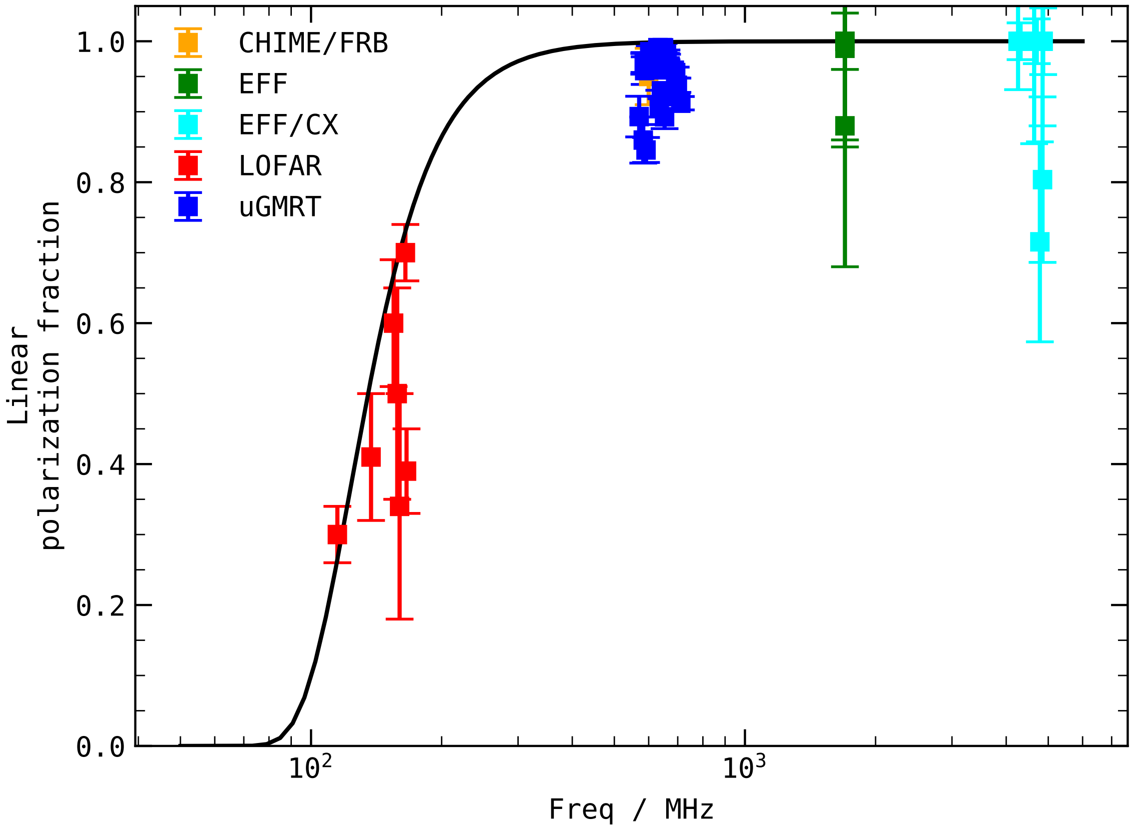

Figure 3.10: Linear polarization fraction versus center frequency of the bursts color-coded by the detection instrument. LOFAR measurements come from Pleunis et al. (2021) and Gopinath et al. (2024), uGMRT measurements only include those which have fluence above 1.1 Jy ms (Bethapudi et al., 2025b), EFF Nimmo et al. (2021), EFF/CX Bethapudi et al. (2023). The black line is the Faraday depolarization with $\sigma_{\mathrm{RM}} = 0.12$ rad m^{-2} (Feng et al., 2022).

emitting bursts. However, it has only been constrained in X-ray using Chandra X-ray telescope and Swift-BAT. Scholz et al. (2020) reports a X-ray luminosity upper limit of 2×10^{40} erg s^{-1} in soft X-ray regime in 0.5-10 keV range using Chandra. In the hard X-ray regime (from 14-195 keV), Laha et al. (2022) report an upper limit of $(5 - 85) \times 10^{44}$ erg s^{-1} using Swift-BAT. Laha et al. (2022) constraint rules out all the known X-ray emitting sources within the Milky Way as a possible progenitor for FRB 20180916B. Moreover, Scholz et al. (2020) also searched for persistent γ-ray emission using Fermi/LAT but did not find any source.

Simultaneous multi-wavelength campaigns provide constraints on the multi-wavelength emission, which can be used to test various emission and progenitor models. They report luminosity or fluence ratios of measurement in multi-wavelength band to that in radio regime, which is a marker for the emission mechanism. Despite a well studied periodicity model which greatly facilitates performing multi-wavelength simultaneous campaigns, no simultaneous multi-wavelength detection has been made so far. Therefore, only upper limits on the luminosity/fluence ratios have been made. Scholz et al. (2020) report a detection of radio burst with CHIME/FRB while observing in X-ray with Chandra. They report a luminosity ratio upper limit to be 4.7×10^7. Trudu et al. (2023) report detection of a radio burst with SRT while observing

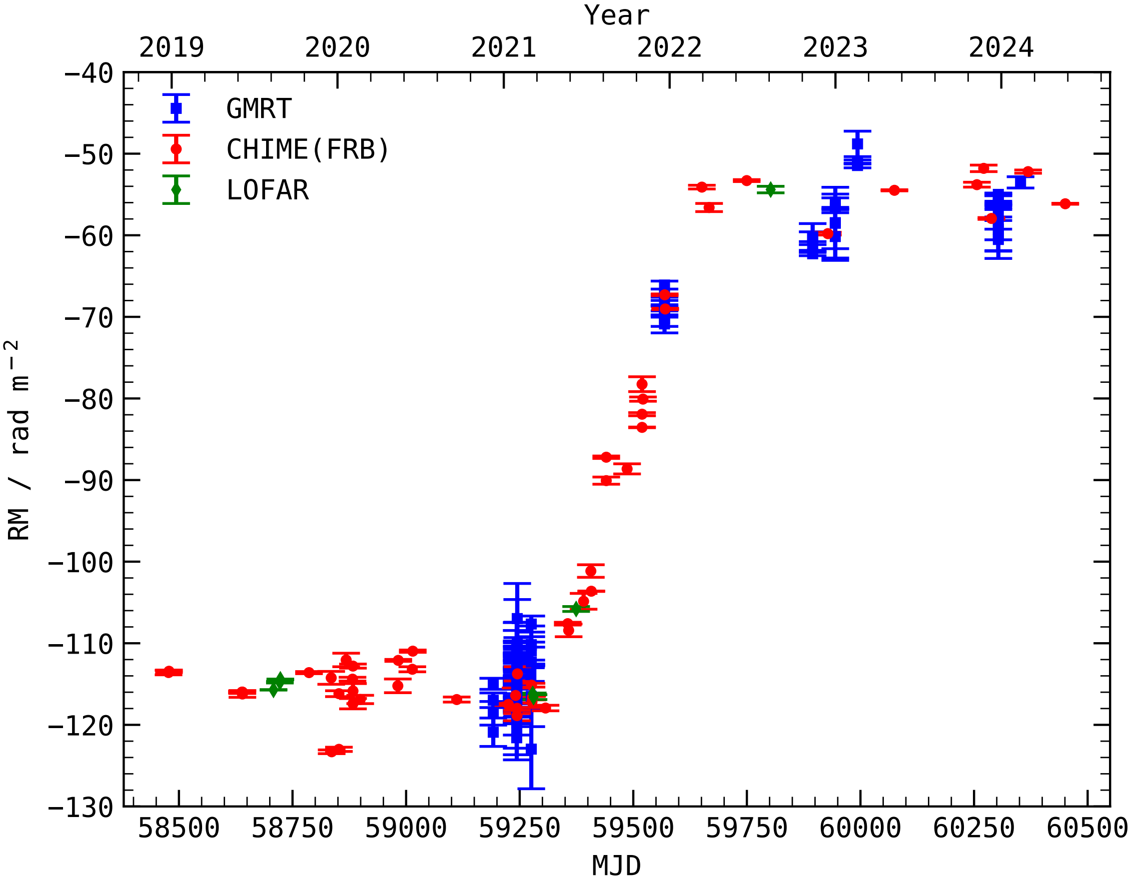

Figure 3.11: Rotation Measure versus MJD of bursts reported by CHIME/FRB (red circles; Pleunis et al., 2021; Mckinven et al., 2023a; Ng et al., 2025), LOFAR (green diamonds; Pleunis et al., 2021; Gopinath et al., 2024) and uGMRT (blue squares Bethapudi et al., 2025b). The top x-axis shows calendar year.

in X-ray with Insight-HXMT, using which they report luminosity ratio upper limit to be $\leq (0.9-1.3)\times10^{7}$. Kilpatrick et al. (2021) performed deep optical observations of the FRB with the Apache Point Observatory in i-band, with which they constraint the luminosity optical-to-radio ratio to be $\leq$ 800. Trudu et al. (2023) also used radio bursts detected using SRT and uGMRT to constraint the luminosity optical-to-radio ratios to be $\lesssim 10^{2}$ using Aqueye+ and SiFAP2 optical telescopes. In addition, Andreoni et al. (2020) conducted observations with Zwicky Transient Factory (ZTF) and CHIME/FRB and report optical-to-radio fluence ratio of $\leq$ 200 in optical bands $g + r$. Lastly, Kilpatrick et al. (2024) performed similar exercize with Gemini-North and report the most stringent optical-to-radio fluence ratio of $(2-7)\times10^{-3}$ in r- and i-bands.

3.6 Progenitor models

Any progenitor model for FRB 20180916B needs to explain (i) repeated burst emission with no apparent periodicity, (ii) periodicity and chromaticity of the active windows, (iii) no change in the period of the active window. For this, there are two leading classes of progenitor models: (i) compact object models which explain periodicity by means of rotational dynamics, and (ii) binary models which explain periodicity through binary motion. In compact object models, the emission comes from the compact object itself which executes dynamics such as rotational or precession or both, and the active window periodicity comes from any of the dynamical timescales of the compact object. In the binary models, the periodicity arises from the binary orbital period. The active window is when the binary system is in a special configuration that facilitates bursts and is model specific.

Active window periodicity due to slow rotation has been studied by Beniamini, Wadiasingh, and Metzger (2020). They argue that really long periods (of 16.34 days) require complicated scenarios of angular momentum transfer and is not well suited for large periods, such as that of FRB 20180916B. Active window periodicity has also been explained with precession, where the mechanism causing precession is different. For example, Zanazzi and Lai (2020) and Levin, Beloborodov, and Bransgrove (2020) consider the torque free precession, where the precession is caused by the oblateness of the magnetar body due to internal magnetic fields. Coming from the other way, Wasserman et al. (2022) investigate the required conditions on the magnetic field structure of the compact object for it to precess and explain Active window periodicity. Lastly, Feng, Yang, and Li (2024) perform time evolution of obliquity of a population of magnetars to provide constraints on the age of the FRB source using the period. The constraints on the age by them are consistent with that from kinematic considerations (Tendulkar et al., 2021) In so far, the precession considered is torque-free as no outside torque is causing it. Sob'yanin (2020), however, consider forced precession where the precession is driven by anomalous electromagnetic torque due to stellar rotation. Yang and Zou (2020) explain how a binary system can also induce precession which can explain Active window periodicity. Lastly, there are also some exotic models which invoke Lense-Thirring effect (Chen, 2020) or jet precession (Chen et al., 2021) to explain the periodicity of the FRB.

Binary models have also been shown to explain the periodicity (Wada, Ioka, and Zhang, 2021). In all the binary models, burst emission is hypothesized to happen around periastron due to effective mass transfer which powers the FRB generation. Tight O/B binaries have been proposed as well (Lyutikov, Barkov, and Giannios, 2020). However, active window periodicity need not be due to orbital period. It could be that the passing of a companion clears the local environment and makes the medium transparent for bursts to pass through and reach the observer. Having said so, Gu, Yi, and Liu (2020) suggest how in order for binary models to explain the periodicity and duty cycle, the eccentricity of the orbit should be high (> 0.95). Zhang and Gao (2020) performed a population synthesize and identified that B-type star binaries are the likely sources for periodic FRBs. Be-type/X-ray binary systems have also been proposed to explain FRB (Li et al., 2021). Other models include accreting stellar binary model (Deng, Zhong, and Dai, 2021). Binary orbits of NS-WD are considered with and without GW damping (Lin et al., 2022). Lastly, interaction of strange star with its planet is also shown to explain FRB (Nurmamat et al., 2024). More exotic models suggest periodic FRBs can be explained by extragalactic asteroid belts (Dai and Zhong, 2020). Similarly, Du et al. (2021) propose a pulsar companion binary system, which also has asteroid belt, can also explain the observed periodicity of FRB. In both the models, bursts arise when the asteroids collide with the compact object. Lastly, there have been few papers which propose to use the change in the periodicity ($\dot{P}$)to constraint the progenitor models (Katz, 2021). Wei, Zhao, and Wang (2022) performs model selection based on the sign of $\dot{P}$. Although, as already noted above, Sand et al. (2023) and Lan et al. (2024) showed that $\dot{P} = 0$ and suggest a binary model for FRB 20180916B.

CHAPTER 4

High frequency study of FRB 20180916B using the 100-m Effelsberg radio telescope

If you eliminate the impossible; whatever remains, however improbable, must be the truth.

Spock, Star Trek (2008)

This chapter describes my contributions to the article published in Monthly Notices of Royal Astronomical Society which appears as S. Bethapudi, L. G. Spitler, R. A. Main, D. Z. Li, and R. S. Wharton (2023), *High frequency study of FRB 20180916B using the 100-m Effelsberg radio telescope*, MNRAS **524**.3 3303, https://doi.org/10.1093/mnras/stad2009, arXiv: `2207.13669 [astro-ph.HE]`. The publication can be found in Appendix A.

Author contributions: SB conducted observations, searched the data for bursts, performed data analysis and wrote the manuscript. LS guided the project and writing. RM provided input into the scattering and scintillation analysis. DL and RW commented on the manuscript.

The bursts of FRB 20180916B at 600 MHz were found to only appear in a 5.1 day active window which repeats every 16.34 days (Chime/Frb Collaboration et al., 2020). That is, the active window of the FRB 20180916B was found to be periodic. Right after this discovery, multiple telescopes at various frequencies performed targeted observations when the FRB 20180916B is expected to be active so as to maximize the detection of bursts. The detections of bursts at frequencies further away from 600 MHz showed deviation from the periodicity model. Bursts at frequencies higher than 600 MHz arrived earlier than the predicted window, whereas, bursts at frequencies lower than 600 MHz arrived much later than the predicted window. That is, it was recognized that periodicity model of FRB 20180916B is not the same for all frequencies of bursts. This property, termed as chromaticity, was highlighted by detections at 1370 MHz by APERTIF (Pastor-Marazuela et al., 2021) and those at 150 MHz by LOFAR (Pastor-Marazuela et al., 2021; Pleunis et al., 2021). The subsequent modeling and testing of the chromaticity is what the first science chapter of the thesis entails.

Firstly, the deviations of the bursts from the periodicity model is to be modeled. To this end, i collected all the published bursts of FRB 20180916B, and from each of the burst, i tabulated its arrival time, frequency range and instrument used in detection. To avoid any biases from considering bursts that were detected in targeted observations, i only used bursts detected by blind surveys. That is, i only included bursts from LOFAR 150 MHz (Pastor-Marazuela et al., 2021; Pleunis et al., 2021), CHIME/FRB 600 MHz (Chime/Frb Collaboration et al., 2020; Pleunis et al., 2021) and APERTIF 1370 MHz (Pastor-Marazuela et al., 2021). Using the periodicity model, i transformed the arrival time of the bursts to phases, where phase corresponds to a particular point in the period. i visualized the center frequency of bursts against the arrival phase of the burst, which clearly demonstrated the frequency dependency on the phase. i realized that not only there is a shift in the active window that depends on the frequency but also the duration of the active window changes. Therefore, i modeled both the shift and the change in duration with two separate power law models.

Using both the models, i can predict the active window at any given frequency. To test this model, i predicted the active window at high frequencies of 4-8 GHz. Then, i conducted observations with 100-meter Effelsberg Radio Telescope within the predicted active windows from 4-8 GHz using ROACH2 backend. The filterbank data produced by the radio telescope is not directly ready to be searched. The filterbank data of 4-6 GHz is processed by one system, whereas that of 6-8 GHz is processed by another system. So, i first preprocessed the data, which involved extracting total intensity filterbank data, correcting the frequency headers, removing the bandpass and normalising the data, and lastly saving it as a SIGPROC filterbank file. i experimented and implemented my own Python scripts which do all of the above preprocessing steps. This step is crucial because standard FRB search softwares expect filterbank data in standard format. The search was performed using PRESTO (Ransom, 2011). i wrote a collection of BASH scripts which automate the whole process. To visualize the candidates outputted by the search program, i also wrote a PYTHON program, which plots a candidate using the raw data after pre-processing and de-dispersing. The complete search of all the observations led to successful detection of 8 bursts at 4-6 GHz and with no bursts detected in 6-8 GHz band.

All of the measurements of the observables from the bursts have been performed by me. First, i extracted the bursts from the raw data which includes all the four Stokes parameters. Then, i performed polarization calibration and corrected for Faraday rotation. Since, the frequency of these bursts is extremely high, i could not measure RM directly and only used literature value of RM from Nimmo et al. (2021). i measured the linear and circular polarization fractions from the calibrated bursts following the procedure laid out in Everett and Weisberg (2001). i also measured PA of the bursts. Using the known SEFD of the instrument, i performed flux calibration and measured the flux and fluences of the bursts. The bursts clearly show scintillation pattern, therefore, i also measured scintillation bandwidths from manually selected specific subbands of the bursts. All of the measurements are provided in the paper. Using all the measured observables, i modeled the observables variability against frequency with the help of power-laws.

The detections of bursts at phases predicted by the chromaticity model validates the chromaticity model. Therefore, towards the end, i investigated and tested various progenitor models of FRB 20180916B against the observed chromaticity model. This involved reading about all the existing progenitor models, which explain the periodicity of the active window, and extending them to explain chromaticity. Lastly, i also compared measured PAs against phases of the detections to also constrain progenitor models as prescribed in Li and Zanazzi (2021).

CHAPTER 5

Rotation Measure study of FRB 20180916B using the uGMRT

> *If you only do what you can do, you will never be more than you are now.*
>
> Master Shifu, Kung Fu Panda (2008)

This chapter explains my contributions i made to the article published in Astronomy and Astrophysics, which appears as S. Bethapudi, L. G. Spitler, D. Z. Li, V. R. Marthi, M. Bause, R. A. Main, and R. S. Wharton (2025b), *Rotation Measure study of FRB 20180916B with the uGMRT*, A&A **694**, A75 A75, https://doi.org/10.1051/0004-6361/202452221, arXiv: `2409.12584 [astro-ph.HE]`. The published paper is attached in Appendix B.

Author contributions: SB searched the data for bursts, performed flux/polarization calibration and Rotation Measure measurements analysis and prepared the manuscript, along with all of its figures. LS guided the project and writing. DL helped with polarization analysis. VRM assisted with data transfer and helped understand the intricacies and conventions of uGMRT polarimetric data. MB, RM and RW commented on the manuscript.

Unlike CHIME/FRB, a transit-type telescope, which can only observe FRB 20180916B for minutes every day, to observe the source for longer durations at a time with a much more sensitive instrument in the same observing band as CHIME/FRB, the source was followed up with the Upgraded Giant Metrewave Radio Telescope (uGMRT). uGMRT is one of the most sensitive radio interferometer in low frequency ($\leq$ 1 GHz) regime and can observe the source for hours at a stretch. Not only to detect bursts, but also to study the polarimetric properties, the full polarization data was recorded. Detecting the bursts, performing polarization calibration of the bursts, and then measuring Rotation Measure (RM) of the bursts form the crux of this paper.

There are two kinds of filterbank streams outputted by the uGMRT: PA and IA. The former is when voltage streams from all the antennas are coherently combined and then filterbanked, hence is called Phased Array. The latter is when voltage streams are incoherently combined and then filterbanked and is called Incoherent Array. All the polarization information only exists in the PA filterbank. IA filterbank is purely total intensity filterbank. Moreover, both the filterbank data are stored with 16 bit resolution.

First and foremost, i wrote a PYTHON program which subtracts a IA filterbank from a PA filterbank and converts the resultant into 8 bit filterbank. Standard search software expects filterbanks to only have 8 bit resolution, therefore this conversion is required. In addition, the subtraction essentially removes all RFI from the resultant filterbank which significantly helps with searching. After converting all the filterbanks, i applied a standard PRESTO based search pipeline and identified bursts.

Then, i wrote another program which extracts bursts from the 16 bit PA filterbank and saves them as PSRFITS format files. PSRFITS format is part of standard pulsar processing software ecosystem, therefore, by converting the bursts into PSRFITS format, one can use all the PSRCHIVE tools and commands for further processing. My program preserves the original dynamic range of the PA data using special columns provided in the PSRFITS format. Moreover, it also fills the correct metadata and stores the data in the correct polarization convention followed by the format definition. All further analysis with the bursts is done using these PSRFITS archives. Firstly, i used PAZI to interactively zap all the RFI channels for every burst. And then, i visually identified the time-frequency extent of every burst and saved it to a JSON file. The extent of burst is termed as ON region and anywhere where there is no burst is termed as OFF region. The temporal extent of the ON region is the width of the burst and the frequency extent is the bandwidth of the burst.

Flux scaling and polarization calibration requires reference source scans, such as unpolarized quasar (3C48), polarized quasar (3C138), test pulsars (PSR B0329+54, PSR J0139+5814), and noise diode scans. These scans also have to be converted into search-mode PSRFITS so that standard PSRCHIVE tools can be used for processing. i wrote a python program which converts PA filterbank of these sources into search-mode PSRFITS files with correct metadata and polarization convention. It assists in calibration when the ON (when the noise diode is turned ON or when looking at the source) filterbank data and the OFF (when the noise diode is turned OFF or when not looking at the source) are within the same file. Therefore, i wrote another program that takes ON PA filterbank and OFF PA filterbank, and stitches them together with some period into a search-mode PSRFITS file. In all the conversions, i have ensured that the full dynamic range of the raw PA filterbank is not lost by using special columns in PSRFITS format which record scales and offsets of the data. Having created the search-mode PSRFITS for all the reference sources, i used DSPSR to fold the PSRFITS and scrunch in time to produce PSRCHIVE folded files. For the pulsars, i fold using the pulsar ephemeredis, but for the rest where i manually stitched ON and OFF with some period, i fold with the same period. All the calibration solutions are derived using these folded archives.

i perform the calibration using SingleAxis model, which has been defined in Section 1.2.6. This model has three parameters: (i) gain G, (ii) differential gain γ, and (iii) differential phase ϕ. While G and γ are modeled freely for every channel, ϕ is modeled as a linear function of frequency with the slope measuring the delay between the two hands of polarization, also known as cable delay. The exact procedure followed to estimate G, γ and ϕ can be found in the paper and is not repeated here. The estimated parameters of the SingleAxis model are bundled into a PACV file which is the standard PSRCHIVE format to save calibration solutions. Then, i calibrated the PSRFITS burst archives using the generated PACV using another PSRCHIVE tool known as PAC. In addition to applying the calibration, PAC also performs parallactic angle correction.

Using the polarization calibrated bursts, i measure RM using my own Python program which does $QU-$fitting. By this procedure, i not only measure RM, but also the linear polarization fraction. My program performs nested sampling the details of which can be found in the paper. i determined the flux scaling using the quasar observations and flux models as published in Perley and Butler (2017). Thereafter, i measured fluxes and fluences of the bursts. With this, i have measured all the observables from all the bursts, which are presented in the paper.

CHAPTER 6

Constraining the origin of the long-term periodicity of FRB 20180916B with polarization position angle

> *Fools have the most fun.*
>
> Adriaen van de Venne (1661)

This chapter describes my contribution to the article S. Bethapudi, D. Z. Li, L. G. Spitler, V. R. Marthi, M. L. Bause, R. A. Main, and R. S. Wharton (2025a), *Constraining the origin of the long-term periodicity of FRB 20180916B with polarization position angle*, A&A **702**, A248 A248, https://doi.org/10.1051/0004-6361/202556347, arXiv: `2507.07651 [astro-ph.HE]`. The entire publication is made available in Appendix C.

Author contributions: SB devised strategy to perform PA calibration, measured one Rotation Measure and Position Angle using all the bursts from each of the observations, studied the variability, tested the progenitor models and prepared the manuscript. DL guided the analysis and provided PA variability tests of models. All authors helped with reviewing and proofreading of the writing.

If PAs of the bursts are determined by the geometry of the system, then by performing a long term study of the PAs, the underlying dynamics of the system can be probed. With this intention, using the calibrated PSRFITS bursts as described in the previous chapters, i studied the short and long term variability of PAs of bursts. To this end, i first devised a PA-calibration strategy using PA-sweeps of test pulsars so that PAs measured from different observations can still be meaningfully compared. Any source RM variations or instrumental bias can affect RM measurements, which in turn can affect PA measurement. Therefore, to account for this, i fitted for one RM and one PA to all the bursts of an observation using $QU-$fitting i developed in the previous chapter. Using the fitted PA, i transferred the PA from center frequency of the band to infinite frequency using the fitted RM. At the same time, i also applied the PA-calibration solution to finally measure PA-calibrated PA measured at infinite frequency, which is denoted by $\langle \mathrm{PA}_\infty \rangle$. All further analysis is done using these $\langle \mathrm{PA}_\infty \rangle$.

Given all the $\langle \mathrm{PA}_\infty \rangle$ measurements, i studied the variability within an observation, within an Activity Cycle and from one Activity Cycle to another. i noted insignificant variations in PAs on timescales of four hours or less. Although only tentatively, i also noted (ii) Activity Phase to Phase variations which is consistent with insignificant variability on hours timescale, and (iii) Activity Cycle to Cycle variations at the same Activity Phase.

i tested these observations against all the progenitor models of FRB 20180916B, which include the following: (a) Slowly rotating model where the rotation of the compact object explains the Active window periodicity of the FRB, (b) Precession model where the precessional period explains the same, (c) A "slow" variation of precessional model where the rotational period explains the periodicity and the precessional period introduces yet another timescale of variability, and lastly (d) Binary models where the binary period explains the Active window periodicity.

In case of (a) slowly rotating model, non-variability of PA and Activity Phase to Phase variations is expected, but Activity Cycle to Cycle variations is not. If the inter cycle variability is concretely determined, constraints on slowly rotating model can be improved. In case of "fast" precession model, lack of short time variability ($\lesssim$ 4 hours) already constrains the geometry significantly that no configuration exists where there is no short-time periodicity in bursts, 30% duty cycle in the Activity Period, and lack of short time variability. Therefore, this model can be directly ruled out. Additionally, the large range of PA values seen across observations can also be directly used to rule out this model. The "slow" variant of precessional model can explain the non-variability of PA, Activity Phase to Phase variations, and also the Activity Cycle to Cycle variation. Moreover, it predicts the Cycle to Cycle variation to be sinusoidal with the precessional period, which can be easily tested with future observations. However, the slow precessional model would inadvertently cause changes in the Active window which has not been seen, that suggests this model cannot be applied to this FRB. Lastly, in case of binary models, no strong constraint can be placed as the models do not predict PA variations. However, there exist relativistic spin precession models of binary systems of neutron stars, for which there are PA models. But, these models predict PA variations on a different periodicity timescale than the orbital period that explains the Active window periodicity. Therefore, these models can also be directly ruled out.

Lastly, i noted the similarity between the intermediate X-ray binary system, Her X-1, and the FRB. Both the sources have periodic windows of heightened activity, and in addition, the periodic activity is known to be stable. Furthermore, this work showed that inter cycle PA variability is almost of the same order as the PA variability seen in the X-ray measurements of Her X-1. Further measurements of not only the FRB, but also the Her X-1 would certainly further illuminate the relationship between the two.

CHAPTER 7

Conclusions

> *Quis leget haec?*
>
> Lucilius

7.1 My future motivation

Even if a star is such that it emits polarized light with constant PA within its own frame, the observed PA depends on the relative orientation between the coordinate system in which the PA is measured and the coordinate system in which the PA is emitted. If any of the involved coordinate systems vary with time, then the observed PA also varies with time. By studying the time variability of PA, the change of coordinate system can be studied. In this way, PA offers a way to study the dynamics of not just the emitting source, but also the observing source.

To understand this better, suppose the PA emitted frame (the coordinate system in which the PA is constant and emitted) is rotating, and the PA measured frame (the coordinate system in which the PA is measured) is fixed. That is, the star is rotating with some period, and the observer is constant. The PA would appear to vary about a fixed value for every rotation of the star. The form of variability is understood with Rotating Vector Model (RVM; Radhakrishnan and Cooke, 1969), which primarily uses only two angles to locate the emitting region and the observer. Since rotation is involved, the understanding is simplified by using spherical coordinates (with r, θ, ϕ) such that all of the rotation is along azimuth axis. The two angles then directly correspond to co-latitude angles. They are ζ for the observer and α for the emitting region. Then, following Radhakrishnan and Cooke (1969), RVM is shown in Eq. 7.1. ϕ_0 is only some reference ϕ, which can be ignored for the purposes of this discussion.

Alternatively, suppose the PA emitted frame is constant but the frame in which the PA is measured is rotating. This is akin to an observer on Earth observing a star which emits constant PA. The rotation of the Earth causes the observer to see different PAs at different times. Moreover, the observed PA would also vary with the same period of the Earth. This form of variability is completely modeled with the parallactic angle, which, unsurprisingly, also only requires two locations to be specified: one for the source and one for the observer. Spherical coordinates are again to describe locations, and again the frame is so defined that the rotation is along the azimuth axis. The source location is often provided in an equatorial inertial coordinate system with right-ascension (ρ) and declination (δ). The rotation of the Earth changes the

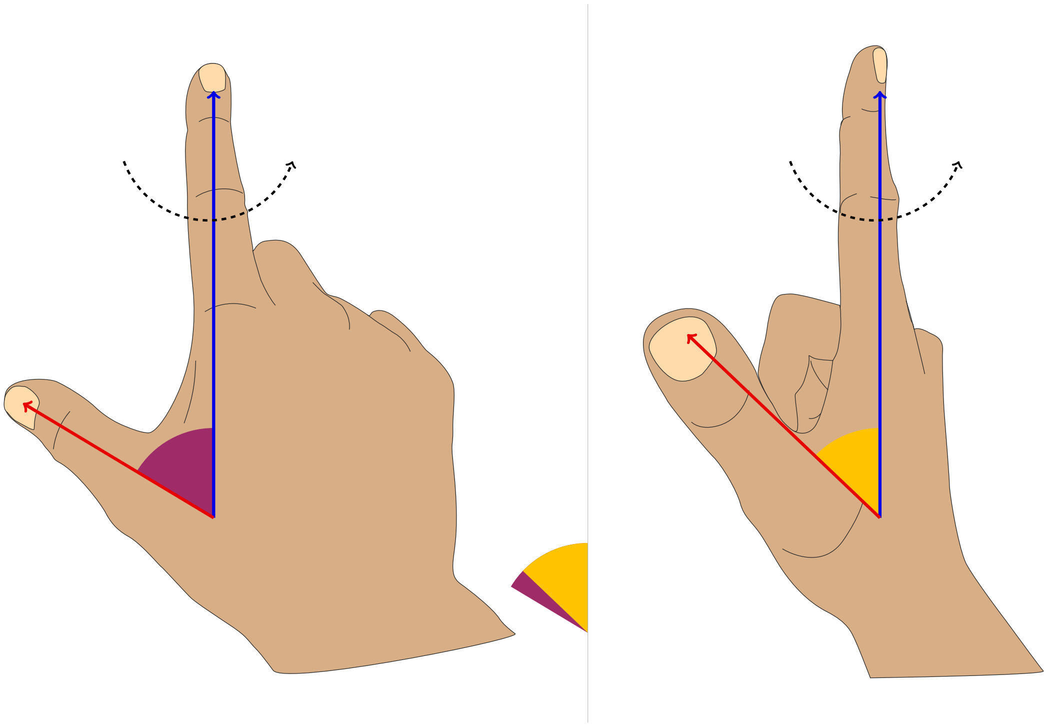

Figure 7.1: Treating index finger as the rotating axis and thumb as the rotating vector, the angle between the two although anatomically the same appears to be different as the thumb pivots about the index finger.

apparent ρ , which depends on Local Sidereal Time, l. Only the geographical co-latitude of the observer is needed which is usually described with latitude, φ. Then, the formula used to compute parallactic angle q is Eq. 7.2.

$$\tan(\mathrm{PA}) = \frac{\sin(\alpha)\sin(\phi-\phi_0)}{\cos(\alpha)\sin(\zeta)-\sin(\alpha)\cos(\zeta)\cos(\phi-\phi_0)} \tag{7.1}$$

$$\tan(q) = \frac{\cos(\varphi)\sin(l-\rho)}{\sin(\varphi)\cos(\delta)-\cos(\varphi)\sin(\delta)\cos(l-\rho)}. \tag{7.2}$$

Both of the above mentioned variability are caused by rotation, which means, their respective effects on PA must be the same. This is obvious when the mathematical formulas are compared. Adjusting for the fact that, φ is latitude and not co-latitude, both the formulae are identical. This showcases its beauty: RVM, which is usually invoked for pulsars with periods ranging from milliseconds to seconds, is exactly the same as parallactic angle corrections, which is usually considered a nuisance and compensated for. All because the underlying dynamics is rotation.

One does not always need stars or the Earth to show this effect. Human hands also show this effect. Supposing the index finger as rotation axis about which thumb is rotating, the angle between the index finger and thumb is anatomically the same if maintained. But, as the whole wrist rotates about the index finger, the angle between the index finger and thumb appears to change. As an example, Fig. 7.1 shows two snapshots of the rotation. The angles are shown with maroon and yellow sectors of circle. The sectors are not the same, even though the anatomy of the hand has not changed.

Studying PAs provide a way to study the rotation which is fundamental right from the human hand and the Earth all the way to the stars. Moreover, rotation is not the only dynamics exhibited, there is also precession which can be studied with PA. Therefore, studying PA is my motivation for the future.

7.2 Conclusions

This conclusion is written as a scientific acknowledgment that appreciates the sciences that made this thesis possible. It possibly also serves as an inspiration to future work.

7.2.1 Polarization is shape of light

The thought of light possessing shape is interesting. Defining polarization simply as linear and circular polarization, or with Stokes parameters, only masks the interest. This whole thesis stands to uncover the different shapes of light and really appreciate them.

7.2.2 Circular polarization is an embarrassment

The first line of Melrose (2003) reads

> The circular polarization of pulsar radio emission is an embarrassment.

Although Melrose (2003) is not a referred publication, finding something like this is bothersome but at the same time extremely motivational. In the entirety of the thesis, circular polarization has not been explicitly dealt with. The bursts from FRB 20180916B have no circular polarization to begin with. Even if they did, circular polarization has no application like the PA does. That is, it cannot be used to probe the dynamics. However, the beauty of polarization is not diminished by its inapplicability. Circular polarization should be understood and pursued for its own sake, as science should be for its own sake.

7.2.3 i love R3

The complete focus of this thesis has been on one singular source, FRB 20180916B. This source, also known as R3, has been the protagonist of this thesis. All the science chapters are based on R3. Therefore, to appreciate this source, the graphic shown in Fig. 7.2 was designed. It is clearly inspired by the famous `i love NY`$^{\text{TM}}$ template. A lot about R3 has been discovered, a lot more remains to be discovered, this thesis would not have been without R3. Thank you R3.

Figure 7.2: Design to appreciate FRB 20180916B, also known as R3, as it is the protagonist of this thesis.

Bibliography

Andreoni, I. et al. (2020), *Zwicky Transient Facility Constraints on the Optical Emission from the Nearby Repeating FRB 180916.J0158+65*,
ApJ **896**, L2 L2, https://doi.org/10.3847/2041-8213/ab94a5,
arXiv: `2005.06273 [astro-ph.HE]` (cit. on p. 50).

Anna-Thomas, R. et al. (2023),
Magnetic field reversal in the turbulent environment around a repeating fast radio burst,
Science **380** 599, https://doi.org/10.1126/science.abo6526,
arXiv: `2202.11112 [astro-ph.HE]` (cit. on p. 37).

Bannister, K. W. et al. (2017),
The Detection of an Extremely Bright Fast Radio Burst in a Phased Array Feed Survey,
ApJ **841**, L12 L12, https://doi.org/10.3847/2041-8213/aa71ff,
arXiv: `1705.07581 [astro-ph.HE]` (cit. on p. 31).

Barsdell, B. R., M. Bailes, D. G. Barnes, and C. J. Fluke (2012), *Accelerating incoherent dedispersion*,
MNRAS **422** 379, https://doi.org/10.1111/j.1365-2966.2012.20622.x,
arXiv: `1201.5380 [astro-ph.IM]` (cit. on p. 31).

Beniamini, P., Z. Wadiasingh, and B. D. Metzger (2020),
Periodicity in recurrent fast radio bursts and the origin of ultralong period magnetars,
MNRAS **496** 3390, https://doi.org/10.1093/mnras/staa1783,
arXiv: `2003.12509 [astro-ph.HE]` (cit. on p. 51).

Bethapudi, S., L. G. Spitler, R. A. Main, D. Z. Li, and R. S. Wharton (2023),
High frequency study of FRB 20180916B using the 100-m Effelsberg radio telescope,
MNRAS **524** 3303, https://doi.org/10.1093/mnras/stad2009,
arXiv: `2207.13669 [astro-ph.HE]`
(cit. on pp. 24, 34, 36, 39, 40, 42, 44, 46, 48, 49, 53, 115–117, 121).

Bethapudi, S. et al. (2025a), *Constraining the origin of the long-term periodicity of FRB 20180916B with polarization position angle*,
A&A **702**, A248 A248, https://doi.org/10.1051/0004-6361/202556347,
arXiv: `2507.07651 [astro-ph.HE]` (cit. on pp. 57, 121).

Bethapudi, S. et al. (2025b), *Rotation Measure study of FRB 20180916B with the uGMRT*,
A&A **694**, A75 A75, https://doi.org/10.1051/0004-6361/202452221,
arXiv: `2409.12584 [astro-ph.HE]`
(cit. on pp. 36, 37, 39–42, 44, 46, 47, 49, 50, 55, 116, 117, 121).

Bhardwaj, M. et al. (2021), *A Nearby Repeating Fast Radio Burst in the Direction of M81*, ApJ **910**, L18 L18, https://doi.org/10.3847/2041-8213/abeaa6, arXiv: `2103.01295 [astro-ph.HE]` (cit. on p. 34).

Bochenek, C. D. et al. (2020), *A fast radio burst associated with a Galactic magnetar*, Nature **587** 59, https://doi.org/10.1038/s41586-020-2872-x, arXiv: `2005.10828 [astro-ph.HE]` (cit. on p. 26).

Britton, M. C. (2000), *Radio Astronomical Polarimetry and the Lorentz Group*, ApJ **532** 1240, https://doi.org/10.1086/308595, arXiv: `astro-ph/9911101 [astro-ph]` (cit. on p. 33).

Burke-Spolaor, S. and K. W. Bannister (2014), *The Galactic Position Dependence of Fast Radio Bursts and the Discovery of FRB011025*, ApJ **792**, 19 19, https://doi.org/10.1088/0004-637X/792/1/19, arXiv: `1407.0400 [astro-ph.HE]` (cit. on p. 31).

Caleb, M. et al. (2017), *The first interferometric detections of fast radio bursts*, MNRAS **468** 3746, https://doi.org/10.1093/mnras/stx638, arXiv: `1703.10173 [astro-ph.HE]` (cit. on p. 31).

Champion, D. J. et al. (2016), *Five new fast radio bursts from the HTRU high-latitude survey at Parkes: first evidence for two-component bursts*, MNRAS **460** L30, https://doi.org/10.1093/mnrasl/slw069, arXiv: `1511.07746 [astro-ph.HE]` (cit. on p. 31).

Chawla, P. et al. (2020), *Detection of Repeating FRB 180916.J0158+65 Down to Frequencies of 300 MHz*, ApJ **896**, L41 L41, https://doi.org/10.3847/2041-8213/ab96bf, arXiv: `2004.02862 [astro-ph.HE]` (cit. on pp. 39, 40, 46, 116).

Chen, H.-Y., W.-M. Gu, M. Sun, T. Liu, and T. Yi (2021), *Reconciling the 16.35-day Period of FRB 20180916B with Jet Precession*, ApJ **921**, 147 147, https://doi.org/10.3847/1538-4357/ac1fe9, arXiv: `2108.08982 [astro-ph.HE]` (cit. on p. 51).

Chen, W.-C. (2020), *Periodically repeating fast radio bursts: Lense-Thirring precession of a debris disk?* PASJ **72**, L8 L8, https://doi.org/10.1093/pasj/psaa060, arXiv: `2006.01552 [astro-ph.HE]` (cit. on p. 51).

CHIME/FRB Collaboration et al. (2018), *The CHIME Fast Radio Burst Project: System Overview*, ApJ **863**, 48 48, https://doi.org/10.3847/1538-4357/aad188, arXiv: `1803.11235 [astro-ph.IM]` (cit. on p. 31).

CHIME/FRB Collaboration et al. (2019a), *A second source of repeating fast radio bursts*, Nature **566** 235, https://doi.org/10.1038/s41586-018-0864-x, arXiv: `1901.04525 [astro-ph.HE]` (cit. on p. 39).

CHIME/FRB Collaboration et al. (2019b), *CHIME/FRB Discovery of Eight New Repeating Fast Radio Burst Sources*, ApJ **885**, L24 L24, https://doi.org/10.3847/2041-8213/ab4a80, arXiv: `1908.03507 [astro-ph.HE]` (cit. on pp. 31, 34, 39).

CHIME/FRB Collaboration et al. (2020), *A bright millisecond-duration radio burst from a Galactic magnetar*,

Nature **587** 54, https://doi.org/10.1038/s41586-020-2863-y,
arXiv: `2005.10324 [astro-ph.HE]` (cit. on p. 26).

Chime/Frb Collaboration et al. (2020), *Periodic activity from a fast radio burst source*,
Nature **582** 351, https://doi.org/10.1038/s41586-020-2398-2,
arXiv: `2001.10275 [astro-ph.HE]` (cit. on pp. 39, 43, 46, 48, 53, 54, 116, 117).

CHIME/FRB Collaboration et al. (2021), *The First CHIME/FRB Fast Radio Burst Catalog*,
ApJS **257**, 59 59, https://doi.org/10.3847/1538-4365/ac33ab,
arXiv: `2106.04352 [astro-ph.HE]` (cit. on p. 31).

Chime/Frb Collaboration et al. (2023),
CHIME/FRB Discovery of 25 Repeating Fast Radio Burst Sources,
ApJ **947**, 83 83, https://doi.org/10.3847/1538-4357/acc6c1,
arXiv: `2301.08762 [astro-ph.HE]` (cit. on p. 31).

Cordes, J. M., I. Wasserman, S. Chatterjee, and G. Batra (2022),
Empirical Assessment of Aperiodic and Periodic Radio Bursts from Young Precessing Magnetars,
ApJ **929**, 97 97, https://doi.org/10.3847/1538-4357/ac4bbd,
arXiv: `2107.12874 [astro-ph.HE]` (cit. on p. 44).

Dai, Z. G. and S. Q. Zhong (2020),
Periodic Fast Radio Bursts as a Probe of Extragalactic Asteroid Belts,
ApJ **895**, L1 L1, https://doi.org/10.3847/2041-8213/ab8f2d,
arXiv: `2003.04644 [astro-ph.HE]` (cit. on p. 51).

Deng, C.-M., S.-Q. Zhong, and Z.-G. Dai (2021),
An Accreting Stellar Binary Model for Active Periodic Fast Radio Bursts,
ApJ **922**, 98 98, https://doi.org/10.3847/1538-4357/ac30db,
arXiv: `2102.06796 [astro-ph.HE]` (cit. on p. 51).

Du, S., W. Wang, X. Wu, and R. Xu (2021), *On the geometry and environment of repeating FRBs*,
MNRAS **500** 4678, https://doi.org/10.1093/mnras/staa3527,
arXiv: `2004.11223 [astro-ph.HE]` (cit. on p. 51).

Everett, J. E. and J. M. Weisberg (2001),
Emission Beam Geometry of Selected Pulsars Derived from Average Pulse Polarization Data,
ApJ **553** 341, https://doi.org/10.1086/320652, arXiv: `astro-ph/0009266 [astro-ph]`
(cit. on p. 54).

Feng, X.-M., Y.-P. Yang, and Q.-C. Li (2024),
Periodic activities of fast radio burst repeaters from precessing magnetars with evolving obliquity,
MNRAS **530** 3641, https://doi.org/10.1093/mnras/stae1092,
arXiv: `2405.08326 [astro-ph.HE]` (cit. on p. 51).

Feng, Y. et al. (2022),
Frequency-dependent polarization of repeating fast radio bursts—implications for their origin,
Science **375** 1266, https://doi.org/10.1126/science.abl7759,
arXiv: `2202.09601 [astro-ph.HE]` (cit. on pp. 47, 49, 117).

Gopinath, A. et al. (2024), *Propagation effects at low frequencies seen in the LOFAR long-term monitoring of the periodically active FRB 20180916B*,
MNRAS **527** 9872, https://doi.org/10.1093/mnras/stad3856,
arXiv: `2305.06393 [astro-ph.HE]` (cit. on pp. 39, 49, 50, 117).

Gu, W.-M., T. Yi, and T. Liu (2020),
A neutron star-white dwarf binary model for periodically active fast radio burst sources,

MNRAS **497** 1543, https://doi.org/10.1093/mnras/staa1914,
arXiv: `2002.10478 [astro-ph.HE]` (cit. on p. 51).

Hampshire, D. P. (2018), *A derivation of Maxwell's equations using the Heaviside notation*,
Philosophical Transactions of the Royal Society of London Series A **376**, 20170447 20170447,
https://doi.org/10.1098/rsta.2017.0447, arXiv: `1510.04309 [physics.gen-ph]`
(cit. on p. 1).

Hankins, T. H., J. A. Eilek, and G. Jones (2016),
The Crab Pulsar at Centimeter Wavelengths. II. Single Pulses,
ApJ **833**, 47 47, https://doi.org/10.3847/1538-4357/833/1/47,
arXiv: `1608.08881 [astro-ph.HE]` (cit. on p. 25).

Hilmarsson, G. H. et al. (2021),
Rotation Measure Evolution of the Repeating Fast Radio Burst Source FRB 121102,
ApJ **908**, L10 L10, https://doi.org/10.3847/2041-8213/abdec0,
arXiv: `2009.12135 [astro-ph.HE]` (cit. on p. 37).

Jessner, A. et al. (2010),
Giant pulses with nanosecond time resolution detected from the Crab pulsar at 8.5 and 15.1 GHz,
A&A **524**, A60 A60, https://doi.org/10.1051/0004-6361/201014806,
arXiv: `1008.3992 [astro-ph.HE]` (cit. on p. 25).

Kahr, B. (2021), *Poincaré and his polarization sphere*,
Chirality **33** 758, https://doi.org/https://doi.org/10.1002/chir.23363,
eprint: `https://onlinelibrary.wiley.com/doi/pdf/10.1002/chir.23363`,
URL: `https://onlinelibrary.wiley.com/doi/abs/10.1002/chir.23363`
(cit. on p. 11).

Karuppusamy, R., B. W. Stappers, and W. van Straten (2010),
Giant pulses from the Crab pulsar. A wide-band study,
A&A **515**, A36 A36, https://doi.org/10.1051/0004-6361/200913729,
arXiv: `1004.2803 [astro-ph.GA]` (cit. on p. 25).

Kaspi, V. M. and A. M. Beloborodov (2017), *Magnetars*,
ARA&A **55** 261, https://doi.org/10.1146/annurev-astro-081915-023329,
arXiv: `1703.00068 [astro-ph.HE]` (cit. on p. 26).

Katz, J. I. (2021), *Testing models of periodically modulated FRB activity*,
MNRAS **502** 4664, https://doi.org/10.1093/mnras/stab399,
arXiv: `2012.15354 [astro-ph.HE]` (cit. on p. 51).

Kaur, B., N. Kanekar, and J. X. Prochaska (2022),
A fast radio burst progenitor born in a galaxy merger,
ApJ **925**, L20 L20, https://doi.org/10.3847/2041-8213/ac4ca8,
arXiv: `2201.07271 [astro-ph.GA]` (cit. on pp. 41, 42, 44, 116).

Keane, E. F. (2018), *The future of fast radio burst science*,
Nature Astronomy **2** 865, https://doi.org/10.1038/s41550-018-0603-0,
arXiv: `1811.00899 [astro-ph.HE]` (cit. on p. 25).

Kilpatrick, C. D. et al. (2021), *Deep Optical Observations Contemporaneous with Emission from the Periodic FRB 180916.J0158+65*, ApJ **907**, L3 L3, https://doi.org/10.3847/2041-8213/abd560,
arXiv: `2011.07561 [astro-ph.HE]` (cit. on p. 50).

Kilpatrick, C. D. et al. (2024), *Limits on Optical Counterparts to the Repeating Fast Radio Burst 20180916B from High-speed Imaging with Gemini-North/'Alopeke*,

ApJ **964**, 121 121, https://doi.org/10.3847/1538-4357/ad2687,
arXiv: `2311.09316 [astro-ph.HE]` (cit. on p. 50).

Laha, S. et al. (2022),
Limits on the Hard X-Ray Emission From the Periodic Fast Radio Burst FRB 180916.J0158+65,
ApJ **929**, 173 173, https://doi.org/10.3847/1538-4357/ac5f3c,
arXiv: `2203.07489 [astro-ph.HE]` (cit. on p. 49).

Lan, H.-T., Z.-Y. Zhao, Y.-J. Wei, and F.-Y. Wang (2024),
The Physical Origin of the Periodic Activity for FRB 20180916B,
ApJ **967**, L44 L44, https://doi.org/10.3847/2041-8213/ad4ae8,
arXiv: `2310.16307 [astro-ph.HE]` (cit. on pp. 44, 51).

Levin, Y., A. M. Beloborodov, and A. Bransgrove (2020),
Precessing Flaring Magnetar as a Source of Repeating FRB 180916.J0158+65,
ApJ **895**, L30 L30, https://doi.org/10.3847/2041-8213/ab8c4c,
arXiv: `2002.04595 [astro-ph.HE]` (cit. on p. 51).

Li, D. and J. J. Zanazzi (2021), *Emission Properties of Periodic Fast Radio Bursts from the Motion of Magnetars: Testing Dynamical Models*,
ApJ **909**, L25 L25, https://doi.org/10.3847/2041-8213/abeaa4,
arXiv: `2101.05836 [astro-ph.HE]` (cit. on p. 54).

Li, Q.-C. et al. (2021),
Periodic Activities of Repeating Fast Radio Bursts from Be/X-Ray Binary Systems,
ApJ **918**, L5 L5, https://doi.org/10.3847/2041-8213/ac1922,
arXiv: `2108.00350 [astro-ph.HE]` (cit. on p. 51).

Lin, Y.-Q., H.-Y. Chen, W.-M. Gu, and T. Yi (2022),
Effects of Gravitational-wave Radiation of Eccentric Neutron Star-White Dwarf Binaries on the Periodic Activity of Fast Radio Burst Sources,
ApJ **929**, 114 114, https://doi.org/10.3847/1538-4357/ac5c49,
arXiv: `2203.06303 [astro-ph.HE]` (cit. on p. 51).

Lorimer, D. R., M. Bailes, M. A. McLaughlin, D. J. Narkevic, and F. Crawford (2007),
A Bright Millisecond Radio Burst of Extragalactic Origin,
Science **318** 777, https://doi.org/10.1126/science.1147532, arXiv: `0709.4301 [astro-ph]`
(cit. on p. 23).

Lorimer, D. R. and M. Kramer (2004), *Handbook of Pulsar Astronomy*, vol. 4 (cit. on p. 25).

Lyutikov, M., M. V. Barkov, and D. Giannios (2020),
FRB Periodicity: Mild Pulsars in Tight O/B-star Binaries,
ApJ **893**, L39 L39, https://doi.org/10.3847/2041-8213/ab87a4,
arXiv: `2002.01920 [astro-ph.HE]` (cit. on p. 51).

Main, R. A. et al. (2022), *Scintillation time-scale measurement of the highly active FRB20201124A*,
MNRAS **509** 3172, https://doi.org/10.1093/mnras/stab3218,
arXiv: `2108.00052 [astro-ph.HE]` (cit. on pp. 37, 121).

Main, R. A. et al. (2023), *Modelling annual scintillation velocity variations of FRB 20201124A*,
MNRAS **522** L36, https://doi.org/10.1093/mnrasl/slad036,
arXiv: `2212.04839 [astro-ph.HE]` (cit. on pp. 37, 121).

Marcote, B. et al. (2020), *A repeating fast radio burst source localized to a nearby spiral galaxy*,
Nature **577** 190, https://doi.org/10.1038/s41586-019-1866-z,
arXiv: `2001.02222 [astro-ph.HE]` (cit. on pp. 39–42, 44, 45, 116).

Marthi, V. R. et al. (2020), *Detection of 15 bursts from the fast radio burst 180916.J0158+65 with the upgraded Giant Metrewave Radio Telescope*,
MNRAS **499** L16, https://doi.org/10.1093/mnrasl/slaa148,
arXiv: `2007.14404 [astro-ph.HE]` (cit. on p. 39).

Marthi, V. R. et al. (2022), *Burst properties of the highly active FRB20201124A using uGMRT*,
MNRAS **509** 2209, https://doi.org/10.1093/mnras/stab3067,
arXiv: `2108.00697 [astro-ph.HE]` (cit. on p. 121).

Masui, K. et al. (2015), *Dense magnetized plasma associated with a fast radio burst*,
Nature **528** 523, https://doi.org/10.1038/nature15769, arXiv: `1512.00529 [astro-ph.HE]` (cit. on p. 31).

Mckinven, R. et al. (2023a), *A Large-scale Magneto-ionic Fluctuation in the Local Environment of Periodic Fast Radio Burst Source FRB 20180916B*,
ApJ **950**, 12 12, https://doi.org/10.3847/1538-4357/acc65f,
arXiv: `2205.09221 [astro-ph.HE]` (cit. on pp. 39, 46–48, 50, 117).

Mckinven, R. et al. (2023b), *Revealing the Dynamic Magnetoionic Environments of Repeating Fast Radio Burst Sources through Multiyear Polarimetric Monitoring with CHIME/FRB*,
ApJ **951**, 82 82, https://doi.org/10.3847/1538-4357/acd188,
arXiv: `2302.08386 [astro-ph.HE]` (cit. on p. 37).

McLaughlin, M. A. et al. (2006), *Transient radio bursts from rotating neutron stars*,
Nature **439** 817, https://doi.org/10.1038/nature04440,
arXiv: `astro-ph/0511587 [astro-ph]` (cit. on p. 25).

Melrose, D. (2003), “What Causes the Circular Polarization in Pulsars?” *Radio Pulsars*,
ed. by M. Bailes, D. J. Nice, and S. E. Thorsett, vol. 302,
Astronomical Society of the Pacific Conference Series 179 (cit. on p. 61).

Ng, C. et al. (2025),
Polarization Properties of 28 Repeating Fast Radio Burst Sources with CHIME/FRB,
ApJ **982**, 154 154, https://doi.org/10.3847/1538-4357/adb0bc,
arXiv: `2411.09045 [astro-ph.HE]` (cit. on pp. 46, 47, 50, 117).

Nimmo, K. et al. (2021), *Highly polarized microstructure from the repeating FRB 20180916B*,
Nature Astronomy **5** 594, https://doi.org/10.1038/s41550-021-01321-3,
arXiv: `2010.05800 [astro-ph.HE]` (cit. on pp. 39, 46, 48, 49, 54, 117).

Nimmo, K. et al. (2023),
A burst storm from the repeating FRB 20200120E in an M81 globular cluster,
MNRAS **520** 2281, https://doi.org/10.1093/mnras/stad269,
arXiv: `2206.03759 [astro-ph.HE]` (cit. on p. 25).

Nurmamat, N., Y.-F. Huang, J.-J. Geng, A. Kurban, and B. Li (2024), *Repeating fast radio bursts produced by a strange star interacting with its planet in an eccentric orbit*,
European Physical Journal C **84**, 210 210, https://doi.org/10.1140/epjc/s10052-024-12572-5,
arXiv: `2211.12026 [astro-ph.HE]` (cit. on p. 51).

Pastor-Marazuela, I. et al. (2021),
Chromatic periodic activity down to 120 megahertz in a fast radio burst,
Nature **596** 505, https://doi.org/10.1038/s41586-021-03724-8,
arXiv: `2012.08348 [astro-ph.HE]` (cit. on pp. 39, 40, 42, 44, 46, 48, 53, 54, 116, 117).

Pearlman, A. B. et al. (2025), *Multiwavelength constraints on the origin of a nearby repeating fast radio burst source in a globular cluster*,

Nature Astronomy **9** 111, https://doi.org/10.1038/s41550-024-02386-6,
arXiv: `2308.10930 [astro-ph.HE]` (cit. on pp. 34, 35, 116, 121).

Perley, R. A. and B. J. Butler (2017), *An Accurate Flux Density Scale from 50 MHz to 50 GHz*,
ApJS **230**, 7 7, https://doi.org/10.3847/1538-4365/aa6df9,
arXiv: `1609.05940 [astro-ph.IM]` (cit. on p. 56).

Petroff, E., J. W. T. Hessels, and D. R. Lorimer (2019), *Fast radio bursts*,
A&A Rev. **27**, 4 4, https://doi.org/10.1007/s00159-019-0116-6,
arXiv: `1904.07947 [astro-ph.HE]` (cit. on p. 23).

– (2022), *Fast radio bursts at the dawn of the 2020s*,
A&A Rev. **30**, 2 2, https://doi.org/10.1007/s00159-022-00139-w,
arXiv: `2107.10113 [astro-ph.HE]` (cit. on p. 23).

Pilia, M. et al. (2020), *The Lowest-frequency Fast Radio Bursts: Sardinia Radio Telescope Detection of the Periodic FRB 180916 at 328 MHz*,
ApJ **896**, L40 L40, https://doi.org/10.3847/2041-8213/ab96c0,
arXiv: `2003.12748 [astro-ph.HE]` (cit. on p. 39).

Platts, E. et al. (2019), *A living theory catalogue for fast radio bursts*,
Phys. Rep. **821** 1, https://doi.org/10.1016/j.physrep.2019.06.003,
arXiv: `1810.05836 [astro-ph.HE]` (cit. on p. 23).

Pleunis, Z. et al. (2021), *LOFAR Detection of 110-188 MHz Emission and Frequency-dependent Activity from FRB 20180916B*, ApJ **911**, L3 L3, https://doi.org/10.3847/2041-8213/abec72,
arXiv: `2012.08372 [astro-ph.HE]` (cit. on pp. 39–42, 44, 46, 48–50, 53, 54, 116, 117).

Radhakrishnan, V. and D. J. Cooke (1969),
Magnetic Poles and the Polarization Structure of Pulsar Radiation,
Astrophys. Lett. **3** 225, https://doi.org/ (cit. on p. 59).

Ransom, S. (2011), *PRESTO: PulsaR Exploration and Search TOolkit*,
Astrophysics Source Code Library, record ascl:1107.017 (cit. on p. 54).

Ravi, V., R. M. Shannon, and A. Jameson (2015),
A Fast Radio Burst in the Direction of the Carina Dwarf Spheroidal Galaxy,
ApJ **799**, L5 L5, https://doi.org/10.1088/2041-8205/799/1/L5,
arXiv: `1412.1599 [astro-ph.HE]` (cit. on p. 31).

Sand, K. R. et al. (2022), *Multiband Detection of Repeating FRB 20180916B*,
ApJ **932**, 98 98, https://doi.org/10.3847/1538-4357/ac6cee,
arXiv: `2111.02382 [astro-ph.HE]` (cit. on pp. 39, 40, 46, 116).

Sand, K. R. et al. (2023), *A CHIME/FRB Study of Burst Rate and Morphological Evolution of the Periodically Repeating FRB 20180916B*, ApJ **956**, 23 23, https://doi.org/10.3847/1538-4357/acf221,
arXiv: `2307.05839 [astro-ph.HE]` (cit. on pp. 39–44, 51, 116).

Scholz, P. et al. (2020), *Simultaneous X-Ray and Radio Observations of the Repeating Fast Radio Burst FRB ~ 180916.J0158+65*, ApJ **901**, 165 165, https://doi.org/10.3847/1538-4357/abb1a8,
arXiv: `2004.06082 [astro-ph.HE]` (cit. on p. 49).

Sob'yanin, D. N. (2020), *Periodic fast radio bursts from forcedly precessing neutron stars, anomalous torque, and internal magnetic field for FRB 180916.J0158+65 and FRB 121102*,
MNRAS **497** 1001, https://doi.org/10.1093/mnras/staa1976,
arXiv: `2007.01616 [astro-ph.HE]` (cit. on p. 51).

Spitler, L. G. et al. (2016), *A repeating fast radio burst*, Nature **531** 202, https://doi.org/10.1038/nature17168, arXiv: `1603.00581 [astro-ph.HE]` (cit. on pp. 24, 31).

Stokes, G. G. (1851), *On the Composition and Resolution of Streams of Polarized Light from different Sources*, Transactions of the Cambridge Philosophical Society **9** 399, https://doi.org/ (cit. on pp. 6, 7).

Tendulkar, S. P. et al. (2021), *The 60 pc Environment of FRB 20180916B*, ApJ **908**, L12 L12, https://doi.org/10.3847/2041-8213/abdb38, arXiv: `2011.03257 [astro-ph.HE]` (cit. on pp. 42, 45, 51, 116).

Thornton, D. et al. (2013), *A Population of Fast Radio Bursts at Cosmological Distances*, Science **341** 53, https://doi.org/10.1126/science.1236789, arXiv: `1307.1628 [astro-ph.HE]` (cit. on p. 31).

Tim Sprenger (2024), *Pulsar Scintillation and Interstellar Lenses*, PhD thesis: Rheinische Friedrich-Wilhelms-Universität Bonn, URL: `https://hdl.handle.net/20.500.11811/11277` (cit. on p. 34).

Trudu, M. et al. (2022), *The northern cross fast radio burst project - II. Monitoring of repeating FRB 20180916B, 20181030A, 20200120E, and 20201124A*, MNRAS **513** 1858, https://doi.org/10.1093/mnras/stac1031, arXiv: `2204.05050 [astro-ph.HE]` (cit. on p. 39).

Trudu, M. et al. (2023), *Simultaneous and panchromatic observations of the fast radio burst FRB 20180916B*, A&A **676**, A17 A17, https://doi.org/10.1051/0004-6361/202245303, arXiv: `2305.18628 [astro-ph.HE]` (cit. on pp. 49, 50).

Wada, T., K. Ioka, and B. Zhang (2021), *Binary Comb Models for FRB 121102*, ApJ **920**, 54 54, https://doi.org/10.3847/1538-4357/ac127a, arXiv: `2105.14480 [astro-ph.HE]` (cit. on p. 51).

Wang, P. et al. (2022), *FRB 20121102A is active again with significantly smaller DM as revealed by FAST*, The Astronomer’s Telegram **15619** 1, https://doi.org/ (cit. on p. 37).

Wasserman, I., J. M. Cordes, S. Chatterjee, and G. Batra (2022), *Nonaxisymmetric Precession of Magnetars and Fast Radio Bursts*, ApJ **928**, 53 53, https://doi.org/10.3847/1538-4357/ac38a6, arXiv: `2107.12911 [astro-ph.HE]` (cit. on p. 51).

Wei, Y.-J., Z.-Y. Zhao, and F.-Y. Wang (2022), *The periodic origin of fast radio bursts*, A&A **658**, A163 A163, https://doi.org/10.1051/0004-6361/202142321, arXiv: `2112.09292 [astro-ph.HE]` (cit. on p. 51).

Xu, H. et al. (2022), *A fast radio burst source at a complex magnetized site in a barred galaxy*, Nature **609** 685, https://doi.org/10.1038/s41586-022-05071-8, arXiv: `2111.11764 [astro-ph.HE]` (cit. on p. 37).

Yang, H. and Y.-C. Zou (2020), *Orbit-induced Spin Precession as a Possible Origin for Periodicity in Periodically Repeating Fast Radio Bursts*, ApJ **893**, L31 L31, https://doi.org/10.3847/2041-8213/ab800f, arXiv: `2002.02553 [astro-ph.HE]` (cit. on p. 51).

Zackay, B. and E. O. Ofek (2017), *An Accurate and Efficient Algorithm for Detection of Radio Bursts with an Unknown Dispersion Measure, for Single-dish Telescopes and Interferometers*,

ApJ **835**, 11 11, https://doi.org/10.3847/1538-4357/835/1/11,
arXiv: `1411.5373 [astro-ph.IM]` (cit. on p. 26).

Zanazzi, J. J. and D. Lai (2020), *Periodic Fast Radio Bursts with Neutron Star Free Precession*,
ApJ **892**, L15 L15, https://doi.org/10.3847/2041-8213/ab7cdd,
arXiv: `2002.05752 [astro-ph.HE]` (cit. on p. 51).

Zhang, X. and H. Gao (2020),
What binary systems are the most likely sources for periodically repeating FRBs?
MNRAS **498** L1, https://doi.org/10.1093/mnrasl/slaa116,
arXiv: `2006.10328 [astro-ph.HE]` (cit. on p. 51).

APPENDIX **A**

Chapter 4 publication

Monthly Notices
of the
ROYAL ASTRONOMICAL SOCIETY

MNRAS **524,** 3303–3313 (2023)
Advance Access publication 2023 July 05

https://doi.org/10.1093/mnras/stad2009

High frequency study of FRB 20180916B using the 100-m Effelsberg radio telescope

S. Bethapudi,[1]★ L. G. Spitler,[1] R. A. Main,[1] D. Z. Li[2] and R. S. Wharton[3]

[1]*Max-Planck-Institut für Radioastronomie, Auf dem Hügel 69, D-53121 Bonn, Germany*
[2]*Cahill Center for Astronomy and Astrophysics, MC 249-17 California Institute of Technology, Pasadena, CA 91125, USA*
[3]*NASA Postdoctoral Program Fellow, Jet Propulsion Laboratory, California Institute of Technology, Pasadena, CA 91109, USA*

Accepted 2023 June 23. Received 2023 June 23; in original form 2022 June 17

ABSTRACT

FRB 20180916B is a repeating fast radio burst (FRB) with an activity period of 16.33 d. In previous observations ranging from ∼150−1400 MHz, the activity window was found to be frequency dependent, with lower frequency bursts occurring later. In this work, we present the highest frequency detections of bursts from this FRB, using the 100-m Effelsberg radio telescope at 4−8 GHz. We present the results from two observing campaigns. We performed the first campaign over an entire activity period which resulted in no detections. The second campaign was done in an active window at 4−8 GHz which we predicted from our modelling of chromaticity, resulting in eight burst detections. The bursts were detected in a window of 1.35 d, 3.6 d preceding the activity peak seen by Canadian hydrogen intensity mapping experiment, suggesting the chromaticity extends to higher frequency. The detected bursts have narrower temporal widths and larger spectral widths compared to lower frequencies. All of them have flat polarization position angle sweeps and high polarization fractions. The bursts also exhibit diffractive scintillation due to the Milky Way, following a $f^{3.90\pm0.05}$ scaling, and vary significantly over time. We find that burst rate across frequency scales as $f^{-2.6\pm0.2}$. Lastly, we examine implications of the frequency dependency on the source models.

Key words: scattering – methods: observational – techniques: miscellaneous – transients: fast radio bursts.

1 INTRODUCTION

Fast radio bursts (FRBs) are bright, microseconds- to milliseconds-duration transients observed from hundreds of MHz to several GHz and which originate from extragalactic distances. The first FRB was discovered in 2007 (Lorimer et al. 2007), and the lack of repeatability motivated theoretical models of cataclysmic origins (Thornton et al. 2013). Discovery of repeat bursts from FRB 20121102A (Spitler et al. 2016) brought to light a new class of repeating FRBs. The focus of the paper is one such repeating FRB, FRB 20180916B, which was discovered by Canadian hydrogen intensity mapping experiment (The CHIME Collaboration 2022, CHIME).

FRB 20180916B is a repeating FRB with an activity period of ∼16 d and an active window of ∼5 d at 600 MHz (Chime/Frb Collaboration 2020). A well determined periodicity meant that observatories know when to observe to increase the likelihood of detecting bursts. Marcote et al. (2020) provided milli-arcsecond localization of the source through very long baseline interferometry (VLBI) with the European VLBI Network associating the FRB to a star-forming region of a massive spiral galaxy at a redshift of 0.0337. Tendulkar et al. (2021) and Mannings et al. (2021) studied the local region with the *Hubble Space Telescope (HST)* and Gran Telescopio Canarias, from which Tendulkar et al. (2021) postulated that FRB 20180916B is likely to be either an old neutron star/magnetar high mass X-ray binary or gamma-ray binary with a late OB-type star. Multiple X-ray campaigns have already been performed, however, no contemporaneous signal has been detected yet (Pilia et al. 2020; Scholz et al. 2020; Tavani et al. 2020). Detection of prompt/contemporaneous emission at different wavelengths, when an FRB is detected, helps place direct limits on the type of emission mechanisms and the nature of the source. Moreover, the presence of any persistent emission in different wavelengths helps in studying the local environment in much greater detail.

FRB 20180916B has been detected by multiple instruments at different radio frequencies across different cycles. LOFAR has detected twenty seven bursts at 150 MHz (Pastor-Marazuela et al. 2021; Pleunis et al. 2021), GMRT five at 300 MHz (Pleunis et al. 2021), GBT eight at 300 MHz (Chawla et al. 2020), SRT three at 328 MHz (Pilia et al. 2020), GMRT four at 400 MHz (Sand et al. 2021), CHIME/FRB fifty five at 600 MHz (Chime/Frb Collaboration 2020; Pleunis et al. 2021), GMRT fifteen at 650 MHz (Marthi et al. 2020), GBT seven at 800 MHz (Sand et al. 2021), VLA/realfast one at 1350 MHz (Aggarwal et al. 2020), APERTIF fifty four at 1370 MHz (Pastor-Marazuela et al. 2021), and lastly Effelsberg(as part of the European VLBI Network) four at 1700 MHz (Marcote et al. 2020). Note that all of these detections are at comparatively low frequency (≲2 GHz).

The idea of observing the source at high frequencies is not novel. Pearlman et al. (2020) performed a hundred hour observing campaign on FRB 20180916B using the deep space network (DSN) in *S*- (2.3 GHz) and *X*- (8.4 GHz) bands simultaneously but did not detect

---

★ E-mail: shining.surya.d8@gmail.com

any bursts. FRB 20121102A has been detected up to 8 GHz (Gajjar et al. 2018) using the GBT. FRB 20 190 520 (Niu et al. 2021) has also been studied with the GBT at 6 GHz (Anna-Thomas et al. 2022). FRB 20200120E (Bhardwaj et al. 2021) was studied with the DSN at ~2 GHz (Majid et al. 2021). High frequency detections are particularly useful in measuring rotation measures (RMs). For example, in case of FRB 20121102A and FRB 20190520, due to the extremely high RM, measuring it at higher frequencies is much easier (Hilmarsson et al. 2021b; Anna-Thomas et al. 2022).

FRB 20180916B burst detections by LOFAR and APERTIF (Pastor-Marazuela et al. 2021; Pleunis et al. 2021, hereafter ZP21, PM21) revealed the frequency dependency in the occurrence of bursts. Specifically, it was noted that bursts at lower frequencies occur later and bursts at higher frequencies occur earlier. In other words, the FRB 20180916B source not only exhibited periodicity but also 'chromaticity' since bursts showed selectivity in phase. In this work, the proposition that the chromaticity continues to higher frequencies is tested.

The structure of the paper is as follows: Section 2 explains the strategy involved in scheduling observations and describes the search procedures. Section 3 presents all of the detected bursts, their polarization, scintillation, and flux–fluence properties. A rate estimate is also reported using literature rates at various frequencies, and the rate–frequency relation is modeled. Section 4 presents various discussions of the results presented here. Lastly, conclusions are presented in Section 5.

2 OBSERVATIONS AND SEARCHES

This section is organized as follows: we describe the observatory and the backend used in Section 2.1, construct a chromaticity model in Section 2.2, report the observations performed in Section 2.3, and finally describe the search strategy employed in Section 2.4.

2.1 Effelsberg

Observations were conducted using the 100-m Effelsberg radio telescope using the S45mm receiver which has linearly polarized feeds and a system equivalent flux density (SEFD) of 25 Jy. The receiver is connected to the ROACH2 backend, which provides `8bit` full Stokes filterbank data at 131.072 μs time resolution in the 4–8 GHz band. It records the entire band as two separate sub-bands, which are 4–6 GHz and 6–8 GHz, each channelized into 2048 channels. Effelsberg observes strong system artifacts in the 4–8 GHz band which reduces sensitivity to bursts, in particular below 4.5 GHz.

2.2 Chromaticity model

ZP21 provide the most up-to-date periodicity model with the reference MJD = 58369.40 and a period of 16.33 d at 600 MHz. The reference MJD corresponds to the start of the first activity cycle in which the source was discovered. This periodicity model is designed to have bursts arriving at 600 MHz (CHIME band) at $\phi = 0.5$ (see Fig. 1; c.f. PM21, fig. 4; ZP21, fig. 9).

We construct a chromatic model as a power-law relation between observing frequency and detected burst phase. Using this model, we predict active windows at 4–8 GHz. The burst detections used to construct our model are chosen carefully: since bursts detected in follow-up campaigns might introduce biases into the model, only a subset of all the detections is used, which are APERTIF *L*-band detections reported in PM21, CHIME/FRB detections reported in ZP21, and LOFAR detections reported in PM21, ZP21. We chose only those observations that have performed a blind search over the entire window and therefore are not biased by any observing choice. Given that the frequency extent of the bursts is varying within an observing bandwidth, the frequency of the bursts is computed as the mean of the start/stop frequencies of the burst. Bursts where the start/stop frequencies are not reported are simply excluded.

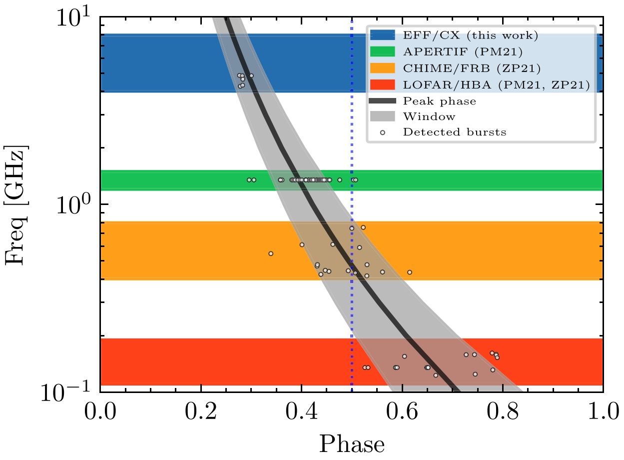

Figure 1. Frequency dependency on the activity phase. The black bold line shows peak-phase frequency dependency (ϕ_P) and the shaded grey region is the FWHM (Δ_P). Coloured bands are observing frequency ranges of various observatories. White dots in each band are the detections by that particular observatory. The vertical dotted blue line denotes $\phi = 0.5$. Higher frequency bursts arrive at an earlier phase and the active window shortens at higher frequencies. Section 2.2 describes the steps taken to produce this fit.

Table 1. Parameters for the power laws presented in this work. The basic form of the power law over frequency *f* considered here is $B(f/600\,\mathrm{MHz})^A$. Errors in burst rate are 95 per cent. All other errors are 1σ. Units are provided wherever relevant.

Equation	*B*	*A*	Refer to
Peak activity phase (ϕ_P)	0.47 ± 0.02	− 0.23 ± 0.05	Section 2.2
FWHM (Δ_P)	53.4 hr ± 15.6 h	− 0.35 ± 0.32	Section 2.2
Burst rate	22.8 ± 4.7 h^{-1}	− 2.6 ± 0.2	Section 3.4
Scintillation bandwidth	0.82 ± 0.06 kHz	3.90 ± 0.05	Section 3.3

Then, bursts are binned into frequency bands of 100 MHz each starting from 100 MHz to 2 GHz. For each band, the mean and standard deviation of the burst phases (which are computed by folding at the activity period) in the frequency band are computed. The mean of the phase is treated as the peak activity phase (ϕ_P) and the standard deviation is used to compute the full width at half-maximum (FWHM, Δ_P). The mean of the burst frequencies in a band is treated as the frequency of the band instead of using the center frequency of the band.

Now, power laws are fitted for ϕ_P and Δ_P against frequency *f*, of the form

$$B\left(\frac{f}{600\ \mathrm{MHz}}\right)^{A}, \tag{1}$$

where *A* and *B* are fit parameters. The fitting is done using SCIPY.OPTIMIZE.CURVE_FIT. The fitting yields peak phase and FWHM parameters as shown in Table 1. The errors are 1σ.

The peak activity phase and FWHM at any frequency *f* is directly given by ϕ_P, Δ_P, where the start and stop phases of the active window are computed as $\phi_P - \frac{1}{2}\Delta_P$ and $\phi_P + \frac{1}{2}\Delta_P$. The power law is graphically presented in Fig. 1. The fitted power laws are extended to the bandwidth of interest (4−8 GHz) and specific phase regions are used to predict time windows to schedule observations.

The chromatic model fitted (Table 1) is not a periodic model and therefore has limitations. Since it is a power law, it asymptotes to zero at sufficiently high frequencies and cannot wrap around, making inferences at high frequencies difficult. Nevertheless, we begin with the assumption that it is valid over the frequency range of interest (4−8 GHz).

2.3 Observations

Each observation started with a test pulsar scan (PSR B0355+54) and a noise-diode scan to check data quality and to provide polarization calibration solution, respectively. In the Cycle 65 observation the 6−8 GHz sub-band recording failed, hence only the lower sub-band (4−6 GHz) was recorded.

The initial observing strategy was to cover an entire period. These observations will be denoted by `PI`. A total exposure of 35.73 h was distributed over 20 d (covering an entire activity cycle of 16.33 d) resulting an average of 1.78 h on source per day. This campaign did not lead to any detections.

When the evidence for a chromatic window became stronger with ZP21 and PM21, the strategy was adapted by developing a chromatic model (Section 2.2). To this end, 40 h were used to schedule observations in the predicted active windows. These will be denoted by `PII`.

Given the inherent uncertainties in the model, the observations were scheduled to be in a phase window starting at 7 GHz and ending at 5 GHz, which corresponds to a phase region [0.238, 0.321] (c.f. Fig. 1, Peak phase, FWHM equations from Table 1). Effelsberg records persistent, periodic radio frequency interference (RFI) below 4.5 GHz, hence we chose to focus on a window above 5 GHz. To make the window symmetric, the start was chosen to be 7 GHz, which makes the length of the window to be 32.5 h. Scheduling in the window was done according to the telescope availability.

All of the observations performed, resulting exposures, and number of bursts are tabulated in Table 2. The same information is also presented graphically in Fig. 2, where the black lines denote exposure against MJD and phase, and the green lined diamonds are detected bursts.

2.4 Search for bursts

All searches for bursts were performed using the PRESTO software package (Ransom 2011). The 4−6 GHz and 6−8 GHz sub-bands were searched separately (see Section 2.1). Since the DM of the source is well known, single pulses are searched at only one DM of the value of 348.820 pc cm^{-3} (Chime/Frb Collaboration 2020). Any error in DM would not result in significant changes to detected bursts, as the observing frequency is quite high. The in band DM delay at 4−6 GHz is about 50 ms (corresponding to ∼400 time samples). For the 6−8 GHz, it is about 17 ms (∼130 time samples). This delay is sufficient to accurately distinguish between RFI and potential candidates.

Each filterbank file was re-processed, which involved whitening every channel (subtracting the mean, dividing by the standard deviation and appropriately scaling into `uint8` bytes). This step removed any bandshape (scales/offsets over channels) and narrow-band persistent RFI and effectively re-digitized the data. After re-digitizing the filterbank data, PRESTO's `rfifind` tool was used to

Table 2. 4–8 GHz observations with Effelsberg. Cycle refers to the activity cycle since the reference MJD. Exposure is the total time spent on FRB 20180916B in hours. The start time is provided in UTC. Phase range corresponds to the exposure in phase units. The number of bursts detected is written in the bursts column.

Cycle	Exposure (h)	Start time	Phase range	Bursts
42	2.22	2020-08-09T16:18:15	0.944–0.950	0
43	0.26	2020-08-10T19:17:35	0.013–0.014	0
43	1.17	2020-08-11T04:25:09	0.036–0.039	0
43	0.96	2020-08-12T05:05:56	0.099–0.102	0
43	2.00	2020-08-13T04:07:52	0.158–0.163	0
43	1.00	2020-08-14T04:25:13	0.220–0.223	0
43	1.00	2020-08-15T20:32:28	0.322–0.325	0
43	0.94	2020-08-17T04:34:38	0.404–0.407	0
43	2.26	2020-08-18T03:40:48	0.463–0.469	0
43	2.55	2020-08-20T00:06:37	0.577–0.583	0
43	2.19	2020-08-21T03:59:26	0.648–0.653	0
43	1.82	2020-08-23T06:11:59	0.776–0.780	0
43	1.78	2020-08-24T03:52:48	0.831–0.836	0
43	1.81	2020-08-25T04:04:49	0.893–0.897	0
44	2.36	2020-08-27T03:36:43	0.014–0.020	0
44	1.85	2020-08-28T03:42:22	0.076–0.080	0
44	1.52	2020-08-29T03:30:17	0.136–0.140	0
44	4.20	2020-08-30T10:14:19	0.215–0.225	0
44	2.02	2020-09-01T03:29:26	0.320–0.325	0
44	1.77	2020-09-03T03:54:42	0.444–0.448	0
60	5.23	2021-05-19T15:05:52	0.271–0.284	2
61	5.13	2021-06-05T06:43:21	0.29–0.303	0
62	4.50	2021-06-21T15:27:00	0.292–0.304	0
65	3.32	2021-08-09T17:32:27	0.298–0.307	1
67	3.35	2021-09-11T07:38:22	0.294–0.303	0
68	3.99	2021-09-27T08:26:18	0.276–0.286	5
69	3.99	2021-10-14T01:37:38	0.299–0.31	0
70	2.99	2021-10-29T23:10:25	0.273–0.281	0
71	5.99	2021-11-15T17:23:14	0.299–0.315	0
72	5.49	2021-12-01T18:05:17	0.281–0.295	0

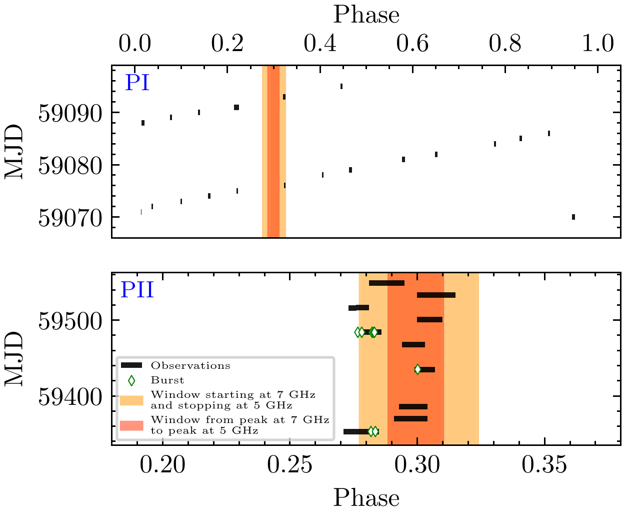

Figure 2. Exposure plotted over MJD and phase for the two observing campaigns. Top: `PI` campaign. Bottom: `PII` campaign. See Section 2.2 and Section 2.3. Solid black lines correspond to the exposure. Green lined diamonds denote detected bursts. Light orange region corresponds to a phase window starting at 7 GHz and stopping at 5 GHz, dark orange corresponds to a phase window from peak at 7 GHz to peak at 5 GHz.

Table 3. Table showing the measured properties of the eight bursts detected. MJD refers to the UTC topocentric timestamp when de-dispersed to 5999.51171875 MHz. Phases of the bursts are reported in the phase column. Peak flux and fluence are calculated from the calibrated time profile of the bursts. Widths are provided as upper limits wherever the bursts are unresolved. *L*-fraction is the total unbiased linear polarization fraction of the bursts. Note that baselines from each of the Stokes time series profile has been removed which causes the unbiased linear polarization to exceed 100 per cent. |*V*|-fraction is the total absolute circular polarization fraction of the bursts. The frequency extent of the bursts is reported in the freq low and freq high columns. Mean PPA is the polarization position angle (PPA) averaged over the burst width.

Burst	MJD	Phase	Peak flux (Jy)	Fluence (Jy ms)	Width (ms)	*L*-fraction (per cent)	|*V*|-fraction (per cent)	Freq low (MHz)	Freq high (MHz)	Mean PPA (deg)
A	59353.802118639	0.28	0.44	0.08	≤ 0.26	72 ± 14	21 ± 17	4490.0	5075.2	− 56.2
B	59353.830062663	0.28	0.75	1.49	3.42	105 ± 3	5 ± 2	4369.8	5041.0	− 62.3
C	59435.751975537	0.3	0.54	0.09	≤0.26	80 ± 12	14 ± 18	4519.3	5182.7	58.3
D	59484.357407934	0.27	1.82	0.42	≤0.26	142 ± 5	2 ± 2	4386.4	5348.8	− 61.4
E	59484.383221707	0.25	0.94	0.14	≤0.26	105 ± 7	–	4128.5	4391.3	− 48.9
F	59484.449512949	0.28	0.36	0.13	≤0.53	101 ± 12	9 ± 10	4685.4	5018.6	− 61.8
G	59484.458202382	0.28	1.84	0.46	≤0.26	111 ± 3	5 ± 3	4048.4	4586.7	− 61.0
H	59484.464427655	0.28	0.18	0.12	0.79	101 ± 15	24 ± 14	4365.9	4914.0	− 72.6

generate a mask to mitigate RFI. The mask was used to de-disperse and create a time series of the data. `single_pulse_search.py` was run on the time series to extract all the single pulses candidates. The minimum S/N threshold used was 6 and the -b flag was passed so as not to exclude bad blocks. The maximum boxcar width was set to 50 samples, which corresponds to ~6.5 ms. Candidates were plotted using custom PYTHON code and were manually vetted.

3 DETECTIONS

We report detection of eight bursts: two bursts detected in the first observation of the campaign (Cycle 60), one in Cycle 65, and five in a single observation (Cycle 68). All of the detections reported here are only in the lower sub-band of 4−6 GHz. The bursts are extracted from the recorded full-Stokes data into fold-mode PSRFITS archives, and all subsequent analysis is performed on these archives. Care has been taken that the burst archives show the correct timestamp.

No attempt is made in estimating DM since the bursts are at high frequencies, possess narrow bandwidths, and the time resolution is not sufficient to resolve the burst structure in all of our bursts. Instead, the most accurate DM estimate, viz 348.772 pc cm^{-3} (Nimmo et al. 2021) is used throughout the analysis as the DM.

Time-of-Arrivals (TOAs) and phases are tabulated in Table 3, UTC topocentric and referenced to the center of the topmost channel (5999.51171875 MHz). Since the majority of the bursts are not time resolved, the PRESTO timestamp is used to calculate the TOA. The spectral widths are measured from visual inspection, and reported in the table. All of the bursts have a bandwidth of around 200 MHz, ∼ 5 per cent of the observing bandwidth. The time resolution of the data proved to be insufficient to resolve the burst structures of majority of the bursts. Hence, the widths reported are to be treated as upper limits for all but bursts-`B,H`. Moreover, for the same reason, the relationship between widths and observing frequency is not probed in detail.

3.1 Flux and fluence

To perform flux calibration, a SEFD of 25 Jy is used[1], and an off-pulse region is carefully chosen to convert from data units into flux units. We observed 3C48 during only one of the observing session (2021 October 14) and were able to measure SEFD from it. We yield an SEFD of 20 Jy which is consistent with the one we used. The off-pulse mean is subtracted and the resulting filterbank is converted from S/N units to flux density units using the radiometer equation. The 2 GHz band is used to generate time series in flux units, even though the frequency extent of the bursts is much smaller. Fluence is measured as the average of the ON-pulse region of the calibrated time series multiplied by the width of the ON-pulse region. The ON-pulse region is identified visually and used as the width since the majority of the bursts are not time resolved. Similarly, the frequency extent of each of the bursts is also visually determined. Peak flux (Jy), fluence (Jy ms), widths (ms), and frequency extent (MHz) are tabulated in Table 3.

3.2 Polarization

The S45mm receiver is equipped with a noise diode, which produces a square wave pure *U*, 100 per cent polarized calibration signal with a period of 1 s and 50 per cent duty cycle. Two minutes of the noise diode scan was recorded at the start of every observation. The scans were folded at the diode period, and any RFI present was exhaustively flagged using PAZI (Hotan, van Straten & Manchester 2004). These scans were then used to compute a calibration solution using PAC from `PSRCHIVE` (Hotan et al. 2004; van Straten et al. 2010), which was then applied to the burst archives. This step also performs the parallactic angle correction. The polarization calibration solution was validated by applying it to the test pulsar (B0355+54), which was observed at the start of every session. The calibrated polarization profile and the PPA sweep is consistent in all of the sessions where bursts were detected and is also tested against the reference pulse profile. This reference profile is the calibrated pulse profile of the same pulsar at 4.8 GHz provided by the European pulsar network database (`epndb`).[2]

Bursts from this source are known to have an RM of ∼−114 rad m^{-2} (Chime/Frb Collaboration 2020; PM21; ZP21). More recently, it was seen that RM has entered a time variable epoch (Mckinven et al. 2022). However, for this study a varying low RM does not produce sufficient rotation for bursts with low bandwidth at high frequencies to be fitted for, so we do not fit for RM. Instead, the

---

[1] https://eff100mwiki.mpifr-bonn.mpg.de/doku.php?id=information_for_astronomers:rx:s45mm

[2] http://www.epta.eu.org/epndb/#hx97b/J0358+5413/hx97b_4850.epn

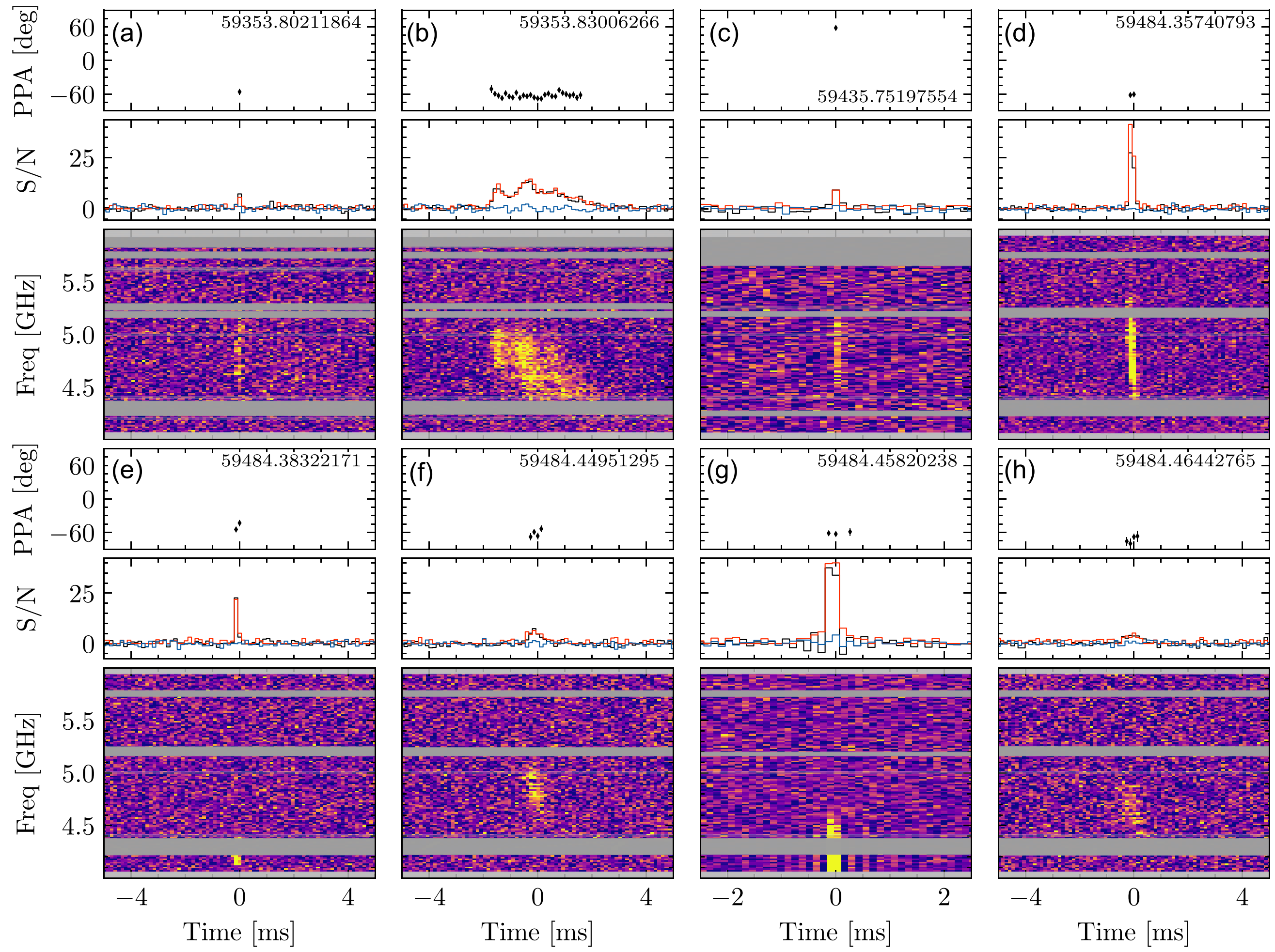

Figure 3. Portrait of the detected bursts. The bottom panel shows de-dispersed filterbank with a time/frequency resolution of 131.072 μs and 15.625 MHz. The middle panel shows unbiased total intensity (black), linear (red), and circular (blue) polarization time series in S/N units. The top panel shows the polarization position angle sweep in degrees. The horizontal grey bands are masked RFI.

calibrated archives are RM corrected using PAM (van Straten et al. 2010) with an RM value of -114.78 rad m^{-2} (ZP21).

Calibrated profiles and PPA curves of all of our detected bursts are plotted in Fig. 3. Linear polarization (L) was estimated using the unbiased estimator as described in Nimmo et al. (2021, 2022) and Everett & Weisberg (2001). The PPA and its error was also estimated as described in those papers. First, the off-pulse statistics was normalized by dividing by the off-pulse standard deviations for each Stokes time series. Linear polarization L was computed as $\sqrt{Q^2+U^2}$. L is de-biased using the off-pulse Stokes-I standard deviation (see section 3.2.1 of Everett & Weisberg 2001). PPA errors are estimated using the procedure prescribed in section 3.2.2 of Everett & Weisberg (2001). Furthermore, we report the absolute circular polarization ($|V|$) of the bursts. We follow the procedure described by Cameron et al. (2020, equation 5). We use the root-mean-square in Stokes-V (σ_v) to compute a factor called b which is $\sqrt{\frac{2}{\pi}} \times \sigma_V$ (Cameron et al. 2020). Then, to de-bias the absolute circular polarization for every on-pulse bin, we measure the difference between absolute Stokes-V and the b. If the difference is positive, the value goes into the de-biased Stokes-$|V|$ time series, otherwise, no circular polarization is said to have been detected. All the bins with non-zero de-biased Stokes-$|V|$ are added to compute the total absolute circular polarization, which is divided by the total Stokes-I to measure the $|V|$-fraction.

Our detected bursts all have ~ 100 per cent linear polarization fraction with observed fluctuations due to low S/N and low time resolution (Beniamini, Kumar & Narayan 2022). Feng et al. (2022) measure the RM scattering (σ_{RM}) of FRB 20180916B. Their predicted polarization fraction at 6 GHz is ~ 99.9 per cent, in agreement with the observed bursts. We also note that some of our bursts possess $|V|$-fractions not consistent with zero. While non-zero circular polarization has not been seen in FRBs at high frequencies (Gajjar et al. 2018), pulsar pulse profiles are known to have non-zero circular polarization at high frequencies (c.f. Johnston & Kerr 2018). While we are confident with our polarization calibration and measurement procedure, and report $|V|$-fractions here, nevertheless, since the bursts reported here are of low S/N and are unresolved, we hope to confirm the presence of $|V|$-fractions with a higher time resolution study.

Flat PPAs are seen in burst-B and to a certain extent in bursts-F, H, while the rest of the bursts are fewer than two samples wide. The flatness of PPAs has already been reported at lower frequencies for the same source (PM21, ZP21) and for other sources such as FRB 20201124A (Hilmarsson et al. 2021a), FRB 20200120E (Nimmo

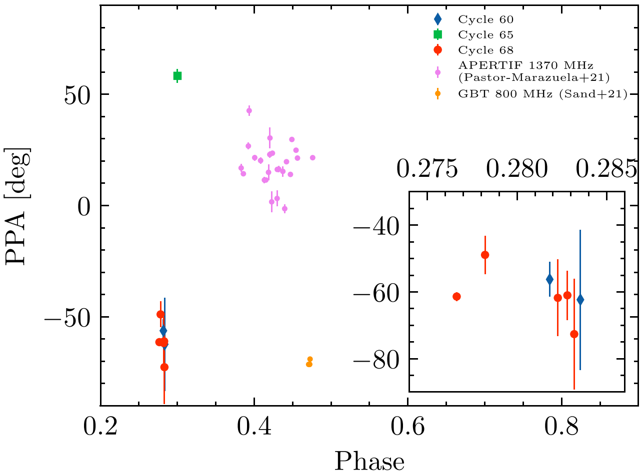

Figure 4. Burst mean PPA versus phase. Mean PPA is the average of the PPA over the ON region. Phase is computed using the periodicity model. The inset zooms in on the points from Cycles 60 and 68 (this work). Note that no absolute PPA angle correction has been done between points from different observatories, therefore, we do not directly compare the PPAs.

et al. 2022), and FRB 20121102A (Gajjar et al. 2018; Hilmarsson et al. 2021b).

In addition, PPAs of all the bursts are plotted against the detection phase in Fig. 4 (also see Table 3). Almost all the bursts have similar PPA except burst-C which has a similar absolute value but with opposite sign. The calibrated test pulsar scan from this day was compared against the reference profile and found to agree. This means that the different PPA of burst-C is physical. It is interesting to note that multiple bursts detected on two separate epochs (Cycles 60, 68) have consistent PPA value and are within 0.01 phase units (∼4 h duration) around phase 0.28. However, burst-C detected at a different epoch which is at phase 0.3 (∼8 h later than the rest) has a different PPA value. Unfortunately, given that it was the only burst detected in that observation and at later phases, we refrain from making any interpretations.

3.3 Scintillation bandwidth

To measure the scintillation bandwidths, we follow the procedure of Main et al. (2022). First, the frequency extent of each burst is identified. Then, the burst flux (which we get after subtracting ON–OFF) is divided by a smoothed version of itself, to remove the intrinsic burst envelope. Since the frequency extent of the bursts is about 200 MHz (c.f. Table 3), a Gaussian kernel with a bandwidth of 200 channels (∼195 MHz) is used to compute the smoothed version. Then, autocorrelation functions (ACFs) of the bursts are computed and the scintillation bandwidth is estimated by fitting Lorentzians to them. While fitting the ACFs, care has been taken to ignore the zero-lag term since it only contains the noise correlations.

For bursts-A, C, F, H, where the scintles are not so prominent, the full visible band is used for the ACF computation. For bursts-B, D, where the scintles are apparent, sub-bands are chosen manually which cover the scintle feature for the computation. Bursts-E, G are excluded from this analysis due to low S/N per channel and a high amount of RFI. The frequency of the measured scintillation bandwidth is simply the median of the band/sub-band chosen. Fig. 5 illustrates the scintillation spectra and ACFs of the bursts reported here.

There have been multiple measurements of the scattering tail and the scintillation bandwidth at lower frequencies. PM21 report a scattering time-scale of 45 ms at 150 MHz, and Chawla et al. (2020) report a scattering upper limit of 1.7 ms at 350 MHz. Both of which can be translated into scintillation bandwidths using the relation $\tau_s \approx 1/2\pi\nu_{\rm scint}$. Sand et al. (2021) report scintillation bandwidths from their GBT detections at 800 MHz. Lastly, Marcote et al. (2020) report a scintillation bandwidth of 59 ± 13 kHz at 1.7 GHz. This work reports the scintillation bandwidth at 4.5 GHz which when fitted with other detections yields a power law as $f^{3.90\pm0.05}$. This is presented graphically in Fig. 6. The agreement with the thin scattering screen which requires the frequency dependency as f^4 is noted. In addition, scintillation bandwidth due to Milky Way is predicted using the NE2001 model (Cordes & Lazio 2002) and plotted in the same Fig. 6.

We report mean scintillation bandwidths at different MJDs scaled to 4.5 GHz using the $f^{3.9}$ relation derived. The scintillation bandwidths are 1.07 ± 0.46 MHz on MJD 59353 (Burst-A, B, Cycle 60), 1.01 ± 0.71 MHz for burst-C observed on MJD 59435 (Cycle 65), and 3.40 ± 0.24 MHz on MJD 59484 (Cycle 68) using Burst-D, F, H. Between Cycle 60 and Cycle 68, the mean scintillation bandwidth varies by $\sim 4.5\sigma$. Individual scintillation bandwidth measurements are plotted in Fig. 7.

3.4 Burst rate

The burst rate varies with fluence and is generally reported as the total burst rate above a fluence threshold value. First, all the published average rates during known active windows at different frequencies are listed below. PM21 report rates with a fluence ($\mathcal{F}$) threshold of 50 Jy ms of $(3.9 \pm 1.3) \times 10^{-2}$ hr^{-1} at 150 MHz and 2.3×10^{-4} hr^{-1} at 1370 MHz. ZP21 publish a burst rate of 0.32 ± 0.08 hr^{-1} above 26 Jy ms at 150 MHz and a CHIME/FRB rate of 0.8 ± 0.3 hr^{-1} at a threshold of 5.1 Jy ms at 600 MHz. Rate scales with this threshold fluence value as $R(\geq \mathcal{F}) \propto \mathcal{F}^{\Gamma}$ (PM21, c.f.) where Γ is found to be -1.5 (PM21). It is also noted that the rate varies over the phase in its active window (PM21, see fig. 4).

Then, the average rate during the active window (R) at 6 GHz is predicted using the published rate estimates at lower frequencies. All of the rates are scaled to bring them to the same fluence threshold of 0.1 Jy ms using the rate–fluence scaling relation mentioned above. Since PM21 and ZP21 both measure a burst rate at 150 MHz, the mean of both of the rates after being brought to the same fluence threshold is used hereon. Thereafter, a power law is fitted and extrapolated to the frequency of interest. The burst rate at 6 GHz is predicted to be 0.05 hr^{-1} at threshold fluence of 0.1 Jy ms.

The burst rate at 6 GHz is estimated assuming a fiducial burst with a width of 1 ms. This burst would then have the fluence limit of 0.207 Jy ms (computed using the quoted SEFD, see Section 3.1). The fluence width scaling is $\mathcal{F} = 0.207\sqrt{\frac{W}{1\ \mathrm{ms}}}$ Jy ms. Only three bursts (B, D, G) are above the fluence limit, therefore, $R(\geq 0.207\ \mathrm{Jy\ ms}) = 0.068^{+0.131}_{-0.054}$ hr^{-1}. All the errors reported here and below are at 95 per cent confidence limits. Furthermore, given that most of the bursts are unresolved, yet another fiducial burst with a width of one time sample is considered. Unresolved bursts (of width 0.131 ms) correspond to a fluence limit of 0.075 Jy ms, and the rate is $R(\geq 0.075\ \mathrm{Jy\ ms}) = 0.18^{+0.18}_{-0.10}$ hr^{-1}. Note that due to the poor time resolution, the rate reported here is only a lower limit. This could mean that the true rate could be higher than the measured rate.

The measured rate is used to fit a power law. The observed rate scales as $f^{-2.64\pm0.20}$. The measured rate equation is written in

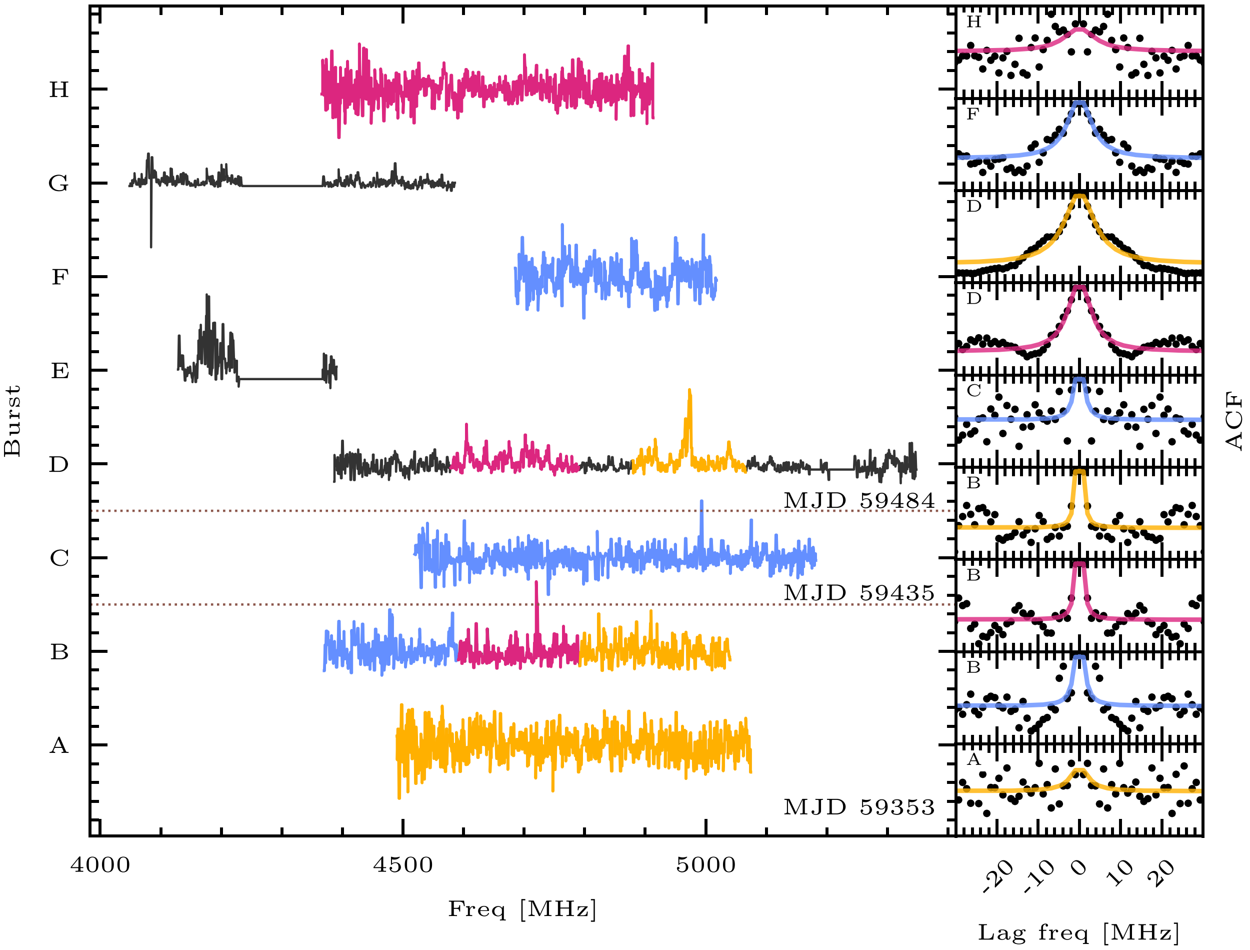

Figure 5. Burst spectra and ACFs. The left-hand panel shows the frequency profile after normalizing (see Section 3.3). Panels to the right show each ACFs of each band/sub-band as a scatter plot and the corresponding Lorentzian fit as the solid line. Each band/sub-band are colour coded. The dotted lines in the left-hand panel mark MJDs of the bursts. Scintillation bandwidth is measured by the Lorentzian fits. It is not measured for bursts-E, -G but they are plotted here for completeness. Bursts-B, -D are manually sub-banded and each sub-band is used for analysis separately. The rest of the bursts are used as a whole.

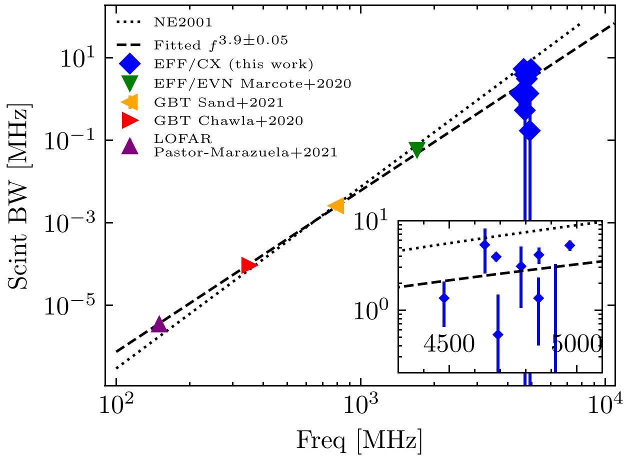

Figure 6. Scintillation bandwidth–frequency dependency. The inset zooms in high frequency detections that are presented here. The power law fitted using all the reported detections so far. See Section 3.3. NE2001 (Cordes & Lazio 2002) is plotted in a dotted line. The fitted power law is plotted in a broken line.

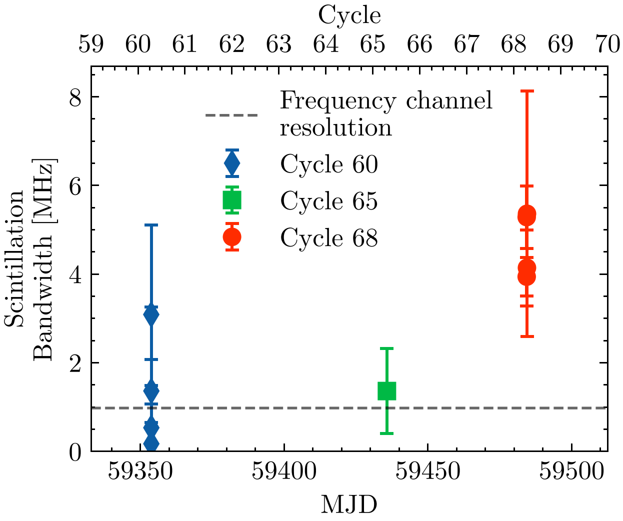

Figure 7. Scintillation bandwidth versus MJD. The top x-axis shows the cycle. All errors are at 1σ. The horizontal broken line is the frequency resolution of the filterbank data.

Table 1. However, we caution that the rate reported here might be underestimated due to the poor time resolution, and the measured rate–frequency relation does not take into account the bursts' limited bandwidth. Modelling such a relationship would help greatly in estimating the rate when observing the source with a large bandwidth instrument, and is left for future work.

The rate at 6 GHz when measured from each observing session is consistent with the rate measured from all the sessions with detections. We report a burst rate of $0.38^{+1.00}_{-0.34}$ hr^{-1} in Cycle 60, $0.30^{+1.38}_{-0.29}$ hr^{-1} in Cycle 65, and $1.25^{+1.67}_{-0.85}$ hr^{-1} in Cycle 68. Rates measured from Cycle 60 and Cycle 65 are consistent with the average rate estimate. However, the rate from Cycle 68 is higher where we detected five bursts, suggesting that the source is not well described by a constant Poisson rate over multiple cycles. Such a long-term non-Poissonianity has already been reported for FRB 20121102A in Oppermann, Yu & Pen (2018); Cruces et al. (2021); Li et al. (2021a); and Jahns et al. (2022). While FRB 20201124A appears to have an underlying Poisson distribution in short observations (Marthi et al. 2022), it remains to be seen if it behaves differently across multiple observing epochs.

4 DISCUSSION

4.1 Evidence for chromaticity at high frequencies

In this paper, we presented results from two observing campaigns: `PI` performed throughout one activity period with roughly daily cadence and `PII` in a predicted active window (see Section 2.2). While both campaigns have similar total exposures (see Table 2), `PII` detected eight bursts, whereas `PI` did not detect any.

An argument for chromaticity at high frequencies is presented as follows: using the rate estimate computed in Section 3.4 (0.18 hr^{-1}) from `PII` assuming Poisson statistics, the probability of detecting at least one burst from `PI` (with exposure of ~35 h) is computed under the assumption that the rate estimated in `PII` holds for the full cycle. The expected number of bursts is λ = rate × exposure = 6.3, so the probability of detecting at least one burst in `PI` is 99.8 per cent. On this basis, the hypothesis that the rate is constant over the entire period (which would mean there is no chromaticity at 6 GHz) is rejected with a significance of $\sim 3.11\sigma$.

However, there exists a major caveat that has to be mentioned: the cycle-to-cycle variations in rate. In Section 3.4, it is shown that the cycle-to-cyle variations in rate are inconsistent with a single Poisson rate. So, it could have been that the cycle observed during `PI` had a particularly low burst rate. Although this is alleviated somewhat by the fact that the average rate used in the above testing is the rate computed across several cycles.

Observations in this work were scheduled using a model as described in Section 2.3. Re-fitting the chromatic model with the detected bursts would bias the model and would lead to circular reasoning. Future studies can attempt to improve the fitting with more exposures in and around the predicted window, and with more detections. In addition, future work should also consider incorporating chromaticity in a periodic model instead of using a power-law-like relation. Additionally, incorporating chromaticity in physical models would be even more insightful.

4.2 High frequency detections

Searches for bursts at higher frequencies help constrain the emission mechanism. To date, high frequency bursts have been detected from FRB 20121102A (Gajjar et al. 2018; Spitler et al. 2018; Pearlman et al. 2020), FRB 20200120E (Majid et al. 2021), and FRB 20190520 (Anna-Thomas et al. 2022). With this work, FRB 20180916B has also joined the rank. Naturally, this begets the question of what is the highest frequency at which bursts can be detectable.

Observations conducted here were in 4−8 GHz, however, bursts were detected only below 5.4 GHz (see Fig. 6). This is despite conducting observations in a predicted window encompassing 5−7 GHz (c.f. Section 2.3, Fig. 2). Non-detection implies several possibilities: the time resolution of the data is not sufficient, the sensitivity of the instrument at the higher end of the band is lower than expected, or the choice of scan window favoured lower end of the band, in which case it would mean that the model is incorrect. The possibility of a cut-off frequency of the bursts cannot be ruled out since this study was done at a poor time resolution. The majority of the bursts detected are not time resolved, which could mean that bursts at higher frequencies are even narrower and the limited time resolution reduced their sensitivity below the detection threshold. In case the model is incorrect, it would require observations over a wider and likely earlier phase range to detect a higher frequency burst.

4.3 Burst properties

Bursts at 150 MHz possess envelope widths of ~50 ms (PM21, ZP21), ~1−2 ms at 600 MHz (ZP21), and, by this work, $\lesssim$0.1 ms at 6 GHz (although the bursts at 150 MHz are heavily scatter-broadened Pastor-Marazuela et al. 2021). While in Marthi et al. (2020), some bursts appear much wider than 2 ms at 650 MHz, we note that bursts from FRB 20180916B possess complex morphology. Like some giant pulses of pulsars (Geyer et al. 2021; Thulasiram & Lin 2021) and repeating FRBs (for example, see Hilmarsson et al. 2021a for FRB 20201124A and Jahns et al. 2022 for FRB 20121102A), bursts of FRB 20180916B are narrowband. Bursts at any observing frequency have a frequency extent of couple of hundred MHz. A trend can be seen: as temporal widths decrease, the spectral widths increase and the fractional bandwidths decrease. To illustrate this, the temporal and spectral widths of the bursts from this work, Marthi et al. (2020); Pilia et al. (2020); Sand et al. (2021); ZP21 and PM21 are plotted in the top panel of Fig. 8. The fractional bandwidth is plotted against temporal widths in the bottom panel. Each point is colour coded by the center frequency of the burst. Note that bursts from APERTIF (PM21) are not included since all those bursts are instrument bandwidth limited. Bursts at the lower end of the spectrum (~150 MHz) possess larger temporal widths but smaller spectral widths, and larger fractional bandwidth. However, bursts at the opposite end (~6 GHz) possess smaller temporal widths, larger spectral widths, and smaller fractional bandwidth.

In the case of FRB 20121102A, we see a similar trend: Jahns et al. (2022) observed bursts at 1.4 GHz, which possess a mean width of 4 ms and burst bandwidth of 250 MHz; Law et al. (2017) report bursts at 3 GHz with mean widths of ~2 ms and mean burst bandwidth of ~450 MHz; and lastly, Gajjar et al. (2018) report bursts at 6 GHz possessing ~0.65 ms widths and ~1.5 GHz of burst bandwidth. This might be a quirk of the underlying emission mechanism itself and could be used to constrain such models. Lastly, we note that the fractional bandwidth is not constant; as plasma lensing predicts an inverse relationship between fractional bandwidth and magnification, plasma lensing alone cannot explain the observed range of spectral widths and fluences (Main et al. 2018, c.f.).

The spectral index (SI) is defined as α where the flux densities at different frequencies (S_f) follow a power law like $S_f \sim f^{\alpha}$. Instead of S_f, it is proposed to consider $\mathcal{F} R_{\mathcal{F}}(f)$ as flux density, where $\mathcal{F}$ denotes the fluence and $R_{\mathcal{F}}(f)$ is the rate measured at a frequency f above the

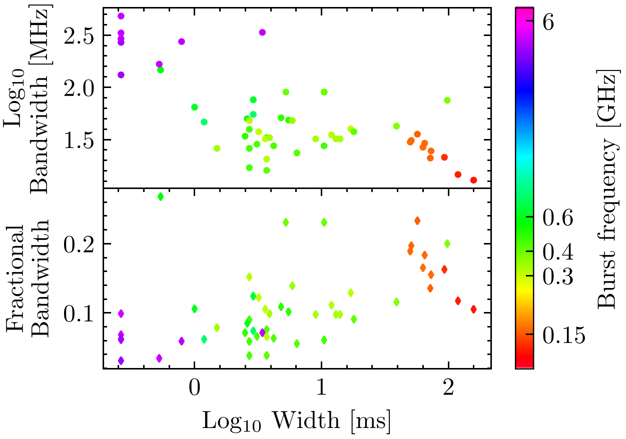

Figure 8. Top: frequency extent versus temporal widths of bursts from FRB 20180916B. Bottom: fractional bandwidth versus temporal widths. Burst data are taken from PM21; ZP21; Marthi et al. (2020); Pilia et al. (2020); Sand et al. (2021) and this work using LOFAR, GBT, SRT, uGMRT, CHIME/FRB, Effelsberg. All points are colour coded by the center frequency of the burst. Note that we have not included bursts detected at 1.37 GHz (which includes APERTIF and Effelsberg) samples as those bursts are band limited, hence would bias this plot.

fluence threshold of $\mathcal{F}$ (see Section 3.4). Dimensionally, both are in the units of Jansky. Following Houben et al. (2019, equation 2), the statistical SI can be measured as the ratio of the rate–frequency index (α) and $\Gamma + 1$ where Γ is the index of the luminosity function (c.f. PM21, also see Section 3.4). Note that Houben et al. (2019) and Sand et al. (2021) follow the convention of rate $\propto \mathcal{F}^{\gamma+1}$ whereas PM21 follow rate $\propto \mathcal{F}^{\Gamma}$ which is followed here. We compute a spectral index of -1.04 ± 0.08, assuming that $\Gamma = -1.5$ (PM21). Sand et al. (2021) also measure the statistical spectral index in a similar method to be $-0.6^{+1.8}_{-0.9}$ for the same source, which is consistent with our measurement. PM21 reported that activity at 150 MHz is higher than that at 1370 MHz. The negative spectral index measurement qualitatively agrees with this.

In the case of pulsars, the distribution of α is measured to be a log-normal distribution with a mean ~ -1.5 (Bates, Lorimer & Verbiest 2013; Jankowski et al. 2018). Giant pulses from the Crab Pulsar exhibit a widespread in the spectral index ranging from -10 to 5 (Karuppusamy, Stappers & van Straten 2010; Eftekhari et al. 2016; Thulasiram & Lin 2021). A spectral index of ~ -1.04 is not implausible in the case of magnetars and pulsars. Lazaridis et al. (2008) and Maan et al. (2022) show the time spectral index variability of XTE 1810–197 ranges from -2 to 5.

The measured scintillation bandwidth over time is plotted in Fig. 7, showing a significant variation in the most recent detections. Given that the scattering is happening in the Milky Way (MW), using `NE2001` (Cordes & Lazio 2002), the probable distance of the scattering screen from the Earth along the line-of-sight of this FRB is estimated as $d_l \sim 2.5$ kpc. The angular extent of the screen is $\theta = \sqrt{\frac{8\,\ln(2) c\tau}{d_{\rm eff}}}$ (Main et al. 2022, c.f. equation 2), where $\tau \approx 1/2\pi\nu_{\rm s}$ is the scattering time-scale which we estimate from the scintillation bandwidth measurement of ~3 MHz at 6 GHz, c is the speed of light in vacuum, and ln is the natural logarithmic function. $d_{\rm eff} \equiv \frac{d d_l}{d - d_l}$ is the effective distance in the FRB-screen-Earth model, where we use $d_{\rm eff} \approx d_l$ since the FRB is extragalactic. Assuming the relative velocity between the screen and the Earth to be $v_{\rm 1e} \sim 30$ km s^{-1} (the orbital velocity of the Earth, assuming no screen velocity), the time taken to see a new portion of the screen is $t \sim \frac{\theta d_l}{v_{le}} \sim 19.2$ d, increasing with $\sim f^{-2}$. Our measured variability of $\nu_{\rm scint}$ is plausible, while changes in the MW scintillation would be expected on time-scales of $\gtrsim$ year at *L*-band and below.

4.4 Current progenitor models

A key observation of chromaticity (c.f. Fig. 1, Section 2.2) which is to be explained by models is that bursts at higher frequencies occur at earlier phases compared to lower frequencies. The observation that active windows at higher frequencies are narrower compared to lower frequencies is also suggested by the fitted chromatic model. However, verifying this requires further observations with exposure windows covering wider phase ranges.

Li & Zanazzi (2021, hereafter DL21) explain the chromatic active window with axially offset magnetic dipole leading to asymmetric emission around the magnetic pole with frequency-related emission height. This leads to conically shaped distinct emission regions for distinct frequency bands. DL21 then discusses the PPA behaviour of various magnetar models, which can be compared with Fig. 4, and will be discussed in the later part of this section.

Li et al. (2021b) and Wada, Ioka & Zhang (2021) (also see Ioka & Zhang 2020) propose binary systems where an FRB producing neutron star is in an elliptical orbit with a compact object or a Be-type star with an accretion disk. While the burst producing mechanism is different in each model, one way these models introduce chromaticity is by employing free–free absorption in the swept-back wind of the companion. This leads to optical depth (along the line of sight) varying with the phase of the neutron star in the binary orbit. But, free–free absorption only explains the phase shifts of lower frequencies since those are more strongly affected than higher frequencies. One way both the binary models explain chromaticity is by calling it a selection effect due to the limited sensitivities of observatories, which are different at different bands. This, in addition with low burst rates outside of the supposed active window, causes chromaticity. However, this leaves the question of why specific active windows have high burst rates at specific frequencies in the first place unanswered. Additionally, Wada et al. (2021) propose another scenario wherein the binary orbit characteristics maps different phases of orbit to different emission frequencies of the bursts. When the neutron star is closer to the companion, it hypothesises, high frequency bursts are detected. And when the neutron star is further away, low frequency bursts are detected. Both the binary models (Wada et al. 2021; Li et al. 2021b) can explain the observed chromaticity.

A slowly rotating neutron star model for FRB 20180916B is discussed in Beniamini, Wadiasingh & Metzger (2020) and Xu et al. (2021). In the model, the PPA can change as a function of the rotation phase, but the cycle to cycle variations in PPA for a given phase are minute (DL21). As seen in Fig. 4, all bursts except Burst-C are detected at close phase and share similar PPAs. Burst-C is observed at a later phase than the other 6 GHz detections. The observed PPA show strong phase-related change, which is still consistent with the slowly rotating neutron star model. More detections around phase 0.3 to see whether the PPA jump always happens in a narrow phase window can potentially provide definitive evidence for the model.

Wei, Zhao & Wang (2022) describe all the precession models, which can be divided into two classes: free and forced precession (see also DL21). The geometry of forced precession has difficulty explaining the asymmetric shift of the active phase against frequency (DL21), hence is not discussed here. DL21 show that a freely precessing magnetar can explain the observed chromaticity and the PPAs. The clustering seen in PPA versus phase (Fig. 4) so far agrees with this model.

In addition to the aforementioned neutron star models, there are jet models in which the FRB period is the precessional period of a jet produced by a compact object and accreation disk (see Katz 2021, 2022). Given that these models do not discuss chromaticity, we refrain from discussing the models here. However, Sridhar et al. (2021) propose a precessing jet model but also postulates a curvature in the jet (due to the drag), which leads to chromaticity. Further testing requires quantifiable predictions from jet-precession models, hence, we defer to future work.

5 CONCLUSIONS

(i) The chromatic activity window of FRB 20180916B extends to 4−8 GHz (Fig. 1). A chromatic model was constructed (Table 1) using the published detections (Section 2.2) at lower frequencies (≲2 GHz). The model was then used to predict active windows at higher frequencies (4−8 GHz) in which observations were scheduled (Section 2.3), leading to the detection of eight bursts (Section 4, Fig. 3). Null-detection from an earlier observing campaign was used to provide evidence for chromaticity (Fig. 2, Section 4.1).

(ii) Eight bursts were detected showing the following properties:

(a) Bursts at 6 GHz are found to be narrower in time, wider in frequency, and have lower fractional bandwidths compared to lower frequency bursts (Fig. 8).

(b) Bursts are found to be highly linearly polarized and possess flat PPAs (Fig. 3, Table 3). PPAs of bursts at particular phase are seen to be clustered, however, one of the bursts which was detected at different phase and has a different PPA (Fig. 4).

(c) Scintillation bandwidth scales as $f^{3.90 \pm 0.05}$ suggesting a thin screen scattering (Fig. 6). Scintillation bandwidth MJD variability is consistent with a screen in the Milky Way (Fig. 7, Section 4.3).

(d) The burst rate varies with frequency as $f^{-2.6 \pm 0.2}$ and the rate is seen to vary from cycle to cycle (Section 3.4). Based on the rate–frequency relation, the spectral index is calculated to -1.04 ± 0.08 (Section 4.3). The poor time resolution of the filterbank data, causing most of the bursts to be unresolved, suggests the rate may be underestimated (Section 3.4).

(iii) The observed chromaticity is applied to FRB 20180916B source models (Section 4.4). The PPA variations in phase (Fig. 4) agree with slowly rotating or freely precessing neutron star, in full agreement with the predictions made by DL21. Observations can be explained by the binary models proposed in Wada et al. (2021) and Li et al. (2021b). Jet-precession models, such as Sridhar et al. (2021), can also explain the observed chromaticity.

In summary, this work reports the first high frequency detection of bursts from FRB 20180916B and establishes that chromaticity exhibited by the source at lower frequencies exists at higher frequencies as well. While the origin of the chromatic periodicity is still unknown, it holds a powerful clue to the physical origin of this source. At the time of writing, FRB 20121102A is the only other FRB repeater with a measured activity period. It would be valuable to determine if it also exhibits similar chromaticity, and if periodicity and chromaticity are common or universal properties of periodically repeating FRBs. The bursts detected in this work are undersampled in time – future studies of this and other FRBs at high frequencies will benefit from higher time resolution or baseband data, which will increase sensitivity and the number of burst detections, and allow for a study of burst morphology and polarization. Future high frequency detections at 4−8 GHz and above will better sample and constrain the active window – frequency relation; with improved measurements, physical scenarios can be tested against the chromatic activity cycle, as well as the polarization angle against frequency and activity phase, which may help elucidate the nature of FRB 20180916B.

ACKNOWLEDGEMENTS

The authors are thankful of Dr. Alex Kraus for scheduling the observations under tight constraints. Special thanks to Ramesh Karuppusamy for resolving out many issues with the receiver backend. SB is extremely gratituous towards Henning Hilmarrson for help with observing and polarization calibrations. SB would also like to extend his thanks to Hsiu-Hsien Lin for his comments and Viswesh Marthi for the discussions. SB would also thank Aristeidis Noutsos for his guidance on circular polarization measurements. Authors would also like to thank Marilyn Cruces for her comments which improved this work and for her help with measuring circular polarization. We acknowledge use of the CHIME/FRB Public Database, provided at https://www.chime-frb.ca/ by the CHIME/FRB Collaboration. Based on observations with the 100-m telescope of the MPIfR (Max-Planck-Institut für Radioastronomie) at Effelsberg. LGS is a Lise Meitner Indepdendent Max Planck research group leader and acknowledges support from the Max Planck Society. Part of this research was carried out at the Jet Propulsion Laboratory, California Institute of Technology, under a contract with the National Aeronautics and Space Administration.

DATA AVAILABILITY

The data underlying this article will be shared on reasonable request to the corresponding authors.

REFERENCES

Aggarwal K., Law C. J., Burke-Spolaor S., Bower G., Butler B. J., Demorest P., Linford J., Lazio T. J. W., 2020, Res. Notes Am. Astron. Soc., 4, 94
Anna-Thomas R. et al., 2022, Science, 380, 599
Bates S. D., Lorimer D. R., Verbiest J. P. W., 2013, MNRAS, 431, 1352
Beniamini P., Wadiasingh Z., Metzger B. D., 2020, MNRAS, 496, 3390
Beniamini P., Kumar P., Narayan R., 2022, MNRAS, 510, 4654
Bhardwaj M. et al., 2021, ApJ, 910, L18
Cameron A. D. et al., 2020, MNRAS, 495, 3515
Chawla P. et al., 2020, ApJ, 896, L41
Chime/Frb Collaboration, 2020, Nature, 582, 351
Cordes J. M., Lazio T. J. W., 2002, preprint (astro–ph/0207156)
Cruces M. et al., 2021, MNRAS, 500, 448
Eftekhari T., Stovall K., Dowell J., Schinzel F. K., Taylor G. B., 2016, ApJ, 829, 62
Everett J. E., Weisberg J. M., 2001, ApJ, 553, 341
Feng Y. et al., 2022, Science, 375, 1266
Gajjar V. et al., 2018, ApJ, 863, 2
Geyer M. et al., 2021, MNRAS, 505, 4468
Hilmarsson G. H., Spitler L. G., Main R. A., Li D. Z., 2021a, MNRAS, 508, 5354
Hilmarsson G. H. et al., 2021b, ApJ, 908, L10
Hotan A. W., van Straten W., Manchester R. N., 2004, Publ. Astron. Soc. Aust., 21, 302
Houben L. J. M., Spitler L. G., ter Veen S., Rachen J. P., Falcke H., Kramer M., 2019, A&A, 623, A42
Ioka K., Zhang B., 2020, ApJ, 893, L26
Jahns J. N. et al., 2022, MNRAS, 519, 666

Jankowski F., van Straten W., Keane E. F., Bailes M., Barr E. D., Johnston S., Kerr M., 2018, MNRAS, 473, 4436
Johnston S., Kerr M., 2018, MNRAS, 474, 4629
Karuppusamy R., Stappers B. W., van Straten W., 2010, A&A, 515, A36
Katz J. I., 2021, MNRAS, 502, 4664
Katz J. I., 2022, MNRAS, 516, L58
Law C. J. et al., 2017, ApJ, 850, 76
Lazaridis K., Jessner A., Kramer M., Stappers B. W., Lyne A. G., Jordan C. A., Serylak M., Zensus J. A., 2008, MNRAS, 390, 839
Li D., Zanazzi J. J., 2021, ApJ, 909, L25 (DL21)
Li D. et al., 2021a, Nature, 598, 267
Li Q.-C., Yang Y.-P., Wang F. Y., Xu K., Shao Y., Liu Z.-N., Dai Z.-G., 2021b, ApJ, 918, L5
Lorimer D. R., Bailes M., McLaughlin M. A., Narkevic D. J., Crawford F., 2007, Science, 318, 777
Maan Y., Surnis M. P., Joshi B. C., Bagchi M., 2022, ApJ, 931, 67
Main R. et al., 2018, Nature, 557, 522
Main R. A., Hilmarsson G. H., Marthi V. R., Spitler L. G., Wharton R. S., Bethapudi S., Li D. Z., Lin H. H., 2022, MNRAS, 509, 3172
Majid W. A. et al., 2021, ApJ, 919, L6
Mannings A. G. et al., 2021, ApJ, 917, 75
Marcote B. et al., 2020, Nature, 577, 190
Marthi V. R., Gautam T., Li D. Z., Lin H. H., Main R. A., Naidu A., Pen U. L., Wharton R. S., 2020, MNRAS, 499, L16
Marthi V. R. et al., 2022, MNRAS, 509, 2209
Mckinven R. et al., 2022, ApJ, 950, 12
Nimmo K. et al., 2021, Nat. Astron., 5, 594
Nimmo K. et al., 2022, Nat. Astron., 6, 393
Niu C. H. et al., 2021, Nature, 606, 873
Oppermann N., Yu H.-R., Pen U.-L., 2018, MNRAS, 475, 5109
Pastor-Marazuela I. et al., 2021, Nature, 596, 505 (ZP21)
Pearlman A. B., Majid W. A., Prince T. A., Nimmo K., Hessels J. W. T., Naudet C. J., Kocz J., 2020, ApJ, 905, L27
Pilia M. et al., 2020, ApJ, 896, L40
Pleunis Z. et al., 2021, ApJ, 911, L3 (PM21)
Ransom S., 2011, Astrophysics Source Code Library, record(ascl:1107.017)
Sand Ketan R. et al., 2022, ApJ, 932, 98
Scholz P. et al., 2020, ApJ, 901, 165
Spitler L. G. et al., 2016, Nature, 531, 202
Spitler L. G. et al., 2018, ApJ, 863, 150
Sridhar N., Metzger B. D., Beniamini P., Margalit B., Renzo M., Sironi L., Kovlakas K., 2021, ApJ, 917, 13
Tavani M. et al., 2020, ApJ, 893, L42
Tendulkar S. P. et al., 2021, ApJ, 908, L12
The CHIME Collaboration, 2022, ApJ Supplement Series, 261, 33
Thornton D. et al., 2013, Science, 341, 53
Thulasiram P., Lin H.-H., 2021, MNRAS, 508, 1947
van Straten W., Manchester R. N., Johnston S., Reynolds J. E., 2010, Publ. Astron. Soc. Aust., 27, 104
Wada T., Ioka K., Zhang B., 2021, ApJ, 920, 54
Wei Y.-J., Zhao Z.-Y., Wang F.-Y., 2022, A&A, 658, A163
Xu K., Li Q.-C., Yang Y.-P., Li X.-D., Dai Z.-G., Liu J., 2021, ApJ, 917, 2

This paper has been typeset from a TEX/LATEX file prepared by the author.

APPENDIX B

Chapter 5 publication

A&A, 694, A75 (2025)
https://doi.org/10.1051/0004-6361/202452221

Astronomy & Astrophysics

Rotation Measure study of FRB 20180916B with the uGMRT

S. Bethapudi[1,⋆], L. G. Spitler[1], D. Z. Li[2], V. R. Marthi[3], M. Bause[1], R. A. Main[1,4,5], and R. S. Wharton[6]

[1] Max-Planck-Institute for Radio Astronomy, Auf dem Hügel 69, 53121 Bonn, Germany
[2] Department of Astrophysical Sciences, Princeton University, Princeton, NJ 08544, USA
[3] National Centre for Radio Astrophysics, Ganeshkhind, Post bag 3, 411 007 Pune, India
[4] Department of Physics, McGill University, 3600 rue University, Montréal, QC H3A 2T8, Canada
[5] Trottier Space Institute, McGill University, 3550 rue University, Montréal, QC H3A 2A7, Canada
[6] Jet Propulsion Laboratory, California Institute of Technology, Pasadena, CA 91109, USA

Received 12 September 2024 / Accepted 11 December 2024

ABSTRACT

Context. Fast Radio Burst 20180916B is a repeating FRB whose activity window has a 16.34-day periodicity that also shifts and varies in duration with the observing frequency. Recent observations report that the FRB has started to show an increasing trend in secular Rotation Measure (RM) after only showing stochastic variability around a constant value of $-114.6\,\mathrm{rad\,m^{-2}}$ since its discovery. RM studies let us directly probe the magnetic field structure in the local environment of the FRB. The trend of the variability can be used to constrain progenitor models of the FRB. Hence, further study of the RM variability forms the basis of this work.

Aims. We studied the local environment of FRB 20180916B. We did so by focusing on polarization properties, namely RM, and studied how it varies with time. The data comes from the ongoing campaigns of FRB 20180916B using the upgraded Giant Metrewave Radio Telescope (uGMRT). The majority of the observations are in Band 4, which is centered at 650 MHz with 200 MHz bandwidth. Additionally, we used a few observations where we had simultaneous coverage in Band 4 and Band 5 (centered at 1100 MHz).

Methods. We applied a standard single-pulse search pipeline to search for bursts. In total, we detected 116 bursts with ~36 hours of on-source time spanning 1200 days from December 2020 to February 2024, with two bursts detected during simultaneous frequency coverage observations. We developed and applied a polarization calibration strategy suited for our dataset. On the calibrated bursts, we used QU-fitting to measure RM. We verified the veracity of calibration solution and RM measurement by performing RM measurements on single pulses of PSR J0139+5814. We also measured various other properties such as rate, linear polarization fraction, and fluence distribution.

Results. Of the 116 detected bursts, we could calibrate 79 of them. We observed in our early observations that the RM continued to follow a secular linear trend, as already seen in past observations. However, our later observations suggest that the source switched from the linear trend to stochastic variations around a constant value of $-58.75\,\mathrm{rad\,m^{-2}}$. It has ceased any secular variability and is only showing stochastic variability. Using the predicted Milky Way RM contribution, we report a tentative detection of a sign flip in the RM in the host galaxy host-frame. We also studied a cumulative rate against fluence and note that the rate at higher fluences (1.2 Jy ms) scales as $\gamma = -1.09(7)$, whereas that at lower fluences (between 0.2 and 1.2 Jy ms) only scales as $\gamma = -0.51(1)$, meaning the rate at the higher fluence regime is steeper than at the lower fluence regime. Finally, we qualitatively assess the two extremely large bandwidth bursts that we detected in our simultaneous multi-band observations.

Conclusions. Future measurements of RM variations would help place stronger constraints on the local environment. Moreover, any periodic behavior in the RM measurements would directly test progenitor models. Therefore, we motivate such endeavors.

Key words. instrumentation: interferometers – instrumentation: polarimeters – methods: data analysis – methods: observational – techniques: polarimetric

1. Introduction

Fast Radio Bursts (FRBs) are short timescale (~1 ms) transient events at radio wavelengths (Lorimer et al. 2007; Petroff et al. 2019, 2022; Bailes 2022). Based on repeatability, there are two classes of FRBs: repeating FRBs (rFRBs) and apparent non-repeating FRBs (nrFRBs). Detecting multiple bursts from the same source enables detailed and cumulative studies of the FRB. For example, rFRBs have been localized post-discovery by various interferometers, including the European Very Long Baseline Inteferometry Network (EVN; Chatterjee et al. 2017; Marcote et al. 2020; Kirsten et al. 2022; Nimmo et al. 2022b). For selected rFRBs that showed scintillation, detecting multiple bursts at multiple epochs enabled the scintillation screen location to be constrained (Main et al. 2022; Ocker et al. 2022), and even led to modeling the effect of orbital motion of Earth on the scintillation timescales (Main et al. 2023; Wu et al. 2024). Moreover, Kumar et al. (2024) and Nimmo et al. (2024) show how scintillation can place constraints on the location of the FRB emission region. Exhaustive follow-up of rFRBs, even with small telescopes, enables the detection of extremely rare bright events and can help in suggesting a link between rFRBs and nrFRBs on the basis of energy distributions (Kirsten et al. 2024). Similar follow-ups with sensitive instruments facilitates performing large number statistics on bursts from various rFRBs (Li et al. 2021; Jahns et al. 2023; Hewitt et al. 2022; Lanman et al. 2022; Zhou et al. 2022). The repeating nature makes it easy to perform a fine time resolution study of bursts, which can probe the underlying emission mechanism (Day et al. 2020; Nimmo et al. 2021, 2022a; Hewitt et al. 2023;

⋆ Corresponding author; `sbethapudi@mpifr-bonn.mpg.de`

Table 1. Band 4 Observations described in this paper (see the auxiliary material for a machine-readable csv file which include actual scan times).

Date	T_{obs}	N	Aux.
2020-11-06	1.51	1	–
2020-11-08	1.84	4	–
2020-11-09	1.84	–	–
2020-12-08	1.68	4	3C138
2020-12-10	0.51	–	–
2020-12-11	1.61	–	–
2021-01-28	1.45	4	B0329+54
2021-01-29	3.68	41	3C138 B0329+54
2021-01-30	1.84	6	3C138 B0329+54
2021-03-01	1.18	1	3C138 B0329+54 J0139+5814
2021-03-02	1.5	7	3C138 B0329+54 J0139+5814
2021-03-04	2.0	–	–
2021-03-16	1.33	–	3C138 NG B0329+54
2021-03-19	1.97	5	–
2021-12-20	1.57	10	3C138 B0329+54
2022-11-11	2.22	4	3C48 3C138 NG B0329+54 J0139+5814
2022-12-31	2.22	4	3C48 3C138 NG B0329+54 J0139+5814
2023-02-18	1.95	7	3C48 3C138 B0329+54 J0139+5814
2023-12-25	1.58	17	3C468.1 NG J0139+5814
2024-01-27	1.48	–	3C468.1 NG J0139+5814
2024-02-12	1.65	1	3C468.1 NG J0139+5814

Notes. Date is specified in UTC. T_{obs} is duration in hours. N is the number of bursts. The Aux. column presents the auxiliary sources observed. A dash in the N column represents no burst detected; a dash in the Aux. column represents no source observed. NG denotes noise diode scan.

Snelders et al. 2023). Certainly, rFRBs allow us to study the FRB phenomena in a much greater detail, which would help us understand the FRB phenomena. This paper focuses on a singular rFRB source and presents polarimetric results.

FRB 20180916B is a rFRB discovered by the Canadian Hydrogen Intensity Mapping Experiment/Fast Radio Burst (CHIME/FRB) experiment (CHIME/FRB Collaboration 2019). It is unique in that its activity windows are periodic with a 16.34-day period (Chime/Frb Collaboration 2020), and they shift and vary in length with observing frequency (Pleunis et al. 2021; Pastor-Marazuela et al. 2021; Bethapudi et al. 2023). In other words, the source exhibits periodicity and chromaticity. The source was localized to an edge of a spiral galaxy at a redshift of 0.0337 with EVN (Marcote et al. 2020). Tendulkar et al. (2021), using Hubble Space Telescope (HST) observations of the host galaxy, placed constraints on the age of the FRB source to be on the order of 10 Myr. Kaur et al. (2022) performed HI spectroscopy observations using the upgraded Giant Metrewave Radio Telescope (uGMRT); they report the host galaxy to be gas-rich and have a low star formation rate (SFR), suggesting the host galaxy might have undergone a minor merger in the recent past. Future sensitive observations would further illuminate the local environment and provide an additional constraint on possible source models.

Mckinven et al. (2023a, hereafter RM23), using CHIME/FRB, report that the Rotation Measure (RM) of bursts from FRB 20180916B has started to change. The RMs are consistent with a single value from its discovery until around MJD 59243, but since then they have started to exhibit an increasing trend. The trend is further corroborated by LOFAR detections (Gopinath et al. 2024, hereafter AG23). FRB 20180916B is not the only rFRB to exhibit significant RM variability. Mckinven et al. (2023b) report nearly all repeaters exhibit RM variability, which suggests that repeaters exist in dynamic magneto-ionic environments. This variability, which is local to the repeater, can be used to constrain the origins of FRB (see, e.g., Yang et al. 2023), which predicts RM variability for different FRB progenitor scenarios. However, Sherman et al. (2023) suggest that host galaxies of rFRBs have statistically larger magnetic fields than that of the Milky Way; that is, they suggest that the host galaxy ISM contributes significantly to the FRB RM. In such a case, decoupling host galaxy contribution and local environment would be particularly challenging, but nevertheless will be crucial to place limits on local environments.

This paper mainly presents polarization results from the ongoing observing campaign of FRB 20180916B with the upgraded Giant Metrewave Radio Telescope (uGMRT). In Sect. 2 we describe the observations and the search strategy utilized. Then, Sect. 3 covers the polarization calibration, flux scaling, and RM measurements. Finally, the results and discussions are presented in Sect. 4, and our conclusions in Sect. 5.

2. Observations and searches

2.1. Observations

Observations were performed using uGMRT (Swarup 1991; Gupta et al. 2017). It is a radio interferometer situated in Khodad, near Pune, India. It consists of 30 parabolic dishes, 45 meters in size, that can be used to perform imaging-mode and phased array-mode observations. It offers observation capability from 100 MHz to 1.4 GHz broken into five bands. Our observations used Band 4 (550–750 MHz) and Band 5 (1000–1200 MHz). Observations from GMRT Proposal Cycle 39 (from October 2020 to March 2021), Cycle 43 (from October 2022 to April 2023), and Cycle 45 (from October 2023 to April 2024), as well as one observation from Cycle 42 (from April 2022 to October 2022), are presented in this paper. Each cycle has its own observing strategy, chiefly the time resolution and frequency coverage. All observations were primarily done in Band 4. However, for five observations of Cycle-39, the entire GMRT array was split into two sub-arrays, where one sub-array performed observations in Band 4 and the other in Band 5. This way, simultaneous coverage of Bands 4 and 5 was achieved. All observations of Cycles 39, 43, and 45 have a time resolution of 327.68 µs, whereas the Cycle 42 observations only have a time resolution of 168.34 µs. The number of channels in all the observations was fixed to 2048. We note that all observations of Cycle 45 were strongly affected by strong ionospheric activity. The observations of Cycles 43 and 45 used the real-time radio frequency interference (RFI) filtering system of the uGMRT (Buch et al. 2022, 2023).

Each individual scan is listed in Table 1 for Band 4 and Table 2 for Band 5. In all the cycles, we recorded full coherency 16-bit phased array (PA) filterbank and Stokes-I 16-bit intensity array (IA) filterbank (Roy et al. 2018). The PA-beam is generated using voltages from individual antennas which are summed in phase, thus is a coherent beam . Instead, the IA-beam is constructed using total intensities of each antenna. All the observations are scheduled in the active windows as predicted by the periodicity and chromaticity model (Chime/Frb Collaboration 2020; Pleunis et al. 2021; Pastor-Marazuela et al. 2021; Bethapudi et al. 2023).

Each observation consists of science scans, which are bracketed by phasing scans of 0217+738 to phase up the signal from all antennas in the array. Unfortunately, our choice of calibrators

Table 2. Band 5 Observations described in this paper.

Date	Time	T_{obs}	N
2020-11-06	21:06:24.758	0.59	1
2020-12-08	19:38:12.345	0.92	–
	20:38:44.277	0.76	2
2021-01-28	14:36:45.729	0.92	2
	15:43:53.603	0.53	1
2021-03-01	13:38:23.638	0.92	1
	14:46:00.369	0.26	–
2021-03-16	08:33:52.918	0.67	–
	09:25:44.085	0.66	–

Notes. Date and Time are specified in UTC. T_{obs} is duration in hours. N is the number of bursts.

and pulsars (for verifying the calibration pipeline) has not been consistent throughout the cycles. Altogether, we observed 3C138 (a polarized quasar), 3C48 and 3C468.1 (unpolarized quasars), noise diode scans (NG), and pulsars: PSR B0329+54 and PSR J0139+5814. Additionally, for some of the observations, we have noise diode scans during which we pointed at an empty patch of sky with the noise diode turned ON. We specify the auxiliary sources in the Aux. column of Table 1. When we discuss the various calibration strategies in Sect. 3.1, we used whichever strategy was possible for an observation based on the available source scans.

2.2. Searches

We subtracted the time aligned IA-beam from the PA-beam and created Stokes-I 8 bit filterbank data. Doing so gets rid of all the RFI common in both beams, while leaving untouched the astrophysical signal, which is only dominantly present in the PA-beam. We then applied a standard PRESTO (Ransom 2011) single-pulse search pipeline. Post subtraction, the data was already clean and we did not need to apply an additional RFI mitigation step (Roy et al. 2018). We searched at a dispersion measure (DM) of 348.82 pc cm^{-3} at the native time resolution. We searched for candidates that are up to 300 samples wide (100 ms). We manually vetted each of the candidates using a diagnostic plot. For each of the manually vetted candidates, we sliced the original 16bit PA-beam data to create a PSRFITS burst archive (Hotan et al. 2004). All the analysis from now on is carried out on these burst archives. The number of bursts we report are listed in Table 1 for Band 4 and Table 2 for Band 5.

We report a total of 116 bursts in Band 4 and seven bursts in Band 5. Out of the 116 Band 4 bursts, we were only able to polarization calibrate 79 of them because we did not schedule auxiliary sources in some observations (see Table 1). Moreover, we also report two simultaneous detections of bursts in Bands 4 and 5. Unfortunately, the Band 4 bursts of the two simultaneous detections could not be calibrated for the same reason as above. We defer polarization calibration of Band 5 bursts to future work.

3. Analysis

Having created PSRFITS burst archive from the PA-beam data, we first employed PAZI (Hotan et al. 2004) to perform extensive RFI cleaning. Then, we selected the burst region with a rectangle such that the visual extent of the entire burst (that is, where the burst is clearly above the background noise) is covered by it. We call this the ON-burst region. The length along time dimension is the width, defined from start of the burst envelope to its end. The length along frequency dimension is the bandwidth of the burst. We then performed polarization calibration and flux scaling as described in Sects. 3.1 and 3.2. Finally, we measured RM and, polarization fractions as described in Sect. 3.3.

3.1. Polarization calibration

uGMRT in Band 4 has a circular basis, which has two hands: Right Circular Polarized (RCP) and Left Circular Polarized (LCP). To calibrate the polarization response of uGMRT, we require a polarized source, such as 3C138 (polarized quasar) or noise diode (NG). 3C48 is unpolarized; however, we can use 3C48 in conjunction with any pulsar, for example PSR B0329+54 or PSR J0139+5814, to perform the calibration. We judiciously choose a calibration strategy based on whichever auxiliary observations are available (see Table 1). Unfortunately, we also have a few observations where no auxiliary source had been observed. We have no way of performing the polarization calibration, and are forced to omit them from the polarization analysis.

SINGLEAXIS is the simplest model for characterizing the polarization response of the system. This model involves GAIN, a scalar gain term that is a multiplicative factor; DGAIN, which accounts for the differential gain between the two hands; and DPHASE, which measures the cross-hand delay, that is, the delay between the RCP and LCP. We model DPHASE(ϕ) as a linear function of observing frequency (in GHz, denoted by f_{GHz}) as $\phi = \psi_{\text{r}} + \pi \text{D}_{\text{ns}} f_{\text{GHz}}$. The ψ_{r} is a constant term which, on a circular basis, is half the position angle of the infalling radiation. D_{ns} is the cross-hand delay in nanoseconds and is also known as cable delay in the literature.

When computing GAIN and DGAIN using quasar scans, we assume that quasars possess no circular polarization (Perley & Butler 2013). In addition, while the quasar flux density is not flat over frequency (Perley & Butler 2017), we assume the quasar flux density to be same throughout the bandwidth of 200 MHz. We make this assumption because throughout the work, we average over the frequency and quote the measurements at one frequency (which is the central frequency of 650 MHz). Since a noise diode is designed to emit constant pure Stokes-U signal across the bandwidth, the assumptions we make above automatically hold true. Then, for all the quasar and noise diode scans, we subtracted OFF (when looking at an empty patch of sky or when the noise diode is turned OFF) from ON (when looking at the quasar or when the noise diode is turned ON) scans and averaged over time to produce Stokes products against frequency. Using this, we measured GAIN and DGAIN algebraically (Britton 2000, see Eq. 14)[1].

We used the Bayesian nested sampling code ULTRANEST (Buchner 2021) to fit for D_{ns} and ψ_{r}. The position angle-like term is fixed to be in $[\frac{-\pi}{2}, \frac{\pi}{2}]$. The D_{ns} is restricted to be in $[-400, 400]$ ns. We note that the sign of the delay is not a consequence for calibration or RM measurements. We model

$$Q + jU = L_p \, I_{\text{smooth}} \exp[1j(\psi_{\text{r}} + \pi \text{D}_{\text{ns}} f_{\text{GHz}})], \tag{1}$$

where L_p is the linear polarized fraction, and I_{smooth} is the Gaussian-smoothed Stokes-I profile over frequency. We used a standard Gaussian likelihood between observed data (Stokes-Q and Stokes-U against frequency) and the model predicted Stokes-Q and -U. Additionally, we treat standard deviation of

---

[1] There is an error in Britton (2000), as mentioned in `SingleAxis.C` of `psrchive` code.

Table 3. Properties of the Band 4 bursts detected in this work.

Burst	MJD	Width ms	Bandwidth MHz	Fluence Jy ms	Flux mJy	RM rad m^{-2}	RM error rad m^{-2}	Linear %	RM$_{\rm ion}$ rad m^{-2}
B1	59191.828612	12.8	122.7	0.40	0.96	−121.12	1.74	84.2	−0.2
B2	59191.834280	10.2	175.6	0.26	0.57	−118.80	1.45	64.1	−0.2
B3	59191.840990	10.2	169.2	0.46	1.02	−117.20	0.90	87.6	−0.2
B4	59191.851290	15.4	121.0	0.86	2.92	−115.22	0.68	98.2	−0.2
B5	59243.408788	8.9	101.0	0.17	0.34	−111.34	3.50	46.5	−0.4
B6	59243.413121	16.1	60.0	0.47	0.85	−116.39	1.38	81.0	−0.4
B7	59243.415825	4.9	38.7	0.37	0.80	–	–	–	−0.3
B8	59243.427116	3.0	85.3	0.33	0.67	−116.48	3.70	50.5	−0.3
B9	59243.431151	10.8	111.5	0.28	0.49	−110.58	1.85	53.5	−0.3
B10	59243.436477	3.6	140.8	0.96	1.85	−115.78	0.69	89.4	−0.3

Notes. MJD refers to topocentric UTC time of the burst when de-dispersed at 348.820 pc cm^{-3} with 750 MHz as the reference frequency. Bandwidth is the frequency envelope of the bursts, measured in MHz. RM refers to the Rotation Measure of the bursts. Linear refers to linear polarization fraction in percentage, which could be more than 100% because we removed the baseline using PSRCHIVE. Width is the time span of the ON-region measured in ms. Flux, measured in mJy, refers to the peak flux in the frequency-averaged flux-calibrated time series. Fluence is the sum over the ON-region of the frequency-averaged flux-calibrated time series, which is measured in Jy ms. RM$_{\rm ion}$ denotes the ionospheric RM contribution seen by uGMRT at the epoch of burst. The full table is available at the CDS and at zenodo.

the OFF scan to be the respective errors in Stokes-Q and -U, and use them in the likelihood. Measuring the cross-hand delay with noise diode scans is straightforward. However, measuring the same using either the 3C138 quasar or pulsars requires a preceding step.

While 3C138 is generally accepted to have zero RM (Perley & Butler 2013), Cotton et al. (1997) suggests the RM to be −2.1 rad m^{-2}. Since we are operating at lower frequencies (compared to L-band and above where VLA operates) where the rotation is more enhanced, we have to take this Faraday rotation into account. In addition, there is also the ionospheric RM contribution, which also inadvertently causes Faraday rotation. The Faraday rotation affects the measurement of the cross-hand delay (ϕ) as both are degenerate. Then, if we incorrectly compensate for cross-hand delay and apply this solution to the bursts, we end up with incorrect RM measurements. Therefore, prior to fitting for ϕ, we de-rotated Stokes-Q and Stokes-U accordingly; that is, we compensated for the spurious RM along the line of sight.

We also measured cross-hand delay using two pulsars, PSR B0329+54 and PSR J0139+5814. Since the pulsars have position angles varying with phase, we do not average over the entire ON-region; instead, we picked just one phase bin which has the highest intensity. We made use of this slice to compute cross-hand delay. As done in the case of 3C138, we also corrected for the literature value of Rotation Measure and ionospheric RM along the line of sight. We estimate the ionospheric RM contribution using Mevius (2018).

3.2. Flux calibration

Flux calibration is performed using the quasar scans. Perley & Butler (2017) is used to estimate the flux scaling which is then applied to the bursts. We note that the flux scaling does not depend on the polarization dimensions, and only affects the scalar GAIN term. Therefore, we can perform flux scaling even for those observations for which we could not perform polarization calibration.

When the calibration is done using quasars (either polarized or unpolarized), the flux calibration is straightforward. When the calibration is done using noise-diode scans, the GAIN term is determined by the noise-diode whose strength is unknown. To circumvent this, we first applied the noise-diode derived calibration solution to the 3C48 quasar scan and then determine the flux scaling from the calibrated 3C48 quasar scan. To those bursts that cannot be polarization calibrated, flux scaling can still be performed because only a known flux source is needed. Having performed flux scaling to all the bursts, we measured the flux and fluence. We first collapsed the frequency axis by averaging over it. Then, we summed over the ON-region to compute the fluence in units of Jy ms. The maximum in the ON-region is the peak flux in mJy. We note that after flux calibration, the OFF-region statistics should be zero mean already, and therefore we do not have to do any OFF-region subtraction here. We tabulate the measurements in Table 3. We assume a 10% error in our flux and fluence measurements as per Nayana & Chandra (2021). For the observations of MJD 60303, MJD 60336 and MJD 60352 (GMRT cycle 45), we could not perform flux calibration because of the heightened ionospheric activity adversely affecting our observations.

3.3. RM and polarization fraction measurements

Faraday rotation introduces sinusoidal variations in Stokes-Q,-U as a function of λ^2, where λ is the wavelength. We employ the method of QU-fitting to measure RM where we directly fit sinusoidals to Stokes-Q,-U as a function of λ^2. We model Stokes-Q,-U as a function of wavelength as

$$Q + jU = L_p\, I_{\rm smooth} \exp[2j({\rm RM}(\lambda^2 - \lambda_c^2) + \psi)], \tag{2}$$

where L_p is the linear polarization fraction, ψ is the position angle, $I_{\rm smooth}$ is the Gaussian smoothened Stokes-I profile as a function of frequency, and λ_c is the wavelength at the center of the burst frequency envelope. We perform the centering to assist in convergence of the fit. Without doing so, we noted a correlation between RM and ψ in our posterior sampling.

We sampled from the posterior using the nested sampling code ULTRANEST (Buchner 2021). We use a standard Gaussian likelihood function with errors in Stokes-Q and -U, and assume flat priors for all the parameters. Our prior on RM ranges from −400 rad m^{-2} to 400 rad m^{-2}, and on L_p from 0 to 1. The prior on ψ is in $[-\frac{\pi}{2}, \frac{\pi}{2}]$. The nested sampling algorithm samples from the posterior distribution directly. We take the median and standard deviation of each of the parameters as the measured value and corresponding error. For every burst, we time-averaged the ON-burst and OFF-burst regions in all Stokes channels. Then, we subtracted OFF-burst from ON-burst and used the ON-OFF Stokes-parameters (which are a function of wavelength) for further analysis. We estimated the errors as the standard deviation of the OFF-burst regions. We find that the errors might be underestimated this way, and furthermore any error in calibration can also introduce systematics in the error that otherwise would be left unaccounted for. Therefore, we introduced EQUAD to the QU-fitting to artificially inflate the errors of Stokes-Q, -U. EQUAD is an additional parameter that is fitted for while measuring RM. The prior of EQUAD is also flat and is set to be in [0., 10.]. In the case that the posterior samples of EQUAD were converging to the boundary values, we re-ran the fitting after suitably increasing the EQUAD range. For each fitting, we produced and visually inspected diagnostic plots.

The measured RMs and corresponding errors are listed in Table 3. Lastly, we verified our RM measurements in Appendix A.1, and we comment about the DPHASE variability and its affect on RM measurement in Appendix B.

3.3.1. Band 5

uGMRT Band 5 data is on a linear basis. We did not perform any calibration in Band 5 because of a lack of good quality calibrator data. Moreover, since we only have two bright bursts in Band 5, we leave the calibration work to future work. Fortunately, because of linear feeds, it is still possible to measure RM without calibration.

RM measurements are done as already mentioned above using ULTRANEST. The only difference is the addition of a Delay parameter. Starting with a pure linear polarized signal (in this formalism with Stokes-Q), the first transformation undergone by the infalling radiation is the Faraday rotation (parameterized by θ). Then the cross-hand delay is realized, which is parameterized by ϕ. These transformations are computed at every frequency channel with $\theta = \text{PA} + \text{RM}(\lambda^2 - \lambda_c^2)$ and $\phi = f_{\text{GHz}} * \pi * \text{D}_{\text{ns}}$, D_{ns} denotes the cross-hand delay in nanoseconds:

$$\begin{pmatrix} Q \\ U \\ V \end{pmatrix} = \begin{pmatrix} 1 & 0 & 0 \\ 0 & \cos(\phi) & -\sin(\phi) \\ 0 & \sin(\phi) & \cos(\phi) \end{pmatrix} \begin{pmatrix} \cos(2\theta) & -\sin(2\theta) & 0 \\ \sin(2\theta) & \cos(2\theta) & 0 \\ 0 & 0 & 1 \end{pmatrix} \begin{pmatrix} L_p \\ 0 \\ 0 \end{pmatrix}. \quad (3)$$

As done with Band 4 RM measurements, we also included EQUAD to expand errors since we are not actually calibrating the bursts.

It should be noted that our assumption of pure Stokes-Q signal need not be the case. Our input (right-most vector) can be a mixed state, but it can be always be written as a rotation matrix applied to be a pure state. Such a rotation matrix would be a constant and can be absorbed into the right-most matrix. Given that in such a case recovering the position angle would not be straightforward, but since we are not measuring position angles, we are tempted to follow this procedure for the sake of simplicity. We applied this method to only two of the high S/N bursts. The measured RM and their uncertainties are mentioned in Sect. 4.2. We make note of the large errors, and attribute them to an inadequate bandwidth of only 200 MHz while measuring at high frequencies.

Prior to measuring the linear polarization fractions of the bursts, we first corrected each burst with the RM measured from it using PAM (Hotan et al. 2004). Then, we followed the procedure of Everett & Weisberg (2001) to de-bias and measure the linear polarization fractions of the bursts. This has already been specified in great detail (see Nimmo et al. 2021; Bethapudi et al. 2023; Gopinath et al. 2024), and hence is omitted here.

4. Results and discussions

4.1. Properties

We report a total of 116 bursts collected over 36.50 hours, with which we report a total rate of 3.1 ± 0.5 h^{-1}. The error is 95% Poissonian error. Moreover, we computed the rate from each observing session as well as the total rate and plot it in Fig. 2 (top panel). We also computed the rate and total exposure as a function of activity phase taking into account all the observations (bottom panel). We used the latest measured period of Sand et al. (2023) to compute the phases of the bursts. Moreover, Sand et al. (2023) also report the period derivative, which is consistent with zero, implying that the computed phases of the bursts are valid even for a large time span of data, such as our dataset. Each observation is binned in phase-axis where every phase bin width is 0.03125 (12.25 hours). In the case when any bin was partially overlapped, we added a fractional weight proportional to the overlap. Thereafter, the exposure and number of bursts per each phase bin was computed, which gives rate as a function of phase. We denote the phase bins where we did not detect any bursts with green triangles. We do not see any rate variability over phase. Pastor-Marazuela et al. (2021) modeled rate as a function of phase using kernel density estimates. We cannot yet perform such an analysis because of insufficient sampling of the phase region. Quantitatively, our total observations compose of 36.5 hours, whereas the active window at 600 MHz is about 50 hours (Pleunis et al. 2021; Bethapudi et al. 2023). Therefore, we suggest we would need at least 100 hours of on-source time in total before we can confidently measure phase variability (Sand et al. 2023).

We investigated the cumulative rate distribution against fluence for our burst sample. Figure 3 shows the cumulative rate above fluence (F) versus fluence for GMRT-Band 4 burst sample as blue squares. We fit broken power laws, where each power law is of the form $\text{Rate}(\geq F) \propto F^{\gamma}$ to it. For our sample we required two break points, 0.18 Jy ms and 1.10 Jy ms, to fit the data. Between 0.18 Jy ms and 1.10 Jy ms, we compute $\gamma = -0.51 \pm 0.01$, and beyond 1.10 Jy ms, $\gamma = -1.09 \pm 0.07$. Of the two breakpoints, we treat the smallest fluence break point as the fluence completeness limit. The fluence completeness for our sample agrees well with what is computed using the radiometer assuming a S/N of 10, a maximum width of 40 ms, and RMS noise of 3.36 mJy[2]. We then repeated the same exercise with the CHIME/FRB FRB 20180916B burst sample (Chime/Frb Collaboration 2020; Pleunis et al. 2021). We plot the cumulative rate versus fluence in the same Fig. 3, but as red circles. For the CHIME sample we required only one breakpoint at 1.67 Jy ms, and γ was fitted to be -1.34 ± 0.11 above it. We note that the uGMRT fluence completeness is ten times smaller than CHIME/FRB, which obviously suggests that GMRT is a sensitive instrument that complements the shallow but daily observations of CHIME/FRB. Pastor-Marazuela et al. (2021) measure γ to be -1.5 ± 0.2 and -1.4 ± 0.1 at 150 MHz (with LOFAR and above 104 Jy ms) and 1370 MHz (with APERTIF and above 7.8 Jy ms), which suggests the γ measurements

---

[2] http://www.ncra.tifr.res.in:8081/~secr-ops/etc/rmsp_advanced/rmsp.html

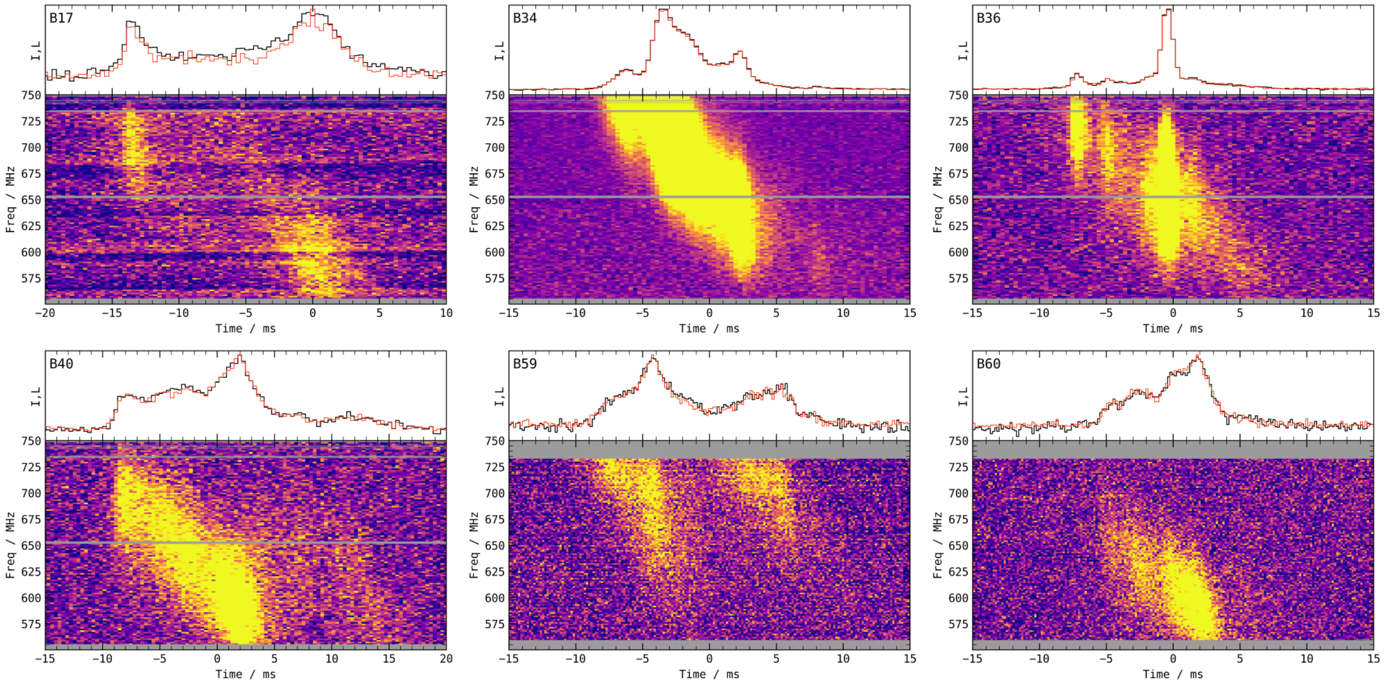

Fig. 1. Selection of polarization calibrated bursts. For each burst, we plot the de-dispersed dynamic spectra, frequency averaged total intensity (black) and RM corrected linear polarized (red) time series. The gray bands are RFI channels that have been zapped. The top left text in the time series panels is the burst ID. The rest of the plots can be found on zenodo.

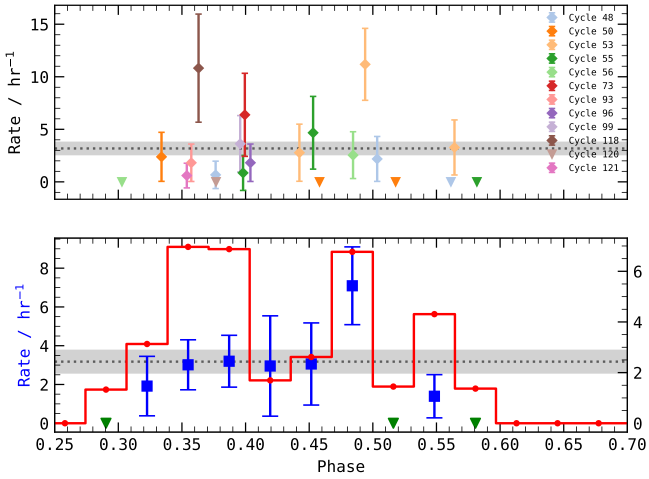

Fig. 2. Rate over activity phase of FRB 20180916B. The horizontal dotted black line is the total average rate. The error bars and the shaded region around the horizontal dotted line correspond to 95% error. *Top:* Rate per phase for each observation color-coded by activity cycle of the source. Detections are marked by diamonds with 95% error bars. Nondetections are marked by triangles. *Bottom:* Rate over activity phase when all observations are considered (see text for more details). The down-pointing green triangles denote nondetection of bursts. The blue squares correspond to rates with 95% error, with y-axis toward the left. The red circles mark the total exposure at the corresponding phase with y-axis toward the right.

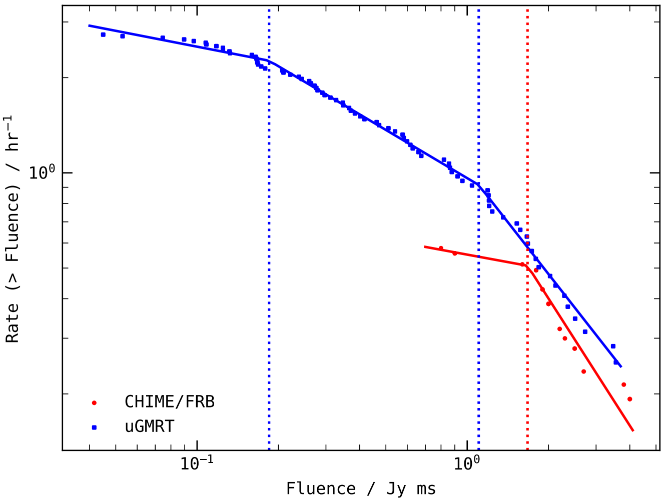

Fig. 3. Rate as a function of fluence for CHIME/FRB sample (Chime/Frb Collaboration 2020; Pleunis et al. 2021, in red) and our sample (in blue). Broken powerlaw are fitted to CHIME and our samples. The blue dotted lines are at 0.18 Jy ms and 1.10 Jy ms. The red dotted line is at 1.67 Jy ms. See text for the γ values.

across frequencies are consistent up to 2σ. However, if it is so that γ at 600–650 MHz is not as steep as compared to other frequencies, it could mean that GMRT is probing a deeper energy regime that is not performed by other telescopes.

We do not observe any noticeable DM variations from the inspection of dynamic spectra of the bursts. This observation is strongly corroborated by Sand et al. (2023), which also do not report any DM variation. Additionally, we do not observe any frequency burst envelope variations between regimes when RM was nonvarying and when RM was varying (Mckinven et al. 2023a, cf. Fig. 4). The linear polarization fractions are consistent with measurements of RM23. Linear polarization of the bursts from this FRB undergo depolarization due to scatter in the RM (Feng et al. 2022). The RM scatter is only 0.12 rad m^{-2}, which predicts bursts to be on average 95% linear polarized at our frequency of operation (650 MHz). We note the inverse variance

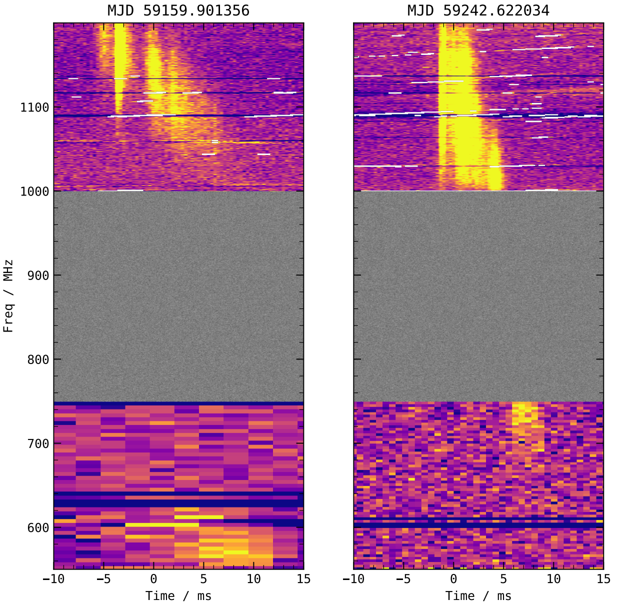

Fig. 4. Time-aligned filterbank data of Band 4 (550–750 MHz) and Band 5 (1000–1200 MHz) showing simultaneous detections. The filterbank data has been de-dispersed to 1200 MHz (top of Band 5). The gray region is random data plotted to show continuity. The white strips are manually flagged RFI. The time-frequency resolution and color-scale have been suitable chosen to clearly display the bursts.

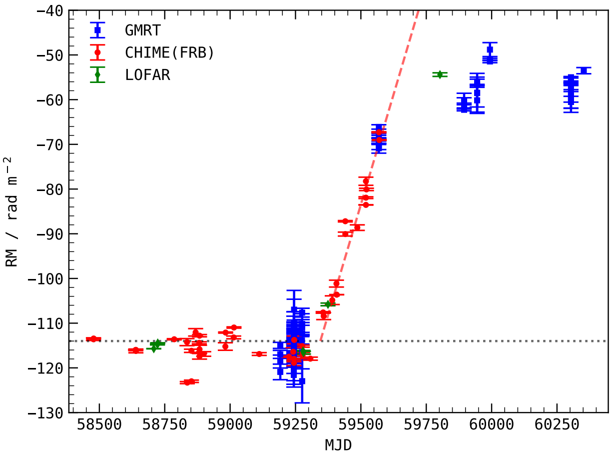

Fig. 5. Observed ionosphere corrected RM against MJD. CHIME/FRB RM23 are shown as red circles. LOFAR points are green diamonds AG23. This work's points are plotted as blue squares. The dotted horizontal line is the reported RM before variability started (Nimmo et al. 2021). The dashed red line is the trend fitted by RM23.

weighted mean linear polarization fraction is 95.0(1)%, which agrees well with the predicted depolarization. Since our linear polarization fraction measurements did not hint at any variability, we did not attempt to fit for RM scatter either on a per observation basis or on the whole. Nevertheless, we encourage the proposition of checking RM scatter variability with time as it could provide a constraint on the temporal variations of RM. We did not measure, and thus, do not report any circular polarization.

4.2. *Multi-band bursts*

We report two instances where we detected bursts in both of the observing bands (550–750 MHz and 1000–1200 MHz) simultaneously. We plot them in Fig. 4 where we de-disperse both the bands to the same reference frequency of 1200 MHz (top of Band 5). In both the cases we observe the burst is brighter in the upper band that precedes the lower band component. In the case of the multi-frequency burst detected on MJD 59242, the Band 4 component follows the structure of the Band 5 component. Moreover, this burst has a bandwidth of at least 500 MHz and a temporal width of 12 ms. In the multi-frequency burst detected on MJD 59159, the frequency structure fades toward the lower edge of Band 5 and it only reappears from the lower edge of Band 4, implying that the frequency structure is discontinuous. The discontinuity could be at least for 450 MHz, as we do not know if there is a burst component in the missing frequency band from 750 MHz to 1000 MHz. Moreover, the burst structure in Band 4 does not closely match that in Band 5. With only two instances in the entire dataset, we refrain from discussing possible physical scenarios that could cause such bursts. However, we detected two instances with only six hours of observing time, which suggests that these instances are not rare phenomena; therefore, we highly recommend large bandwidth observations of not just FRB 20180916B but also other rFRBs.

We tried to compare the RMs between the multi-frequency components. For the multi-frequency burst on MJD 59159, the Band 5 RM is −105.38 ± 3.6 rad m^{-2}. For the multi-frequency burst on MJD 59242, the Band 5 RM is −120.4 ± 4.5 rad m^{-2}. We could not measure Band 4 RM because we could not perform polarization calibration. For the MJD 59191 burst, we have no auxiliary scans (see Table 1). For the MJD 59242 burst, our DPHASE solution did not converge, and we could not generate a calibration solution. However, we know that on these MJDs, the RM had not started to change (see the following section). If we assume RM from the epoch when it was not changing (−114.6 rad m^{-2}; Nimmo et al. 2021), the Band 5 RM measurements are within 3σ.

4.3. *Band 4 RM*

We plot our observed ionospheric corrected RMs against MJDs in Fig. 5 (blue squares). In the same figure, we plot measurements by CHIME/FRB (Mckinven et al. 2023a, red circles) and LOFAR (Pleunis et al. 2021; Gopinath et al. 2024, green diamonds). We highlight the strong consistency between our RM measurements and the CHIME/FRB measurements around MJD 59569. This agreement also musters confidence in our RM measurements. Prior to MJD 59300 the RM is not seen to vary. From MJD 59300 until until MJD 59700, the measurements vary in a linear fashion. RM23 fitted a linear trend to the RM against time with slope of 0.197(6) rad m^{-2} day^{-1}. This trend is shown with a red broken line in Fig. 5. After MJD 59800, with one LOFAR detection (Gopinath et al. 2024, MJD 59802) and our detections, we see that the RM measurements no longer follow the linear trend of RM23. When seen altogether, we note that RM was exhibiting stochastic variability from MJD 58500 until MJD 59300, then from MJD 59300 to MJD 59700 it exhibited a secular variation, but from MJD 59800 until the end of our measurements at MJD 60352, the RM is seen to vary only stochastically. We also note that as of now, the stochastic variability before and after the linear trend is of the same duration. Future observations would be crucial not only to observe if the increasing trend resumes, but also to see if RM ever goes back to its original value.

Mckinven et al. (2023b) shows that most rFRBs exhibit secular RM evolution, often with $\frac{\Delta \mathrm{RM}}{\mathrm{RM}} \sim 1$. This is also seen in FRB 20180916B. Futhermore, FRB 20180916B is one of the few sources that shows time spans of secular RM variation as well as time spans of no RM variation. Other such sources are PSR J1745-2900 (Eatough et al. 2013), which exhibits RM variability and which parallels FRB 20180916B (Desvignes et al. 2018, see Fig. 3). The RM of PSR J1745-2900 was also seen to vary in a linear fashion (Mckinven et al. 2023a); however, further monitoring shows that the linear trend ceased, but the RM still continued to increase (Gregory Desvignes, priv. comm.). FRB 20121102A (Spitler et al. 2014) has a large absolute RM ($\sim 10^5$) and has exhibited decreasing RM evolution. It also has epochs where the evolution halts (Hilmarsson et al. 2021a; Plavin et al. 2022). There is also FRB 20190520B (Niu et al. 2022), which has an extreme |RM| value and variability. It has already undergone two sign flips within a span of 200 days (Anna-Thomas et al. 2023). FRB 20180301A (Luo et al. 2020), in addition to RM variability with one sign flip, also shows a clear dispersion measure (DM) variability (Kumar et al. 2023). FRB 20201124A (Lanman et al. 2022) showed substantial short-term variability (Hilmarsson et al. 2021b; Xu et al. 2022), but only for a span of 40 days, and became quiescent afterward. On the contrary, FRB 20220912A does not exhibit any RM variability when observed with FAST over s timescale of two months (Zhang et al. 2023).

We investigated if the increasing RM trend shows sign reversal. The Milky Way contribution of RM is estimated to be -98 ± 40 rad m^{-2} (Hutschenreuter et al. 2022). The largest predicted Milky Way contribution is -58 rad m^{-2} and the largest ionospheric RM corrected RM measured (on MJD 59993) is -48.8 ± 1.56 rad m^{-2}. There is a tentative detection of sign flip. There are three possible scenarios for observed RM trend: (i) changing electron density, (ii) changing path length of the magnetized Faraday screen, and (iii) changing magnetic field (see also Mckinven et al. 2023b). Changing electron density or path lengths of the active media along the line of sight would cause correlated variations in the DM, which neither RM23 nor Sand et al. (2023) observe; we do not see these variations either. The presence of a sign flip in the RM would strongly suggest that the variations seen are due to changing magnetic fields. Future observations will be extremely crucial in probing if the tentative detection of sign flip is genuine. If that is the case, it would make FRB 20180916B the third FRB, after FRB 20190520B (Anna-Thomas et al. 2023) and FRB 20180301A (Kumar et al. 2023), to show a sign reversal. Lastly, we strongly urge efforts be made to study the large-scale magnetic field structure of the FRB host galaxy. Such a study would provide an alternative line of evidence for the average magnetic field measurements, and would elucidate the role that past mergers (Kaur et al. 2022) may have played in the creation of FRB sources.

There are multiple models involving persistent radio sources (PRSs) at the FRB location that predict RM (and DM) evolution. These models have been proposed for FRB 20121102A, FRB 20190520B, and FRB 20201124A, all of which have PRS detections (Chatterjee et al. 2017; Niu et al. 2022; Bruni et al. 2024). For instance, Piro & Gaensler (2018) postulate that an expanding shocked supernovae remnant (SNR) is the cause of DM and RM evolution. The FRB emitting object is within the SNR and the shocked boundary between the ejecta and background ISM provides the necessary conditions to affect DM and RM with time. Similarly, Margalit & Metzger (2018) propose that the FRB source, a magnetar, is embedded in a magnetized wind nebula (MWNe), which causes the DM and RM variations. Interestingly, Bruni et al. (2024) also attribute RM evolution with PRS, and propose a correlation between luminosity of the PRS and the magnitude of the observed RM. This relation holds for FRB 20121102A and FRB 20190520B, both of which have |RM| in 10^5 rad m^{-2} (Hilmarsson et al. 2021a; Anna-Thomas et al. 2023), and also for FRB 20201124A whose |RM| is on the order of 650 rad m^{-2} (Hilmarsson et al. 2021b; Xu et al. 2022). However, there has only been an upper limit on the luminosity of FRB 20180916B Marcote et al. (2020), which implies that the magnitude of RM of FRB 20180916B is low. This adds weight to the model. A common feature for the above models is the predicted monotonic RM trend. Testing for the monotonic nature of the RM variation can be easily performed by future measurements, but this could only form weak evidence for the presence of PRS. A lack of robust detection of PRS, as in the case of FRB 20180916B, makes applying RM evolution models, which require a PRS, a bit far-fetched.

Lastly, we highlight that on 29 January 2021, we observed a rate of 11.4 ± 3.4 hr^{-1}. That rate is almost 5σ higher than the global rate. Thereafter, the RM variability was seen. We explored the possibility that this could be more than coincidence. On the one hand, the rate increase is statistically significant. However, the 29 January 2021 observation has around four hours of on-source time which is twice the usual on-source time. A period of nonvariability and a period of variability that are demarcated by a short period of heightened activity makes it plausible that the heightened activity could also have been caused by the same mechanism that is causing the observed RM trend. At this point, we merely make this speculation and hope future observations when such similar heightened rates are visible would make this connection more evident.

5. Conclusions

First, we devised multiple strategies to polarization calibrate the bursts in the dataset. Each strategy was designed to make use of the available auxiliary scans taken during the observing session (Sect. 3.1). Then, we implemented a pipeline to measure the RM of the polarization calibrated bursts using QU-fitting (Sect. 3.3). Using this fitting, we first corrected for the Faraday rotation and measured the polarization properties of the bursts (Sect. 3.3). We also verified the calibration solution using pulsar scans, and commented on how the calibration solution would affect subsequent RM measurements (Appendices A.1 and B).

From our observing campaign, we detected 116 bursts with 36.5 hours on source spanning over 1200 days. Our findings are the following:

- For a few of the sessions, we performed simultaneous observations of FRB 20180916B in Band 4 (650 MHz) and Band 5 (1.1 GHz). We leave the proper calibration of the Band 5 bursts to a future work, but we tried to measure the RMs of the two uncalibrated brightest bursts in our sample (Sect. 3.3). The bursts show varied structures, and the fact that we detected two bursts within six hours of observing advocates for future large bandwidth observations (Sect. 4.2).
- We plot the time variability of RM in Fig. 5. The linear trend seen by RM23 is no longer consistent with the data, and the source has entered a regime where the RM is only varying stochastically. We report a tentative detection of a sign flip in RM, strongly suggesting that the RM variations are driven by magnetic field variations. Future observations will trace the

RM variations and would certainly provide new insights into possible scenarios. Lastly, we motivate a large-scale magnetic field study of the FRB host galaxy to elucidate any preferred magnetic field structure that could be causing the observed RM variations.

Data availability

All the code for GMRT Coherence data reduction and analysis is provided in GMRT-FRB. Machine-readable csv files of Tables 1 and 3, and the burst plots (Fig. 1) are available on zenodo. Tables 1 and 3 are available at the CDS via anonymous ftp to `cdsarc.cds.unistra.fr` (`130.79.128.5`) or via `https://cdsarc.cds.unistra.fr/viz-bin/cat/J/A+A/694/A75`. Any additional data will be made available on request.

Acknowledgements. SB would like to thank a lot of people: Simon Johnston for useful discussions about polarization calibration strategy, Frank Schinzel for helping understand time variability of calibration solutions, Gregory Desvignes for extensive and exhaustive help with the manuscript. We thank the staff of the GMRT that made these observations possible. VRM gratefully acknowledges the Department of Atomic Energy, Government of India, for its assistance under project No. 12-R&D-TFR-5.02-0700. GMRT is run by the National Centre for Radio Astrophysics of the Tata Institute of Fundamental Research. LGS is a Lise Meitner Independent Max Planck research group leader and acknowledges support from the Max Planck Society. Part of this research was carried out at the Jet Propulsion Laboratory, California Institute of Technology, under a contract with the National Aeronautics and Space Administration.

References

Anna-Thomas, R., Connor, L., Dai, S., et al. 2023, Science, 380, 599
Bailes, M. 2022, Science, 378, abj3043
Bethapudi, S., Spitler, L. G., Main, R. A., Li, D. Z., & Wharton, R. S. 2023, MNRAS, 524, 3303
Britton, M. C. 2000, ApJ, 532, 1240
Bruni, G., Piro, L., Yang, Y.-P., et al. 2024, Nature, 632, 1014
Buch, K. D., Kale, R., Naik, K. D., et al. 2022, J. Astron. Instrum., 11, 2250008
Buch, K. D., Kale, R., Muley, M., Kudale, S., & Ajithkumar, B. 2023, JApA, 44, 37
Buchner, J. 2021, J. Open Source Software, 6, 3001
Chandra, P., Kumar, S. S., Kudale, S., et al. 2023, arXiv e-prints [arXiv:2310.04335]
Chatterjee, S., Law, C. J., Wharton, R. S., et al. 2017, Nature, 541, 58
CHIME/FRB Collaboration (Andersen, B. C., et al.) 2019, ApJ, 885, L24
Chime/Frb Collaboration (Amiri, M., et al.) 2020, Nature, 582, 351
Cotton, W. D., Dallacasa, D., Fanti, C., et al. 1997, A&A, 325, 493
Day, C. K., Deller, A. T., Shannon, R. M., et al. 2020, MNRAS, 497, 3335
Desvignes, G., Eatough, R. P., Pen, U. L., et al. 2018, ApJ, 852, L12
Eatough, R. P., Falcke, H., Karuppusamy, R., et al. 2013, Nature, 501, 391
Everett, J. E., & Weisberg, J. M. 2001, ApJ, 553, 341
Feng, Y., Li, D., Yang, Y.-P., et al. 2022, Science, 375, 1266
Gopinath, A., Bassa, C. G., Pleunis, Z., et al. 2024, MNRAS, 527, 9872
Gupta, Y., Ajithkumar, B., Kale, H. S., et al. 2017, Curr. Sci., 113, 707
Hewitt, D. M., Snelders, M. P., Hessels, J. W. T., et al. 2022, MNRAS, 515, 3577
Hewitt, D. M., Hessels, J. W. T., Ould-Boukattine, O. S., et al. 2023, MNRAS, 526, 2039
Hilmarsson, G. H., Michilli, D., Spitler, L. G., et al. 2021a, ApJ, 908, L10
Hilmarsson, G. H., Spitler, L. G., Main, R. A., & Li, D. Z. 2021b, MNRAS, 508, 5354
Hotan, A. W., van Straten, W., & Manchester, R. N. 2004, PASA, 21, 302
Hutschenreuter, S., Anderson, C. S., Betti, S., et al. 2022, A&A, 657, A43
Jahns, J. N., Spitler, L. G., Nimmo, K., et al. 2023, MNRAS, 519, 666
Kaur, B., Kanekar, N., & Prochaska, J. X. 2022, ApJ, 925, L20
Kirsten, F., Marcote, B., Nimmo, K., et al. 2022, Nature, 602, 585
Kirsten, F., Ould-Boukattine, O. S., Herrmann, W., et al. 2024, Nat. Astron., 8, 337
Kumar, P., Luo, R., Price, D. C., et al. 2023, MNRAS, 526, 3652
Kumar, P., Beniamini, P., Gupta, O., & Cordes, J. M. 2024, MNRAS, 527, 457
Lanman, A. E., Andersen, B. C., Chawla, P., et al. 2022, ApJ, 927, 59
Li, D., Wang, P., Zhu, W. W., et al. 2021, Nature, 598, 267
Lorimer, D. R., Bailes, M., McLaughlin, M. A., Narkevic, D. J., & Crawford, F. 2007, Science, 318, 777
Luo, R., Wang, B. J., Men, Y. P., et al. 2020, Nature, 586, 693
Main, R. A., Hilmarsson, G. H., Marthi, V. R., et al. 2022, MNRAS, 509, 3172
Main, R. A., Bethapudi, S., Marthi, V. R., et al. 2023, MNRAS, 522, L36
Marcote, B., Nimmo, K., Hessels, J. W. T., et al. 2020, Nature, 577, 190
Margalit, B., & Metzger, B. D. 2018, ApJ, 868, L4
Mckinven, R., Gaensler, B. M., Michilli, D., et al. 2023a, ApJ, 950, 12
Mckinven, R., Gaensler, B. M., Michilli, D., et al. 2023b, ApJ, 951, 82
Mevius, M. 2018, RMextract: Ionospheric Faraday Rotation calculator, Astrophysics Source Code Library [record ascl:1806.024]
Nayana, A. J., & Chandra, P. 2021, ApJ, 912, L9
Nimmo, K., Hessels, J. W. T., Keimpema, A., et al. 2021, Nat. Astron., 5, 594
Nimmo, K., Hessels, J. W. T., Kirsten, F., et al. 2022a, Nat. Astron., 6, 393
Nimmo, K., Hewitt, D. M., Hessels, J. W. T., et al. 2022b, ApJ, 927, L3
Nimmo, K., Pleunis, Z., Beniamini, P., et al. 2024, arXiv e-prints [arXiv:2406.11053]
Niu, C. H., Aggarwal, K., Li, D., et al. 2022, Nature, 606, 873
Ocker, S. K., Cordes, J. M., Chatterjee, S., et al. 2022, ApJ, 931, 87
Pastor-Marazuela, I., Connor, L., van Leeuwen, J., et al. 2021, Nature, 596, 505
Perley, R. A., & Butler, B. J. 2013, ApJS, 206, 16
Perley, R. A., & Butler, B. J. 2017, ApJS, 230, 7
Petroff, E., Hessels, J. W. T., & Lorimer, D. R. 2019, A&A Rev., 27, 4
Petroff, E., Hessels, J. W. T., & Lorimer, D. R. 2022, A&A Rev., 30, 2
Piro, A. L., & Gaensler, B. M. 2018, ApJ, 861, 150
Plavin, A., Paragi, Z., Marcote, B., et al. 2022, MNRAS, 511, 6033
Pleunis, Z., Michilli, D., Bassa, C. G., et al. 2021, ApJ, 911, L3
Ransom, S. 2011, Astrophysics Source Code Library [record ascl:1107.017]
Roy, J., Chengalur, J. N., & Pen, U.-L. 2018, ApJ, 864, 160
Sand, K. R., Breitman, D., Michilli, D., et al. 2023, ApJ, 956, 23
Sherman, M. B., Connor, L., Ravi, V., et al. 2023, ApJ, 957, L8
Snelders, M. P., Nimmo, K., Hessels, J. W. T., et al. 2023, Nat. Astron., 7, 1486
Spitler, L. G., Cordes, J. M., Hessels, J. W. T., et al. 2014, ApJ, 790, 101
Swarup, G. 1991, in IAU Colloq. 131: Radio Interferometry. Theory, Techniques, and Applications, eds. T. J. Cornwell, & R. A. Perley, ASP Conf. Ser., 19, 376
Tendulkar, S. P., Gil de Paz, A., Kirichenko, A. Y., et al. 2021, ApJ, 908, L12
Wu, Z., Zhu, W., Zhang, B., et al. 2024, ApJ, 969, L23
Xu, H., Niu, J. R., Chen, P., et al. 2022, Nature, 609, 685
Yang, Y.-P., Xu, S., & Zhang, B. 2023, MNRAS, 520, 2039
Zhang, Y.-K., Li, D., Zhang, B., et al. 2023, ApJ, 955, 142
Zhou, D. J., Han, J. L., Zhang, B., et al. 2022, RAA, 22, 124001

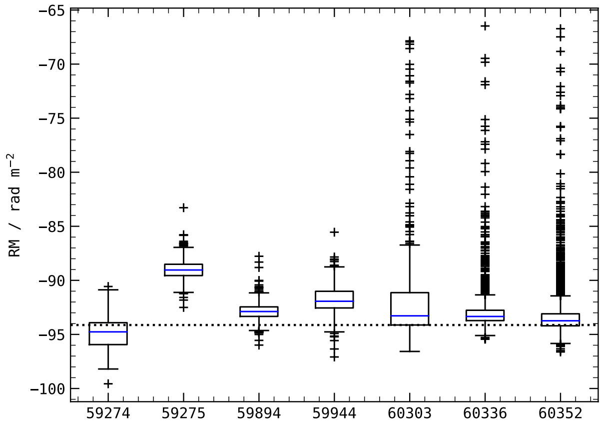

Fig. A.1. Boxplot of ionospheric corrected RM measurements of single pulses from PSR J0139+5814 taken on different days. The blue line in each box denotes the median. Each box spans for Inter-Quartile-Range. The horizontal dotted line is the literature RM value for the pulsar. The large number of outliers on MJDs 60303, 60336 and 60352 is due to the heightened ionospheric activity reported in the GMRT Cycle 45 observations.

Appendix A: Verification of calibration

A.1. RM verification

We have seven observations of PSR J0139+5814. We perform a single-pulse search (as described in Sect. 2), polarization calibrate (see Sect. 3.1), and measure RM (Sect. 3.3) from each of the single pulses. We use this dataset of single pulses to verify RM measurements.

We show a boxplot of the measured ionospheric corrected RM in Fig. A.1. We also plot the literature RM value with the horizontal dotted line. With this plot, we want to highlight the spread in RM values seen with single pulses in a given observation. And, the quirk that RM measurements are not completely consistent from observation to observation suggesting some systematic at play. Similar deviation from literature value was detected for the same pulsar in Chandra et al. (2023). The large tail we observe in case of observations of MJD 60303, MJD 60336 and MJD 60352 is due to the strong ionospheric activity recorded in GMRT Cycle 45.

Appendix B: DPHASE variability

Rotational measurements are extremely sensitive to the cross-hand delay because the degeneracy described earlier. Therefore, we have to exercise extreme caution in measuring the delay and uncovering any systematics. GMRT being an interferometer where phasing operation is performed before every science scan, the DPHASE is susceptible to change on macroscopic variables (like ambient temperature and such). Investigating the underlying factors requires much more carefully planned study and is beyond the scope of this paper.

We plot the cross-hand delay we measure from scans of 3C138, noise diode and pulsar J0139+5814 against MJD, day-of-year and hour-of-day in Fig. B.1. The delay seems to vary from observation to observation. In almost all the cases, we only have a single measurement in an observation. However, observations of 12 Nov 2022 and 31 Dec 2022, we have noise diode scans and PSR J0139+5814 pulsar scans. The cross-hand delay measurement from all of them is consistent within an observation. The standard deviation of measurements of those observations is less than 0.1 ns. This can also be seen in the plot in the bottom panel where points follow a horizontal line.

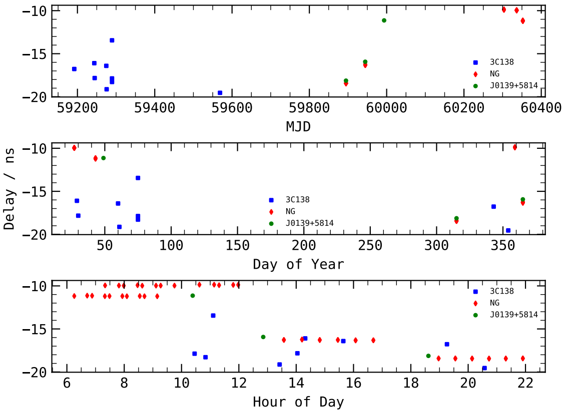

Fig. B.1. Cross-hand delay measurements from different scans: 3C138, noise diode, and PSR J0139+5814 plotted against MJD, day-of-year, and hour-of-day. The sign of the delay is purely a mathematical artifact.

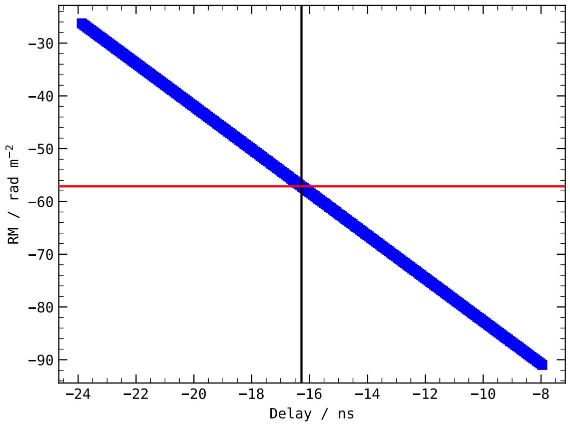

Fig. B.2. RM measurements when calibrating for different cross-hand delay. The black vertical line is the delay measurement from noise diode scan. The red horizontal line is the RM measurement. See text for details.

The fact that multiple delay measurements taken within an observation are consistent even with multiple phasings lends confidence to our RM measurements throughout the dataset. Alternatively, we investigate how much an error in cross-hand delay affects RM measurements. We take the B78 burst which was observed on MJD 59944. We construct multiple calibration solutions (PACV) files where GAIN and DGAIN are the same but only the cross-hand delay (D_{ns}) is varied. We apply each calibration solution to the burst and perform RM measurement as mentioned in Sect. 3.3. We plot the cross-hand delay versus the measured RM in Fig. B.2. In the same figure, we plot the measured RM of B78 as red horizontal line and the black vertical line is the cross-hand delay used to calibrate this burst. We note that a 2 ns difference in the delay measurement causes $O(10)$ difference in RM measurement. Nevertheless, as mentioned above, the variability we have seen in the delay measurement, which is less than 0.1 ns, does not affect our confidence in our measurements.

APPENDIX C

Chapter 6 publication

A&A, 702, A248 (2025)
https://doi.org/10.1051/0004-6361/202556347

Astronomy & Astrophysics

Constraining the origin of the long-term periodicity of FRB 20180916B with polarization position angle

S. Bethapudi[1,⋆], D. Z. Li[2], L. G. Spitler[1], V. R. Marthi[3], M. L. Bause[1], R. A. Main[4,5,1], and R. S. Wharton[1]

[1] Max-Planck-Institute for Radio Astronomy, Auf dem Hügel 69, Bonn 53121, Germany
[2] Department of Astrophysical Sciences, Princeton University, Princeton, NJ 08544, USA
[3] National Centre for Radio Astrophysics, Ganeshkhind, Tata Institute of Fundamental Research, Post Bag 3, Pune – 411 007, India
[4] Department of Physics, McGill University, 3600 rue University, Montréal, QC H3A 2T8, Canada
[5] Trottier Space Institute, McGill University, 3550 rue University, Montréal, QC H3A 2A7, Canada

Received 10 July 2025 / Accepted 1 September 2025

ABSTRACT

Context. The repeating fast radio burst (FRB) FRB 20180916B produces bursts in a 5.1 day active window that repeats with a 16.34 day period. Models have been proposed to explain the periodicity using dynamical phenomena of neutron stars such as rotation, precession, or orbital motion. The polarization position angle (PA) of the bursts can be used to distinguish and constrain the origin of the long-term periodicity of the FRB.

Aims. We aim to study the PA variability on short (within an observation) and long timescales (from observation to observation). Given the periodicity of the source, we also study the PA variations within the active window and across multiple windows. Then, we compare the observed PA variability with the predictions of various dynamical progenitor models for the FRB.

Methods. We used the calibrated burst dataset detected by uGMRT in Band 4 (650 MHz) published in our earlier work. We transformed the PA measured at 650 MHz to infinite frequency such that PAs measured in different observations are consistent, and finally we measured the changes within and across active windows.

Results. We find that the PA of the bursts varies according to the periodicity of the source. We constrained the PA variability to be less than seven degrees on timescales less than four hours for all MJDs. We also tentatively find that the PA varies within an active window with a variability of a few degrees per hour. In addition, we tentatively note the PA measured at the same phase in the active window varies from one cycle to another.

Conclusions. Using the findings, we constrained the rotational, precession, and binary progenitor models involving compact objects, where the emission originates from the magnetosphere of the compact object. The rotational model partially agrees with the observed PA variability, but it requires further study to be fully constrained. We robustly rule out all flavors of precessional models where the precession of a neutron star either explains the periodicity of the FRB or the variability from one cycle to another. We can rule out the relativistic spin precession binary model. Lastly, we observed similarities between FRB 20180916B and an X-ray binary system, Her X 1, and explicitly note that the two sources exhibit a similar form of PA variability.

Key words. methods: observational – techniques: polarimetric

1. Introduction

Fast radio bursts (FRBs) are short duration transient events that occur in the radio regime of the electromagnetic spectrum (Lorimer et al. 2007; Petroff et al. 2019, 2022; Bailes 2022). FRB 20180916B (CHIME/FRB Collaboration 2019) is a repeating FRB source that emits bursts within a window that is (i) periodic, with a period of 16.34 days (Chime/Frb Collaboration 2020), and (ii) chromatic such that it shifts in time and varies in duration with observing frequency (Pastor-Marazuela et al. 2021; Pleunis et al. 2021; Bethapudi et al. 2023). Even with over 100 activity windows having been observed since the discovery of FRB 20180916B, there has been no measurable change in period (Sand et al. 2023; Lan et al. 2024). Published bursts of FRB 20180916B across wide frequencies exhibit a flat or unchanging position angle (PA) over burst timescales (Nimmo et al. 2021; Pastor-Marazuela et al. 2021; Pleunis et al. 2021; Bethapudi et al. 2023; Mckinven et al. 2023; Sand et al. 2022; Gopinath et al. 2024). Moreover, the rotation measure (RM) of the FRB has been known to vary in a step-like fashion (Mckinven et al. 2023; Gopinath et al. 2024; Bethapudi et al. 2025; Ng et al. 2025). The causes for periodicity, chromaticity, lack of any variability in period, and step-like variability in RM is not known. There have been many progenitor models to explain FRB 20180916B (Levin et al. 2020; Zanazzi & Lai 2020; Beniamini et al. 2020; Wada et al. 2021). A subset of those models explain periodicity using some form of dynamics such as rotation, precession, or binary motion. Collectively, these models are referred to as dynamical models. Each dynamical model has its own geometry and predicts unique temporal variability of PA on short and long timescales. We took inspiration from Li & Zanazzi (2021) and studied the temporal PA variations and compared what is observed and what is predicted by the various dynamical models. In this way, we hope to understand the geometry of the system and produce novel knowledge about the source.

The PA of the polarized light measures its orientation with respect to the plane of the sky. If the nature of emission is such that the PA is tied to the geometry of the system, then by studying the PA variations, we can track the geometric variations. Such insights into geometry have already been demonstrated through study of the PA variations of pulsars. Pulsars are fast spinning neutron stars, and they emit electromagnetic radiation, primarily in radio (Lorimer & Kramer

---

⋆ Corresponding author: `sbethapudi@mpifr-bonn.mpg.de`

2012). The radio emission is thought to originate from the open magnetic field lines of its dipolar magnetic field. The open field lines co-rotate with the spinning neutron star. Therefore, the PA of the emission shows the imprint of the co-rotation. This imprint is modeled with the rotating vector model (hereafter RVM; Radhakrishnan & Cooke 1969; Everett & Weisberg 2001). Recent works, such as Johnston et al. (2023, 2024), have shown that RVM can explain the observed PA sweep in over 80% of the pulsars in the Thousand-Pulsar-Array program (Johnston et al. 2020). Moreover, long-term studies of PAs of pulsars and magnetars (highly magnetized neutron stars; Kaspi & Beloborodov 2017) have elucidated novel geometrical phenomena. For instance, Desvignes et al. (2019) performed RVM modeling of PA data of a binary pulsar system PSR J1906+0746 over a time span of 10 years and measured drift of the spin axis due to relativistic spin precession. Similarly, Meng et al. (2024) studied the relativistic spin precession of a double neutron star system PSR J1946+2052 using PA data collected over 3 years. Additionally, by fitting RVMs to PA data of magnetar XTE 1810-197 at different MJDs, Desvignes et al. (2024) reported how the magnetar relaxes its internal structure over the course of several days after X-ray burst activity. Clearly, long-term modeling of PA data enables study of the geometric variations exhibited by the emitting body, provided the PA tracks the geometry.

Features seen in PAs of FRBs could also be indicative of geometry, but connecting the PAs of the FRBs to a geometry has not been straightforward. So far, RVM modeling has only been attempted with few non-repeating FRBs that display "informative" (non-flat) PA sweeps. FRB 20221022A is a non-repeating FRB detected by CHIME/FRB, which presented an S-curve-like PA sweep similar to what is predicted by RVM (Mckinven et al. 2024). Furthermore, Mckinven et al. (2024) have performed RVM modeling assuming different duty cycles and attempted to constrain the geometry. In addition, Bera et al. (2024) has reported the discovery of a non-repeating FRB, FRB 20210912A, by ASKAP that exhibits PA variations between its two sub-components. Bera et al. (2024) tried to explain the variation by fitting RVM to the PA time series. However, such a geometric origin need not always be the case. For example, Bera et al. (2025) describe two non-repeating FRBs whose polarization features evolve within burst duration, possibly indicating a plasma birefringent propagation medium. In this case, the variation of the PA does not need to exclusively track the geometry. However, such exotic polarization features and propagating media are uncommon in FRBs, and FRB 20180916B does not exhibit any of such features. Significantly, a long-term study of PAs of repeating FRBs has not yet been attempted, but with this paper, we attempt to conduct such a study with FRB 20180916B. In Sect. 2, we describe the collection of bursts and all the analysis steps we performed to accurately measure PA, which can be compared between observations. We study the variability of PA across various timescales and measure the rates of the variability in Sect. 3. We compare the observer PA variability with that predicted by the dynamical models in Sect. 4. Lastly, we present our discussions and conclusions in Sect. 5 and Sect. 6, respectively.

2. Data and analysis

This section describes all the data processing steps taken to measure PAs of the bursts. All the bursts were detected with the uGMRT (Swarup 1991; Gupta et al. 2017) in Band 4 (550–750 MHz) with Phased Array mode of operation, the details of which can be found in Bethapudi et al. (2025) (hereafter SB24). Table 1 of SB24 lists all the observations and number of bursts per each observation. It also lists various auxiliary sources, such as noise diode, quasars and known pulsars, which have been used in flux/polarization calibration and testing the performance of the search pipeline. In this paper, we show the activity phase, the number of bursts and the maximum time separation among bursts per each observation in Table 1. We use the periodicity model presented in Sand et al. (2023) to compute activity cycle and activity phase of the bursts. That is, we use reference MJD of 58369.4 and period of 16.34 days. Activity phase is a number between 0 and 1, which linearly maps to the period. Activity cycle is the integer number of periods elapsed since the reference MJD. We first convert the bursts from PSRFITS to TIMER format using PAM (Hotan et al. 2004). Then, we apply the calibration solutions as derived in SB24 using PAC, which also performs parallactic angle correction. From hereon, we only refer to the calibrated burst archive in TIMER format.

2.1. PA calibration

The PAs are measured with respect to the sky frame. To meaningfully compare PAs measured from different observations, PA measurements have to be in the same sky frame. Therefore, we need to perform PA calibration so that PA measurements of a some known source with known and fixed PA from different observations are consistent and representative of the true PA value. This is usually achieved using polarized quasars, such as 3C138 and 3C286, whose PAs are modeled and fitted for as a function of observing frequency (Perley & Butler 2013). However, we do not have multiple observations when 3C138 was observed. Therefore, we employed a different strategy here. We make use of known pulsars, PSR B0329+54 and PSR J0139+5814, to perform PA calibration. That is, we make use of PA-sweeps of the pulsars to perform PA calibration. Our choice of using pulsars and not standard quasars implies our PA measurements although consistent among themselves, are not in any absolute frame as defined in Perley & Butler (2013). That is, we have only taken care of inter-observation PA offsets, and there may be a global PA offset which would bring them into the absolute reference frame of Perley & Butler (2013). Naturally, PA calibration and thus further analysis was only done with those observations where we observed either of the two pulsars.

As our PA references, we used the European Pulsar Network Database (EPNDB) 610 MHz pulse profiles of PSR B0329+54[1] and PSR J0139+5814[2]. We fold all the B0329+54 and J0139+5814 scans (see Table 1, auxiliary sources column SB24) using DSPSR (van Straten & Bailes 2011) and calibrate using the same procedure and calibration solution we used to calibrate the bursts from the respective observations. We also used same QU-fitting procedure (SB24) to estimate RM and also correct for it using PAM. Then, we phase align all the pulsar archives with their corresponding EPNDB reference pulse profile. We do the phase alignment by minimizing the cross-correlation between Stokes-I integrated profiles. Now, measuring position angle correction is simply a matter of measuring the offset in the position angle sweep of the observed pulsar with respect to the reference PA sweep.

---

[1] https://psrweb.jb.man.ac.uk/epndb/#gl98/J0332+5434/gl98_610.epn

[2] https://psrweb.jb.man.ac.uk/epndb/#gl98/J0139+5814/gl98_610.epn

In the end, there can only be one PA reference. The EPNDB pulsar profiles of PSR B0329+54 and PSR J0139+5814 need not be in the same reference frame themselves and have to be brought to the same frame. To do so, we note that we have four observations (MJD 59274, MJD 59275, MJD 59944, MJD 59993) where we have scans of both of the test pulsars. We measure PA corrections from each of the test pulsars from all the four observations, which are tabulated in Table A.1. We note that the difference between the PA corrections found using PSR B0329+54 and PSR J0139+5814 is consistent with mean of 42.50 and standard deviation of 1.75 deg. This consistency in the difference across multiple MJDs strongly convinces us that (i) PAs can be calibrated, and (ii) a single PA reference can be constructed using either of the test pulsars. Therefore, we set EPNDB PSR B0329+54 as our main reference and correct EPNDB PSR J1039+5814 by 42.5 deg so that it agrees with the PA frame of EPNDB PSR B0329+54. Then, for all the observations where we use PSR J0139+5814 to do PA calibration, we use this corrected EPNDB PSR J0139+5814. We show the phase-aligned Stokes-I and PA calibrated PA-sweeps for each of the pulsar scans from different observations in Figure A.1. The reference source and the corrections for each observation are shown in Source and Correction columns of Table 1.

Lastly, we note that PSR B0329+54 has a complicated PA sweep and also is seen to undergo mode changes within our dataset. Moreover, its peak linear polarization fraction is not high. However, we note that for all the observations where we use PSR B0329+54 for PA calibration, the Stokes-I profile and the PA-sweep agree well (see Figure A.1). In hindsight, PSR B0329+54 might not have been an ideal choice. Nevertheless, we are confident in our consistent position angle measurements and leave to a future work on acquiring absolute position angles.

2.2. Measuring RM

When light passes through an ionized medium with magnetic fields threading along the propagating direction, the PA of light undergoes rotation. This effect is known as Faraday rotation. It is mathematically understood as

$$\mathrm{PA}_\lambda = \mathrm{PA}_\infty + \mathrm{RM}\lambda^2, \tag{1}$$

where λ is the wavelength of light, PA_∞ is the PA measured at ∞ frequency (or also the initial PA), and PA_λ is the PA measured at wavelength λ after the light has propagated through the medium with rotation measure RM. Within our observing setup, which covers from 550 MHz to 750 MHz with around 2048 channels, PA measured in each channel is different and linear in λ^2. PA_∞ is the true PA of emission from the source and only that can be used to study long-term variability. Any finite frequency would have undergone some Faraday rotation and would not truly be the PA as emitted by the source. Therefore, using Eq. (1), PA measurements at any finite frequency are brought to infinite frequency to recover PA_∞, which are then used to study long-term PA variability. Using PA at the infinite frequency allows us to account for the fact that the RM of FRB 20180916B varies on timescales of days (Mckinven et al. 2023; Gopinath et al. 2024, SB24). However, we emphasize that our measurement of PA_∞ is only as good as our measurement of RM. Any noise in our RM measurement introduces noise in our PA_∞ measurement. Therefore, this sub-section wholly focuses on accurately measuring RM using Eq. (1).

PA variability against wavelength (or frequency) is not exclusive to Faraday rotation. In our observing setup, polarization is expressed in circular basis, which has two basis elements: Right Circular Polarization (RCP) and Left Circular Polarization (LCP). The phase of the cross-correlation of the two basis elements is degenerate with the PA of light. Moreover, the phase of the cross-correlation is also a parameter of the polarization calibration model, known as DPHASE (denoted with ϕ; Britton 2000). In our calibration strategy (SB24), we modeled DPHASE as a linear function over the observing band. That is, $\phi = \psi_r + \pi \mathrm{D}_{\mathrm{ns}} f_{\mathrm{GHz}}$, where f_{GHz} is frequency in GHz, the slope, D_{ns}, is known as cable delay measured in nanoseconds, as it directly corresponds to the delay between RCP and LCP[3]. And, the bias, ψ_{r}, behaves like twice the PA. The definitions used here are the same as SB24 (Also see Eqs. 4 and 5 of Nimmo et al. 2021). Using observations in which multiple noise diode scans were taken, we note that the parameters of the linear model, D_{ns} and ψ_r, are consistent with one another (see Figure A.2 and Sect. A.2).

Nevertheless, we note departures from the linear modeling of DPHASE. Figure A.3 shows the difference between the modeled DPHASE and observed DPHASE across the bandpass from the multiple noise diode scans of different MJDs. Deviations from the linear assumption are seen predominantly at the band edges, although are not limited to the edges. When the bursts are calibrated with linearly modeled DPHASE, the deviations from the linear model interfere with RM measurements. This is particularly exacerbated by the band-limited emission of some of the bursts, because when the frequency span with significant non-linear DPHASE deviations overlaps with the burst emission, it would cause QU-fitting algorithm to under-/over-compensate the RM parameter to improve the fit. As an illustration, we show the frequency spans and RM measurements of a subset of individual bursts detected on MJD 59243, where we had around forty bursts in total in Figure B.1. We also plot the inverse variance weighted average of RM using all the bursts with a vertical red line. We only selected bursts which occupy half of the total band. From the plot, we clearly see that bursts which occupy the upper edge of the band overestimate the average RM, while bursts which occupy the lower edge of the band underestimate the RM. These spurious RM measurements, which are non-physical, are caused by DPHASE deviations from the linear model. Therefore, we did not use RM measurements of individual bursts in any way for further analysis. However, we note that the average computed using all the bursts is less impacted by this effect, as the average also uses bursts with large bandwidths, but nevertheless, if a subset of individual RM measurements are affected by DPHASE deviations, any ensemble average would also be affected. As mentioned before, our PA measurement strongly depends on our RM measurements. Because we see nonphysical biases in our RM measurements, we do not use individual RM measurements or any average of individual RM measurements to correct for Faraday rotation and measure PA.

While individual burst RM measurements would suffer from DPHASE deviations, simultaneously fitting one RM and one PA to all the bursts from an observation would diminish the impact of such deviations. In addition, any PA variability that is not linear in λ^2 is not a Faraday rotation and will be seen in the difference between the data and the fit. Of course, such a fit would not be possible if the source inherently exhibits RM and PA variability within an observation. Therefore, we hypothesize and attempt to fit one RM and one PA to all the bursts from an observation and then repeat the procedure for all the

---

[3] When light of frequency f propagates through a distance of L, it acquires a phase (ϕ) of $\frac{2\pi L f}{c}$. Then, the difference in phase ($\Delta\phi$) due to different propagation lengths (ΔL) is $\frac{2\pi \Delta L f}{c}$. If ΔL is a constant of f, $\Delta\phi$ is a linear function of f.

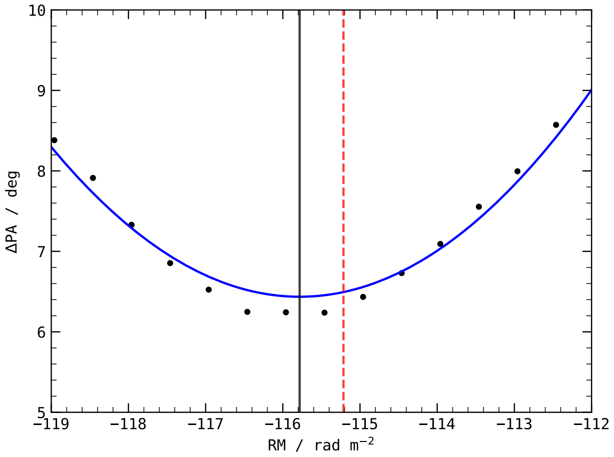

Fig. 1. Applying one RM to all the bursts detected during the observation of MJD 59243 and measuring the standard deviation of all the PA measurements from every time bin of every burst. Repeating this procedure for multiple RMs yields the black dots. The blue line is the fitted parabola. The vertical black line is the center of the fitted parabola. The red dashed vertical line is the RM measured after fitting using all the bursts. See Table 1 and Sect. 2.2.

observations. We extract normalized Stokes-q, u, that is Stokes-Q, U divided by $\sqrt{Q^2 + U^2}$, from every time-frequency bin with burst emission for all the calibrated bursts in an observation and perform QU-fitting using the normalized Stokes-q, u. We follow the same QU-fitting procedure used in SB24, where fitting is done with respect to the center frequency. We also employ EQUAD to artificially inflate the errors as already used in SB24. We only used a normalized Stokes-q, u here to avoid having to fit a linear polarization fraction (L_p) parameter for each burst, which would require us to fit for a large number of parameters. Although the fitting was done using QU-fitting, we show the fit outcomes as PA against λ^2 in Figure B.2, as the two approaches are equivalent. The top panels show the PA as a function of λ^2 with data in black dots and fitted model in red line. The bottom panels show binned averaged PA residuals also against λ^2. The residuals are first binned according to the original frequency resolution of bursts and averaged to clearly show the departures from the linear DPHASE model. The top x-axis in both the panels shows observing frequency. λ_c is wavelength of the center frequency. It is evident that (i) all the bursts from an observation fit with one RM and one PA, and (ii) there are structures in error that are indicative of unmodeled DPHASE variation over frequency. See, for example, the averaged errors in upper edge of frequency bands of MJDs 59243, 59568 and 60303, or the averaged errors in lower edge of frequency bands of MJD 59993. Lastly, we report the RM and the error in RM in Table 1.

We illustrate the difference between the above approach of fitting one RM to all the bursts and inverse variance weighted average in Figure B.3. The top panel shows the difference of one RM fitted to all bursts (denoted with `one`) and the weighted average (denoted with `wrm`) for all MJDs. The bottom panel shows the significance of difference. A horizontal black dotted line is drawn at 3σ. The number in parenthesis next to MJDs is the number of bursts detected. The difference, although within 3σ, significantly changes the measured PA. In our observing band, from 550 MHz to 750 MHz, an RM offset of even one unit causes an offset in PA$_\infty$ by over 12 deg. Therefore, we only use one fitted RM for all the bursts to measure PAs. Moreover, we show the RM versus MJD using the measured RM, along with measurements from CHIME/FRB (Mckinven et al. 2023; Ng et al. 2025) and LOFAR (Gopinath et al. 2024) in Figure B.4.

Lastly, our choice of fitting one RM and one PA to all the bursts of an observation, which although works, has to be motivated from the data. To this end, we performed an experiment using all the bursts taken on the observation of MJD 59243, where we have over forty bursts. We apply one RM to all the calibrated bursts and measure the standard deviation of all the measured PAs from every time-sample of every burst. We repeat this procedure for different RMs. When we plot the standard deviation, denoted as ΔPA, against the applied RM, we get a parabola as shown in Figure 1 with black dots. The blue line shows the best fit parabola and the vertical black line is the center of the parabola. The vertical red dashed line is the fitted RM as described in the previous paragraph. With this, we note that one RM exists which reduces the spread in PAs, suggesting that fitting one RM and one PA to all the bursts of an observation is valid. Additionally, Figure B.5 shows by simulation, the spread in PA is only minimized if all the bursts indeed have the same RM and PA. If any one of either RM or PA is not the same, we do not recover any parabola, which further indicates that our attempt is valid.

2.3. Measuring PA

Having measured one RM and one PA for each observation, and having shown that one RM and one PA fits all the bursts within an observation, we bring the fitted PA from center frequency to infinite frequency using Eq. (1). The fitting, as mentioned before, is done with respect to center frequency of 650 MHz. At the same time, we apply the PA calibration correction as determined in Sect. 2.1 to compensate for PA offsets. The PA-calibrated, fitted PA at infinite frequency is denoted by $\langle \mathrm{PA}_\infty \rangle$. The long-term analysis of FRB 20180916B is conducted with $\langle \mathrm{PA}_\infty \rangle$. Alternatively, we can also extract using fitted RM and individual calibrated bursts. We apply the fitted RM to all the bursts of an observation using PAM, and extract PA and PA error time series using PDV The PA measured using PDV is with respect to the center frequency of the band, which can be easily brought to infinite frequency using Eq. (1). Thereafter, we compensate for PA offsets. The PA-calibrated, PA-measurements of individual bursts are denoted by PA$_\infty$.

The average of PA$_\infty$ is consistent with $\langle \mathrm{PA}_\infty \rangle$, that is, the average of PSRCHIVE derived measurements is consistent with the fitted PA. Therefore, we only used $\langle \mathrm{PA}_\infty \rangle$ as a measure of average. Instead of using the error in PA we get while fitting and propagating it, we use the standard deviation of PA$_\infty$ as a measure of error in $\langle \mathrm{PA}_\infty \rangle$. The reason is as follows: the standard deviation of PA measurements from individual bursts would include the spread in PA due to DPHASE variations, intrinsic RM variations as we fit one RM to all the bursts and any intrinsic PA variations. For this same reason, we do not propagate the RM error into ΔPA, as that would have already been considered when taking standard deviation. Moreover, the fit error in PA is only of the order of 1 deg, which we think is heavily underestimated. We tabulate the $\langle \mathrm{PA}_\infty \rangle$ and ΔPA measurements in Table 1. PA$_\infty$ measurements of each of the individual bursts are only presented in electronic form (see Data availability).

2.4. Credibility of measurements

We have had to use different calibration strategies using variety of different sources. The bursts of MJD 59243, 59244, 59274, 59275 and 59568 were calibrated using a single scan

Table 1. Measured properties from every observation.

Phase	Cycle	MJD	Sep h	N	RM rad m^{-2}	ΔRM rad m^{-2}	⟨PA$_\infty$⟩ deg	ΔPA deg	Source	Correction deg
0.355	93	59894	1.3	4	−61.54	0.23	−51.93	3.86	J0139+5814	49.39
0.355	121	60352	0.0	1	−56.48	0.50	−10.49	4.94	J0139+5814	78.47
0.363	118	60303	2.1	11	−58.79	0.53	1.85	7.48	J0139+5814	69.94
0.396	99	59993	1.9	3	−52.63	0.36	−21.08	4.22	B0329+54	54.40
0.397	55	59274	0.0	1	−118.56	0.80	−12.49	3.92	B0329+54	61.42
0.400	73	59568	0.7	10	−68.97	0.48	−26.08	5.27	B0329+54	65.43
0.403	96	59944	2.6	5	−57.61	0.49	−30.65	4.85	B0329+54	47.88
0.453	55	59275	1.3	6	−113.04	0.39	−80.98	4.98	B0329+54	39.86
0.494	53	59243	4.1	39	−115.21	0.27	−35.86	6.27	B0329+54	65.93
0.562	53	59244	0.3	4	−113.64	0.56	−65.21	6.11	B0329+54	57.41

Notes. RM and ⟨PA$_\infty$⟩ refer to Rotation Measure and Position Angle at infinite frequency fitted to all the bursts from one burst. ΔPA refers to the standard deviation of the PA$_\infty$ of all the bursts from an observation. Cycle and Phase correspond to the activity cycle and activity phase of detection of bursts. Sep denotes the time separation between the first and the last burst of the observation. Source and Correction refer to the PA correcting astronomical source and the PA offset measured in degrees. N denotes the number of bursts detected in the observation.

of 3C138 taken at the beginning of the observation. The bursts of MJD 59894, 59944, 60303, 60352 were calibrated using that noise diode scan that is nearest to when the burst occurred. The noise diode failed during the observation of MJD 59993. Therefore, the bursts of that observation were calibrated using the unpolarized quasar 3C48 and the PSR J0139+5814 pulsar following procedure described in SB24.

From the multiple noise diode scans taken within one observation but on different MJDs, in addition to the deviations from linear model of DPHASE (Figure A.3), we also observe variability in DPHASE data of one calibration scan to another (even with a separation of less than 30 minutes), although which is not significant enough to cause a change in linear DPHASE modeling and its linear parameters. Figure A.4 shows the variability as the difference between the DPHASE data of first scan and that of the consecutive scans for every observation. While we only noted the deviations and variations in DPHASE in the case of multiple noise diode scans, as DPHASE variations are a property of the observing instrument, we expect our calibration solutions constructed from quasars and pulsars to also suffer from the same issue. However, we reiterate that in spite of these variations, D_{ns} and ψ_r parameters are consistent (Figure A.2) and do not show this variability reconfirming the validity of our calibration solutions.

In light of these instrumental deviations and variations of DPHASE, we investigate the impact this would have on our RM and PA measurements. Narrow band bursts show biases in RM measurements, as noted in Figure B.1. However, broad band bursts do not show those biases, as DPHASE deviations do not mimic Faraday rotation since they are not linear in λ^2. We checked this by simulating bursts with known RM, PA and no structure, and superimposing the DPHASE deviations (as shown in Figure A.3) into simulated bursts' PA as a function of frequency. Then, we recovered the true RM and PA, with differences in RM $\lesssim 0.2\,\mathrm{rad\,m^{-2}}$ and PA $\lesssim 0.4$ deg, from all the simulated bursts which reaffirms us that broad band bursts are robust to DPHASE deviations. Having shown that broad band bursts are immune to DPHASE deviations, and since we fit for one RM and one PA using all the bursts of an observation, we are mimicking broad band bursts. To visualize this, we computed the cumulative distribution of the frequency spans of bursts detected within an observation in Figure B.6. The black bold line shows the cumulative uniform distribution over the frequency band. The collection of bursts from any observation occupies the whole band and thus behaves similar to a broad band burst and must be immune to DPHASE deviations. Therefore, we compare ⟨PA$_\infty$⟩ across observations, but since our fitting procedure does not take DPHASE deviations into account, which would manifest as colored noise when QU-fitting, there might be some bias. So, we err on the side of caution and only treat ⟨PA$_\infty$⟩ variability across observations at this point as preliminary. Accounting for the bias to robustly study the PA variability across observations will be taken up in a future work.

3. PA variability

We divided our discussion on PA variability in two parts: (i) intra-observation variability includes changes from burst to burst within a single observation (typically 2–4 hours) and (ii) inter-observation variability presents long-term changes on timescales ≥ day.

3.1. Intra-observation

In order to investigate burst-to-burst PA variations within an observation, we plot the PA$_\infty$ time series of every burst consecutively with different colors for different bursts in individual subplots for each observation in Figure 2. The PA$_\infty$ time series are rotated by -⟨PA$_\infty$⟩ from Table 1 so that they are all centered at 0. The gray shaded region is the 1σ error as presented in Table 1. Since PA$_\infty$ is plotted one after the other, there is no time-axis as such. It is simply concatenating PA$_\infty$ time series of bursts of an observation and plotting them with different colors. We note that PA$_\infty$ measurements are consistent with a single value even on the timescale of hours. This is also evident from the fact that we were able to fit all the bursts with a single PA and RM value (Sect. 2.2). That is, there is no sign of secular variability when the time separation between the bursts is of the order of hours (the "Sep" column in Table 1 provides the time separations). Since the maximum time separation in our dataset is about four hours (MJD 59243), we report an upper limit on variations of PA$_\infty$to be ≤7 deg within 4 hours (ΔPA of MJD 59243 from Table 1), and moreover, we note that this upper limit holds for all MJDs.

3.2. Inter-observation

We start with a reminder that all inter observation PA variability is preliminary at this point. We first study the PA variability

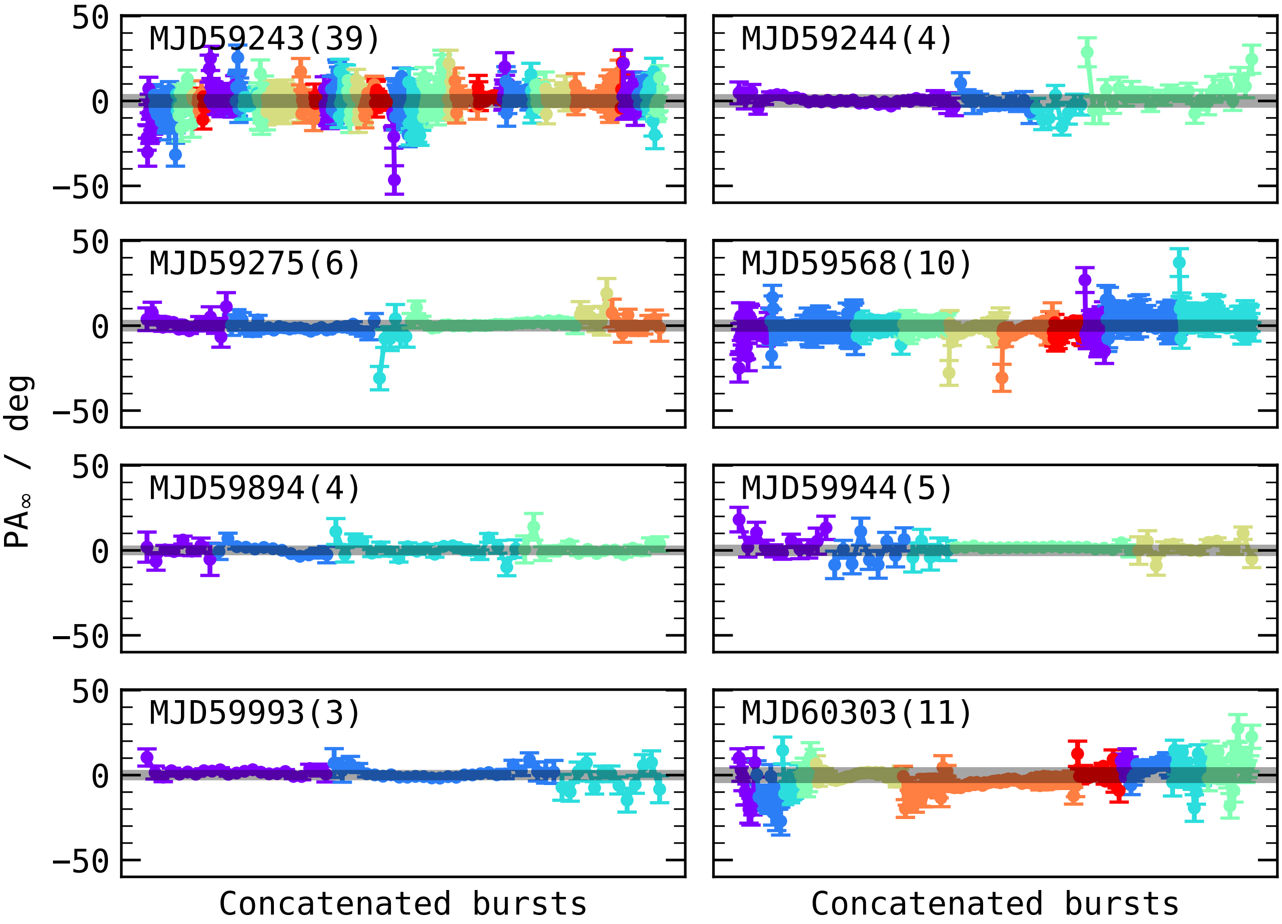

Fig. 2. PA_∞ values of every time sample of each burst plotted one after the another in individual subplots for every MJD. Each PA_∞ has been rotated by $\langle PA_\infty \rangle$ taken from Table 1. The different colors indicate different bursts. The shaded region around it is ΔPA, as reported in Tab. 1. The top left text in each subplot is the corresponding MJD and the number of bursts in parenthesis.

directly over MJD and over activity phase. PA variability could be tied with the periodicity of the FRB and must also be studied accordingly. The periodicity allows us to break time into an activity cycle and activity phase. PA can be independently varying over both activity phase and activity cycle. To disentangle both notions of variability, we followed the logic of studying PA variability by keeping either the activity phase or activity cycle constant and varying the other. Therefore, in the following subsections, we study the PA variations along three fronts: (i) the complete dataset versus MJD; (ii) the complete datasets, as well as measurements within a single activity cycle (intra-cycle), versus activity phase; and lastly (iii) measurements taken around the same activity phase (inter-cycle). In all the above-mentioned cases, $\langle PA_\infty \rangle$ measured across multiple observations are compared. Which, as already mentioned in Sect. 2.4, might possibly carry some bias. Therefore, we caution from overly interpreting the results at this point.

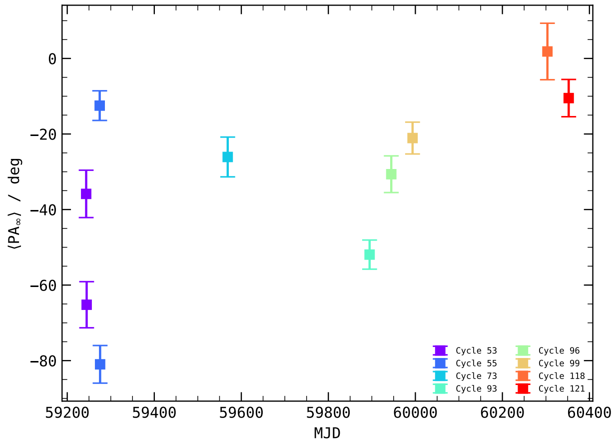

Fig. 3. $\langle PA_\infty \rangle$ versus MJD. The points are color coded according to their corresponding activity cycle.

3.2.1. PA versus MJD

Figure 3 shows $\langle PA_\infty \rangle$ versus MJD. The colors indicate different activity cycles of the measurements, and the color-scheme used here is the same throughout the paper. We emphasize again here that we have corrected for long-term instrumental PA variation by aligning the PA swings of PSR B0329+54 and PSR J0139+5814 at different times (see Sect. 2.1 and Figure A.1). For FRB 20180916B, we observe a total spread in PA of about 80 deg over the ~1100 days of monitoring, but $\langle PA_\infty \rangle$ versus MJD does not show clear evidence of a linear trend. However, we note that if there exists variability as a function of activity Phase and/or activity cycle, looking at PA against MJD may hide clear trends of this variability.

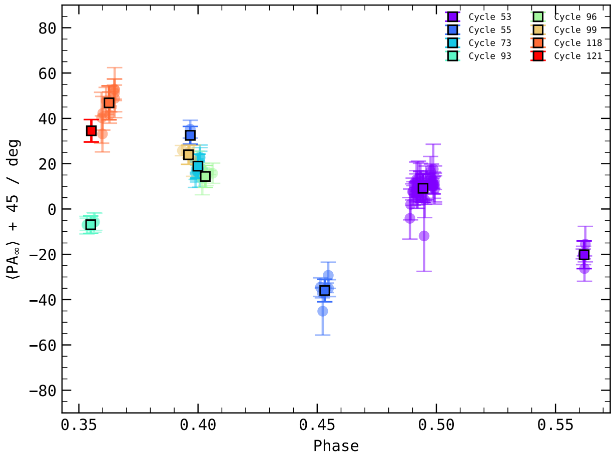

Fig. 4. $\langle \mathrm{PA}_\infty \rangle$ versus activity phase of FRB 20180916B plotted with markers with a black border. PA_∞ versus activity phase of the bursts plotted with faint markers. Both PA_∞ and $\langle \mathrm{PA}_\infty \rangle$ have been rotated by 45 deg.

3.2.2. PA versus phase

We plot $\langle \mathrm{PA}_\infty \rangle$ and PA_∞ versus activity phase in Figure 4 as markers with black border and faint markers respectively. We note that to avoid PA wrap arounds, we have rotated PA_∞ and $\langle \mathrm{PA}_\infty \rangle$ by 45 deg. The range of $\langle \mathrm{PA}_\infty \rangle$ measurements in both the datasets is around 80 deg. Although, we have 10 measurements, they occur only at five distinct activity phases.

We have two instances with more than one measurement from the same activity cycle (see Table 1). Two observations were made in (i) Cycle-53 on MJD 59243 and 59244 and (ii) Cycle-55 on MJD 59274 and 59275. Cycle-53 observation pair phase ranges from 0.494 to 0.562 (26.52 hours), whereas Cycle-55 observation pair ranges from 0.397 to 0.453 (22.13 hours). We study the variability within the same activity cycle, which we call intra-cycle variability, using the rate of change of PA. In Cycles 53 and 55, the rates of change of PA computes to be −58.8 and −29.2 deg activity phase^{-1} respectively, or in regular units, −1.0 and −3.2 deg h^{-1} respectively or For both the pairs, the significance of variability is at least 3σ. Interestingly, we note that rates of change of PA is different for these two pairs, which suggests rate of intra-cycle variability depends on activity phase.

We test if intra-cycle variability is consistent with the observed non-variability of $\mathrm{PA}_\infty \leq 7$ deg over four hours of observation of MJD 59243 (activity cycle 53, see Sect. 3.1 for details). With the intra-cycle variability slope of −1.0 deg h^{-1} from Cycle-53, in a span of four hours, we expect to see variations of around 4 deg. The ΔPA of MJD 59243 observation (whose session was four hours in duration) is 6.27 deg, which means observed intra-cycle variation is consistent at 1.5σ with our non-variability of PA observation. This suggests that PA is varying against activity phase slowly enough that on timescales of four hours or less, the PA appears to be constant.

3.2.3. Inter-cycle at a constant phase

Two of the five clusters in activity phase have more than one $\langle \mathrm{PA}_\infty \rangle$ measurement. $\langle \mathrm{PA}_\infty \rangle$ measurements of MJD 59894, 60303, and 60352 are within a phase separation of 0.008 (three hours), with a mean phase of 0.359. We denote this cluster by $\mathbf{G}_1$. Also, $\langle \mathrm{PA}_\infty \rangle$ measurements of MJD 59274, 59568, 59944 and 59993 all are within a maximum phase separation of 0.006 (2.75 hours) and a mean phase of 0.400, which we denote by $\mathbf{G}_2$. We plot the $\langle \mathrm{PA}_\infty \rangle$ versus activity cycle for both the clusters in Figure 5 in blue and red respectively. The top x-axis is in MJD since the reference MJD of the periodicity model of FRB 20180916B. The $\langle \mathrm{PA}_\infty \rangle$ measurements where we only have one burst are shown with black markers. We find that for both the clusters there is a clear sign of variability. That is, $\langle \mathrm{PA}_\infty \rangle$ measurements taken at the same activity phase varies against activity cycle. While we do not see a clear trend, if we ignore the $\langle \mathrm{PA}_\infty \rangle$ measurements with only one burst (shown with black markers), we still notice variability. Therefore, we report inter-cycle variability and wait until more $\langle \mathrm{PA}_\infty \rangle$ measurements are made at similar activity phases to further characterize it.

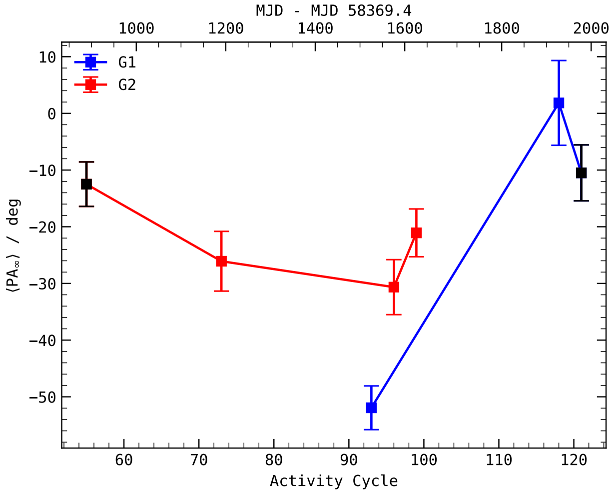

Fig. 5. $\langle \mathrm{PA}_\infty \rangle$ versus activity cycle for the two phase clusters: $\mathbf{G}_1$ and $\mathbf{G}_2$. $\mathbf{G}_1$ refers to the $\langle \mathrm{PA}_\infty \rangle$ measurements made at around Phase 0.359 (MJD 59894, 60303 and 60352) and $\mathbf{G}_2$ at around Phase 0.400 (MJD 59274, 59568, 59944, 59993). See Sect. 3.2. The black markers are used to denote those $\langle \mathrm{PA}_\infty \rangle$ measurements with only one burst. The top x-axis shows MJD of the $\langle \mathrm{PA}_\infty \rangle$ measurements. We emphasize that the reference MJD of the top x-axis is that of the periodicity model of FRB 20180916B.

Simply, as an order of magnitude estimate, we can compute the rates of change from the two clusters. The rates of change is around ∼0.1 deg day^{-1} For comparison, when studying $\langle \mathrm{PA}_\infty \rangle$ versus MJD, we noted 80 deg change over 1100 days, which amounts to a rate of change of 0.07 deg day^{-1} which is partly consistent with what we measure here. The inter-cycle variability is of the order of deg day^{-1}, whereas the intra-cycle variability is of the order of deg h^{-1}, which suggests there are two scales of variability. Having said so, we do not have sufficient measurements to fully study the inter-cycle variability. It could be simply PA variability linear in time which does not follow the periodicity of the source. At this point, we cannot comment further. We again remind that we have performed PA calibration and have performed PA-calibration, that is accounted for any inter-observation PA offsets using PA-sweeps of pulsars (Sect. 2.1 and Figure A.1).

4. Constraints on progenitor models

In this section we connect the observed PA variability in conjunction with the periodicity of the FRB 20180916B, to what is predicted by various progenitor models and place constraints on the geometry of the models. We only focus on neutron star progenitor models, that is, where bursts originate from the magnetosphere of the neutron stars. Since they originate from the magnetosphere, the PA of the bursts carry the information about the dynamics of the neutron stars. Specifically, we test various progenitor models against the following observations:

O$_1$ Non-variability or limited variability of PAs ≤ 7 deg for up to at least four hours at all activity phases
O$_2$ Intra-cycle variability with a rate of $\sim$1 deg h^{-1} or 80 deg over 0.2 Phase units
O$_3$ Tentative detection of inter cycle variability with a variable rate of $\sim$0.1 deg day^{-1} which depends on activity phase

Since, we are treating all inter observation PA variability results as preliminary, we nevertheless discuss them in terms of models, but refrain from ruling out any model solely based on them at the moment (also see Sect. 2.4).

4.1. Slow rotation

In a slowly rotating neutron star model for FRB 20180916B, the rotational period is the period of the FRB (16.34 days; Beniamini et al. 2020; Li & Zanazzi 2021). It is analogous to a typical pulsar except that the period is extremely large. We understand the geometry the following way: an inertial frame is attached to the center of the neutron star such that the rotation axis is along the Z-axis (toward up), X-axis is toward right, and the observer is located somewhere in the XZ-plane. We suppose that burst emission is directed along an arbitrary axis co-rotating with the neutron star, which we call the emission axis. We illustrate the geometry in Figure 6 (*left*). The PA is the angle between the planes formed by observer and rotation axis, and observer and emission axis. It is illustrated in the same figure. Moreover, the burst emission has the same PA along the emission axis at all times. In case of pulsars, this emission axis is the dipolar magnetic axis and the emission mechanism is curvature radiation (Mitra et al. 2024). As the neutron star rotates, the projection of the emission axis on the sky changes. This change in projection of the emission axis is tracked by the PA of the observed emission. We note that this change in PA is not caused by the emission mechanism, but due to the rotation motion, hence is dynamical and geometrical in nature. The projection is modeled with RVM (Everett & Weisberg 2001):

$$\tan(\mathrm{PA}_0 - \mathrm{PA}) = \frac{\sin(\alpha)\sin(\phi - \phi_0)}{\sin(\zeta)\cos(\alpha) - \cos(\zeta)\sin(\alpha)\cos(\phi - \phi_0)}. \quad (2)$$

Here, α and ϕ_0 are the magnetic axis co-latitude and longitude in the inertial frame respectively. ζ is the co-latitude of the observer, which is also known as viewing angle and PA$_0$ is the projection of the spin-vector in the sky. The magnetic field need not just be dipolar; axis-symmetric multi-pole magnetic fields also follow RVM (Qiu et al. 2023). Therefore, our testing is still valid even if our assumption of dipolar magnetic field does not hold. However, the same cannot be said for general multi-pole magnetic fields.

In this model, since the period is large, the PA shows a slow rate of change, which satisfies **O**$_1$. In addition, we expect intra-cycle PA variations, which satisfies **O**$_2$. Modeling of the intra-cycle PA variations with more measurements would help further constrain this model. If the intra-cycle PA variations are RVM-like, the magnetic field configuration would be dipole-like. However, in any case, there would be no variations in PA across the activity cycle at the same activity phase, contrary to **O**$_3$. In other words, according to this model, all the variations seen in **G**$_1$ and **G**$_2$ are random. This would be equivalent to the random variations in PAs of individual pulses of pulsars compared to that of the integrated pulse at the same phase (See Figure 2 Johnston et al. 2024). (Also see Figure 1 of Mitra et al. (2007) where the PA values show scatter about the RVM curve.) Lastly, we observed the range of $\langle \mathrm{PA}_\infty \rangle$ measurements span across 80 deg. Within the RVM model, the range of PA values is decided by α. A larger α leads to a larger range of PA values. However, with $\langle \mathrm{PA}_\infty \rangle$ measurements at only five distinct activity phases, any RVM modeling or constraining α would not be robust. Therefore, we defer actual RVM fitting to future work.

4.2. Fast precession

In the fast precession model for FRB 20180916B, the burst emitting neutron star is rotating with a spin period and is also freely precessing with a precessional period (Zanazzi & Lai 2020; Li & Zanazzi 2021). Free precession implies there are no resultant torques on the compact object, which implies, the angular momentum is a constant of motion. The precessional period is assumed to be the activity period of the FRB (16.34 days), and the spin period is predicted to be of the order of seconds (Levin et al. 2020; Zanazzi & Lai 2020). Our geometry for precession is identical to that presented in Li & Zanazzi (2021). The geometry of this case is described as follows: Instead of inertial frame, we attach a body fixed frame at the center of the neutron star such that the precession axis (or the symmetric axis, the axis along which the body is symmetric) is along Z-axis and the emission region (which is fixed in body fixed frame) is in XZ-plane. The rotation axis is at a separation of δ (θ in Jones & Andersson 2001). We make a reasonable assumption that rotation dominates the angular momentum, thereby, the separation between the rotation axis and angular momentum axis ($\hat{\theta}$ in Jones & Andersson 2001) is extremely small, and is of the order of the square of the deformity of the neutron star. Then, PA is defined as the angle between the planes formed by observer and rotation axis, and observer and emission axis. Because of our assumption, this PA definition is with respect to a constant reference axis (like angular momentum axis). δ is treated as a free parameter, which is known as the wobble angle (Jones & Andersson 2001). We provide a cartoon illustration in Figure 6 (*right*). The observer in the body fixed frame executes the precession dynamics, which can be understood as the observer rotating about the rotation axis with rotational period and the rotation axis rotating about the precession axis with precessional period. If we define the observer to be at ζ separation from rotation axis (like in Sect. 4.1), we note that co-latitude of observer as seen in the body fixed frame changes from $|\zeta - \delta|$ to $\zeta + \delta$ within a rotational period. This co-latitude variability happens for every rotational period at every precessional phase. Ultimately, it causes PA variations over the rotational period timescales.

We observed that PA is $\leq$7 deg on timescale of at least four hours (**O**$_1$) for multiple observations. If the emission region was such that it only partially overlapped with the trajectory of observer, we would have been able to recover the periodicity. Since no short timescale periodicity has been found in FRB 20180916B, we suggest that the emission region is large enough to not cause any periodicity signature. We also know that the modulation of PA values constrains α, which gives us the constraint $\alpha \ll \zeta$. The maximum range of α is $|\delta + \theta|$, and therefore, $|\delta + \theta| \ll \zeta$. If the variability of PA is constrained to be $\leq$7 deg (**O**$_1$), both δ and $\theta \lesssim 10$ deg, which causes $\zeta \gtrsim 30$ deg. In words, the rotation axis and emission axis are in close proximity to the precession axis, but the observer is far away from the rotation axis.

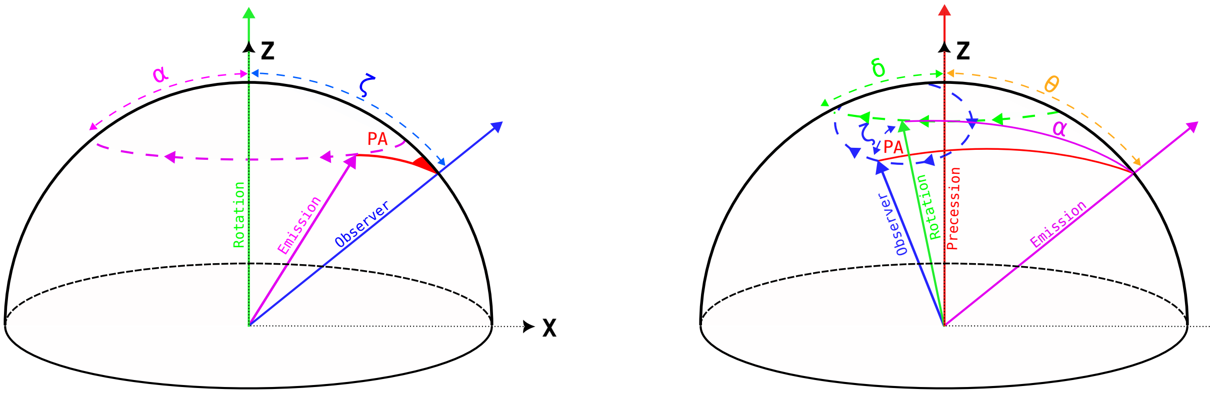

Fig. 6. Illustration of rotation (*left*) and precession (*right*) geometries considered here. The left image is shown in the inertial coordinate system, which is fixed at the center of the neutron star. The right image is shown in the body fixed coordinate system. The *X*-axis is toward the right. The *Z*-axis is up. In case of rotation (*left*), the rotation axis is along *Z*-axis. In case of precession (*right*), the precession axis (symmetric axis) is along *Z*-axis. Motion is illustrated with large dashed line having arrows at regular intervals. The measured PA is appropriately marked.

Firstly, such a configuration cannot produce a modulation of 80 deg of $\langle \text{PA}_\infty \rangle$ over activity phase (Figure 4). In addition, a fast precession model also cannot explain inter cycle variation ($\mathbf{O}_3$). The geometry of the entire system at any activity phase is identical for all activity cycles, which implies the observed PAs cannot be different for different activity cycles at the same activity phase. The above inter-observation PA variability results directly make fast precession extremely unlikely. Regardless, even by only relying on intra-observation PA non-variability result ($\mathbf{O}_1$), we can concretely rule out fast precession model. With the above-mentioned geometric constraint from $\mathbf{O}_1$, it is almost impossible to provide an emission region which is large enough to cover all the spin-phases but which can only provide 30% duty cycle in activity period.

4.3. Slow precession

The slow precession model for FRB 20180916B is similar to the fast precession model, except that the spin period is the activity period of the FRB (that is, 16.34 days) and the precessional period is much longer than the activity period. Therefore, this model is the equivalent to a combination of slow rotation, which explains non-variability and intra-cycle variability ($\mathbf{O}_1$ and $\mathbf{O}_2$), and free precession, invoked to explain inter-cycle variability ($\mathbf{O}_3$). However, precession would cause a gradual change in the active window that has not been seen, which implies this model cannot directly explain the periodicity.

An alternate test for this model would be to study the inter-cycle variability. If that variability is indeed caused by precession, PAs at the same activity phase would exhibit sinusoidal variations with a period given by the precessional period, and the range of variation would be of the order of δ (defined in Sect. 4.2). We provide a simulation of this effect in Appendix C. We cannot yet estimate the precession period. However, a lower limit of the precessional period would be the maximum time span of activity phase clusters – $\mathbf{G}_1$ and $\mathbf{G}_2$, as we do not observe a full period yet, which is around 800 days. Now, if we assume an ellipticity of 10^{-4} (Levin et al. 2020) or 10^{-6} – 10^{-8} (Desvignes et al. 2024), and a rotational period of 16.34 days, the precessional period is $\sim\frac{10^5}{\cos(\delta)} - \frac{10^{10}}{\cos(\delta)}$ days. Even if we take the smallest precessional period of $\sim 10^5$ days, a maximum time span of 800 days would only mean a precessional phase span of 3 deg. For us to observe at least 50 deg of $\langle \text{PA}_\infty \rangle$ variation within the 3 deg precessional phase span suggests an extremely large sinusoidal amplitude or δ, which is highly unlikely. Therefore, we conclude that maximum precessional period would be much less than $\sim 10^5$ days. We defer the attempt to accurately measure precessional period until inter cycle variability is measured with more significance and its variability is characterized.

4.4. Binary models

There are various binary models proposed to explain the periodicity and chromaticity of FRB 20180916B, but in this work, we only focus on such models where one of the bodies is a burst emitting compact object (Ioka & Zhang 2020; Wada et al. 2021; Li et al. 2021). For instance, in Ioka & Zhang (2020) and Wada et al. (2021), the emitting object is a neutron star, while in Li et al. (2021) the central object is a Be-type star with a disk and the bursts arrive from a compact object orbiting the star. In all cases, the period of the binary orbit is assumed to be the activity period of the FRB (16.34 days).

Whether or not PAs carry any information about the binary motion depends on whether there is coupling between the emitting object's angular momentum and the system's orbital angular momentum (Hamilton & Sarazin 1982). In point mass Keplerian dynamics, there is no such coupling. The orientations of the objects are not governed by their binary motion. If PAs track the instantaneous orientation of the object, such PAs would not carry any information about the binary motion and thus could not be used to probe binary models. However, if we assume a binary model scenario where the PA of the emitted burst is purely a function of the true anomaly of the burst emitting object, we can perform some model testing. As the orbital period is the same as the activity period, the predicted intra-cycle PA variability will match the observed variability. Then to explain inter cycle variability, we would need to invoke some form of binary precession. Modeling and testing such scenarios is a work in itself and requires much more measurements for any meaningful test. Hence, it will be taken up in future work.

That said, there are PA models for relativistic spin precession (Kramer & Wex 2009), which have been used for Double Neutron Star systems such as PSR J1906+0746 (Desvignes et al. 2019) and PSR J1946+2052 (Meng et al. 2024). In this case, we suppose the orbital period to be activity Period of the FRB. The lack of any PA variations over rotational period timescales constrains α, just like in the case of Fast precession (Sect. 4.2). In addition, due to relativistic spin precession, the projection of

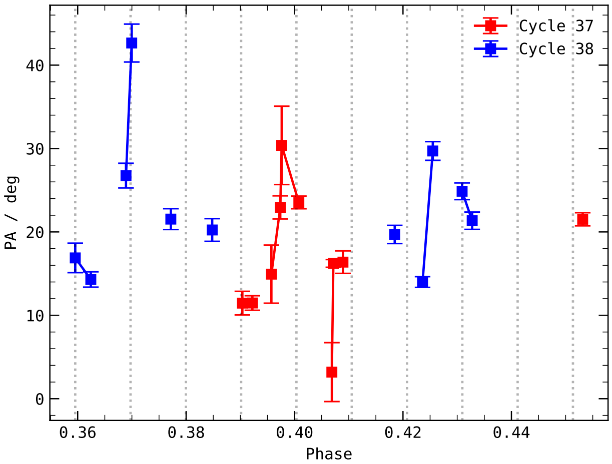

Fig. 7. Position angle measurements of bursts detected by APERTIF at 1370 MHz in activity cycle-37 and -38 (Pastor-Marazuela et al. 2021). Line connecting squares denotes measurements taken in the same observing session. The black dotted line is drawn for every four hours of phase-separation.

the spin vector (Ψ_0) changes all the time throughout the orbit on spin-precession timescale (Eq. 6; Meng et al. 2024). That is, Ψ_0 is periodic with precessional period and does not depend on orbital phase (which is activity phase in this case). However, we do not see any such signature in $\langle \mathrm{PA}_\infty \rangle$ versus MJD (Sect. 3.2.1) and we know there are two scales of variability – intra-cycle and inter cycle are tied with the periodicity of the FRB (orbital period). Therefore, we do not suppose a relativistic spin precession model can explain the observed PA variations.

5. Discussions

5.1. APERTIF PA sample

Pastor-Marazuela et al. (2021) measured PAs from the bursts detected using APERTIF at 1370 MHz at different activity phases and cycles. They report a range of PA values of around 44 deg over a phase span of 0.1 (1.5 days), while we report a range of $\langle \mathrm{PA}_\infty \rangle$ values of around 80 deg (Figure 4 and Sect. 3.2.2) and a phase span of 0.2 (3.25 days). Moreover, Pastor-Marazuela et al. (2021) have multiple PA measurements within Cycle-37 and -38, which we use here to test intra-cycle variability. We plot the PA measurements of Cycle-37 (in red) and Cycle-38 (in blue) against activity phase in Figure 7. We connect those measurements which are done in the same observing session with a line. Moreover, we add vertical dotted lines at intervals of 4 hours starting from the smallest phase.

Unlike in our analysis, Pastor-Marazuela et al. (2021) used a singular RM value for all the bursts, which were detected across multiple observations and cycles, and in addition, the bursts have been absolutely calibrated, i.e., PAs can be studied across Phase and Cycle. While we observe PA variability <7 deg over four hour timescale, Pastor-Marazuela et al. (2021) observes much rapid variability on these timescales. Furthermore, PAs measured from bursts within the same observing epoch also exhibit large variability, contrary to what we report. We cannot test inter cycle variability as the Pastor-Marazuela et al. (2021) dataset does not multiple measurements at the same activity phase.

This inconsistency can be explained in the following way. The PA measurements of Pastor-Marazuela et al. (2021) have been made after correcting all the bursts with the same RM of $-115\,\mathrm{rad\,m^{-2}}$. All the measurements were made when the RM was only stochastically varying (Mckinven et al. 2023). The standard deviation of the RM measurements in the stochastic regime (before MJD 59200) is about $3\,\mathrm{rad\,m^{-2}}$ (Mckinven et al. 2023). PA measurements are at frequency of 1370 MHz, which even for a RM variability of the order of $3\,\mathrm{rad\,m^{-2}}$ causes a PA variability of about 8 deg. Therefore, the observed variability by Pastor-Marazuela et al. (2021) could be due to the use of a single RM for all observations rather than observation-specific RMs as used in this analysis.

5.2. Her X-1

Her X-1 is an intermediate mass accreting X-ray binary pulsar system in which the neutron star spins with a period of 1.24 seconds, the orbital period is 1.70 days and the whole system also shows a superorbital period of 35 days. The super-orbital period in Her X-1 has been attributed to a precessing accretions disk (see, e.g., Katz 1973). In recent work by Heyl et al. (2024), neutron star's polarization profile was modeled with RVM at different times, through which the superorbital periodicity is explained using complex rotational dynamics involving rotation and precession of the neutron star, accretion disk and the companion. The activity of Her X-1 switches states of activity multiple times over the superorbital periodicity (Scott et al. 2000). It has two ON-states known in literature as main-on and short-on. According to Heyl et al. (2024), the activity variability of Her X-1 is caused by the crustal precession, which brings the active emission region into the line of sight of the observer at specific precessional phase. The extent of active region along the line of sight determines the scale and length of activity seen. We can immediately draw many parallels between Her X-1 and FRB 20180916B. Firstly, the rate variability over superorbital period is analogous to rate variability seen over active window (Pastor-Marazuela et al. 2021, SB24). Moreover, if the observer sees different emission regions at different phases, and if such emission regions emit at different frequencies, we could directly also explain chromaticity (c.f. Li & Zanazzi 2021).

The superorbital periodicity of Her X-1 is known to be stable (Staubert et al. 2009). If the cause of that periodicity is indeed precession, one would assume various damping mechanisms to be at play, which would lengthen the period with time (Katz 2021). However, Heyl et al. (2024) show how torque interactions between disk and the star balance out the opposing torques such that the resultant motion is effectively torque free. Now compare with FRB 20180916B for which Sand et al. (2023) and Lan et al. (2024) report that the period of FRB 20180916B is stable over at least two years.

Heyl et al. (2024) notes a change of about 8 deg in the Ψ_0 between two main-on states, which are separated by over an year (Table 1, χ_p column of Heyl et al. 2024). The PA variability gives a slope of $0.02\,\mathrm{deg\,day^{-1}}$. This is largely consistent with the inter-cycle variability slopes we measure in Sect. 3.2. Heyl et al. (2024) suggest that this variability is caused by a change in the angular momentum. While it is unclear at the moment what could be causing the angular momentum changes, we note that in free-precession regime the angular momentum is a constant of motion, as there are no torques involved. As noted in the previous paragraph, even if there are multiple torques at play and if all the torques balance out, the resulting system can maintain its period and also change its angular momentum.

Her X-1 is observed in optical and X-rays, with only a marginal detection in radio at 9 GHz(van den Eijnden et al. 2018). If FRB 20180916B is a source similar to Her X-1, we should expect to see temporal variability of optical and X-ray light curves over rotational and/or binary period timescales. This temporal variability should be persistent irrespective of the state of FRB 20180916B in radio. However, no such optical or X-ray emission is detected. One reason could be the burst emission is beamed elsewhere. Although more likely, it could be due to large distance of FRB 20180916B (140 Mpc) compared with that of Her X-1 (7 kpc). If we assume a X-ray luminosity of $\sim 10^{37}$ erg s^{-1} for Her X-1(Brecher 1972), and if we place Her X-1-like source at the distance of FRB 20180916B, the observed X-ray luminosity is ten times less than the upper limit provided by Swift-BAT (Laha et al. 2022). Which suggests that large distance is hindering any X-ray detection. And if Her X-1 (or other such systems that exhibit superorbital periodicity, see Kotze & Charles 2012) are similar to FRB-sources, we should expect to detect FRB-like bursts. In so far, no such bursts have been detected, which could suppose that comparison is not so direct.

5.3. Other repeating FRBs

The current population of known repeating FRBs shows a diversity of PPA behavior within single bursts, as well as between bursts within a single observation. (We reiterate that this is the first robust study of PPA variation between different observations.) FRB 20121102A also exhibits flat PPA curves within individual bursts (Hilmarsson et al. 2021), and notably, bursts within a single observation can also be fit with a single RM and PPA value (Michilli et al. 2018). A small sample of bursts from FRB 20200120E show flat PPAs across a burst but jumps in the PPA value from burst-to-burst (Nimmo et al. 2022). This is in contrast to FRB 20180301A, FRB 20201124A, FRB 2022012A, which show swings in PAs across the duration for some bursts and burst-to-burst variations within an observation (e.g., Luo et al. 2020; Jiang et al. 2022; Zhang et al. 2023). That said, there is evidence that some of this may due to propagation effects through the plasma (Uttarkar et al. 2024; Xu et al. 2022), which complicates the connection between the PPA and the geometry at the emission site.

FRB 20180916B's PPA properties are most similar to FRB 20121102A. Interestingly FRB 20121102A is also the only other repeating FRB with a known activity periodicity (Rajwade et al. 2020; Braga et al. 2025). With a sample size of two, it is difficult to judge whether this is simply a coincidence. Moreover, the host galaxies and local environments of the two sources are different. FRB 20180916B is on the edge of a star forming region within a spiral galaxy and has no associated PRS (Marcote et al. 2020), while FRB 20121102A is in a star forming region in a low metallically dwarf galaxy and has a PRS (Marcote et al. 2017; Tendulkar et al. 2017). If they have the same progenitor, it needs to be able to be present in both these environments.

5.4. Future strategies

Future observing campaigns should focus on studying intra-cycle variability and robustly investigating inter cycle variability. Studying intra-cycle variability requires repeated observations of the source within the same activity cycle for multiple cycles. Investigating inter cycle variability would require us to perform observations at the same activity phase on many different activity cycles. Therefore, in addition to being able to track the source over long times, we would also need a sufficient burst rate to robustly measure the RM and track the PA variability. Given these requirements, we argue that the uGMRT is the first choice for this endeavor. uGMRT can observe the source for around 11 hours continuously on average, which means it would require over ten days to cover the entire 5.1 days active window at 600 MHz. In addition, uGMRT at 650 MHz observes a rate of well over one per hour (SB24).

Performing a long-term PA variability study requires a stable PA reference frame so that we do not introduce any PA offsets. In this study, we test for this stability by using multiple pulsar observations taken on four different epochs. We find agreement between the PA offset found using each of the pulsar PA sweeps when compared to the respective PA reference sweep (see Table A.1). This agreement should be valid throughout the span of the study. Considering that the reference PA frame used here is non-standard, it would be worthwhile to connect the reference PA frame with absolute reference frames such as those defined in Perley & Butler (2013). Such a connection would also be useful as an independent probe of PA validity.

We have to improve our calibration strategy. From this study, we find that deviations from our linear model of DPHASE exist and impact our RM measurements. Therefore, sophisticated calibration strategies could first be developed. Alternatively, we can improve our fitting strategy to include Gaussian Processes that can can account for DPHASE variations to measure unbiased RM and PA estimates. In addition, our procedure of fitting one RM and PA to all the bursts is althought robust, it requires a sufficient number of bursts to perform as expected. Future observing strategies could take that into account and observe the source for sufficiently long duration. All in all, this work seeks to prompt many future work in this direction, and in particular, study such PA variations of other repeating FRBs. Of all the known repeating FRBs, in particular, we want to highlight FRB 20200120E which has been localized to a globular cluster (Kirsten et al. 2022). The properties of the bursts strongly suggest that young pulsar progenitor model produces bursts (Nimmo et al. 2022). If that is the case, PAs of the bursts would already carry an RVM-like signature, which can provide further evidence.

6. Conclusions

We have presented consistent, almost absolute calibrated PA measurements of 84 bursts of FRB 20180916B collected over a time span of 1200 days with the uGMRT at 650 MHz. We have performed a PA calibration (Sect. 2.1 and Figure A.1), showed and fit one RM and one PA to all the bursts from an observation (Sect. 2.2), and measured observation averaged PA and its error from all the observations (Sect. 2.3).

We suggest that PA variability is best understood when studied in conjunction with the periodicity of the FRB. While we report the following findings, we note that possible biases in $\langle \mathrm{PA}_\infty \rangle$ make comparison with $\langle \mathrm{PA}_\infty \rangle$ across different observations only preliminary at this point (Sect. 2.4):

- The variability in PA is constrained to be ≤7 deg over timescales of four hours ($\mathbf{O}_1$) in all observations.
- The PA varies over activity phase, which we referred to as intra-cycle variability, with a variability of $\sim\pm 1\ \mathrm{h}^{-1}$ ($\mathbf{O}_2$) or 80 deg over 0.2 Phase units.
- We also report that the PA varies with activity cycle, which we have studied by using $\langle \mathrm{PA}_\infty \rangle$ measured at the similar activity phases. We call this variability inter-cycle variability, which is of the order of 0.1 deg day^{-1} ($\mathbf{O}_3$).

We are able to place constraints on various dynamical models for the FRB using the above-mentioned findings. Given that our inter-observation PA variability is only preliminary, we tested the models based on $\mathbf{O}_2$ and $\mathbf{O}_3$ but do not rule out any solely based on them.

- A slowly rotating model due to the large rotational period can explain the limited variability over timescales of hours and intra-cycle variability (**O**$_1$ and **O**$_2$). We conclude that a slowly rotating model can explain FRB 20180916B. However, such a model cannot explain inter-cycle variability (**O**$_3$) without suggesting the observed inter-cycle variability is purely caused by random variations.
- Fast precession models predict rotational-timescale PA variability, which is at odds with the non-variability of PA on timescales of hours (**O**$_1$). Moreover, satisfying **O**$_1$ causes the model to contradict the following observations: (i) a lack of any short timescale periodicity, (ii) a 30% duty cycle of the active window, and (iii) observed PA versus activity phase modulation (**O**$_2$). In addition, a fast precession model cannot explain **O**$_3$.
  Therefore, at this point, we successfully rule out the fast precession model.
- The slow precession model is equivalent to the combination of slow rotation and free precession, which can explain **O**$_1$, **O**$_2$, and **O**$_3$. However, under this model, the active window should change with time, which has not been observed. Notwithstanding, this model predicts sinusoidal inter-cycle PA variations that can also be used to test this model with future measurements.
- Testing binary models, where the binary orbital period causes the periodicity of the source, requires models to make PA predictions, which as of now, none of the proposed models do. Testing such models will be done in a future work. Nevertheless, if we suppose FRB 20180916B is similar to a double neutron star system exhibiting relativistic spin precession (Kramer & Wex 2009), **O**$_1$ can constrain the RVM geometry. However, $\langle \mathrm{PA}_\infty \rangle$ variations would not follow the periodicity of the FRB, which contradicts **O**$_2$ and **O**$_3$.

Lastly, we compared FRB 20180916B with the Her X-1 system and highlighted many similarities in Sect. 5.2. The most insightful of them all is the consistency between the rate of PA variability of Her X-1 measured in the X-ray using IXPE (Heyl et al. 2024) and the inter-cycle variability of FRB 20180916B measured in the radio using uGMRT. Continuing the long-term study of PAs of both the systems can possibly provide new avenues to compare and understand both objects.

7. Data availability

All the burst averaged PA$_\infty$ measurements are available at the CDS via `https://cdsarc.cds.unistra.fr/viz-bin/cat/J/A+A/702/A248`. Any other data from this article will be shared on any request to the corresponding author.

Acknowledgements. SB is grateful to Gregory Desvignes for his attention to detail, his comments on this work, and most importantly his patience, all of which greatly improved the quality of the paper. SB also extends his gratitude to the reviewer for their comments. We thank the staff of the GMRT that made these observations possible. GMRT is run by the National Centre for Radio Astrophysics of the Tata Institute of Fundamental Research. VRM gratefully acknowledges the Department of Atomic Energy, Government of India, for its assistance under project No. 12-R&D-TFR-5.02-0700. LGS is a Lise Meitner Independent Max Planck research group leader and acknowledges support from the Max Planck Society.

References

Bailes, M. 2022, Science, 378, abj3043
Beniamini, P., Wadiasingh, Z., & Metzger, B. D. 2020, MNRAS, 496, 3390
Bera, A., James, C. W., Deller, A. T., et al. 2024, ApJ, 969, L29
Bera, A., James, C. W., McKinnon, M. M., et al. 2025, ApJ, 982, 119
Bethapudi, S., Spitler, L. G., Main, R. A., Li, D. Z., & Wharton, R. S. 2023, MNRAS, 524, 3303
Bethapudi, S., Spitler, L. G., Li, D. Z., et al. 2025, A&A, 694, A75
Braga, C. A., Cruces, M., Cassanelli, T., et al. 2025, A&A, 693, A40
Brecher, K. 1972, Nature, 239, 325
Britton, M. C. 2000, ApJ, 532, 1240
CHIME/FRB Collaboration (Andersen, B.C., et al.) 2019, ApJ, 885, L24
Chime/Frb Collaboration (Amiri, M., et al.) 2020, Nature, 582, 351
Desvignes, G., Kramer, M., Lee, K., et al. 2019, Science, 365, 1013
Desvignes, G., Weltevrede, P., Gao, Y., et al. 2024, Nat. Astron., 8, 617
Everett, J. E., & Weisberg, J. M. 2001, ApJ, 553, 341
Gopinath, A., Bassa, C. G., Pleunis, Z., et al. 2024, MNRAS, 527, 9872
Gupta, Y., Ajithkumar, B., Kale, H. S., et al. 2017, Curr. Sci., 113, 707
Hamilton, A. J. S., & Sarazin, G. L. 1982, MNRAS, 198, 59
Heyl, J., Doroshenko, V., González-Caniulef, D., et al. 2024, Nat. Astron., 8, 1047
Hilmarsson, G. H., Michilli, D., Spitler, L. G., et al. 2021, ApJ, 908, L10
Hotan, A. W., van Straten, W., & Manchester, R. N. 2004, PASA, 21, 302
Ioka, K., & Zhang, B. 2020, ApJ, 893, L26
Jiang, J.-C., Wang, W.-Y., Xu, H., et al. 2022, Res. Astron. Astrophys., 22, 124003
Johnston, S., Karastergiou, A., Keith, M. J., et al. 2020, MNRAS, 493, 3608
Johnston, S., Kramer, M., Karastergiou, A., et al. 2023, MNRAS, 520, 4801
Johnston, S., Mitra, D., Keith, M. J., Oswald, L. S., & Karastergiou, A. 2024, MNRAS, 530, 4839
Jones, D. I., & Andersson, N. 2001, MNRAS, 324, 811
Kaspi, V. M., & Beloborodov, A. M. 2017, ARA&A, 55, 261
Katz, J. I. 1973, Nat. Phys. Sci., 246, 87
Katz, J. I. 2021, MNRAS, 502, 4664
Kirsten, F., Marcote, B., Nimmo, K., et al. 2022, Nature, 602, 585
Kotze, M. M., & Charles, P. A. 2012, MNRAS, 420, 1575
Kramer, M., & Wex, N. 2009, Class. Quant. Grav., 26, 073001
Laha, S., Wadiasingh, Z., Parsotan, T., et al. 2022, ApJ, 929, 173
Lan, H.-T., Zhao, Z.-Y., Wei, Y.-J., & Wang, F.-Y. 2024, ApJ, 967, L44
Landau, L. D., & Lifshitz, E. M. 1976, Mechanics, Third Edition: Volume 1 (Course of Theoretical Physics), 3rd edn. (Butterworth-Heinemann)
Levin, Y., Beloborodov, A. M., & Bransgrove, A. 2020, ApJ, 895, L30
Li, D., & Zanazzi, J. J. 2021, ApJ, 909, L25
Li, Q.-C., Yang, Y.-P., Wang, F. Y., et al. 2021, ApJ, 918, L5
Lorimer, D. R., & Kramer, M. 2012, Handbook of Pulsar Astronomy (Cambridge, UK: Cambridge University Press)
Lorimer, D. R., Bailes, M., McLaughlin, M. A., Narkevic, D. J., & Crawford, F. 2007, Science, 318, 777
Luo, R., Wang, B. J., Men, Y. P., et al. 2020, Nature, 586, 693
Marcote, B., Paragi, Z., Hessels, J. W. T., et al. 2017, ApJ, 834, L8
Marcote, B., Nimmo, K., Hessels, J. W. T., et al. 2020, Nature, 577, 190
Mckinven, R., Gaensler, B. M., Michilli, D., et al. 2023, ApJ, 950, 12
Mckinven, R., Bhardwaj, M., Eftekhari, T., et al. 2024, arXiv e-prints [arXiv:2402.09304]
Meng, L., Zhu, W., Kramer, M., et al. 2024, ApJ, 966, 46
Michilli, D., Seymour, A., Hessels, J. W. T., et al. 2018, Nature, 553, 182
Mitra, D., Rankin, J. M., & Gupta, Y. 2007, MNRAS, 379, 932
Mitra, D., Basu, R., & Melikidze, G. I. 2024, Universe, 10, 248
Ng, C., Pandhi, A., Mckinven, R., et al. 2025, ApJ, 982, 154
Nimmo, K., Hessels, J. W. T., Keimpema, A., et al. 2021, Nat. Astron., 5, 594
Nimmo, K., Hessels, J. W. T., Kirsten, F., et al. 2022, Nat. Astron., 6, 393
Pastor-Marazuela, I., Connor, L., van Leeuwen, J., et al. 2021, Nature, 596, 505
Perley, R. A., & Butler, B. J. 2013, ApJS, 206, 16
Petroff, E., Hessels, J. W. T., & Lorimer, D. R. 2019, A&A Rev., 27, 4
Petroff, E., Hessels, J. W. T., & Lorimer, D. R. 2022, A&A Rev., 30, 2
Pleunis, Z., Michilli, D., Bassa, C. G., et al. 2021, ApJ, 911, L3
Qiu, J. L., Tong, H., & Wang, H. G. 2023, ApJ, 958, 78
Radhakrishnan, V., & Cooke, D. J. 1969, Astrophys. Lett., 3, 225
Rajwade, K. M., Mickaliger, M. B., Stappers, B. W., et al. 2020, MNRAS, 495, 3551
Sand, K. R., Faber, J. T., Gajjar, V., et al. 2022, ApJ, 932, 98
Sand, K. R., Breitman, D., Michilli, D., et al. 2023, ApJ, 956, 23
Scott, D. M., Leahy, D. A., & Wilson, R. B. 2000, ApJ, 539, 392
Staubert, R., Klochkov, D., Postnov, K., et al. 2009, A&A, 494, 1025
Swarup, G. 1991, in IAU Colloq. 131: Radio Interferometry. Theory, Techniques, and Applications, eds. T. J. Cornwell, & R. A. Perley, ASP Conf. Ser., 19, 376
Tendulkar, S. P., Bassa, C. G., Cordes, J. M., et al. 2017, ApJ, 834, L7
Uttarkar, P. A., Shannon, R. M., Lower, M. E., et al. 2024, MNRAS, 534, 2485
van den Eijnden, J., Degenaar, N., Russell, T. D., et al. 2018, MNRAS, 473, L141
van Straten, W., & Bailes, M. 2011, PASA, 28, 1
Wada, T., Ioka, K., & Zhang, B. 2021, ApJ, 920, 54
Xu, H., Niu, J. R., Chen, P., et al. 2022, Nature, 609, 685
Zanazzi, J. J., & Lai, D. 2020, ApJ, 892, L15
Zhang, Y.-K., Li, D., Zhang, B., et al. 2023, ApJ, 955, 142

Table A.1. Position angle offsets determined from pulsars PSR B0329+54 and PSR J0139+5814 but from the same observation.

MJD	Correction / deg		
	B0329+54	J0139+5814	Difference
59274	61.42	20.81	40.61
59275	39.86	-1.75	41.62
59944	47.88	2.76	45.13
59993	54.40	10.78	43.62

Notes. Correction column refers to the PA offset to be accounted for. Difference column corresponds to the difference between the PA corrections derived from PSR B0329+54 and PSR J0139+5814.

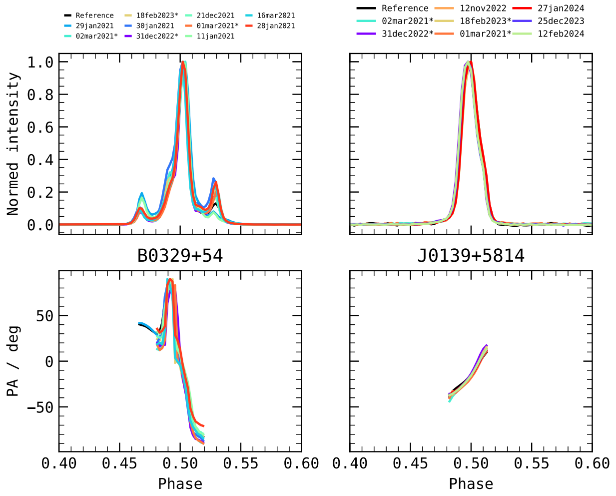

Fig. A.1. Stokes-I integrated frequency averaged pulse profiles (*top*) and PAs against phase (*bottom*) of PSR B0329+54 and PSR J0139+5814 observed at Band 4. See text for details.

Appendix A: Calibration verification

A.1. PA calibration

We plot the phase aligned Stokes-I integrated pulse profiles pulsars PSR B0329+54 and PSR J0139+5814 in the *top* row of Figure A.1. Each line is color-coded by the day of observation. Reference refers to the EPNDB 610 MHz profiles. The *bottom* panel shows the matched PA against phase curves. We verify our PA correction and measurement by noticing that when we transfer PA correction from PSR B0329+54 to PSR J0139+5814 on observations `01mar2021`, `02mar2021`, `12nov2022`, `31dec2022` and `18feb2023`, all the PSR J0139+5814 PA phase curves agree. Such an agreement is not expected and strongly convinces us that we have taken care of any intra-observation PA rotations.

A.2. DPHASE modeling

As uGMRT is an interferometer, it requires phasing of the antennas at regular intervals to produce and maintain a coherent beam on the source. Here, we check if our DPHASE linear modeling is valid from scan to scan within an observation. Figure A.2 shows ψ_r and D_{ns} measurements from multiple noise diode scans taken during multiple observations. The consistency not just in D_{ns}, but also in ψ_r implies uGMRT has a stable polarization response within an observation. Incorrect D_{ns} directly impacts RM measurements and unstable ψ_r affects PA measurements. (Also see Figures B1 and B2 of SB24).

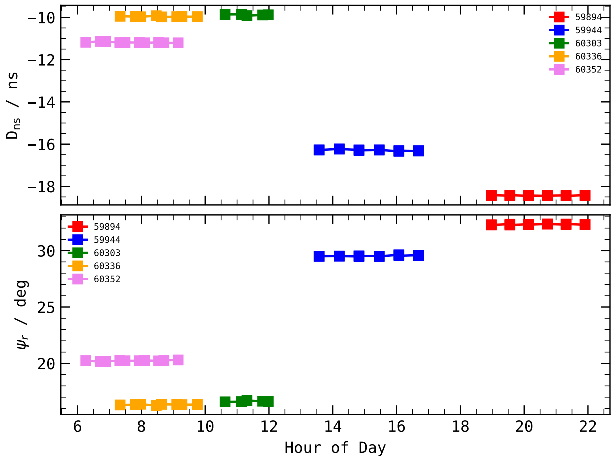

Fig. A.2. Variability of DPHASE parameters, D_{ns} and ψ_r, which are computed using noise diode scans from different MJDs plotted against Hour of Day when the scan was taken. The sign of D_{ns} is purely by convention.

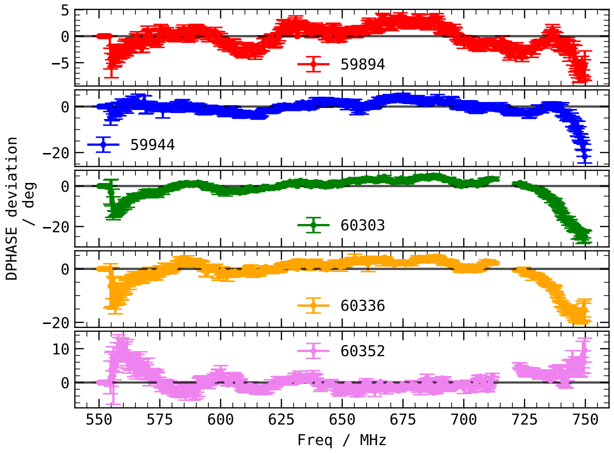

Fig. A.3. Deviations from linear DPHASE modeling shown against frequency using noise diode scans taken on different MJDs. Each panel shows deviation where each DPHASE fitted model is subtracted from the DPHASE data.

The linear DPHASE modeling is simply a model. In every panel of Figure A.3, we show the resultant when linear DPHASE fitted model is subtracted from dataDPHASE for all the noise diode scans we observed in the specific MJD. Since we have multiple noise diode scans, we show the mean and standard deviation computed for every frequency channel with errorbars. We notice departures from the linear model to be of the order of ±15 deg. We also note the following: (i) the deviations are consistent from scan to scan, and (ii) every observation has different form of deviation. As mentioned in the main text, the impact of these unmodeled deviations on the resultant PA is insignificant. When averaged over the entire band, these deviations only change the averaged PA by order of 1 deg.

Even though linear model and deviations from the linear model are consistent from one noise diode scan to another, DPHASE variations from one noise diode scan to another noise diode scan are of the order of ±10 deg. To illustrate this, we subtract the DPHASE data of the first noise diode scan from that of all the remaining noise diodes scans. We show the resultant against frequency for every observation in Figure A.4. We note the following: (i) variations are persistent in all the scans, as seen

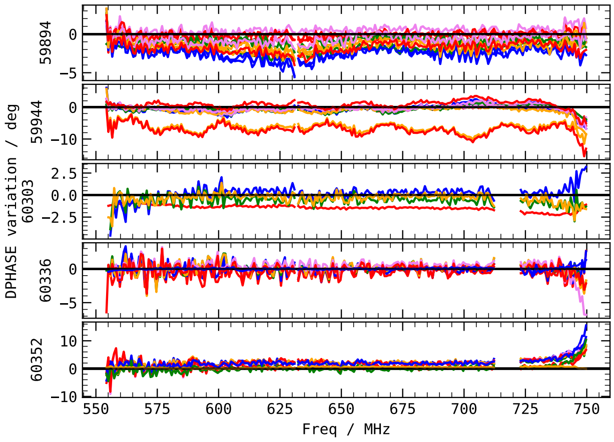

Fig. A.4. Variations of DPHASE from scan to scan shown against frequency for different MJDs. Each panel shows the difference of DPHASE between the first noise diode scan and the n^{th} scan for every observation.

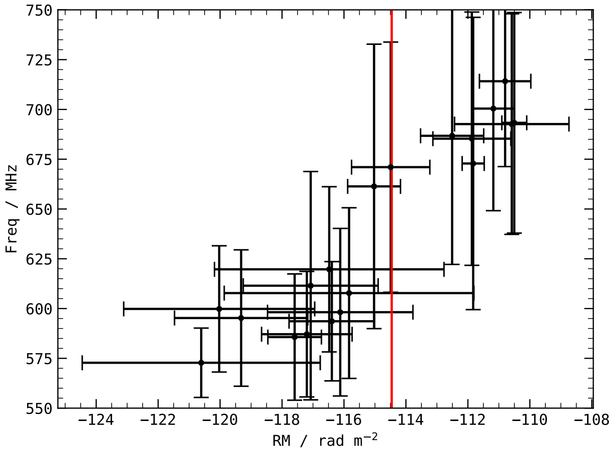

Fig. B.1. Bandwidth versus measured RM for a selection of bursts detected on MJD 59243. The bandwidth is shown as error in y-axis, while x-axis error refers to RM error. The red line is the inverse variance weighted RM average. Bursts have been selected such that they occupy around half of the entire observing band. The observed trend is non physical and caused by DPHASE deviations from the linear model used to calibrate. See Sect. 2.2.

in MJD 60352 at 750 MHz, (ii) variations are drastic as seen in MJD 59944.

Appendix B: Plots

Appendix C: Slow precession simulation

In the inertial coordinate system defined in the main text (Sect. 4.3, only the observer axis and the angular momentum axis are constants of motion. The emission axis, however, varies with time in the inertial frame. The angles between the projections of emission axis and angular momentum axis onto the plane perpendicular to the observer axis is defined as the PA. We note that this requires the emission axis to be in the same inertial frame as the observer axis. The projection of the angular momentum axis onto the same plane serves as a reference PA (PA_0). We bring the emission axis defined in the body-fixed frame using (α and ϕ_0) into inertial frame using Euler angles (ϕ, θ, ψ) where the angles may or may not be functions of time. The Euler angles are defined in ZXZ format. The formalism here is similar to Sect. 37 of Landau & Lifshitz (1976) and that used in Heyl et al. (2024). The $\theta = \delta$, that is, it is the spin misalignment angle. ϕ and ψ track the rotational and precessional phase longitudes respectively. Therefore, ϕ and ψ are defined as the following:

$$\phi = 2\pi \frac{t}{P_{\text{spin}}} + \phi_0$$

$$\psi = 2\pi \frac{t}{P_{\text{pre}}},$$

where t is the time and P_{spin} and P_{pre} are the spin and precessional periods respectively. We note how ϕ_0 can be re-defined as the initial value of the ϕ as both are degenerate. There may also be a precessional phase offset which we have omitted here for simplicity.

For the toy model, we set $\delta = 10$ deg, $\Psi_0 = 0$ deg, $\alpha = 4$ deg, $\phi_0 = 200$ deg and $\zeta = 90$ deg. Moreover, we set spin period and precessional period to be 10 and 1000 days respectively. Then, we measure the PAs for different spin phases and cycles. We illustrate the PA versus spin phase for different spin cycles in Figure C.1 (*top*). The different colors imply different spin cycles. We identify three unique spin phases (which we marked with vertical dotted lines of different colors) and plot the PA versus spin cycle at each of the spin phases in bottom panel of the same figure. We highlight that a slow precession model shows intra-cycle variability (variability over spin phase) and inter-cycle variability in the form of sinusoids (variability over spin cycle). The period of the sinusoids is the same irrespective of the spin phase but the amplitude varies.

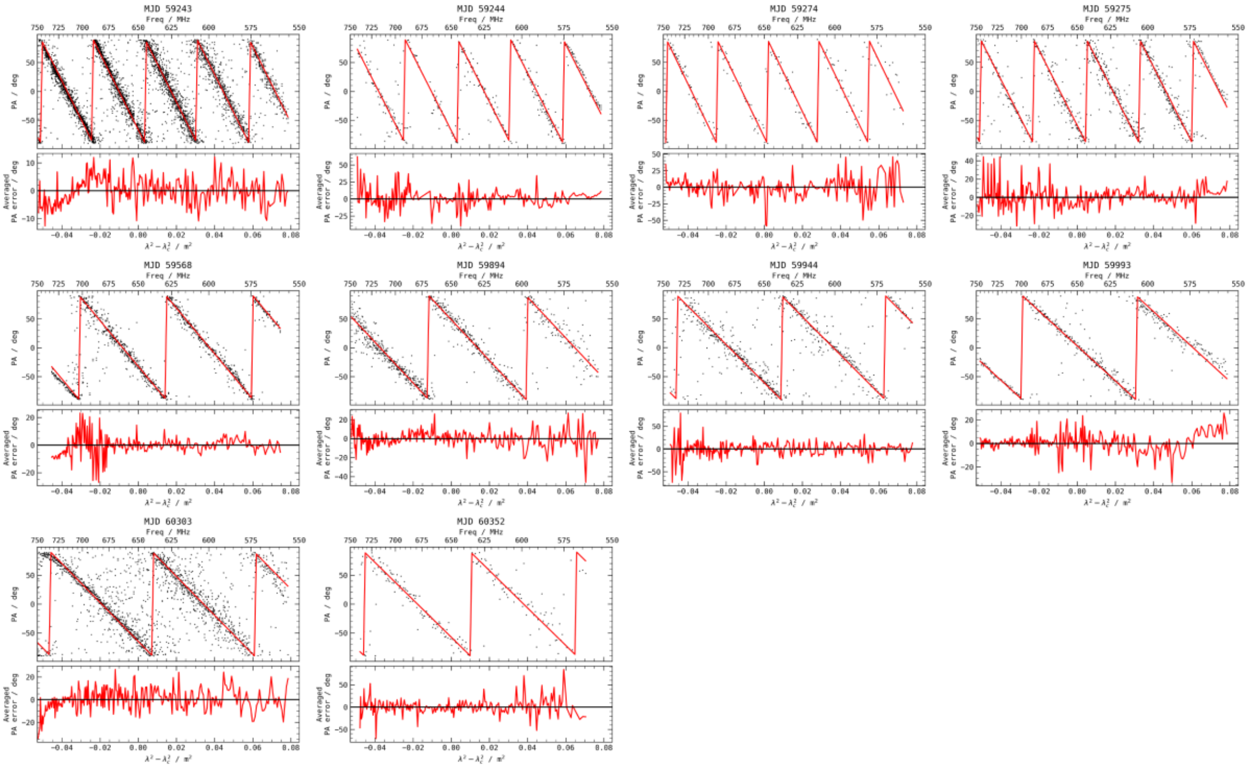

Fig. B.2. Outcomes of fitting one RM and one PA to all the bursts from an observation. Each plot corresponds to one observation. The top panels show PA against $\lambda^2 - \lambda_c^2$ where λ_c is the wavelength of the center frequency of the band. The individual data points are shown with black dots and the red line corresponds to the fitted model. The top x-axis shows frequency in MHz. The bottom panels show averaged error between data and fitted model. The horizontal black line is drawn at 0 deg.

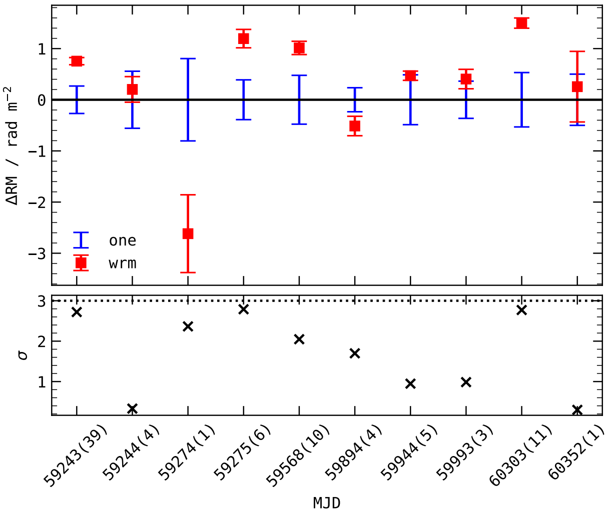

Fig. B.3. Difference between one RM fitted to all bursts in an observation (shown with `one` as legend) and the inverse variance weighted average of each individual QU-fitted RM measurements from each burst of the observation (shown with `wrm` as legend). The top panel only shows the difference with error-bars. The bottom panels shows the significance of difference. The horizontal black dotted line is drawn at 3σ. The number in parenthesis refers to the number of bursts detected in the respective MJD.

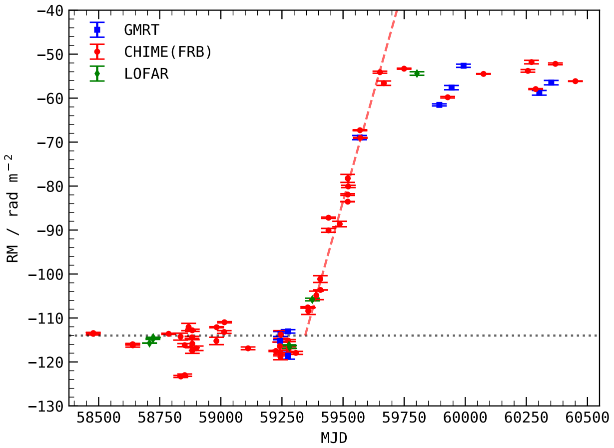

Fig. B.4. Rotation measure versus MJD. CHIME/FRB measurements (Mckinven et al. 2023; Ng et al. 2025) are shown in red circles and LOFAR measurements (Gopinath et al. 2024) are shown in green diamonds. GMRT points, shown in blue squares, are the fitted RM values presented in Table 1.

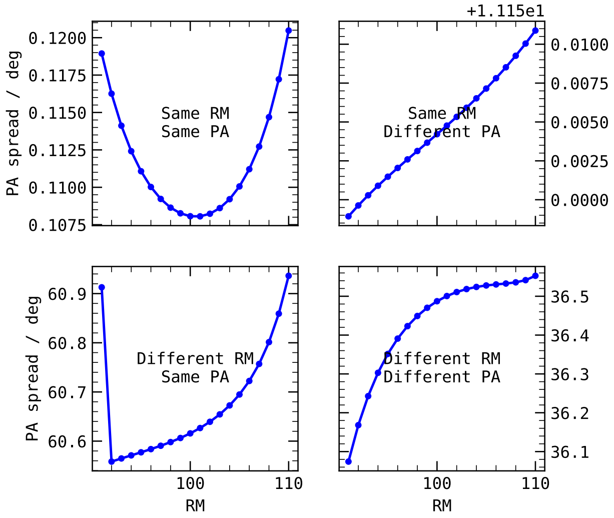

Fig. B.5. Showing by means of simulation that spread in PA is only minimized when bursts have a non-varying RM and PA. We simulated 15 bursts with same RM and same PA *(top left)*, same RM but different PA *(top right)*, different RM but same PA *(bottom left)*, and different RM and different PA *(bottom right)*. In each of the cases, we corrected for one RM and measured the spread in PA after correction, which is plotted with blue dots in each of the subplots. The spread in PA is greatly minimized and appears similar to a parabola only in the case of same RM and same PA.

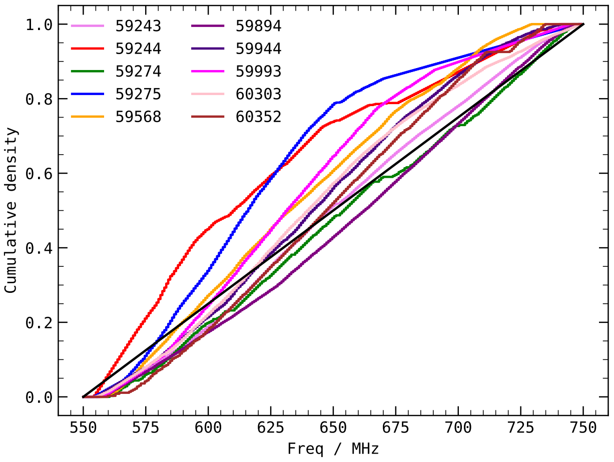

Fig. B.6. Cumulative distributions of the bursts of an observation over frequency band. The black bold line is the cumulative uniform distribution. Bursts from every observation occupy the whole observing band.

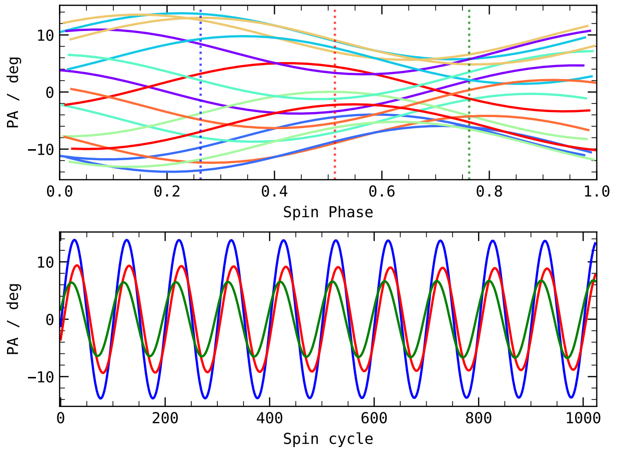

Fig. C.1. Position angles measured using a mock model of slow precession. The parameters of the models are as follows: $\delta = 10, \Psi_0 = 10, \alpha = 4, \phi_0 = 200$ and $\zeta = 90$ where all the angles are in degrees. *Top* shows PA versus Spin phase for different Spin cycles using different colors. The three vertical dotted lines mark the Spin phases chosen to show PA versus Spin cycle in the *bottom* panel. See Sect. 4.3.

List of Figures

List of Tables

List of publications

This thesis is built on the following publications

- S. Bethapudi, L. G. Spitler, R. A. Main, D. Z. Li, and R. S. Wharton (2023), *High frequency study of FRB 20180916B using the 100-m Effelsberg radio telescope*, MNRAS **524**.3 3303, https://doi.org/10.1093/mnras/stad2009, arXiv: `2207.13669 [astro-ph.HE]`
- S. Bethapudi, L. G. Spitler, D. Z. Li, V. R. Marthi, M. Bause, R. A. Main, and R. S. Wharton (2025b), *Rotation Measure study of FRB 20180916B with the uGMRT*, A&A **694**, A75 A75, https://doi.org/10.1051/0004-6361/202452221, arXiv: `2409.12584 [astro-ph.HE]`
- S. Bethapudi, D. Z. Li, L. G. Spitler, V. R. Marthi, M. L. Bause, R. A. Main, and R. S. Wharton (2025a), *Constraining the origin of the long-term periodicity of FRB 20180916B with polarization position angle*, A&A **702**, A248 A248, https://doi.org/10.1051/0004-6361/202556347, arXiv: `2507.07651 [astro-ph.HE]`

Other publications include

- V. R. Marthi, S. Bethapudi, R. A. Main, H. H. Lin, L. G. Spitler, R. S. Wharton, D. Z. Li, T. Gautam, U. L. Pen, and G. H. Hilmarsson (2022), *Burst properties of the highly active FRB20201124A using uGMRT*, MNRAS **509**.2 2209, https://doi.org/10.1093/mnras/stab3067, arXiv: `2108.00697 [astro-ph.HE]`
- R. A. Main, G. H. Hilmarsson, V. R. Marthi, L. G. Spitler, R. S. Wharton, S. Bethapudi, D. Z. Li, and H. H. Lin (2022), *Scintillation time-scale measurement of the highly active FRB20201124A*, MNRAS **509**.3 3172, https://doi.org/10.1093/mnras/stab3218, arXiv: `2108.00052 [astro-ph.HE]`
- R. A. Main, S. Bethapudi, V. R. Marthi, M. L. Bause, D. Z. Li, H. H. Lin, L. G. Spitler, and R. S. Wharton (2023), *Modelling annual scintillation velocity variations of FRB 20201124A*, MNRAS **522**.1 L36, https://doi.org/10.1093/mnrasl/slad036, arXiv: `2212.04839 [astro-ph.HE]`
- A. B. Pearlman, P. Scholz, S. Bethapudi, J. W. T. Hessels, V. M. Kaspi, F. Kirsten, K. Nimmo, L. G. Spitler, E. Fonseca, B. W. Meyers, I. H. Stairs, C. M. Tan, M. Bhardwaj, S. Chatterjee, A. M. Cook, A. P. Curtin, F. A. Dong, T. Eftekhari, B. M. Gaensler, T. Güver, J. Kaczmarek, C. Leung, K. W. Masui, D. Michilli, T. A. Prince, K. R. Sand, K. Shin, K. M. Smith, and S. P. Tendulkar (2025),

Multiwavelength constraints on the origin of a nearby repeating fast radio burst source in a globular cluster, Nature Astronomy **9** 111, https://doi.org/10.1038/s41550-024-02386-6, arXiv: `2308.10930 [astro-ph.HE]`

Summary

Background

Fast Radio Bursts (FRBs) are transient emissions from extragalactic sources in radio wavelengths. The emissions have durations of milliseconds and bandwidths of hundreds of MHz. Propagation through the cold, tenuous plasma causes dispersion much like how visible light splits into its components when propagating through a prism. The amount of dispersion suffered by the light is a proxy for the distance traveled. In case of FRBs, the large amounts of dispersions unequivocally suggest extragalactic origin. In addition, large flux densities of the bursts despite large distances suggest these bursts to be extremely energetic events. The first FRB was discovered serendipitously in 2007 with the Parkes radio telescope. It was an extremely bright event with flux density of 30 Jy[1]. Multiple follow-up efforts post its discovery did not yield any more detections, suggesting the event to be an one-off event. This discovery raised enough interest within the community that searches for new FRBs were undertaken. Which, in turn, yielded new FRB events.

The one-off nature of FRBs quickly came under test with the discovery of first repeating FRB source, FRB 20121102A. That is, the FRB source emits multiple bursts not just in one, but multiple observing sessions. It opened the possibility that FRB sources need not only be of one-off nature. Detection and subsequent study of multiple bursts from the same source allowed for a much detailed study of the FRB phenomena. Detection of bursts by interferometers made it possible to localize the FRB source on fine angular scales, which, in turn, made it possible to study the FRB source across different wavelengths. It allowed for the tracking of many observables from not just along temporal axis, but also over frequency axis. Some of the observables include dispersion measure (DM) which accounts for the total electron density along the line of sight, rotation measure (RM) which accounts for the product of magnetic field and electron density along the line of sight, Position Angle (PA) which is the orientation of the linear polarization component of the burst and et cetera. The temporal variability of such observables have been greatly studied as these provide an insight and help constraint the local environments of the FRB source. However, the same could not be said for one-off FRBs as they only provid one measurement.

Despite continuing efforts, the number of known FRBs was scarce due to the lack of a dedicated FRB search telescope which can search for FRBs across large swaths of sky simultaneously. With the commissioning of large field-of-wide blind search instruments, such as Canadian Hydrogen Intensity Mapping Experiment/Fast Radio Burst (CHIME/FRB), discovery rates of FRBs skyrocketed. Soon after, multiple new FRB repeating sources were also discovered. Discovery of tens of repeating FRB sources and hundreds of apparent non-repeating FRB events begged the question if there is any fundamental difference

---

[1] 1 Jy ≡ 10^{-26} W m^{-2} Hz^{-1}.

between the two populations. More importantly, it brought forth the question of how such astronomical sources produce multiple bursts, which till date is yet to be answered.

Fast Radio Burst 20180916B is a repeating FRB discovered by the CHIME/FRB. Bursts from this FRB appear only in active window that is periodic with 16.34 days. However, bursts do not show any periodicity in seconds or hours timescale. It is one of the two repeating FRBs which are known to have periodic active windows. The FRB source was localized to the outer edge of a quiescent spiral galaxy, situated at a redshift of 0.0337. Bursts from this FRB source were observed to have downward drifting structure, which has also been seen in other repeating FRBs, such as FRB 20121102A. Moreover, they possessed extremely high linear polarization fractions, and have been detected from 100 MHz to 6 GHz. HI spectral line study showed the FRB source location to be in the middle of two opposing velocity fields, already suggesting the FRB source environment to be unique. Many diverse progenitor models came forward to explain the periodic nature of the active windows, however, no consensus has been reached yet.

This thesis

This thesis focuses on high frequency and polarimetric studies of FRB 20180916B. Low frequency ($\lesssim$ 1 GHz) studies of the FRB 20180916B showed the active window depends on the observing frequency. At lower frequencies, the active window becomes longer and starts late. Whereas, at higher frequencies, the active window becomes narrower and starts early. The frequency dependency of the active window is termed as “chromaticity”. Chromaticity, in addition to periodicity, becomes harder to explain and requires special configurations within the models. Polarimetric studies which tracked the RM of the bursts showed characteristic RM evolution. RM measurements since the discovery up to an epoch only varied stochastically, post which started to vary secularly in a linear fashion. Such a stochastic-secular varying trend was not seen in other repeating FRBs, and further complicated the source models of this FRB.

The first work of this thesis starts by modeling the dependency of active window on frequency with power laws using burst detections at low frequencies ($\lesssim$ 1 GHz). Then, the models are extrapolated to high frequencies to predict the active windows at 4 – 8 GHz. Observations using the 100-meter Effelsberg Radio Telescope were conducted within the predicted active windows, which led to the first high frequency detection of bursts of this FRB. The high frequency detections confirmed the chromatic behavior of the active windows (Fig. 3.9). Moreover, they revealed a frequency dependency in the burst morphology that bursts at high frequencies are broadband but narrower in time, compared to those at lower frequencies (Fig. 3.4). Observables measured from the high frequency detections corroborated with their low frequency counterparts. For example, burst rates (Fig. 3.3), scintillation bandwidth (Fig. 3.1), and linear polarization fractions (Fig. 3.10).

The second work of this thesis involves tracking the RM evolution of the FRB 20180916B using bursts detected by the upgraded Giant Metrewave Radio Telescope (uGMRT) in the 550-750 MHz band. To this end, first a polarization calibration strategy was designed that works with uGMRT data. Then, a RM measurement strategy was implemented and used to measure RM from the detected bursts. Continuous tracking of the RM measurements revealed the secular variations, which was reported in earlier works, ceased, and the RM has started to again vary stochastically (Fig. 3.11). The RM trend seen as part of this work, was also corroborated by CHIME/FRB. Moreover, observations with uGMRT allowed for studying burst statistics against burst fluences, which revealed a steep drop in rate at higher fluences (Fig. 3.2).

The third and final work of this thesis studies the orientation (or Position Angle) of the linear polarized component of the bursts of FRB 20180916B. It uses the same dataset as was used in the RM study, but focuses solely on studying PA variations. It first notes that RMs and PAs of bursts detected within an observation are consistent with one single RM and PA measurement. That is, RM and PA do not vary within an observation. Therefore, all the PA measurements from an observation are averaged and further compared. But to consistently compare PAs from different observations and through different RMs, the observation averaged PA measurements were compensated for per-observation offsets and brought to infinite frequency. All subsequent PA variability was performed using these measurements. This study conclusively revealed that (O_1) variability of PAs was constrained to be less than 7 degrees within four hours, and tentatively revealed (O_2) variability of PAs within an active window was constrained to be of the order of few degrees per hour and (O_3) variability of PAs from one active window to another at the same activity phase was constrained to be around 0.1 degree per day.

The PA studies, done as part of the third work of this thesis, are particularly useful in constraining the origin of the active window periodicity of FRB 20180916B. PA variability can be directly tied to the dynamics of the FRB emitting source, by means of which, its dynamics can be probed. This way, those models which use dynamics such as rotation or precession to explain the active window periodicity can be directly tested. Given the observed PA variability O_1, precession based models can be directly ruled, as these models predict PA variations on seconds timescales. While rotational models are supported by O_1, they are disfavored by O_2 and O_3. But since, O_2 and O_3 are tentative at this point, testing rotational models shall be taken up in future work.

It is for the first time that long term PA studies led to constrains on the progenitor models of FRB 20180916B. Although long term PA variability is not robustly studied, it is naturally going to be the focus of the future work. In addition to continuing tracking the PA variations of FRB 20180916B, similar efforts for other repeating FRBs would also prove to be equally illuminating. Lastly, the O_3 or the slow active window to window PA variability at the same phase, which is of the order of 0.1 degree per day, seems to agree very well with a similar form of variability seen in a X-ray neutron star binary system, Hercules X 1, that has been measured in X-ray polarimetric studies. This connection seen in PA studies in radio and X-ray can be particularly helpful in providing new insights into FRB 20180916B.

Acknowledgements

i dedicate my thesis to my dead father, Rajasekhar Bethapudi, who is never going to read it. He cared for me, entertained my curiosity, and always supported me no matter the cost.

My mother, Ramadevi Bethapudi, who was there and not there; She supported me as much as she could. i hope she finds some pride and consolation from this thesis.

My middle school science teacher, N. Soundarajan: i want to be as good a teacher as you were for me.

My Bachelors research advisor, Shantanu Desai: you showed me the path which led to this thesis.

My Masters advisor, Matthew Kerr: you enabled me to explore my ideas and advised me about the this PhD opportunity.

My PhD advisor, Laura Spitler: thank you for letting me be as independent and as reckless as i wanted to be. i felt truly free during my PhD.

My pod squad from Bachelors - *White House*: Kunal Kakade, Aman Patel, Mohit Pathak, Kunal Sahu. Playing Counter Strike with you all during the pandemic when i was new in Germany helped me a lot.

My brother during Bachelors, Sanjan Prakash: i genuinely thank you for the brotherhood.

My Brownsville friends: Yiqian Qian (Benny Albert) and Weihui Wang (sempai). My stay in Brownsville would not have been so memorable without you two. Being roommates with Benny was so much fun. Sempai's support, especially when i was moving to Germany, is something i greatly cherish.

My dear friend Jaswanth Subramanyam: You enrich my life with your presence and your friendship. This thesis would not be what it is without all the experiences and activities and things we shared and did.

Andrei Kazantsev: i will not forget the Köln Karneval of 2023 and the Desi Night in Düsseldorf. i will also not forget the support you lend even without being asked. Du bist ein echter Freund.

Joscha Jahns-Schindler: The 21 days of Korea trip during the FRB2022 conference is something i will never forget. Du hast mich ausgehaltet und das ist leider nicht einfach.

Sarwar Khan: Cochem retreat, Dresden hiking, tere ghar ke parties and late night mein city ghumne jana. Yeh saab nice memories hai which helped me through my journey.

Mein liebe Nicole: Wir hatten uns wegen unseres Vermieter getroffen. Du wohntest in dem 2 Etage und ich in der Keller. Wir hatten vielmals geredet, Plans gemacht und in guter Zeit, hatten uns in Partnerschaft gefunden. Alltag leben mit dir is sehr Spaß, aber manchmal angstrend. Du bist ein Kunst. Ein mausi, wie klein als dir, könnte nicht befunden. Diese Doktorarbeit würde nicht komplett sein, ohne ihre Unterstuztung. Die letzte 9 Monate bis zur abgeben dieser Arbeit haben mir gezeigt, dass ich dieser Arbeit ohne Sie nicht geschafft hätte.

The wonderful city of Bonn which felt like home. The river Rhine which i fell in love with. The Fiddler's pub where i had many Guinness. All of these also helped me with my thesis.

ich möchte auch ganz Deutschland danke. Es hat mich akzeptiert, mir seine Kultur gezeigt und mir die Freiheit gegeben, alles zu tun, was ich wollte. ich habe größten Respekt vor Ihnen in meinem Herz.